The impact of different industrial related abiotic stresses on maize photosynthesis

Hugo Opperman

20116772

Thesis submitted for the degree *Philosophiae Doctor* in Botany at the Potchefstroom Campus of the North-West University

NORTH-WEST UNIVERSITY
YUNIBESITI YA BOKONE-BOPHIRIMA
NOORDWES-UNIVERSITEIT

Promoter: Dr. J.M. Berner

Co-promoter: Prof. G.H.J. Krüger

November 2015

Table of contents

List of Figures

Chapter 1

Figure 3.8 A & B: Fluorescence transients normalized between steps L (0.03 ms) and K (0.3 ms). Both these partial transients were also plotted as difference kinetics, $\Delta V_{LK} = V_{LK,\ treatment} - V_{LK,\ control}$. A = IMP 52-11, B = PAN 6411.

Figure 3.9 A & B: Fluorescence transients normalized between steps $F_{0.1ms}$ and F_{1ms}. Both these partial transients were also plotted as difference kinetics, $\Delta V_{Kn} = V_{Kn,\ treatment} - V_{Kn,\ control}$. A = IMP 52-11, B = PAN 6411.

Figure 3.10 A & B: Fluorescence transients normalized between steps $F_{1\ ms}$ and $F_{10\ ms}$. Both these partial transients were also plotted as difference kinetics, $\Delta V_{Jn} = V_{Jn,\ treatment} - V_{Jn,\ control}$. A = IMP 52-11, B = PAN 6411.

Figure 3.11 A & B: Fluorescence transients normalized between steps $F_{10\ ms}$ and $F_{100\ ms}$. Both these partial transients were also plotted as difference kinetics, $\Delta V_{In} = V_{In,\ treatment} - V_{In,\ control}$. A = IMP 52-11, B = PAN 6411.

Figure 3.12 A & B: Fluorescence transients normalized between steps $F_{100\ ms}$ and $F_{300\ ms}$. Both these partial transients were also plotted as difference kinetics, $\Delta V_{Hn} = V_{Hn,\ treatment} - V_{Hn,\ control}$. A = IMP 52-11, B = PAN 6411.

Figure 3.13: Relative PSI maximum oxidation activity, expressed as $PSI_{max\text{-}ox}$, under varying O_3 concentrations for IMP 52-11 and PAN 6411.

Figure 3.14 A & B: Relative P700 (PSI) oxidation kinetics (A) and relative re-reduction kinetics of $P700^+$ (B) of IMP 52-11 and PAN 6411 under varying O_3 concentrations.

Figure 3.15 A & B: Multi-parametric (radar) plots showing the influence of the various O_3 concentrations on key photochemical and electron transport parameters for IMP 52-11 (A) and PAN 6411 (B).

Figure 3.16 A & B: An electron flux model showing the correlation between relative P700 oxidation rate (v_{ox}) and relative PEPc regeneration or electron transport rate (J_{max}) as a fraction of the control. Open stars depict a model of the ideal coupling correlation if 100% of PSI reduced NADPH were used for ATP formation and CO_2-assimilation. A = IMP 52-11, B = PAN 6411.

Chapter 4

Figure 4.1: Yearly average of PM in the atmosphere in the Highveld area from 1994-2012.

Figure 4.2: Suggested and reported routes of entry of nanoparticles into plants.

Figure 4.3: Schematic diagram showing the key reported nanoparticle interactions leading to plant toxicology.

Figure 4.4: Photo-catalytic action of TiO_2 which can lead to ROS formation and subsequent interactions of these ROS with organic and inorganic compounds.

Figure 4.5: Scheme, showing the locations and mechanisms of key detoxifying enzymes.

Figure 4.6 A & B: $A:C_i$ curves of the net CO_2-assimilation rate (A) versus intercellular CO_2 concentration (C_i) for various nano-TiO_2 (Figure 4.6 A) and nano-SiO_2 (Figure 4.6 B) treatments for *Zea mays L.*

Figure 4.7 A & B: Relative PEPc activity under varying nano-TiO_2 (A) and nano-SiO_2 (B) concentrations.

Figure 4.8 A & B: Relative maximal rate of PEPc regeneration capacity and electron transport with varying nano-TiO_2 (A) and nano-SiO_2 (B) concentrations.

Figure 4.9 A & B: Change in stomatal conductance (g_s; $mmol.m^2.s^{-1}$) with change in C_i under nano-TiO_2 (A) and nano-SiO_2 (B) concentrations.

Figure 4.10 A & B: Relative change in water use efficiency (WUE) with varying nano-TiO_2 (A) and nano-SiO_2 (B) concentrations.

Figure 4.11 A & B: Change in fast kinetics chlorophyll *a* fluorescence (PF) and modulated 820 nm reflection ($MR_{820\ nm}$) with varying nano-TiO_2 (A) and nano-SiO_2 (B) concentrations.

Figure 4.12 A-C: Normalisation between points O and P in PF transient, V_{OP} (Figure 4.12 A) for the different TiO_2 concentrations. Differential variable fluorescence normalized (normalized to control) between points O and P, ΔV_{OP} (Figure 4.12 B) for the different TiO_2 concentrations. Figure 4.12 A & B are both over 4 decades in time ($F_{0.03\ ms}$ to F_{300ms}). Differential normalizations between OJ, JI and IP in the PF transient are shown in Figure 4.12 C for the various TiO_2 concentrations. These are shown as a composite figure to illustrate the normalisations in 1 decade time progression ($F_{0.03\ ms}$ to $F_{3\ ms}$, $F_{3\ ms}$ to $F_{30\ ms}$ and $F_{30\ ms}$ to $F_{300\ ms}$).

Figure 4.13 A-D: Differential variable fluorescence normalized between points OK, OI and JP (Figure 4.13 A-C) to show ΔV_{OK}, ΔV_{OI} and ΔV_{JP} for the various TiO_2 concentrations. Figure 4.13 A is over 1 decade in time ($F_{0.03\ ms}$ to $F_{0.3\ ms}$), whilst Figures 4.13 B & C are over 2 decades in time ($F_{0.03\ ms}$ to $F_{30\ ms}$ and $F_{3\ ms}$ to $F_{300\ ms}$). Differential normalizations between $F_{0.01\ ms}$ to $F_{1\ ms}$, $F_{1\ ms}$ to $F_{10\ ms}$, $F_{10\ ms}$ to $F_{100\ ms}$ and $F_{100\ ms}$ to $F_{300\ ms}$ in the PF transient are shown in Figure 4.13 D for the various TiO_2 concentrations. These are shown as a composite figure to illustrate the normalisations in a 1 decade time progression.

Figure 4.14 A-C: Normalisation between points O and P in PF transient, V_{OP} (Figure 4.14 A) for the different SiO_2 concentrations. Differential variable fluorescence normalized (normalized to control) between points O and P, ΔV_{OP} (Figure 4.14 B) for the different SiO_2 concentrations. Figure 4.14 A & B are both over 4 decades in time ($F_{0.03\ ms}$ to $F_{300\ ms}$). Differential normalizations between OJ, JI and IP in the PF transient are shown in Figure 4.14 C for the various SiO_2 concentrations. These are shown as a composite figure to illustrate the normalisations in 1 decade time progression ($F_{0.03\ ms}$ to $F_{3\ ms}$, $F_{3\ ms}$ to $F_{30\ ms}$ and $F_{30\ ms}$ to $F_{300\ ms}$)

Figure 4.15 A-D: Differential variable fluorescence normalized between points OK, OI and JP (Figure 4.15 A-C) to show ΔV_{OK}, ΔV_{OI} and ΔV_{JP} for the various SiO_2 concentrations. Figure 4.15 A is over 1 decade in time ($F_{0.03\ ms}$ to $F_{0.3\ ms}$), whilst Figures 4.15 B & C are over 2 decades in time ($F_{0.03\ ms}$ to $F_{30\ ms}$ and $F_{3\ ms}$ to $F_{300\ ms}$). Differential normalizations between $F_{0.01\ ms}$ to $F_{1\ ms}$, $F_{1\ ms}$ to $F_{10\ ms}$, $F_{10\ ms}$ to $F_{100\ ms}$ and $F_{100\ ms}$ to $F_{300\ ms}$ in the PF transient are shown in Figure 4.15 D for the various SiO_2 concentrations. These are shown as a composite figure to illustrate the normalisations in 1 decade time progression.

Figure 4.16 A & B: Changes in relative partial driving force processes and accumulative relative total driving force (DF_{total}) at different nano-TiO_2 (A) and nano-SiO_2 (B) concentrations.

Figure 4.17 A & B: An electron flux model showing the correlation between relative P700 oxidation rate (v_{ox}) and relative PEPc regeneration or electron transport rate (J_{max}) as a fraction of the control. Open stars depict a model of the ideal coupling correlation if 100% of PSI reduced NADPH were used for ATP formation and CO_2-assimilation (i.e. $\varepsilon = 0$). A = nano-TiO_2, B = nano-SiO_2.

Figure 4.18: Original suggested possible charge transfer between active and non-active chlorophyll antennae. Open shapes indicate active antennae, closed shapes indicate inactive antennae and arrows indicate charge transfer. Small circles indicate infiltration sites of nano-TiO_2 amongst the chlorophyll antennae.

List of Tables

Nomenclature

A	assimilation rate
A_0	assimilation rate when no stomatal limitation exists, i.e. C_a=C_i
A_{350}	assimilation rate at normal atmospheric CO_2-concentration (360 ppm)
ABS	absorption
ABS/RC	absorption per reaction centre
ABA	abscisic acid
ADP	adenosine diphosphate
AMD	acid mine drainage
APX	Ascorbate peroxidase
ASH	ascorbic acid
ATP	adenosine triphosphate
ATPase	ATP synthase
CAT	catalase
CE	carboxylation efficiency
CET	cyclic electron transport
Chl	chlorophyll
Chl *a*	Chlorophyll *a*
Chl *b*	Chlorophyll *b*
C_a	externally applied CO_2 concentration
C_i	internal CO_2 concentration
Cyt b6f	cyctochrome b6f complex
Cyt f	cyctochrome f
D	leaf-air vapour pressure deficit
DCMU	3-(3,4-dichlorophenyl)-1,1-dimethylurea
DF_{total}	total driving force for photochemical activity (electron transport)
DI_0/RC	energy dissipation per reaction centre
DTT	di-thiotreitol
DW	dry weight
DHAR	dehydro-ascorbate reductase
E	transpiration rate
EC	electron carriers
ENM	engineered nano-material
EPR	electron paramagnetic resonance
ETR	electron transport rate
ETC	electron transport chain

F_d	ferredoxin
FNR	ferredoxin-$NADP^+$-reductase
F_o	initial fluorescence level (when all reaction centres are open)
F_J	fluorescence intensity at the J-step (2-3 ms)
F_I	fluorescence intensity at the I-step (20-30 ms)
$F_m = F_P$	maximum chlorophyll fluorescence level (when all reaction centres are closed)
F_V	variable fluorescence intensity
F_t	fluorescence intensity at time, t
FQR	ferredoxin-quinone-reductase
FR	far-red
g_s	stomatal conductance
g_{H20}	stomatal conductance for water vapour
g_{CO2}	stomatal conductance for CO_2
GOPX	guaicol peroxidase
GPX	glutathione peroxidase
GR	glutathione reductase
GSH	glutathione
GST	glutathione-S-transferase
I_{inc}	incident light flux
IRGA	infra-red gas analysis
J_{max}	maximal electron transport rate driving regeneration of Rubisco or PEPc
l	% stomatal limitation
LED	light emitting diode
LHC	light harvesting complex
MDHAR	monodehydroascorbate reductase
MGDG	monogalactosyl diacylglycerol
M-PEA	multifunctional plant efficiency analyser
$MR_{820\ nm}$	modulated reflection at 820 nm
MR_{min}	minima of the MR curves, maximum oxidation state of PSI
NADP	oxidized nicotinamide adenine dinucleotide phosphate
NADPH	reduced nicotinamide adenine dinucleotide phosphate
NDH	NAD(P)H dehydrogenase
NADP-ME	NADP malic enzyme
NBT	nitro blue tetrazolium
NP	nanoparticles
NRET	non-resonant electron transfer chain
NPQ	non-photochemical quenching

OEC	oxygen evolving complex
P680	primary electron donor of PSII
$P680^+$	oxidised primary electron donor of PSII
P700	primary electron donor of PSI
$P700^+$	oxidised primary electron donor of PSI
PC	plastocyanin
PEC	predicted environmental concentration
PEPc	phosphoenol-pyruvate carboxylase
3-PGA	3-phosphoglycerate
Pheo	pheophytin
PI_{ABS}	performance index for energy conservation from photons absorbed to the reduction of intersystem electron acceptors
PI_{total}	performance index for energy conservation from photons absorbed to the reduction of PSI end electron acceptors
PF	prompt fluorescence
PPFD	photosynthetic photon flux density
PSI	photosystem I
PSI_{max-ox}	maximum oxidation capacity of PSI
PSII	photosystem II
PQ	plastoquinone
PQH_2	plastoquinol
PTOX	plastoquinol terminal oxidase
PVP	poly-vinylpyrrolidone
Q_A	primary quinone electron acceptor of PSII
Q_B	secondary quinone electron acceptor of PSII
RCs	reaction centres
RC/ABS	reaction centres per absorption
RDF	response determining factors
RE	reduction of end electron acceptors
ROS	reactive oxygen species
Rubisco	ribulose 1,5-bisphosphate carboxylase/oxygenase
RuBP	ribulose 1,5-bisphosphate
SOD	superoxide dismutase
SSR	stress specific reaction
TR	photon trapping
v_{ox}	rate of PC and PSI (P700) photochemical oxidation
v_{red}	rate with which PC and PSI ($P700^+$) is re-reduced by arriving electrons from PSII

V_{cmax}	maximal rate Rubisco or PEPc carboxylation
W_a	external water vapour concentration and
W_i	internal water vapour concentration
WUE	water use efficiency
ΔpH	pH gradient across the thylakoid membrane
Γ:	CO_2-compensation point when no net assimilation exists, i.e. CO_2 uptake by photosynthesis equals CO_2 produced by respiration
$\varphi_{Po} = F_v/F_m$	maximum quantum yield of primary photochemistry
φ_{Eo}	quantum yield for electron transport
φ_{Ro}	quantum yield of electron transport from Q_A^- to the PSI end electron acceptors
ψ_{Eo}	probability that a trapped excitation moves an electron into the electron transport chain beyond Q_A^-
δ_{Ro}	efficiency of electron movement from the reduced intersystem electron acceptors to the PSI end electron acceptors
γRC	probability that a PSII Chl molecule functions as a reaction centre
ε	percentage decoupling

Declaration and Copyright statement

Declaration

I declare that no portion of the work referred to in the thesis has been submitted to obtain any other degree or qualification at any other institution.

Copyright Statement

Abstract

The impact of different industrial related abiotic stresses on maize photosynthesis:
A Thesis submitted to the North-West University (Potchefstroom campus) for the degree of *Philosophiae Doctor* – November 2015

During the past few decades, a sharp rise in industrial activity in the mineral rich Highveld region of South Africa has been seen. Together with this increase in industrial activity, an accompanying increase in urbanization is also evident. As a result of increased industrial activity and urbanization, a large increase in environmental pollution followed, which resulted in the area being declared a priority area. In this study, three distinct types of industrial related pollution sources (ionic metal species, ozone and nano-fine particle matter) were investigated in terms of their impact on maize photosynthesis. Maize was chosen because most of the maize in South Africa is produced in the heavily industrialized Highveld area. The efficiency of the partial processes of photosynthesis is often used as abiotic stress indicators.

The influence of different concentrations of Cu, Fe, Mn and Zn on PSII and PSI electron transport was investigated for a South African maize cultivar (IMP 52-11). The non-invasive (*in vivo*) techniques of chlorophyll *a* fluorescence induction (JIP-test) and modulated reflection at 820 nm (MR_{820nm}) were measured simultaneously to follow the PSII and PSI activity, respectively. We could demonstrate that both deficient and excess heavy metals concentrations resulted in significant decreases ($p \leq 0.05$) in PSII and PSI activity, which has never been presented before in so much detail. Metal deficiency induced down-regulation was attributed to a lowering in metal specific electron carriers containing these metals as co-factors, resulting in lower PSII and PSI activity.

The photosynthetic sensitivity of two popular South African maize cultivars (IMP 52-11 and PAN 6411) to chronic O_3 exposure was also investigated. Two different cultivars were used in order to determine whether or not these cultivars have similar sensitivities to O_3 induced stress. The effect of O_3 on both photosynthetic electron transport and photosynthetic gas exchange was monitoried (in parallel) by means of chlorophyll *a* fluorescence, MR_{820nm} reflection and infrared gas analysis, in both cultivars. Although a concentration dependent inhibitory effect was found in both cultivars, the data suggested that PAN 6411 was less sensitive to the chronic O_3 exposure than IMP 52-11, showing lower stomatal, mesophyll and electron transport limitation. Furthermore, a simple and novel decoupling model was proposed for the first time, with which a new parameter, ε, could be obtained. The % decoupling (ε) is indicative of the amount of decoupling (electron losses) between PSI and CO_2-assimilation.

Furthermore, chlorophyll *a* fluorescence, MR_{820nm} reflection, photosynthetic gas exchange and antioxidant capacity studies were also used to evaluate the influence of increasing concentrations of nano-TiO_2 and nano-SiO_2 foliar sprays, with regard to the photosynthetic efficiency of the IMP 52-11 maize cultivar. Both particles caused significant ($p \leq 0.05$) reductions in both the photochemical (electron transport) and biochemical (Calvin Benson Cycle) phases of photosynthesis. The negative effect of TiO_2 was ascribed to its photocatalytic activity, which induced increased ROS formation. Given that SiO_2 is rather inert, the decrease in photosynthetic efficiency at high SiO_2 concentration was attributed to the increased stomatal closure. This increased stomatal limitation caused a decrease in the electron demand for CO_2-assimilation and subsequent electron buildup. The decoupling model was used to determine ε under increasing stress conditions. The increase in ROS formation and the consequent increase in antioxidant activity, which coincided with an increase in ε, suggested that the electrons lost between PSI and CO_2-assimilation were being lost to alternative electron acceptors such as O_2.

Key words: Maize, abiotic stress, heavy metals, ozone, nanoparticles, photosynthesis, chlorophyll *a* fluorescence, photosynthetic gas exchange.

Opsomming

Die impak van verskillende industriële verwante abiotiese stresfaktore op mielies fotosintese: 'n Proefskrif voorgelê aan die Noordwes-Universiteit (Potchefstroom -kampus) vir die graad Doctor Philosophiae - Februarie 2015

Gedurende die afgelope paar dekades, het 'n skerp styging in die industriële aktiwiteit in die mineraal ryke Hoëveld-streek van Suid-Afrika plaasgevind. Saam met hierdie verhoging in die industriële aktiwiteit het 'n gepaardgaande toename in verstedeliking ook plaasgevind. Die verhoogde industriële aktiwiteit en verstedeliking het 'n groot toename in omgewingsbesoedeling teweeg gebring, wat daartoe gelei het dat die gebied tot 'n prioriteitsgebied verklaar is. In hierdie studie is drie afsonderlike tipes industriële verwante besoedelingsbronne (ioniese metaal spesies, osoon en nano-fyn deeltjies materie) ondersoek in terme van die impak daarvan op mielie-fotosintese. Mielies is gekies omdat die meeste van die mielies in Suid-Afrika geproduseer word in die swaar geïndustrialiseerde Hoëveld-streek. Die doeltreffendheid van die gedeeltelike prosesse van fotosintese word dikwels gebruik as abiotiese stresaanwysers.

Die invloed van verskillende konsentrasies van Cu, Fe, Mn en Zn op PSII en PSI elektronoordrag van 'n Suid-Afrikaanse mieliekultivar (IMP 52-11) is ondersoek. Die nie-indringende (*in vivo*) tegnieke van chlorofil *a* fluoressensie-induksie (JIP-toets) en gemoduleerde 820 nm refleksie (MR_{820nm}) is gelyktydig gemeet om PSII en PSI aktiwiteit onderskeidelik te bepaal. Beide tekort en oormaat konsentrasie toestande van swaarmetale het gelei tot beduidende dalings in PSII en PSI aktiwiteit. Metaaltekort-geïnduseerde afregulering is toegeskryf aan 'n verlaging in metaalspesifieke elektrondraers wat gelei het tot 'n verlaging in PSI en PSII aktiwiteit.

Die fotosintetiese sensitiwiteit van twee Suid-Afrikaanse mieliekultivars (IMP 52-11 en PAN 6411) t.o.v. chroniese O_3 blootstelling is ook ondersoek. Die effek van O_3 op fotosintetiese elektronoordrag en fotosintetiese gaswisseling is gemeet met behulp van chlorofil *a* fluoressensie, MR_{820nm} refleksie en fotosintetiese gaswisseling. Alhoewel 'n konsentrasie afhanklike inhiberende effek in beide kultivars bevind is, het die data daarop gewys dat PAN 6411 minder sensitief vir die chroniese O_3 blootstelling as IMP 52-11 was. Hierdie verskynsel is toegskryf aan 'n geringer mate van huidmondjie-, mesofil- en elektronoordragbeperking. 'n Nuwe eenvoudige fotosintetiese ontkoppelingsmodel is voorgestel, waardeur 'n nuwe parameter, ε, verkry kon word . Die % ontkoppeling (ε) is 'n aanduiding van die heoveelheid ontkoppeling (elektron verliese) tussen PSI en CO_2-assimilering.

Chlorofil *a* fluoressensie, MR_{820nm} refleksie, fotosintetiese gaswisseling en anti-oksidant kapasiteitsstudies is ook gebruik om die invloed van toenemende konsentrasies nano-TiO_2 en nano-SiO_2 blaarbespuitings op die fotosintese van die IMP 52-11 mieliekultivar te evalueer. Beide deeltjies

het 'n verlaging in die fotosintetiese doeltreffendheid veroorsaak. Die negatiewe effek van TiO_2 is toegeskryf aan die fotokatalitiese aktiwiteit wat verhoogde huidmondjie-opening en 'n toename in ROS-vorming veroorsaak het, a.g.v. TiO_2 se vermoë om as elektronskenker op te tree. Gegewe dat SiO_2 inert is, is die afname in die fotosintetiese doeltreffendheid by hoë SiO_2 konsentrasies toegeskryf aan verhoogde huidmondjiesluiting wat 'n afname in elektron aanvraag deur CO_2-assimilering veroorsaak. Die ontkoppelingsmodel was weereens gebruik om ε te bepaal onder toenemende nano-deeltjie konsentrasies. Die toename in ROS vorming en antioksidant aktiwiteit, tesame met 'n toename in ε, het daarop gewys dat die elektrone wat verlore raak tussen PSI en CO_2-assimilering, aan alternatiewe elektronontvangers soos O_2 geskenk is.

Sleutel woorde : Mielies, abiotiese stres, swaar metale, osoon, nanopartikels , fotosintese , chlorofil *a* fluoressensie, fotosintetiese gaswisseling.

Acknowledgements

I herein express my sincerest gratitude towards:

- My Heavenly Father, God Almighty, for bestowing me with the required cognitive ability and perseverance to complete this study.
- Faculty of Natural Sciences and the Botany department at the North-West University (NWU, Potchefstroom campus) for the use of their facilities during the study.
- The National Research Foundation (NRF) for the funding required during the study.
- My Promotors, Dr. Jacques Berner and Prof. Gert Krüger, for their continued scientific and most appreciated, moral support throughout the duration of my research, as well as their conscientious contribution to the writing of my thesis.
- Prof. Henning Krieg at the Chemistry department of the NWU, whom I've known for many years, for his valuable scientific input during this study, especially during the writing of my thesis.
- All of my family members for the continued encouragement throughout my study.
- To all my friends, especially my best friend Jacques Hepple, I want to express my deepest gratitude for keeping me sane through the difficult and stressful times!
- A special thank goes to my mother, who fell ill during this study, for 28 years of unconditional love and support. I love you and wish you a speedy recovery mom.
- Prof. Reto Strasser, for his exceptional insight and contributions during my study and as a whole, for his amazing contributions to the field of photosynthesis and in particular chlorophyll fluorescence research.
- Lastly, to my loving wife, Sanmari Opperman, for her love, patience and understanding during my study. Without her I would not have been able to cope. I love you so much.

'Science is art and without art, science would just be production without fantasy.'

Reto Jörg Strasser

Chapter 1

General introduction

Chapter 1: General introduction

1. General introduction to environmental pollution

Pollution is the introduction of contaminants into the natural environment that causes adverse changes. Pollution can take the form of chemical substances or energy, such as noise, heat or light. Pollutants, the components of pollution, can be either foreign substances (anthropogenic) or naturally occurring contaminants. Although pollution had been known to exist for a very long time (at least since people started using fire thousands of years ago), it had seen the growth of truly global proportions only since the onset of the industrial revolution during the 19th century.[1,2] The industrial revolution brought with it technological progress such as discovery of oil and its virtually universal use throughout different industries. At the same time, of course, development of natural sciences led to the better understanding of negative effects produced by pollution on the environment. Environmental pollution is a problem both in developed and developing countries. Factors such as industrialization, population growth and urbanization invariably place greater demands on the planet and stretch the use of natural resources to the maximum.[1,2] Chemical substance pollution can principally be subcategorized according to the three main states of matter: i) liquid (ionic pollution such as heavy metal ions), ii) gaseous (air pollution such as ozone) and solid state matter (such as very fine metal oxide nano-particulates). All of these types of matter have been shown to have a very high prevelance in heavily industrialized/urbanized areas due to anthropogenic activities.

1.1 Enviromental stress

Any living organism is subjected to a set of environmental conditions throughout its lifespan. These conditions may be favourable for development, but in reality, these conditions are very rarely optimal. All living organisms will be subjected to sub-optimal environmental conditions at one or more occasions in their lifetime. Sub-optimal conditions can be caused by a single or a series of stress factors. To understand the reactions of a particular organism in a certain situation, individual external influences, or so-called stress factors, are usually considered separately, if at all possible. In plants, these stress factors have principally been divided into two sub-categories, i) biotic stress- and ii) abiotic stress factors.[29]

Biotic stress resulting from interactions with other organisms, are, for example, infection or mechanical damage by herbivory or trampling, as well as effects of symbiosis or parasitism. Abiotic stress factors include temperature, humidity, light intensity, the supply of water and minerals, and CO_2.[30] These are the parameters and resources that determine the growth of a plant. Stress effects and responses caused by it can be used as a measure of the strength of the stress on a scale of intensity, ranging from deficiency to excessive supply.

Many other abiotic stresses have been identified over the years and all have been found to limit 'normal' physiological function. Figure 1.1 is a schematic listing of the most common biotic- and abiotic stress factors that limit plant growth.[2] Abiotic and biotic stresses cause alterations in the normal physiological processes of all plant organisms, including the economically important crops. Plant damage and decrease in their productivity most often take place due to naturally occurring unfavourable factors of the environment (natural stress factors) - extreme temperatures, water deficit or abundance; increased soil salinity, high solar irradiance, early autumn or late spring ground frosts; pathogens etc. Recently, along with these factors plant organisms are subjected to a large scale of new stressors related to human activity (anthropogenic related stress factors) – toxic environmental pollutants such as pesticides, noxious gasses (SO_2, NO_x, O_3 and photochemical smog), photo-oxidants, soil acidification and mineral deficit due to acid rains, overdoses of fertilizers and heavy metals (Fig. 1.1).

All these stresses decrease the biosynthetic capacity of plant organisms, alter their normal functions and cause damages which may lead to plant death.[1-3]

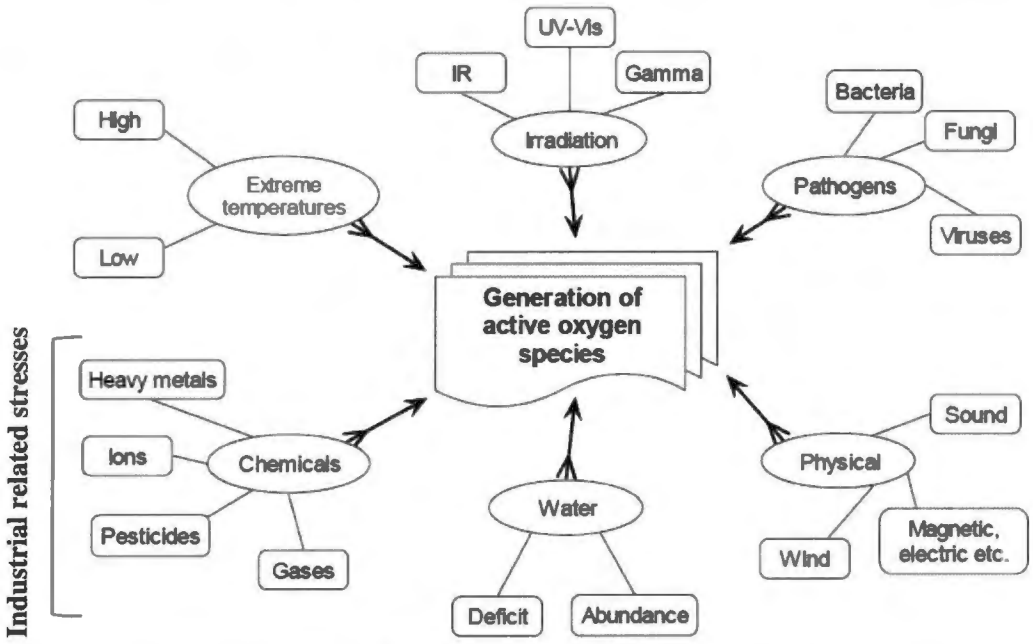

Figure 1.1: Schematic summary of most common stress conditions reported for plants.[30]

As a result of these numerous stress conditions, plants have developed certain adaptations in an attempt to minimize the limiting effect of these stresses. Under stress, a cascade of reactions take place, ranging from the activation of genes, up-regulation in the production of signalling and stress quenching compounds as well as stress avoidance mechanisms. In a typical situation, after a stress is sensed by the plant, genes are activated to produce signalling hormones (primary signalling messenger) such as abscisic acid (ABA), which elicit certain responses.[31] Inhibition of electron

transport carriers and CO_2-assimilation is often the consequence of stress conditions. The danger exists that the amount of electrons produced by the light flux exceeds the capacity of the photosynthetic apparatus (under a certain set of conditions) for photochemical energy conservation, in which case dissipative pathways become essential for avoiding photoinactivation.[33,42] The reaction center of photosystem II is a highly effective light-driven electron pump. The electrons it takes from water must be transported to and consumed by external acceptors to avoid damaging reduction of electron carriers. During photorespiration, oxygen can serve as an effective electron sink in addition to carbon assimilation, because coupled electron flow to oxygen is linked to photorespiratory ATP consumption, which leads to the formation of reactive oxygen species (ROS). Reactive oxygen species have been shown to act as secondary signalling messengers (Figure 1.1).[3] Reactive oxygen species are species of oxygen which are in a more reactive state than molecular oxygen, resulting from excitation or incomplete reduction of molecular oxygen. Generally, ROS consist of free radical ($O_2^{\bullet -}$, $RO^{\bullet}$, $HO_2^{\bullet}$, $OH^{\bullet}$) and non-radical forms (H_2O_2, $^1O_2$). For plants, ROS have certain advantages and disadvantages which appear to be concentration dependent.[31] On the one hand; they are highly reactive, toxic and harmful by-products of normal cellular metabolism, causing oxidative damage to proteins, lipids, carbohydrates and DNA, which ultimately results in cell death in plants. On the other hand, it has also been proved that ROS can affect gene expression and signal transduction pathways, which mean that cells may use ROS as biological stimuli and signals to activate and regulate various genetic stress-response processes.[33] One such genetic response is an increase in the production and activity of cellular detoxifying entities of which there are numerous. These detoxifying entities are often sub-categorized into enzymatic- and non-enzymatic detoxifying systems. Enzymatic detoxifiers include the following enzymes: superoxide dismutase (SOD), catalase (CAT), ascorbate peroxidase (APX), glutathione reductase (GR), mono-dehydroascorbate reductase (MDHAR), dehydro-ascorbate reductase (DHAR), glutathione peroxidase (GPX), peroxidase (POD) and glutathione-S-transferase (GST). Non-enzymatic compounds such as ascorbic acid (ASH), proline, glutathione (GSH), phenolic compounds and several amino acids which also play a vital role in protecting plants from oxidative damage.[32]

As mentioned earlier, the production of ROS is part of the normal metabolic processes and the natural detoxifying systems of the plant keep the damage caused by ROS in check, but once under stress, the rate of ROS production can increase dramatically. When this happens, these detoxifying systems can become overwhelmed and can no longer effectively protect the cellular systems, resulting in oxidative damage to membrane structures, proteins, lipids, carbohydrates and DNA.[34] This causes down-regulation of the plants' metabolic processes, which ultimately leads to reduced vegetative growth, yield and finally death.

1.2 Maize in South Africa

In developing countries, such as South Africa, food security is a very real problem. Agriculture and more specifically, field-crop production stands central as a means to supply food security and self-sustenance for South Africa. Maize is the most important grain crop in South Africa, being both the major feed grain and the staple food of the majority of the South African population. About 48% of maize produced in South Africa is white and the remaining 52% is yellow maize (2013). White maize is primarily used for human consumption, while yellow maize is mostly used for animal feed production. Approximately 700 000 tons of maize was produced during the 2013 growing season. The value of maize production was on average around 50 billion rand from the 2010-2013 period.[1] Because of the large climate variations in South Africa over the various regions and provinces, only parts of South Africa is conducive to maize production.[1] Fihure 1.2 shows the major and minor maize growing regions in South Africa.

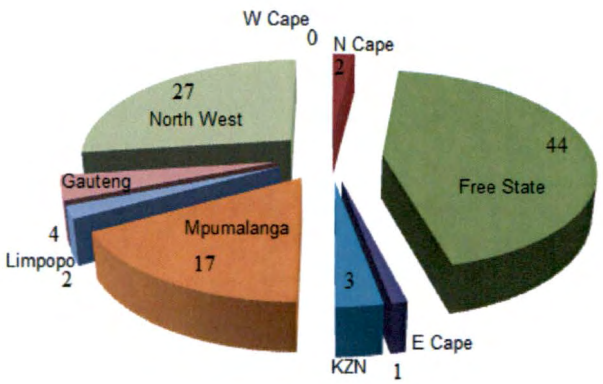

Figure 1.2: The % contribution by provinces to maize production during the 2012/13 production season.[1]

Large parts of these maize growing areas are usually subjected to large variations in rainfall and water availability, with drought (< 300 mm per annum) conditions often placing a strain on the production capacity. It therefore becomes imperative to monitor other stress conditions that can have a negative effect on crop and especially maize production. Figure 1.3 is a map showing the major maize producing areas in South Africa. In 2013, it was established by an independent survey, that PAN 6411 and IMP 52-11 were the most popular maize cultivars grown, with combined seed sales of almost 60% of the total amount sold in 2012.[10]

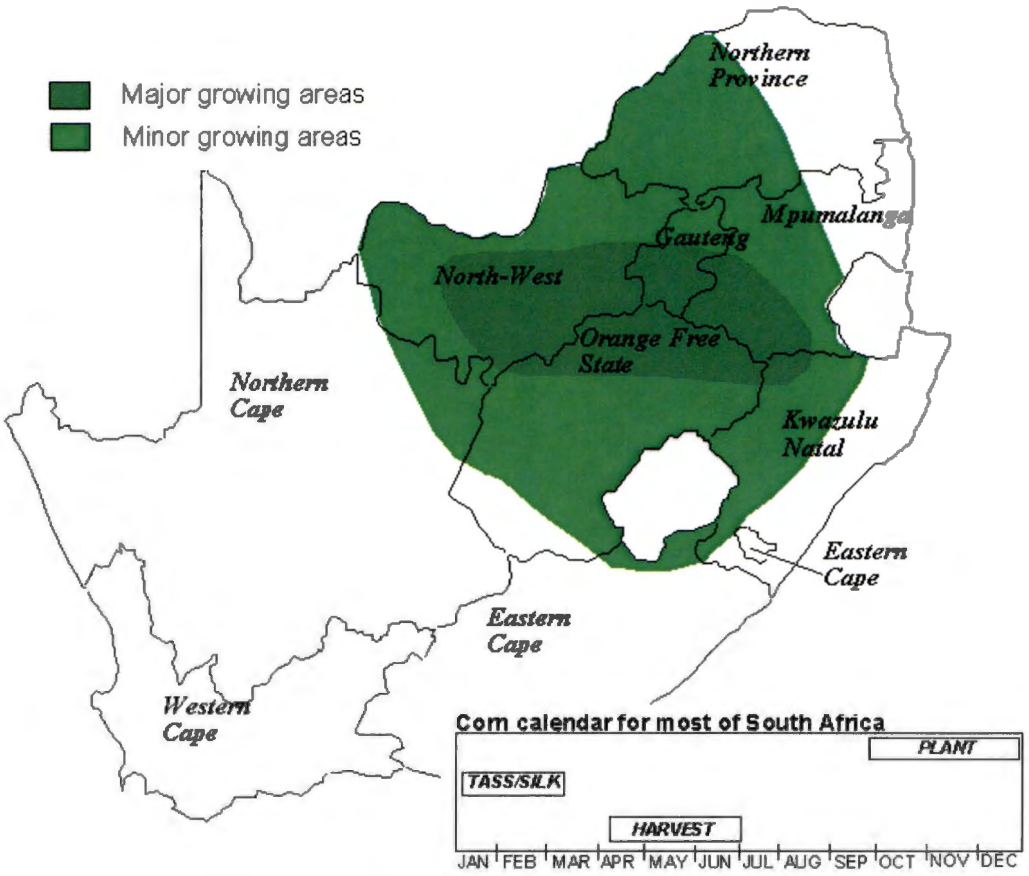

Figure 1.3: A map of the major maize producing areas in South Africa.[1]

1.3 Industrial related stress in a South African context

1.3.1 Industrial operations impacting maize production

South Africa is very rich in minerals, with a very diverse mineralogical distribution. Excavation of the rich mineral resources has led to a large increase in industrialization in South Africa over the last few decades. Industrial activities such as mining, energy production and other value adding manufacturing practices, combined with the increased development of human settlements, have placed increasing strain on the environment and agricultural land previously only used for crop- and horticulture production.[2] Most, if not all anthropogenic activities, result in the release of large amounts of waste and by-products into the environment. These industrial sectors have a very big impact on the soil, water and air qualities in the areas surrounding these industries, which place increasing strain on natural and agricultural vegetation.

1.3.1.1 Metal effluent as a source of pollution

1.3.1.1.1 Metal pollution sources in South Africa

In South Africa, metal pollution has been reported to originate from many sources. Table 1.1 shows some metal types and their pollution sources that have been reported previously.

Table 1.1: Metals types and sources of metal pollution in South Africa.[2,10,11]

Metal	Source
Cadmium	Laundrettes, electroplating workshops, plastic manufacturing, pigments, enamels, paints
Chromium	Alloys, preservatives, dying and tanning activities, metal coatings
Copper	Electronics, plating, electrical wires, paper, textiles, rubber, printing, plastic
Iron	Galvanising, electroplating, polishing
Lead	Fuel additive, batteries, pigments, roofing, fishing weights
Zinc	Domestic wastes, galvanizing, batteries, paints, fungicides, textiles, cosmetics, pulp, paper-mills, and pharmaceutics
Nickel	Alloys, electroplating, nickel-cadmium batteries, laundrettes, paints
Mercury	Dental practices, clinical thermometers, glass mirrors

Although all of these metal pollution sources may have an impact on the environment, the bulk of the metal pollution originates predominantly from the mining sector in South Africa, where processes such as acid mine drainage (AMD) have been identified as a particular source of concern to the environment. Acid mine drainage arises primarily when the mineral pyrite ('fool's gold' or iron disulphide) comes into contact with oxygenated water.[2]

$$2FeS_2\,(s) + 7O_2\,(aq) + 2H_2O \rightarrow 2Fe^{2+} + 4SO_4^{2-} + 4H^+ \qquad (1)$$

The pyrite undergoes oxidation in a two-stage process, the first producing sulphuric acid and ferrous sulphate and the second orange-red ferric hydroxide and more sulphuric acid. Pyrite is a common minor constituent in many mineral deposits and is associated with South African coal (it is the main host of sulphur in coal, the source of acid rain) and the gold deposits of the Witwatersrand Basin. During normal weathering of these mineral deposits, acid is produced through oxidation at a very slow rate, so slow that natural neutralisation processes readily remove the acidity. However, during mining and mineral extraction, the rock mass is extensively fragmented, thereby dramatically increasing the surface area and consequently the rate of acid production. Certain host rocks,

particularly those containing large amounts of calcite or dolomite, are able to neutralise the acid. This is not the case for South African coal and gold deposits in which these the natural neutralising processes are overwhelmed and large quantities of acidic water are released into the environment by mining activities, initially into the groundwater and ultimately into streams and rivers. The acidic water increases the solubility of base metal such as aluminium, copper, manganese, zinc, iron and other heavy such as lead and cadmium, depending on the metals which may be present in the affected region. The overall effect is to render the waste water toxic to varying degrees. Rainwater falling on the dumps oxidises the pyrite, forming sulphuric acid which percolates through the dump, dissolving heavy metals in transit, emerging from the base of the dump to join the local groundwater as a pollution plume. This polluted water ultimately emerges on the surface in streams draining the areas around the dumps. Streams draining the tailings dumps are therefore typically acidic and have high sulphate and heavy metal concentrations. Ultimately, the water becomes neutralised by a combination of dilution and reaction with river sediment or various minerals in soils, but certain constituents have relatively high solubilities and remain in the water, particularly sulphate.[3]

The distribution of South Africa's coal and gold mines (which are the primary sources of AMD) are primarily situated in the maize growing areas. South African coal occurs in layers within sedimentary rocks of the Karoo Supergroup. These are widespread, but coal mining is for the large part restricted to the provinces of Kwazulu-Natal, Gauteng, North West and Limpopo.[4] South African gold occurs in layers of conglomerate rock which form part of the approximately 7000 m thick sequence of sedimentary rocks of the Witwatersrand Supergroup. The layers average about a metre in thickness. The conglomerates are not uniformly gold-bearing and only in certain localised areas are gold present in economically recoverable concentrations. These areas form the goldfields and within any individual goldfield, only a few of the conglomerate layers have been mined.[2,4] These goldfields mainly stretches over large areas of the Gauteng, North West and Free State provinces, which coincides with the largest maize growing areas in South Africa (see Fig 1.3 & Fig 1.4). Table 1.2 shows some sources and types of metals that have been identified in the several sub-basins in South Africa.

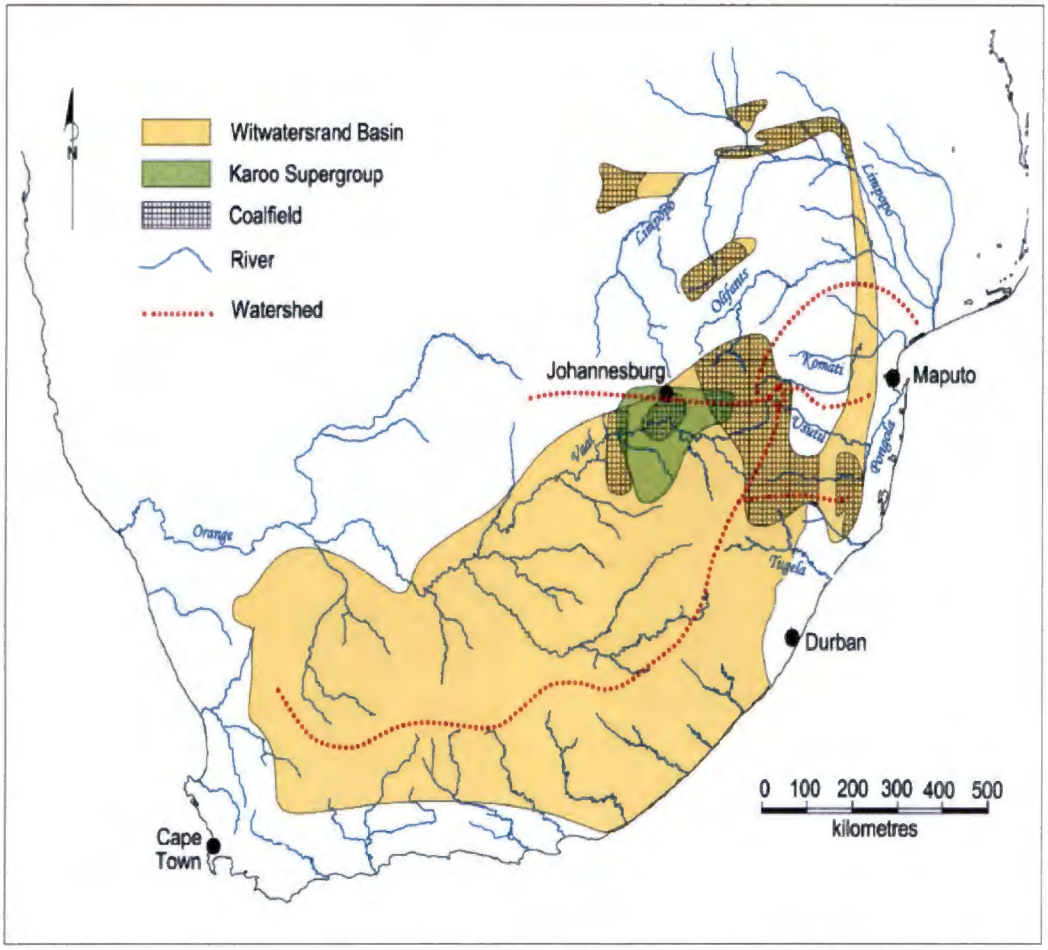

Figure 1.4: The distribution of coal an gold mines within the Karoo Supergroupand and Witwatersrand basin.[2]

Table 1.2: Identified locations and metal types that have been found to cause pollution in the several sub-basins in South Africa.[10,11]

Sub-basin	Type of Mining	Water Quality Issues
Motloutse	Base metals, smelters	Copper, nickel
Shashe	Gold, base metals, smelters, alluvial gold	Bismuth, copper, nickel, mercury
Mzingwane	Gold, base metals, small-scale	Arsenic, cobalt, mercury, nickel
Mwenezi	Small-scale, other (emerald)	Chromium
Marico	Base metals, smelters, other	Chromium, lead, zinc
Crocodile	Gold, base metals, smelters, other	Copper, chromium, iron, lead, manganese, silver, zinc
Laphalala	Base metals, other	Lead, tin,
Theuniskloof	Base metals, other	Iron, manganese
Mogalakwena	Gold, base metals, smelters, other	Antimony, tin
Sand	Small-scale	Copper, mercury, nickel, zinc
Nzhelele	Other	Lead, nickel
Riet & Little Olifants	Base metals, smelters	Copper, iron, manganese
Middle Olifants	Gold, base metals, other	Chromium, copper, iron, manganese, tin, zinc
Steelpoort	Base metals, smelters	Chromium, copper, iron, manganese, molybdenum, vanadium
Selati	Gold, base metals, smelters, other	Antimony, arsenic, cadmium, copper, iron, manganese, mercury, zinc
Middle Letaba and Great Letaba	Gold, base metals, small-scale, other	Antimony, arsenic, iron, mercury, tin
Shingwedzi	Gold, small-scale	Arsenic, mercury

Once in the river and soil water, these solubilized metal constituents can have a profound impact on the health of the surrounding vegetation such as maize.[2,3] These metals are persistent and tend to accumulate in the environment, especially in the sediments. The chemical characteristics of metals are responsible for the fact that all metals ultimately become toxic at elevated concentrations.[9] Abnormally high concentrations can cause the inability of organisms to excrete, sequester or

otherwise detoxify themselves, especially in the case of non-essential metals. They can also become strongly enriched in the aquatic food chain, through a process referred to as bio-magnification. Organisms can accumulate metals to levels above those which are required for normal physiological functioning.[9] The measurement of metal concentrations in these organisms provides the basis for the use of bio-accumulative indicators of the degree of metal pollution in various aquatic ecosystems.

The quality of the water that decants from mine voids is extremely poor, as can be seen from the water discharging from the Western Basin. The sulphate concentration is typically around 3500 $mg.L^{-1}$ and the pH ranges between 2 to 3. The water has high concentrations of iron and other base metals, often reaching metal concentrations of up to 70-130 $mg.L^{-1}$ in water sources adjacent to the mine areas as well as water sources that are fed by AMD runoff streams.[9] Depending on the chemical mass of the element; this translates to roughly 0.1-0.5 mM of metal concentration in the water. It must be noted that these values vary greatly, depending on the rainfall, AMD rate, mining production activity, soil and water pH as well as the distance from the pollution source.

1.3.1.1.2 Effect of metal pollution on plants and the environment

Metals can be present in the environment either as ions, complex molecules, or in combination with other metals or particulates as colloids and precipitates.[10] There are several factors that determine how toxic a metal is to the biological receptors and how far a metal can travel from its source. Toxicity depends on the type of metal, the chemical interactions of the metal with other metals and the presence of organic compounds which may increase the bio-availability and spread of the toxic metal.[11] The flow rate and volume of water, the physical make-up of sediments, water temperature, oxygen, pH and salinity also influences: (i) how toxic a metal is in a given environment; (ii) determines the speciation (the proportion of metals in different forms); and (iii) the mobility of the heavy metals.[10,11]

Soil and water contamination by heavy metals is a major concern because at high concentration they can harm human life and the environment.[12] Once heavy metals are deposited in the soil and water systems, they are not degraded and persist in the environment for a long time and cause serious environmental pollution.[12] They accumulate in soils and plants and would have a negative influence on physiological activities of plants such as photosynthesis, gaseous exchange and nutrient absorption (competition between the absorption of metals can cause deficiencies), resulting in a reduction of plant growth and dry matter accumulation.[13]

To understand the mode of action leading to heavy metal toxicity in living cells, their chemical properties have to be considered. Most of the heavy metals are transition metals with an incompletely filled δ-orbital present as cations under physiological conditions. The physiological redox range of

aerobic cells stretches from –420 mV to +800 mV.[13] Therefore, heavy metals of biological significance can be divided into two groups of redox active and inactive metals. Metals with lower redox potentials than those of biological molecules can not participate in biological redox reactions. Auto-oxidation of redox active metals such as Fe^{2+} or Cu^{2+} results in $O_2^{\bullet-}$ formation and subsequent H_2O_2 and $OH^{\bullet}$ production, via the Fenton-type reactions. Cellular injury by this type of mechanism is well documented for iron. Many enzymes contain metals in positions important for their activity. The displacement of one metal by another will normally also lead to inhibition or loss of enzyme activities. Divalent cations such as Cu^{2+}, Mn^{2+} and Zn^{2+} were found to displace Mg^{2+} in ribulose-1,5-bisphosphate-carboxylase/oxygenase and resulted in loss of activity.[4] Displacement of Ca^{2+} by Cd^{2+} in the protein calmodulin, important in cellular signalling, led to an inhibition in the calmodulin-dependent phosphodiesterase activity in radish.[13] These examples show that, according to their chemical and physical properties, three different molecular mechanisms of metal toxicity can be distinguished: (i) production of reactive oxygen species by auto-oxidation and Fenton reaction, (ii) blocking of essential functional groups in biomolecules and (iii) displacement of essential metal ions from biomolecules. More information on the effect of some of the effects of metals on plant growth will be given in Chapter 2 of this thesis.

1.3.1.2 Atmospheric pollution originating from industrial activities

Industrial activities, urbanization around heavily industrialized areas and the increased energy demand of these events, have contributed to significant increases in atmospheric pollution, especially around these industrialized areas.[5] The large number of industries in South Africa are responsible for a magnitude of atmospheric emission sources.[6] Coal-fired power stations and other volatile chemical manufacturing industries are the main source of atmospheric emissions. The most abundant emissions are nitrogen oxide (NO_x), sulphur based gasses, which includes sulphur dioxide (SO_2), hydrogen sulphide (H_2S), volatile organic compounds (VOC's), ammonia (NH_3) and ozone (O_3).[6] Two gasses which have received particular attention, because of their propensity to cause serious limitations on vegetation growth, are SO_2 and O_3.[7] For the purpose of this study, only the impact of O_3 will be discussed in more detail.

1.3.1.2.1 Ozone

Unlike other gaseous pollutants, O_3 forms naturally when sunlight interacts with oxygen molecules (photochemical reaction) in the stratosphere (10-50 km above the ground) to form a three-atomic molecular combination of oxygen (O_2). UV-sunlight of a short wavelength is used to complete this photochemical reaction.[8] In the troposphere (< 10 km above the ground), O_3 is formed by a photolytic

reaction involving NO_x and VOC's. Ozone is formed when excessive amounts of NO_2 is broken down (photolysis) through a reaction catalysed by light with a wavelength (λ) shorter than 400 nm,

$$NO_2 + h\nu\ (\lambda < 400\ nm) \rightarrow NO + O \quad (2)$$

whereafter, molecular oxygen reacts with molecular di-oxygen (O_2) to form O_3.

$$O^{2-} + O_2 \rightarrow O_3 \quad (3)$$

Furthermore, tropospheric O_3 can also be formed through the photolysis of VOC's, where hydroxyl radicals ($OH^{\cdot}$) are formed. These free radicals catalyse the oxidation of moderately oxidised volatile organic species (such as aldehydes), which in the presence of NO_x, forms O_3 as a by-product.[8]

Critical levels for O_3 are defined on the basis of expression by a cumulative exposure over a threshold concentration for a given length of time. The general critical threshold concentration is considered to be at 40 ppb. From there the term AOT40 (accumulated exposure over a threshold of 40 ppb) was derived. The AOT40 is mathematically expressed and calculated as follows:[8]

$$\text{AOT40} = \sum_{i=1}^{n} (CO_3 - 40) \text{with } O_3 > 40 \text{ ppb}$$

1.3.1.2.2 Ozone as pollution source in South Africa

Ozone measurements at various O_3 monitoring Highveld sites have reported maximum hourly mean concentrations in the range of 76 to 110 ppb.[14] The results of a more recent long term study published in 2013, which measured the O_3 concentration at various sites around South Africa, found that the hourly mean could reach up to 130 ppb, proving that the increase in industrialisation in South Africa has a definite effect on the O_3 levels.[15] In Figure 1.4, it is clear that the regions that have the highest monthly average O_3 concentrations, also coincides with the major maize producing areas in South Africa (also see Figure 1.3).

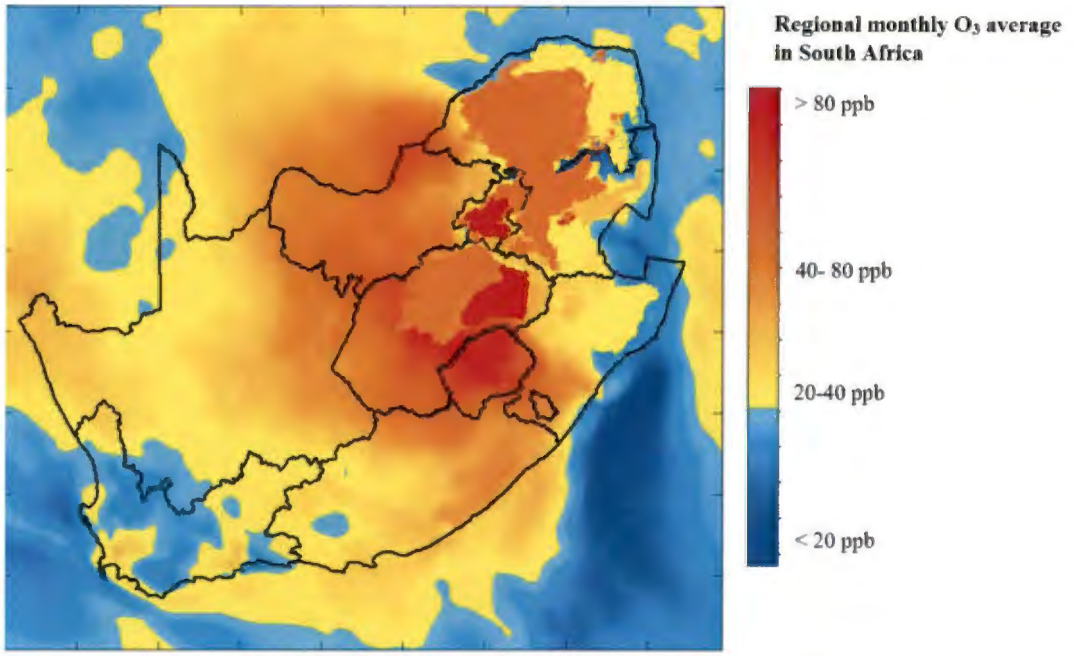

Figure 1.5: Model mof the regional ozone distribution in South Africa in 2013.[14]

1.3.1.2.3 Ozone as plant stress

Previous studies have reported that 2-4 hours exposure times with a O_3 concentration > 50 ppb have certain negative effects on plant growth and development.[14] It is however important to note that the threshold dose of O_3 that causes injury, varies greatly between species and even cultivars of the same species.[17] Furthermore, plant responses to air pollutants also vary with varying climatic conditions. In hot, dry climates the responses may be influenced by water and temperature stresses, which can even protect plants from air pollutants. For example, in drought conditions, plants respond to water stress by closing their stomata in order to reduce the loss of water by transpiration. Subsequently, the uptake of air pollutants decreases and damage to plants is reduced.[17] A more detailed description on the uptake and effect of O_3 on plants will be given in Chapter 3 of this thesis.

1.3.1.3 Nano-sized particulate matter as environmental pollutant

1.3.1.3.1 Nanoparticle sources and classification

Particles and suspended particle matter (SPM's) in the very fine (nano-sized) range have been present on earth for millions of years and have been used by mankind for thousands of years. Soot for instance, as part of the Black Carbon continuum, is a product of the incomplete combustion of fossil fuels and vegetation; it has a particle size in the nanometer to micrometer range and therefore falls partially within the ''nanoparticle'' domain. Recently, nanoparticles (NP) have attracted a lot of attention because of our increasing ability to synthesize and manipulate such materials. At present,

nanoscale materials find use in a variety of different areas such as electronic, biomedical, pharmaceutical, cosmetic, energy, environmental, catalytic and material applications. Because of the potential of this technology there has been a worldwide increase in investment in nanotechnology research and development. Table 1.3 shows the composition, origin and examples of the most commonly identified nanoparticles.

Table 1.3: Classification of the most commonly found nanoparticles.[19]

Occurence	Composition	Origin	Examples
Natural	Carbon containing	Organic colloids	Humates, fulvates
		Organism	Viruses
		Soot	Fullerenes
		Aerosols	Organic acids
	Inorganic	Oxides	Magnetite
		Metals	Ag, Au
		Geogenic oxides	Fe-oxides
		Clays	Allophane
		Atmospheric aerosols	Sea salt
Anthropogenic (manufactured, engineered or waste product)	Carbon containing	Combustion by-products	Carbon nano-tubes
		Soot	Fullerenes
		Polymeric NP	Polyethylene glycol
	Inorganic	Oxides	TiO_2, SiO_2
		Metals	Ag, iron
		Salts	Metal-phosphates
		Alumino-silicates	Zeolites, clays, ceramics

1.3.1.3.2 Nanoparticles in the environment

Data on the current use and production of NPs are sparse and often conflicting. One estimate for the production of engineered nanomaterials (ENPs) was 2000 tons in 2004, but this figure was expected to increase to 58,000 tons in 2010-2020.[18] A study in the United states of America found that areas that are subjected to high industrial activity, especially in the metal and cosmetic product manufacturing sectors, produce effluent containing almost 50 $\mu g.L^{-1}$ NPs in their waste water.[20] Although these concentrations sounds relatively low, the size, surface area and chemical properties of

some NPs, such as metal oxides, can cause them to persist in the environment and the concentration can increase over time.[19,20]

Due to a shortage of actual data, a model was developed recently by the Swiss government to evaluate the levels and fate of titanium dioxide (TiO_2) NPs in the environment. TiO_2 and SiO_2 NPs are of particular concern because of its high volume production rates, for use in the cosmetics, sunscreen, electronics and water purification industries. An elementary step towards a quantitative assessment of the risks of new compounds or pollutants (chemicals, materials) to the environment is to estimate their environmental concentrations. Thus, the calculation of predicted environmental concentrations (PECs) builds the basis of a first exposure assessment. The Swiss model computes distributions of PECs by means of stochastic stationary substance/material flow modeling. The evolved model is basically applicable to any substance with a distinct lack of data concerning environmental fate, exposure, emission and transmission characteristics. The model input parameters and variables consider production, application quantities and fate of the compounds in natural and technical environments. To cope with uncertainties concerning the estimation of the model parameters (e.g. transfer and partitioning coefficients, emission factors), as well as the uncertainties about the exposure causal mechanisms (e.g. level of compound production and application) themselves, calculations incorporating uncertainty analysis, Monte Carlo and Markov Chain Monte Carlo simulations were built into the model. The combination of these methods is appropriate to calculate realistic PECs when facing a lack of data. The proposed model was programmed and carried out with the computational tool R and implemented and validated with data for an exemplary case study of flows of the engineered NPs in Switzerland.[21] In 2010, the model estimated that annual emissions of carbon nanotubes, nano-Ag, and nano-TiO_2 were 300 kg, 6200 kg and 473000 kg into surface waters in Switzerland, resulting in concentrations in surface waters within the microgram range for TiO_2.[22] Another Swiss survey indicated that the estimated annual production of nanomaterials was 2,419 ton.[23] This figure is much higher than estimates made by the Royal Society and those in the Royal Academy of Engineering report on Nanotechnology for the year 2010. To our knowledge, no studies reporting the exact concentration of NPs in the South African environment have been published.

It has been estimated that up to 10% of the engineered NPs (ENP) pass through a wastewater treatment plant and are discharged into surface waters, which means that several tons of these particles enter the environment annually.[24] Upon release into the environment, NPs have several fates, which leads to inevitable contact with living organisms.

1.3.1.3.3 Interactions of nanoparticles with living organsims

Figure 1.6 shows the some suggested pathways and interactions of NPs in the enivironment.[20]

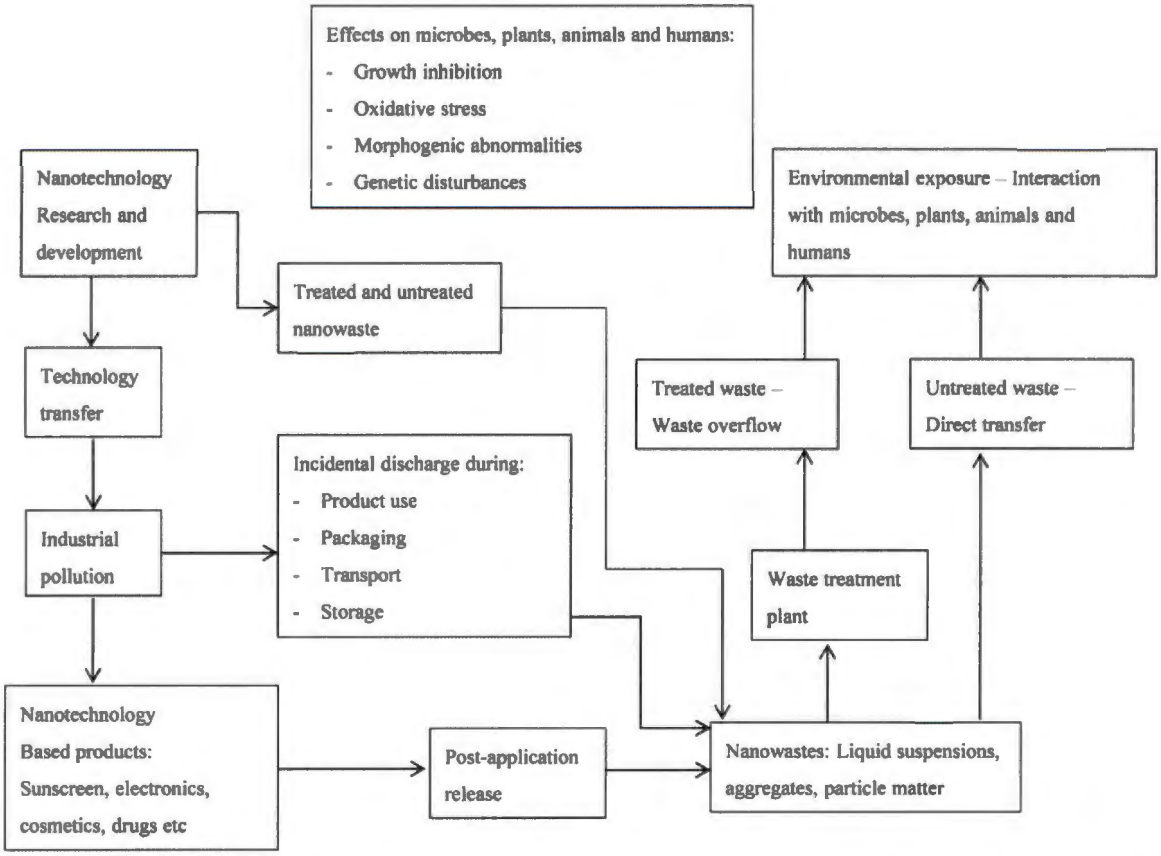

Figure 1.6: Scheme showing the suggested pathways, interactions and effects of NPs within the enivironment.[20]

From the literature it is evident that the uptake, translocation and accumulation of NPs depends on the species of plant, the size, type, chemical composition, functionalization and stability of the NPs in a system.[25] Features like size, shape and surface characteristics may augment or change the reactivity of a previously inert bulk material, and in turn, this change may generate a toxic response.[25] Once released into the open environment, nanoparticles may chemically react in various ways, or may undergo photo-induced chemical changes. Nanoparticles exposed to the environment may be transformed by moisture, sunlight, soil components and by the action of living organisms, among other factors. Some fabricated nanoparticles (like TiO_2) show photo-catalytic activity on exposure to UV-light and can generate reactive oxygen species (ROS) that produce genetic alterations, cellular damage and metabolic changes.[26]

1.3.1.3.4 Nanoparticle effects on plants

It is assumed that various types of engineered nano-materials (ENMs) have different entry routes, behavior and the influence on plants. Furthermore, different, or even opposing conclusions have been drawn from most studies on the interactions between ENMs with plants.[27] Interaction between ENMs and plants can be categorized under phytotoxicity, uptake, translocation and accumulation. Current literature revealed that all of the aforementioned interactions depend on the species of the plant, the type, size, chemical composition, stability and functionalization of ENMs.[27] Several avenues for the uptake of nanomaterials by plants are proposed. Some of the data suggested that the nanomaterials could enter plants by being bound to a carrier protein, through aquaporins, ion-channels or endocytosis via the creation of new pores.[27]

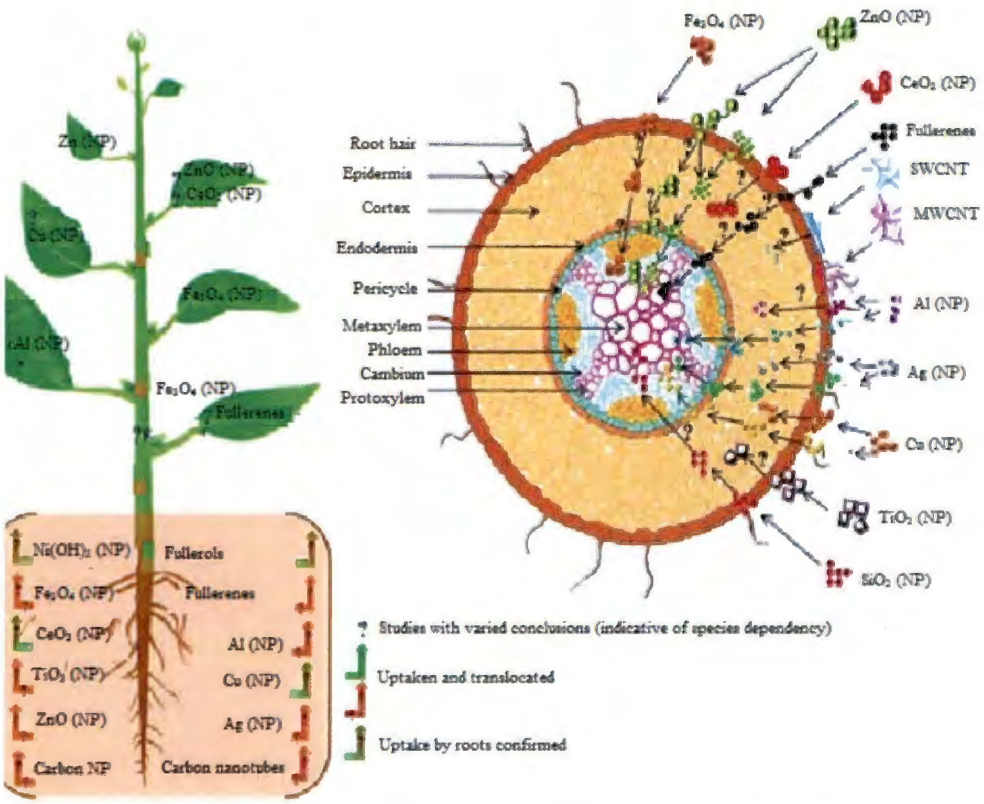

Figure 1.7: Previously studied nanoparticles and possible reported routes of entry in plants.[27]

When ENMs is applied on the surface of leaves, they will enter through the stomatal openings or through the bases of trichomes and then translocated to various tissues.[27] However, the accumulation of ENMs on leaf surface causes foliar heating, which results in alterations in gas exchange, due to stomatal obstruction, causing changes in various physiological and cellular functions of plants. The application of microscopy techniques visualizes and tracks the transport and deposition of ENMs

inside the plants.[28] More information on the observed effects of nanoparticles on plants will be given in Chapter 4.

1.4 Photosynthesis

One key process that has been found to be extremely sensitive to stress factors and dynamic environmental conditions is photosynthesis.[35,36] Throughout the literature, many authors have observed a decrease in photosynthetic efficiency under both biotic- and abiotic stress conditions. For an in-depth review on some literature surrounding these observations please see Handbook of photosynthesis, Taylor and Francis, 2nd ed., 2005.[37] For the purpose of this thesis we will only be focussing on the effect of **industrial related abiotic stresses on photosynthesis and related processes.** Abiotic stress has been shown to suppress photosynthesis by affecting photosynthetic pigments, soluble proteins, proteins in thylakoid membranes, the electron transport chain, photophosphorylation and CO_2-fixation.[37] However, depending on their tolerance level, plants have different responses to abiotic stress. These tolerance levels are often as a result of interspecies and intercultivar genetic variance.[38] The importance of studying and understanding the effect of abiotic stresses on the physiology related to stress responses in different plants has become increasingly emphasized.

Photosynthesis is the process of capturing and converting light energy to chemical energy and storing the energy through the synthesis of carbohydrates, by consuming water and carbon dioxide whilst releasing oxygen as a by-product. In plants and algae, the process of photosynthesis occurs in specialized organelles known as chloroplasts, which contain the photosynthetic apparatus. Photosynthesis primarily occurs in the mesophyll cells of plant leaves. Regulation of energy flow to optimise carbon fixation and prevent light induced damage is the main goal of photosynthesis. Photosynthesis consists of two major processes: the light-dependent electron transport chain (ETC) and the light-independent carbon fixation steps through the Calvin-Benson cycle.

1.4.1 Light-dependent reactions (light capturing and ETC)

The light reactions take place in the thylakoid membranes, inside the chloroplast. Light energy is captured by a series of pigments localized in light harvesting complexes (LHC) and reaction centres (RC) in two complexes: photosystem I (PSI) and photosystem II (PSII). Plants absorb light through light harvesting pigments; chlorophyll, carotenes, xanthophylls etc., which are organized in chlorophyll protein complexes and the light harvesting complex (LHC).[40] Of these light harvesting pigments, chlorophyll, absorbs by far the most of the incoming light photons. Furthermore, chlorophyll can be divided into two distinct types; chlorophyll *a* (Chl *a*) and chlorophyll *b* (Chl *b*).

Figure 1.8 shows the structure of these 2 types of chlorophyll pigments. In essence these two pigments are identical, with the exception of terminal –CHO (aldehyl) functional group in Chl *b* replacing the terminal $-CH_3$ (methyl) group in Chl *a*. Chorophyll *a* absorbs light in the blue and red regions of the visible electromagnetic spectrum (at 662 nm and 430 nm respectively).

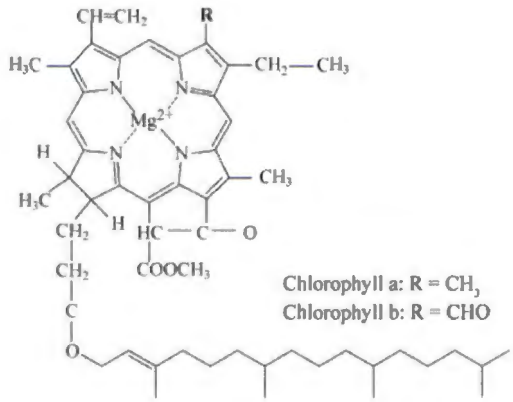

Figure 1.8: Structure of chlorophyll *a* and *b*.[39]

Most of the PSII centres are localized in the chloroplast appressed thylakoid membrane regions, often termed the grana stack. In contrast, PSI centres are mainly localized in the non-appressed thylakoid membrane regions or in stroma lamellae.[40,41,42] Once incoming photons are captured by the LHC, the energy is transferred to reaction centres (RCs) through resonance energy transfer. In the RCs, the absorbed energy causes transition in specialized Chl *a* molecules, P680 (in PSII with a 680 nm absorption centre) and P700 (in PSI with a 700 nm absorption centre), from a ground state to an excited state, where an electron is promoted to an orbital with greater potential energy.[41] As a result, a charge separation takes place as P680 passes an electron to the first stage of the non-resonant electron transfer (NRET) chain. Four charge separation events following the absorption of at least 4 photons are required to oxidize 2 water molecules via a multi-nuclear Mn_4Ca cluster, termed the oxygen evolving complex (OEC), which subsequently releases an oxygen molecule and thereby increasing the electrochemical potential in the lumen by 4 protons. The mechanism of water splitting in this cluster occurs through four electron oxidation process with five intermediate 'S' states, 4 of these are meta-stable (S_0, S_1, S_2, S_3) and one short-lived state (S_4) with higher mean oxidation levels.[43] Apart from four manganese atoms and single calcium atom, the OEC consists of five oxygen atoms.[43] Photosystem II can thus be considered as an enzyme, catalysing the photolysis of water molecules.[42] Electrons generated by the oxidation of water are transferred via a series of electron transporters (each with a lower redox potential) to PSI. In order for an electron to be transferred to PSI, it first has to become oxidized through secondary photon absorption. The series of electron transporters between PSII and PSI are collectively called intersystem electron transporters.[44]

Photosystem II is a water-plastoquinone oxidoreductase and is regarded as the key enzyme of oxygenic photosynthesis. Firstly, electrons are transferred to the primary quinone receptor, Q_A, followed by electron transfer to the secondary quinone, Q_B. These two quinone acceptors act as an electron transfer intermediate between P680 and the cytochrome b_6f complex (Cyt b_6f).[44] The cytochrome b_6f complex mediates electron transport between plastoquinol (PQH_2) and plastocyanin (PC). The Cyt b_6f complex consists of several subunits, which includes heme-proteins and the Rieske iron-sulphur protein (2Fe-2S protein). A more detailed description of the Cyt b_6f complex has been described in the literature.[45] Thereafter, electrons are transferred from the Cyt b_6f complex to plastocyanin (PC), which is a mobile copper containing protein that acts as the transport link between PSII and PSI.

Once the electrons reach PSI, they are transported via a series of transporters which includes 3 iron-sulphur centres (F_x, F_A and F_B) to ferredoxin, Fd (which is also an iron containing protein sub-unit).[15] Ferredoxin NADP-reductase (FNR) and ATP-synthase uses the electrons of reduced Fd and catalyses the reduction reaction of $NADP^+$ to form NADPH and ADP to form ATP via the reactions in equations 1 & 2, respectively:

$$2NADP^+ + 2e^- + 2H^+ \xrightarrow{FNR} 2NADPH \quad (1)$$

$$ADP + Pi \xrightarrow{3H^+,\ ATP\text{-synthase}} ATP \quad (2)$$

Figure 1.9 shows the localities of the photo-systems, OEC and various electron transporters in the ETC.[15]

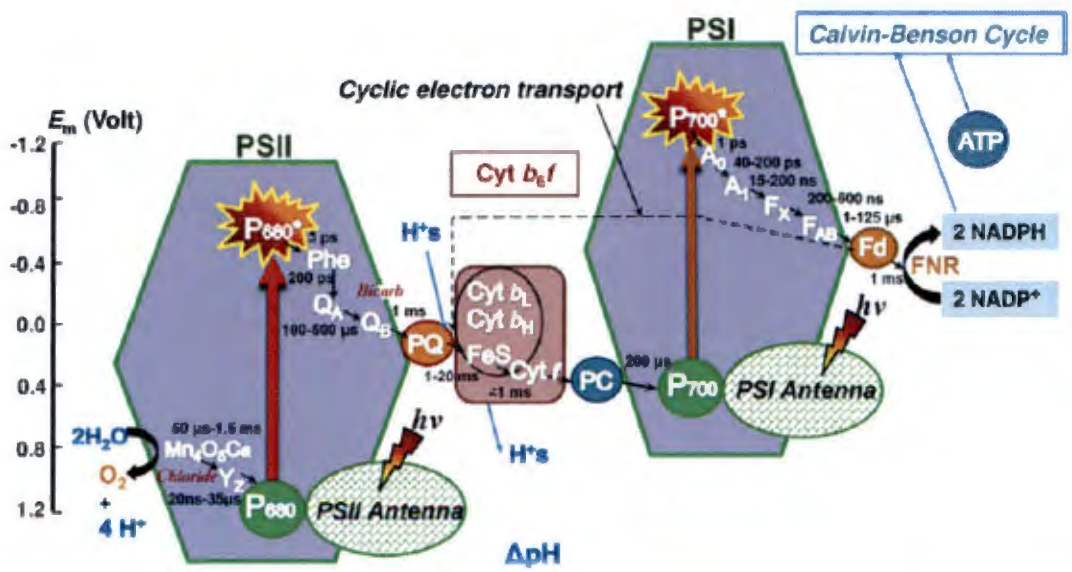

Figure 1.9: The Z-Scheme for electron transport in photosynthesis showing the localities of the various transition metals within the electron transport chain.[44]

The electron transport process described above is known as linear electron transport. Alternatively, electrons in reduced F_d and NADPH can also be transported back to Cyt b_6f by a process known as cyclic electron transport (CET). This electron transport pathway was first identified in 1954.[46] Two possible CET mechanisms have been suggested in literature. The first was reported by Johnson, 2005 and it involves the transfer of electrons from reduced Fd to Cyt b_6f via plastoquinone through a reaction catalysed by ferredoxin quinone reductase (FQR).[47] Secondly, CET has also been suggested to occur via direct electron transfer from NADPH to plastoquinone by a reaction mediated by NAD(P)H dehydrogenase (NDH).[47,48] Although the exact mechanism of CET is yet to be completely understood, most authors agree that the function of CET is to help build-up a pH gradient across the thylakoid membrane, thereby increasing non-photochemical quenching (NPQ) of chlorophyll *a* fluorescence, resulting in a subsequent decrease of reactive oxygen specie (ROS) production and an increase in ATP formation.[49-51]

Irrespective of whether electrons are transported via linear- or cyclic electron transport, the goal of electron transport remains the formation of NADPH and ATP, which is used in the Calvin-Benson cycle where CO_2 is fixed in order to form carbohydrates.

1.4.2 Light-independent reactions (Calvin-Benson cycle)

1.4.2.1 C_3-photosynthesis

Although the Calvin-Benson cycle is driven by ATP and NADPH formed during the light-dependent phase, thus not dependent on light energy, most of the Calvin-Benson cycle enzymes (including the primary carboxylation enzyme, ribulose 1,5-bisphosphate) need light for activation.[23] The Calvin-Benson cycle is a cyclic process that takes place in the chloroplast stroma. It consumes ATP, NADPH and CO_2 to finally produce carbohydrates. The cycle comprises 3 main steps. The first involves carboxylation of CO_2-bound ribulose 1,5-bisphosphate (RuBP) through a reaction catalysed by the primary carboxylation enzyme, ribulose-1,5-bisphosphate carboxylase/oxygenase (Rubisco). This results in the formation of two 3-phosphoglycerate (3-PGA) molecules. The second step, in which 3-PGA is reduced, comprises of two distinct reactions. In the first reaction, 3-PGA is phosphorylated by ATP in a reaction mediated by phosphoglycerate kinase. Secondly, the phosphorylated 3-PGA product is reduced by NADPH (formed during electron transport) to form triose phosphate, via a reaction mediated by glyceraldehyde 3-phosphate dehydrogenase. In the last step, triose phosphate can either be used in sucrose or starch formation, or it can be used in the regeneration of RuBP.[52] In essence, 3 CO_2 molecules are needed to produce 6 triose phosphates, of which 5 are re-incorporated into the cycle for RuBP regeneration through a reaction that consumes ATP. This means that only one

triose phosphate is actually used in sugar and starch formation. Figure 1.10 shows the respective steps involved in the Calvin-Benson cycle.

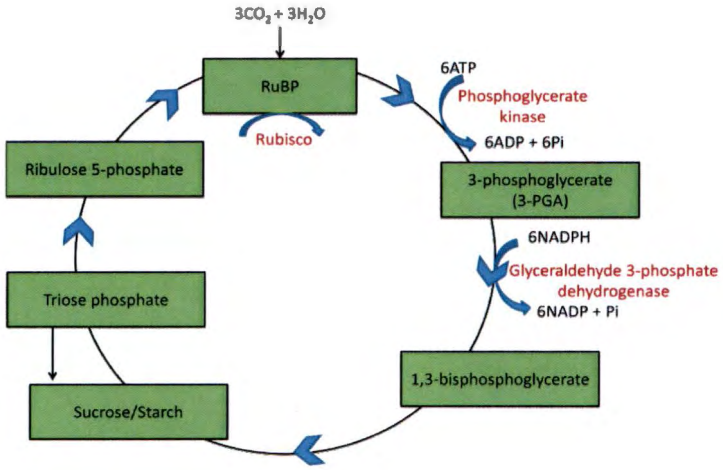

Figure 1.10: A simplified scheme showing the three main steps involved in the Calvin-Benson cycle.[52]

1.4.2.2 C_4-photosynthesis

The above mentioned discussions describe the light-independent reactions of C_3-photosynthesis. Because Rubisco fixes both CO_2 and O_2, an inevitable competition occurs between the binding sites on this enzyme. The oxygenase activity limits its capacity for CO_2-assimilation. About 3 billion years ago the atmosphere was rich in CO_2 with very low levels of free molecular O_2. As plant life increased, the levels of free molecular O_2 did too. As a result of this, conditions became more and more unfavourable for effective photosynthesis, because of increasing photorespiration and subsequent ROS formation. This marked the beginning of the age of oxygenic photosynthesis.[53] Plants had to adapt to the new O_2-rich conditions, giving rise to C_4-photosynthesis. It involves an additional prerequisite step for CO_2-assimilation, by which CO_2 is assimilated by phosphoenol-pyruvate carboxylase (PEPc) in the mesophyll cells, resulting in the formation of C_4-acids.[52] In maize, in which the predominant C_4 acid decarboxylase is NADP malic enzyme (NADP-ME), the C_4-cycle consumes 2 ATP per CO_2 transferred and can therefore be described as an ATP-driven CO_2 pump.[52] ATP generation from electron transport chain is therefore critical in the regeneration of these enzymes involved in CO_2-fixation. These C_4-acids are then transported to the Rubisco containing bundle-sheath cells, where they are decarboxylated, causing the release of CO_2 around Rubisco. The concentration of CO_2 now exceeds that of O_2 (around Rubisco), subsequently resulting in the fact that the binding equilibrium favours CO_2 binding.[53] Figure 1.11 shows a schematic illustration of the various steps of C_4-photosynthesis.[53] This offers obvious advantages for C_4-plants (maize, sugarcane etc.). The

advantages of C_4-photosynthesis is eloquently described by a number of reviews, in particular a review by Ehleringer and Monson, 1993.[54]

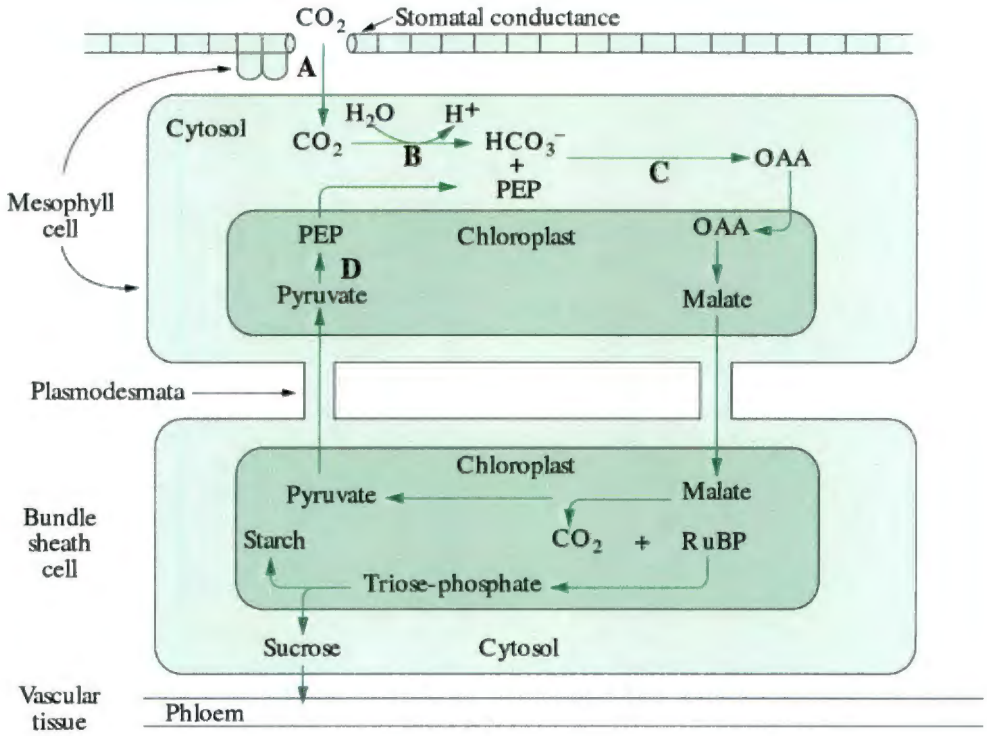

Figure 1.11: A simplified scheme showing the various steps of C_4-photosynthesis.[53]

1.4.3 Alternative electron acceptors

Under stressful conditions, a shift in the relative redox active state can sometimes cause electrons to be used for the reduction of electron acceptors other than $NADP^+$ and ATP. The redox active state is defined as the rate at which electrons are generated and used for subsequent CO_2-assimilation. Electron generation usually occurs at a much faster rate than the biochemical reactions around NADP and ATP.[55] Normally, this equilibrium is closely regulated to prevent the formation of ROS. Biotic- and abiotic stresses can disrupt this redox equilibrium, resulting in the need for electrons to be donated to alternative electron acceptors. Plants have developed some strategies to limit ROS production at these sub-optimal conditions through processes like CET as well as nitrogen- and sulphur reduction.[56] Furthermore, when the stress is short lived, plants use strategies like non-photochemical quenching as a photo-protection strategy to dissipate excess energy in the form of heat.[26] However, when the stress is long term, other strategies have to be employed to relieve the excitation pressure. A very important approach often used by plants is the process of photo-respiration, by which electrons are donated to molecular oxygen that populates the chloroplastic environment, in an attempt to reduce photo-oxidation and damage to the photosynthetic apparatus.[57,58]

In conditions where there is a lower electron demand for CO_2-assimilation (when CO_2 uptake- or assimilation is inhibited), or over-reduction of electron transporters occurs as a result of a disruption in the flow of electrons in the electron transport chain, photorespiration may be employed by the plant. Terminal PSI O_2-reduction has been reported repeatedly. This produces O_2^- which is converted by superoxide dismutase (SOD) to H_2O_2 in a reaction known as the Mehler reaction.[54] Hydrogen peroxide is converted to H_2O through a catalytic reaction by ascorbate peroxidase (APX), whilst monodehydroascorbate (MDA) is also produced.[53] Furthermore, other processes such as the water-water cycle and plastoquinol terminal oxidase (PTOX) can also be employed to scavenge excess electrons.[55,59]

1.5 Techniques to evaluate stress effects on photosynthetic efficiency

In the last few decades, with the advent of more sophisticated technology, photosynthesis research has become much more advanced. The focus has shifted to a more holistic view of the processes involved in photosynthesis. This is only possible because of the quality (ability) of systems available for research, but more specifically, the systems that allow accurate non-invasive *in vivo* measurements of both the i) light dependent- and ii) light independent processes of photosynthesis.

Two techniques often used to follow the efficiency of these two distinct steps in photosynthesis are chlorophyll *a* fluorescence induction and infra-red photosynthetic gas analysis (IRGA) measurements. Chlorophyll *a* fluorescence induction is used to measure the events around the light dependent phase of photosynthesis, which includes photon absorption and electron transport efficiency processes. Infra-red photosynthetic gas analysis is used to evaluate the efficiency of the light-independent physiological processes. The data provided by the IRGA measurements provide insights into stomatal response, CO_2-assimilation, CO_2-assimilation enzyme kinetics and water use efficiency, just to name a few.

1.5.1 Chlorophyll *a* fluorescence

In the early 1930's, Hans Kautsky observed the phenomenon of chlorophyll *a* fluorescence after photosynthetic samples were exposed to actinic light after a substantial period of darkness.[60] These characteristic spectral curves are termed the fluorescence transient or fluorescence induction. Higher plants and algae exhibit a characteristic fluorescence induction curve, consisting of two very distinct phases, i.e. i) the fast fluorescence rise and ii) slow fluorescence decrease. The absorption of photons by antenna molecules is a very fast process and occurs within femtoseconds, leading to the formation of excited chlorophylls (Chl*).[61] The excitation energy can be used to produce 3 main phenomena when the excited chlorophyll decays (de-excitation) to its ground state. Firstly, the absorbed energy

can be used to produce photochemical energy, which is the primary process involved in electron generation (and finally NADPH and ATP synthesis). The effectiveness of this process is the crux around which the technique of chlorophyll *a* fluorescence is based. The quantum yield of of primary photochemistry determines the efficiency with which primary electron acceptor, Q_A (in the electron transport chain), is reduced. Secondly, de-excitation energy can be used to generate chlorophyll *a* fluorescence, which is the emission of red light originating from the antenna chlorophyll *a* molecules of PSII. There is a general agreement that at room temperature chlorophyll *a* fluorescence of plants in the spectral region 680-740 nm is almost exclusively emitted by PSII and it can therefore be used to evaluate the fate of its excitation energy.[61] Thirdly, most of the excess energy not used in photochemistry or fluorescence is dissipated in the form of heat.[62]

It is important to note that there are several different types of fluorescence measurements, but for the purpose of this thesis we will only give a short review of dark adapted direct (prompt or fast kinetics) chlorophyll *a* fluorescence techniques. For a review on the types of fluorescence measurements please see Baker 2008.[63]

In the current study, the prompt (fast kinetics) chlorophyll *a* measurements were conducted using a multifunctional plant efficiency analyser (M-PEA, Hansatech, UK). Leaves were dark adapted for 60 min before they were illuminated with a 1 s pulse of a continuous red light (627 nm, 5000 µmol photons $m^{-2}s^{-1}$) while recording the fast kinetics chlorophyll *a* fluorescence. The light source has a fast time resolution (~20 µs) with a high data acquisition capacity.

Using the theory of energy fluxes in bio-membranes by Strasser 1978 & 1981, Strasser and co-workers developed a model that relates the fast fluorescence rise of chlorophyll *a* fluorescence to the physical and biochemical excitation processes involved in energy capture and electron transport.[64] By making use of simple algebraic equations expressing the equilibration of the total energy influx with the total energy out-flux for each pigment system, the contribution of each de-excitation process can be approximated. This is done by taking into consideration all possible pathways of communication between energy transfer pathways.[64]

Following a dark period (1 hour dark adaptation), the photosynthetic sample is illuminated by continuous actinic light and the fluorescence transient signal is recorded. When plotted on a logarithmic timescale, this transient has several inflection points. The fast (prompt) phase is labelled as OJIP, where O is for origin, the first measured minimal level, J and I are intermediate levels, and P is the peak.[44] Figure 1.12 shows the shape and respective steps of a typical OJIP curve.

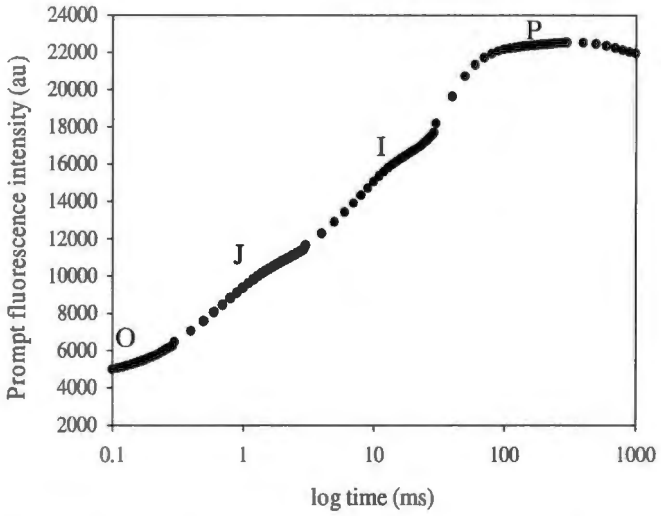

Figure 1.12: An illustrative example of the characteristic steps (O-J-I-P) of a typical prompt fluorescence transient. A detailed background of the history of the nomenclature around the respective steps is available in the literature.[65]

1.5.1.1 Analysis of the prompt fluorescence (OJIP) transient

As mentioned in section 1.2.1, incoming photons are absorbed by chlorophyll antennae. Active reaction centres (RCs) on the antennae pigments 'trap' and convert the excitation energy to photochemical energy, which is used to reduce Q_A. After a dark adaptation period (sample kept in darkness for at least 1 hour) the electron acceptor side of PSII is mostly in the oxidized state (open RCs). This means that the absorption capacity of the active RCs are at their maximum, whilst the fluorescence produced is at its minimum, which is seen as F_O in the induction curve.[15,35] This inflection point corresponds to the O-phase seen in Figure 1.12. After the O-point (point = inflection point), a sharp rise is seen towards the J-point, known as the OJ-rise. The OJ-phase is related to the photochemical reactions of the RCs up to the reduction of Q_A (single turnover events). The time scale of this phase is in the order of 2-3 ms. Following the J-point in the transient, another fluorescence rise is seen up to the I-point (at 20-30 ms). The JI-phase has been related to the events surrounding intersystem electron transport (between PSII and PSI, i.e. Q_B, Cyt b_6f etc.) involved in the multiple turnover events of electron transport, used for Q_A re-oxidation.[65] The final rise from the I to the P-point (at 300 ms) in the induction curve (IP-phase) has previously been shown to be a reflection of electron transport from intersystem transporters efficiency up to the reduction of PSI end electron acceptors.[66-68] The JI- and IP-phases are much slower than the fast photochemical phase (OJ-phase). Furthermore, the P-point corresponds to the maximal fluorescence intensity (F_m), i.e. all RCs are now closed (reduced). From the OJIP-curve variable (V) fluorescence curves (OP normalization, V_{OP}) and difference in variable fluorescence (ΔV) curves, showing specific bands (ΔV_{OJ}, ΔV_{JH}, ΔV_{OK}, ΔV_{KJ},

ΔV_{JI}, ΔV_{IH}, ΔV_{Kn}, ΔV_{Jn}, ΔV_{In} and ΔV_{Hn} (n = narrow)), can be constructed using the following normalization equations:

i) ΔV_K in ΔV_{OJ} normalization, $\Delta V_{OJ} = [(F_t - F_{0.03\ ms})/(F_{3\ ms} - F_{0.03\ ms})]_{treatment} - [(F_t - F_{0.03\ ms})/(F_{3ms} - F_{0.03\ ms})]_{control}$

ii) ΔV_I in ΔV_{JH} normalization, $\Delta V_{JI} = [(F_t - F_{3ms})/(F_{300\ ms} - F_{3\ ms})]_{treatment} - [(F_t - F_{3\ ms})/(F_{300\ ms} - F_{3\ ms})]_{control}$

iii) ΔV_J in ΔV_{KI} normalization, $\Delta V_{KI} = [(F_t - F_{0.3\ ms})/(F_{30\ ms} - F_{0.3\ ms})]_{treatment} - [(F_t - F_{0.3\ ms})/(F_{30\ ms} - F_{0.3\ ms})]_{control}$

iv) ΔV_{LK} normalization, $\Delta V_{LK} = [(F_t - F_{0.03\ ms})/(F_{0.3\ ms} - F_{0.03\ ms})]_{treatment} - [(F_t - F_{0.03\ ms})/(F_{0.3\ ms} - F_{0.03\ ms})]_{control}$

v) ΔV_{KJ} normalization, $\Delta V_{KJ} = [(F_t - F_{0.3\ ms})/(F_{3\ ms} - F_{0.3\ ms})]_{treatment} - [(F_t - F_{0.3\ ms})/(F_{3\ ms} - F_{0.3\ ms})]_{control}$

vi) ΔV_{JI} normalization, $\Delta V_{JI} = [(F_t - F_{3\ ms})/(F_{30\ ms} - F_{3\ ms})]_{treatment} - [(F_t - F_{3\ ms})/(F_{30\ ms} - F_{3\ ms})]_{control}$

vii) ΔV_{IH} normalization, $\Delta V_{IH} = [(F_t - F_{30\ ms})/(F_{300\ ms} - F_{30\ ms})]_{treatment} - [(F_t - F_{30\ ms})/(F_{300\ ms} - F_{30\ ms})]_{control}$

viii) ΔV_{Kn} normalization, $\Delta V_{Kn} = [(F_t - F_{0.1\ ms})/(F_{1\ ms} - F_{0.1\ ms})]_{treatment} - [(F_t - F_{0.1\ ms})/(F_{1\ ms} - F_{0.1\ ms})]_{control}$

ix) ΔV_{Jn} normalization, $\Delta V_{Jn} = [(F_t - F_{1\ ms})/(F_{10\ ms} - F_{1\ ms})]_{treatment} - [(F_t - F_{1\ ms})/(F_{10\ ms} - F_{1\ ms})]_{control}$

x) ΔV_{In} normalization, $\Delta V_{In} = [(F_t - F_{10\ ms})/(F_{100\ ms} - F_{10\ ms})]_{treatment} - [(F_t - F_{10\ ms})/(F_{100\ ms} - F_{10\ ms})]_{control}$

xi) ΔV_{Hn} normalization, $\Delta V_{Hn} = [(F_t - F_{10\ ms})/(F_{100\ ms} - F_{10\ ms})]_{treatment} - [(F_t - F_{10\ ms})/(F_{100\ ms} - F_{10\ ms})]_{control}$

The validation of V and ΔV in variable fluorescence phases and peaks obtained by the various normalizations to obtain these peaks, are described in detail in the literature.[69] The rationale and normalization time periods for the various normalizations is depicted in Figure 1.13. The normalizations were constructed to isolate and compare (to control, which is normalized to zero) certain parts of the fluorescence transient. The individual parts represent distinct processes in the light reactions of photosynthesis, starting from photon capture behaviour up to electron transport through PSI. The lower the decade (d) number is, the 'narrower' or the sharper the peaks (bands) of interest becomes. The narrower ΔV_{Xn} (X = K, J, I ,H) bands will provide a more accurate representation of the events corresponding with that specific time-interval, because it effectively excludes the influence of overlapping or bordering (adjoining) events. The various ΔV-bands (resulting from differential variable fluorescence phases) were constructed using equations i-xi.

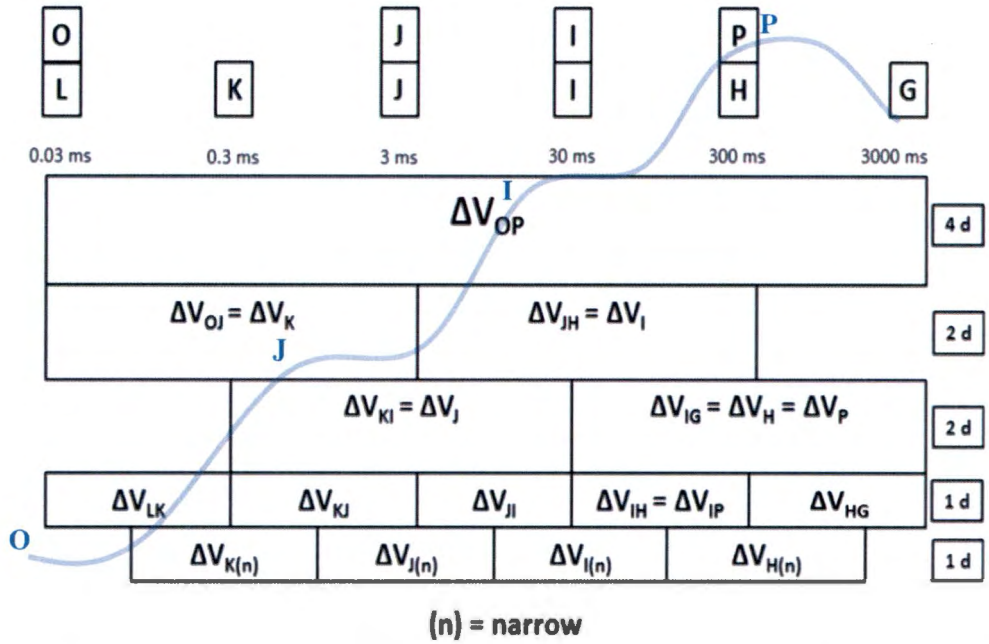

Figure 1.13: The various time decades resulting in the respective variable and differential variable fluorescence peaks.

These various normalizations can be shown graphically in any number of ways, in order to best visualize changes in the respective phases (as brought about by a specific stress or treatment). The maximum and minimum amplitude of theses normalization bands can be shown as simple maxima and minima graphs (Chapter 2), as individual isolated bands (showing the whole particular band, Chapter 3) or they can be graphically illustrated as combined normalization curves, which demonstrate the total change over the whole timespan of the prompt fluorescence transient (Chapter 4). All of these different types of data presentations will be shown, in order to show the versatility with which the data can be manipulated and presented.

1.5.1.2 Association of normalization bands with events in the electron transport process

From the information provided in Section 1.4.1.1 and various other experiments with copounds such as 3-(3,4-dichlorophenyl)-1,1-dimethylurea (DCMU), which blocks electron transport at the Q_B site in electron transport chain, Strasser and coworkers were able to assign certain explanations for the appearance of the various bands in Figure 1.13. Table 1.4 gives the reported meanings of some of the reported variable fluorescence bands, together with the time it appears in the fluorescence transient.

Table 1.4: Characteristic variable fluorescence bands.

Difference in variable fluorescnce band (ΔV)	Meaning of band	Ref. no.
ΔV_L-band (at 0.03 ms)	A positive ΔV_L-band is indicative of a loss in cooperation between chlorophyll antennae because there is less active antennae able to absorb incoming photons.	66, 67, 69
ΔV_K-band (at 0. 3 ms)	The presence of the ΔV_K-band has been suggested to indicate the inactivation of the oxygen evolving complex (OEC), resulting in the loss of structural integrity, which allows stronger reducing (non-water) entities such as ascorbate and proline that populate cellular and chloroplastic environments to reduce Q_A. This enables faster and greater electron donor reactions, which will inevitably cause the over reduction of Q_A and/or it can indicate an increase in the functional antenna size (competitive inhibition).	64-69
ΔV_J-band (2-3 ms)	A positive ΔV_J-band has been attributed to the accumulation of reduced Q_A, i.e. a decrease in the re-oxidation of Q_A^-. This points to a decrease in electron transport past Q_A.	64, 67, 68
ΔV_I-band (20-30 ms)	ΔV_I-bands have been related to the electron transport events around the intersystem electron transporters before the PSI acceptor side. According to the literature a positive ΔV_I-band is related to a build-up of electrons at the intersystem electron transporters before the PSI electron acceptors, or a lowering in the reduction of PSI electron acceptors.[37,58]	57, 67, 69
ΔV_H-band = ΔV_{IP}-phase (100-300 ms)	A positive ΔV_H-band or ΔV_{IP}-phase points to a lowering PSI end electron acceptor reduction. Increased ΔV_H amplitudes can be interpreted as an accumulation of reduced PSI electron carriers before $NADP^+$ and Ferredoxin.	60, 64, 67, 69

1.5.1.3 Calculating JIP-parameters from the prompt fluorescence (OJIP) transient

Strasser and co-workers (1978-1981) developed mathematical equations and derivatives based on de-excitation constants, energy fluxes and probabilities, as a means to analyse the OJIP-induction curve. The collective name given to this analysis method is the JIP-test. The JIP-test utilizes particular parts of the fluorescence transient related to specific electron transport processes and calculates biophysical parameters related to these transport processes.[64] With the JIP-test, one is able to estimate changes in light absorption (also called energy trapping), yield of primary photo-chemistry (Q_A-reduction) as well as electron transport probabilities and efficiencies between electron transport phases up to the reduction of PSI end electron acceptors (NADPH and ATP).[64,68] Moreover, the JIP-test can also be used to elucidate possible structural (and cooperative) changes within the chlorophyll antenna bed.[15,35] The JIP-test equations are based on theory of energy fluxes in biomembranes, which supports the general derivation for the actual quantum yield of primary photochemistry $\varphi_{Po} = TR_o/ABS = 1 - F_o/F_M$. These equations explain that each energy flux of the energy cascade from the photon absorption flux (ABS) is converted into a free energy flux (RE), transported via electron transport (ET), and stored by the reduction of end-electron acceptors of photosystem I (PSI). The formulae and definitions of terms used in the JIP-test are listed in Table 1.5. In Figure 1.14 a simplified scheme of the processes involved in the calculation of the JIP-parameters is shown.

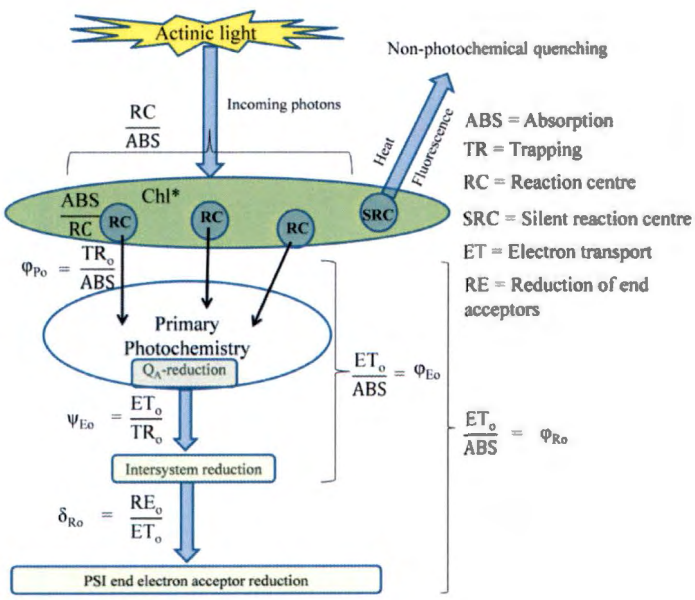

Figure 1.14: A simplified scheme showing the processes involved in the calculation of the JIP-parameters. According to the model only 'active' RCs are able to convert absorbed photons into photochemical energy. Damaged (inactive RCs) are referred to as silent reaction centres which dissipate incoming photons in the form of heat. This process is known as non-photochemical quenching.[64]

Table 1.5: Formulae and descriptions of calculated JIP-parameters that are generally used to describe biophysical parameters, quantum yields/probabilities that electrons are transported to specific parts in the electron transport processes as well as some performance indexes.[64]

Extracted parameter	**Description**
F_O	Initial fluorescence intensity when all PSII RCs are open
F_J	Fluorescence intensity at the J-step (2-3 ms)
F_I	Fluorescence intensity at the I-step (20-30 ms)
$F_M = F_P$	Maximal fluorescence intensity when all PSII RCs are closed (300 ms)
Biophysical parameters	**Description**
$EC/RC = S_m = Area/(F_M\text{-}F_O)$	Total number of electron carriers per RC of PSII
Quantum yields and efficiencies/probabilities	**Description**
$\varphi_{Po} = TR_O/ABS = 1 - (F_O/F_M)$	$(1 - F_O)/F_M$ or F_V/F_M, maximum quantum yield of primary photochemistry
$\psi_{Eo} = ET_O/TR_O = (F_M - F_J)/(F_M - F_O)$	Probability that a trapped excitation moves an electron into the ETC beyond Q_A^-
$\delta_{Ro} = RE_O/ET_O = (F_M - F_I)/F_M - F_J)$	Efficiency of electron movement from the reduced intersystem electron acceptors to the PSI end electron acceptors
$\varphi_{Eo} = ET_O/ABS = \varphi_{Po} . \psi_{Eo} = [1 - (F_O/F_M)] . [(F_M - F_J)/(F_M - F_O)]$	$((1 - F_O)/F_M)\psi_{Eo}$, quantum yield for electron transport
$\varphi_{Ro} = RE_O/ABS = \varphi_{Po} . \psi_{Eo} . \delta_{Ro} = [[1 - (F_O/F_M)] . [(F_M - F_J)/(F_M - F_O)] . [(F_M - F_I)/F_M - F_J)]$	The quantum yield of electron transport from Q_A^- to the PSI end electron acceptors
$\gamma RC = Chl_{RC}/Chl_{Total} = RC/(ABS + RC)$	Probability that a PSII Chl molecule functions as a RC
RC/ABS	The concentration of PSII reaction centres per Chl
ABS/RC	$(Chl_{Antenna} + Chl_{RC})/Chl_{RC}$, A measure of the PSII Antenna size
Performance indexes	**Description**
$PI_{ABS} = (\gamma_{RC}/1 - \gamma_{RC})(\varphi_{Po}/1\text{-}\varphi_{Po})(\psi_{Eo}/1\text{-} \psi_{Eo})$	Performance index for energy conservation from photons absorbed to the reduction of intersystem electron acceptors
$PI_{total} = PI_{ABS}(\delta_{Ro}/1\text{-} \delta_{Ro})$	Performance index for energy conservation from photons absorbed to the reduction of PSI end electron acceptors

1.5.2 Modulated 820 nm reflection

The above mentioned processes describe mainly the reactions around PSII. In addition, the activity of PSI has previously been approximated by its characteristic 820 nm reflection spectrum. More advanced systems such as the Multifunctional Plant Efficiency Analyser M-PEA (Hansatech Instrument Ltd., King's Lynn, Norfolk, PE30 4NE, UK) have the ability to simultaneously measure both the fast fluorescence decay (PSII) and modulated reflection signal 820 nm ($MR_{820\ nm}$) for PSI. From the reflected $MR_{820\ nm}$ the ratio MR/MR_0, where MR_0 is the value at the onset of the actinic illumination (after dark adaptation) can be calculated.[69] The signal is related to the ratio of incident light flux (I_{inc}) and the light flux absorbed at 820 nm (I_{abs}). A direct correlation exists between an increase in $(I_{abs}/I_{inc})_{820\ nm}$ and a decrease in the amplitude of MR/MR_0. Furthermore, $(I_{abs}/I_{inc})_{820\ nm}$ is also indicative of a decrease in the ratio between absorbed and incident flux at 700 nm.[69] Figure 1.15 shows an illustrative example of changes in the modulated reflection signals expressed by the MR/MR_0 ratio normalized to zero at 500 ms. The 500 ms point was selected because it represents the maximum time it takes for PSII electrons to re-reduce oxidised PC^+ and PSI electron acceptors.[69]

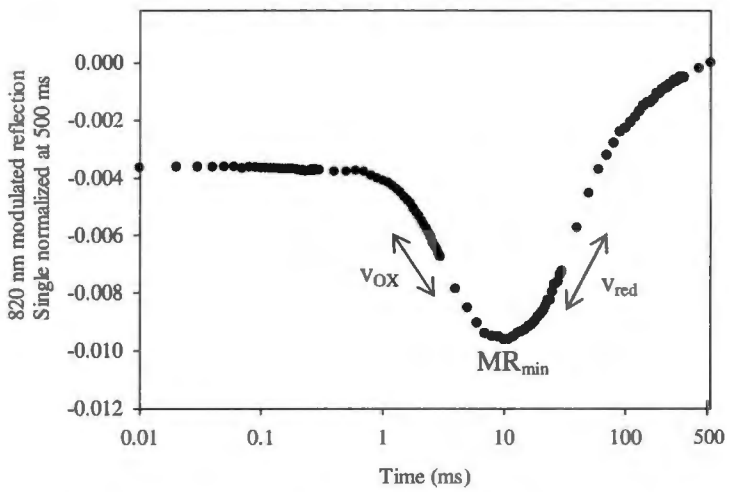

Figure 1.15: An example of the changes in the modulated reflection signal expressed by the MR/MR_0 ratio normalized to zero at 500 ms plotted on a logarithmic timescale.

The initial decay (slope) of MR_{820nm} intensity (Figure 1.15), due to PSI redox change, represents the rate of PC and PSI photochemical oxidation (v_{ox}), whilst the secondary slope (v_{red}) reflects the re-reduction rate of PC and PSI by PSII.[67,69] A change in v_{ox} can thus be interpreted as a change in the rate at which electrons move through PC and PSI, whereas v_{red} reflects the rate with which PC and PSI is re-reduced by arriving electrons from PSII. The reflection values corresponding to the minima of the MR curves (MR_{min}) are used to deduce the maximum oxidation state of PSI, or in other words

the maximum amount of electron flow through PSI before electrons from PSII arrives.[70] MR_{min} corresponds to the time range of the JI-phase of fast chlorophyll fluorescence induction curve.[69,70]

1.5.3 Infra-red photosynthetic gas analysis (IRGA) measurements

In C_3 plants, CO_2 diffusion from the atmosphere to Rubisco in the chloroplasts takes place via an intricate mechanism. Most authors agree with the photosynthetic gas exchange model of Farquhar and Sharkey (1982), which suggests that the three main components through which the CO_2 has to diffuse are; i) boundary layer of turbulent air around the leaf surface, ii) diffusion into the stomata (stomatal conductance) and lastly iii) into the mesophyll cells where the chloroplasts are found.[71] Once at the active site of Rubisco in the stroma of the chloroplasts, CO_2-assimilation can take place. One type of system often used to measure the stomatal conductance (to CO_2 and water vapour) and CO_2-assimilation rate is infra-red gas exchange analysis (IRGA). Infra-red gas exchange analysis operates on the principle that hetero-atomic gas molecules (such as CO_2) absorb radiation at specific infrared (IR) wavelength, resulting in a spectrum that is unique for each gas. Infra-red gas exchange analysis systems measure the amount of transmission disruption of the IR wavelength caused by the presence of CO_2 between the radiation source and a detector. The reduction in transmission is a function of the concentration of CO_2. The most popular IRGA system used is called a closed system IRGA, by which a leaf is enclosed in a sealed chamber whilst keeping (supplying) the chamber 'atmosphere' at an exact CO_2 concentration and monitoring the the rate of CO_2-assimilation over time.[71,72] Given that the regeneration rate of ribulose-1,5-bisphosphate carboxylase/oxygenase (Rubisco) is dependent on the rate of electron transport from the electron transport chain and that the rate of electron transport is light dependent, it is important to note that these measurements are not only influenced by the CO_2 concentration applied, but also by the artificial light intensity applied (Photosynthetic photon flux density, or PPFD in $\mu mol.m^{-2}.s^{-1}$) within the chamber. Changes in gas exchange parameters can be measured by keeping the PPFD constant at a saturating level of ~ 1200 $\mu mol.m^{-2}.s^{-1}$, to ensure that Rubisco is fully activated, whilst varying the CO_2 concentration with time, thereby measuring the CO_2 response of the test plant. Moreover, the measurement can also be made by keeping the CO_2 concentration constant and varying the PPFD with time, in so doing measuring the light response of the plant.[72]

Figure 1.16 is a schematic representation of the diffusion processes that govern CO_2 entry into subcellular plant organelles, where: C_a is the externally applied CO_2 concentration, C_i is the intercellular CO_2 concentration, W_a is the external water vapour concentration and W_i is the internal water vapour concentration.

1.5.3.1 C_3-photosynthesis model

A model for C_3-plants was developed by Farquhar and Sharkey (1982) to translate data attained by this type of analysis to meaningful data that can be used to evaluate the changes in limitations (at a given set of conditions) with regard to CO_2-acquisition (stomatal limitation), CO_2-assimilation rate (mesophyll limitation) and transpiration.[71]

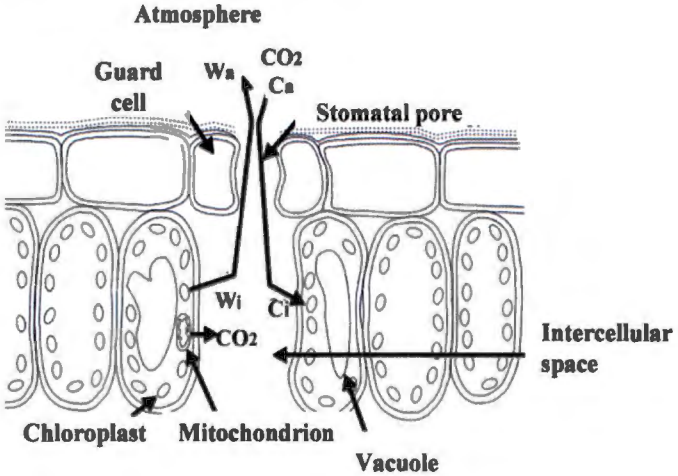

Figure 1.16: Scheme showing the diffusion processes that governs CO_2 entry into subcellular plant organelles.[73]

The data from the gas exchange measurements are used to construct an A:C_i curve, where A is the CO_2-assimilation rate in $\mu mol.m^{-2}.s^{-1}$ and C_i in $\mu mol.mol^{-1}$ is once again the internal CO_2 concentration.[70] The A:C_i response is obtained by simultaneously measuring assimilation and transpiration rate (E in $mmol.m^{-2}.s^{-1}$) over a wide range of external CO_2 concentrations (C_a) and a known leaf-air vapour pressure deficit (D in Pascal). Under the assumption that CO_2 diffuses from the atmosphere into the sub-stomatal cavity, by the same route with which water vapour leaves the sub-stomatal cavity, the leaf diffusive conductance for carbon dioxide ($g_{CO2} = g_{H2O}/1.6$) can be determined from E, D and the diffusivities of CO_2 and water vapour.[71,73] According to the model of Farquhar and Sharkey (1982) the gas exchange and photosynthetic parameters are calculated from measurements of both the CO_2 concentration surrounding the leaf (C_a) and A. C_i can then be calculated by Equation 3:

$$C_i = C_a - A/g_{CO2} \qquad (3)$$

According to the model (in C_3 plants) photosynthesis is considered to be limited by the maximal rate Rubisco carboxylation, V_{pmax} ($\mu mol\ m^{-2}\ s^{-1}$), and by the maximal electron transport rate driving regeneration of Rubisco, J_{max} ($\mu mol\ m^{-2}\ s^{-1}$).[74,75] These parameters can be estimated by making use of

A:C_i curves, which are constructed by plotting the obtained C_i (x-axis) values versus A (y-axis).[45,46] An example of such an A:C_i curve and the method with which the mentioned (and other) parameters are estimated, is shown in Figure 1.17 below.

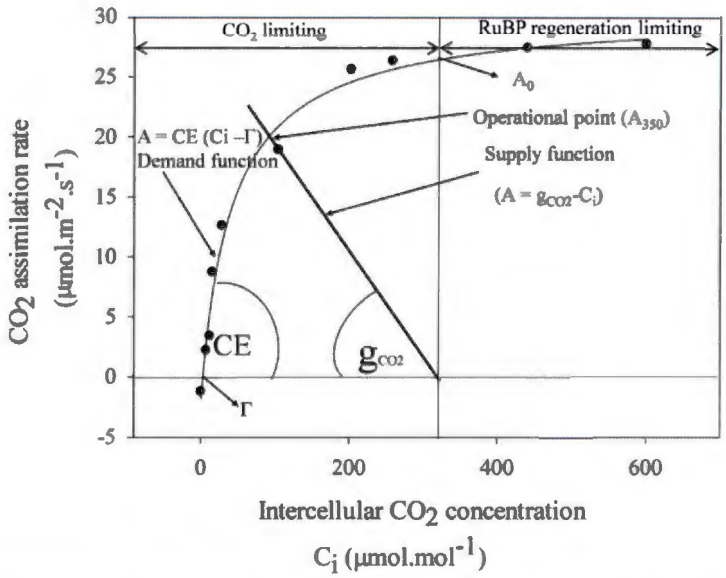

Figure 1.17: An example of a typical A:C_i curve showing the supply and demand functions that can be used to calculate C_i, V_{pmax} (carboxylation efficiency, CE), stomatal conductance to CO_2 (g_{CO2}) as well the CO_2 compensation point. The supply function [$A = g_{CO2}(C_a - C_i)$], corresponding to the demand function [$A = CE(C_a - \Gamma)$], was drawn by simply joining the value of $C_i - C_a = 360$ ppm on the abscissa to the point giving A_{350} at this value of C_a.[75]

The nomenclature used in Figure 1.17 is discussed below:[73]

A_0: Assimilation rate when no stomatal limitation exists, i.e. $C_a = C_i$ ($\mu mol.m^{-2}.s^{-1}$)

A_{350}: Assimilation rate at normal atmospheric CO_2-concentration chosen here as 360 ppm ($\mu mol.m^{-2}.s^{-1}$)

Γ: CO_2-compensation point ($\mu mol.mol^{-1}$) when no net assimilation exists, i.e. CO_2 uptake by photosynthesis equals CO_2 produced by respiration

g_{CO2}: Stomatal conductance to CO_2 ($mmol.m^{-2}.s^{-1}$)

V_{cmax} (CE): Carboxylation efficiency (rate) by Rubisco or PEPc ($mol.m^{-2}.s^{-1}$)

J_{max}: Maximal assimilation rate / rate of Rubisco or PEPc regeneration ($\mu mol.m^{-2}.s^{-1}$)

C_i: Internal CO_2 concentration ($\mu mol.mol^{-1}$)

C_a: External CO_2 concentration ($\mu mol.mol^{-1}$)

$$l \quad = \quad \% \text{ stomatal limitation} = \frac{A_0 - A_{350}}{A_0} \text{ X } 100$$

1.5.3.2 C_4-photosynthesis model

As mentioned earlier (Section 1.2.2), the primary enzyme involved in CO_2-assimilation by C_4 plants is phosphoenol-pyruvate carboxylase (PEPc).[53] Von Caemmerer and Furbank (1999) elaborated the model of Farquhar and Sharkey in order to estimate the the maximal carboxylation rate of PEPc, V_{pmax}, as well as the maximal rate of PEPc regeneration capacity and electron transport, J_{max}.[71,76] The model of Von Caemmerer and Furbank is shown schematically in Figure 1.18 below, after which the equations derived from this model will be discussed, as well as the implications for C_4-photosynthesis modelling.

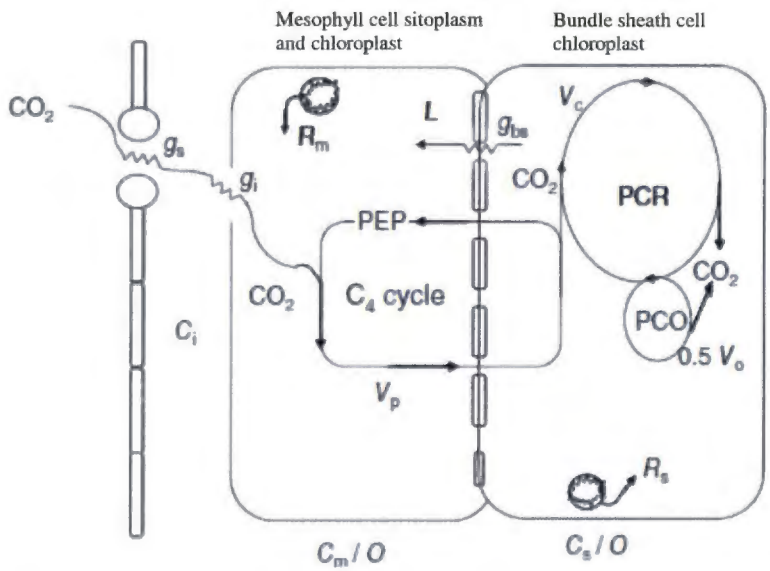

Figure 1.18: Scheme of the C_4-photosynthesis model from von Caemmerer & Furbank.[76]

After passing the stomatal (g_s) and the mesophyll cell (g_i) conductance, CO_2 is initially fixed in the mesophyll by phosphoenolpyruvate (PEP) carboxylase into C_4 acids that are then decarboxylated to supply CO_2 to ribulose-1-5-bisphosphate (Rubisco), which is localized in the bundle-sheath chloroplasts (Figure 1.11). The well co-ordinated functioning of mesophyll and bundle-sheath cells, accomplished through specialized leaf anatomy, produces a high CO_2 concentration in the bundle sheath, strongly inhibiting photorespiration. However, the elevated CO_2 in the bundle-sheath cells is sustained at the cost of extra ATP, required for the regeneration of PEPc. The conductance for CO_2 transfer from intercellular air spaces to mesophyll cells may be large enough in C_4 leaves. However, the bundle-sheath conductance (g_{bs}) is a major factor that determines the rate of CO_2 leakage from the bundle sheath to the mesophyll (L), and g_{bs} should be small enough for concentrating CO_2 in the bundle sheath. Carbon dioxide can originate from mitochondrial dark respiration (R_m, R_s) in

mesophyll and bundle sheath cells, respectively.[76] Following the model of von Caemmerer and Furbank, the following two equations specific for C_4-photosynthesis can be written:

$$L = g_{bs}(C_s - C_m) \quad (4)$$

where C_m is the CO_2 level in the mesophyll cell, and C_s is the CO_2 level at the carboxylation site of Rubisco in the bundle sheath chloroplast.

$$A = V_p - L - R_m \quad (5)$$

where V_p is the rate of PEP carboxylation, and R_m is the mitochondrial respiration occurring in the mesophyll, which for practical purposes can be set to $0.5R_d$. The rate of PEP carboxylation (V_p) can be limited either by the activity of PEP carboxylase or by the rate of electron transport. For the enzyme-limited case, von Caemmerer and Furbank used a Michaelis–Menten equation to describe V_p (Michaelis–Menten constant of PEPcase for CO_2 (K_p) = 80 µbar at 25°C).[76]

Table 1.6: Photosynthesis parameters (constants) for the C_4 model at 25°C.[76]

Parameter	Value	Description
V_{cmax}	60 µmol.m^{-2}.s^{-1} or variable	Maximum Rubisco activity
K_c	650 µbar	Michaelis constant of rubisco for CO_2
K_o	450 mbar	Michaelis constant of rubisco for O_2
γ^*	0.000193 (0.5/2590)	$0.5/(S_{c/o})$, half reciprocal of rubisco specificity
V_{pmax}	120 µmol.m^{-2}.s^{-1} or variable	Maximum PEP carboxylase activity
V_{pr}	80 µmol.m^{-2}.s^{-1} or variable	PEP regeneration rate
K_p	80 µbar	Michaelis constant of PEP carboxylase for CO_2
g_s	3 mmol.m^{-2}.s^{-1}	Bundle-sheath conductance to CO_2
g_o	0.047 g_s	Bundle-sheath conductance to O_2
R_d	$0.01V_{cmax}$	Leaf mithocondrial respiration
R_m	$0.5R_d$	Mesophyll mithocondrial respiration
α	$0 < \alpha < 1$	Fraction of PSII activity in the bundle-sheath
x	0.4	Partitioning factor of electron transport rate
J_{max}	400 µmol electrons m^{-2}.s^{-1}	Maximal electron transport rate

Figure 1.19 shows graphically how these eqations are derived and can be applied to gas exchange measurements.

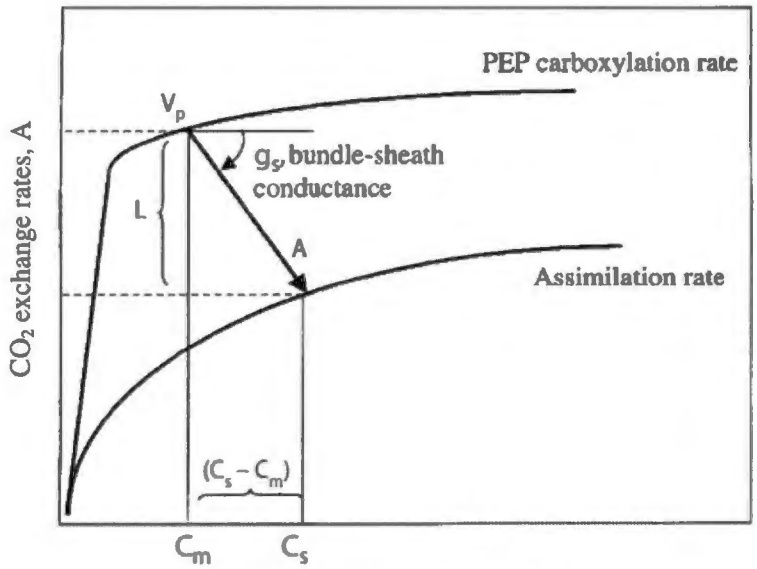

Figure 1.19: Graphical summary of the main features of the C_4-photosynthetic pathway. The two curves are the rate of phosphoenolpyruvate (PEP) carboxylation, V_p, as a function of mesophyll CO_2 partial pressure, C_m, and CO_2-assimilation rate, A, as a function of bundle-sheath CO_2 partial pressure, C_s. The slope of the arrow connecting the two curves gives the bundle-sheath conductance $g_s = L/(C_s - C_m)$ and the leak rate $L = V_p - A$.[76]

1.6 Problem statement & aims and objectives

Due to a growing world population, the need has arisen to maximize the production capacity of arable agricultural land. Developing countries continue to struggle to produce sufficient food crops, which results in the fact that large populations suffer from malnutrition, especially in Sub-Saharan Africa.[77,82] At present more than 80% of the world's cereal is produced in United States, Canada, Australia and Argentina.[78,79] Crop production is central in the world food supply and abiotic stressors have been shown to significantly influence and limit crop production in regions where these stress conditions exist.[80] In 1982, Boyer indicated that environmental factors may limit crop production by as much as 70% .[81] A 2007 FAO report stated that only 3.5% of the global land area is not affected by some environmental constraints. During the last few decades, with the advent of the industrial revolution, anthropogenic activities have placed further stress on the environment and struggling agricultural crop production.

In South Africa, maize is regarded as the most important starch and carbohydrate sources to its population. Maize is primarily grown in the Highveld and western parts of South Africa (see Figure 1.3). In 2007, a large part of this maize growing region was declared as a high priority area, because of the many sources of environmental pollution that have been identified in the area. The largest

contributors to environmental pollution in the area are related to a tremendous increase in industrial activities and subsequent urbanization. Effectively, three forms of pollution have been identified, which includes ionic (dissolved solids such as heavy metal ions), atmospheric pollution (such as ozone) and particulate matter (very fine water insolubles). All of these forms of pollution have been shown to cause significant decreases in the growth and yield of natural and agricultural vegetation.

This thesis aims to evaluate the influence of selected types of these three identified forms of industrial related pollution sources on popular South African maize (*Zea mays L.*) cultivars. Because of its tremendous sensitivity, photosynthesis has been shown previously as an effective tool with which to study the influence of such abiotic stresses on vegetation. Subsequently, the main emphasis of this study focussed on the sensitivity of the maize cultivars to the selected types/forms of industrial related pollution sources. Firstly, the influence of different concentrations (from deficiency to toxicity levels) of transition metals (copper, iron, manganese and zinc) vital to efficient plant metabolic functionality was evaluated. The latter stress is mainly soil condition orientated. The 2nd stress that was evaluated is the atmospheric pollution source, ozone (O_3), which has previously been shown to cause more damage to vegetation world-wide than all the other air pollutants combined.[53] Thirdly, the effect of a relatively new type of abiotic stress termed manufactured nanoparticles, was assessed. TiO_2- and SiO_2 nanoparticles were chosen for the study, mainly because of their low dissolution propensity. More information on the 3 investigated abiotic stresses will be provided in the 3 experimental chapters (Chapter 2-4).

1.7 Outline of thesis

In Chapter 1 the concept of plant stress is discussed, outlining the types of stresses that have been identified and shown to limit growth and yield performance. The importance and growing areas of maize in South Africa are highlighted. The sources and common levels of the the studied pollution types are given. Some literature on the effect of the studied pollution types on plants is reviwed. The processes comprising the main events of photosynthesis and some popular techniques (chlorophyll *a* fluorescence and photosynthetic gas exchange) used to study these processes are also described. The concept and role of the photo-protective alternative electron acceptors in the electron transport chain is discussed.

In Chapter 2 various transition metals (copper, iron, manganese and zinc) are reviewed in terms of their role in plants, as well as certain reported toxicity effects. The influence of deficient and excess concentrations of the studied transition metals on the photosynthetic electron transport (PSI and PSII) of a popular South African maize cultivar (IMP 52-11) was investigated, by making use of

chlorophyll *a* fluorescence and modulated 820 nm reflection, respectively. Furthermore, the effect of these treatments on the biomass accumulation of the treated plants was also evaluated.

In Chapter 3 chlorophyll *a* fluorescence, modulated 820 nm reflection and photosynthetic gas exchange measurements were used to evaluate the photosynthetic and stomatal sensitivity of two different South African maize cultivars, PAN 6411 and IMP 52-11, to various reported O_3 concentrations. Moreover, a decoupling model was also constructed in an attempt to show an increase in decoupling (electron losses) between the electron transport and CO_2-assimilation phases, with increasing O_3 concentration.

In Chapter 4 chlorophyll *a* fluorescence, modulated 820 nm reflection and photosynthetic gas exchange measurements were used to examine the effect of increasing concentrations of TiO_2- and SiO_2 nanoparticles on photosynthetic electron transport, stomatal behaviour and CO_2-assimilation properties of the IMP 52-11 maize cultivar. In addition, the decoupling model (from Chapter 3) was again constructed to show increased decoupling (electron losses) between the electron transport and CO_2-assimilation phases, with increasing nanoparticle concentration. Furthermore, the concentration of popular ROS markers and the activity of antioxidant enzymes were measured in order to establish if the nanoparticle treatments caused an increase in alternative electron acceptor reduction.

In Chapter 5 the most important findings described in the experimental chapters are summarised and discussed. Furthermore, the efficacy of the methods used to assess the influence of the studied environmental pollution types, is evaluated. The new knowledge gained from the current study is highlighted and some recommendations for future work are made.

1.8 References

1. Report: Trends in the Agricultural Sector, South African Department of Agriculture, Forestry and Fisheries, 2013.
2. T.S. McCarthy, The impact of acid mine drainage in South Africa, South African Journal of Science, 107, 712-719, 2011.
3. D.W. Blowes, C.J. Ptacek, J.L. Jambor, C.G. Weisener, The geochemistry of acid mine drainage, In: Holland HD, Turekian KK, editors. Treatise on geochemistry. Oxford: Elsevier, p. 150–204, 2003.
4. F.D.I. Hodgson, R.M. Krantz, Investigation into groundwater quality deterioration in the Olifants River catchment above the Loskop Dam with specialised investigation in the Witbank Dam sub-catchment, WRC Report 291/1/98. Pretoria: Water Research Commission; 1998.
5. M. Agrawal, Effects of air pollution on agriculture: An issue of national concern, National Academy of Sciences, India, 28, 93-106, 2005.

6. A.M. van Tienhoven, Forestry problems in Africa, [In:] Innes, J.L., Haron, A.H. (eds.) Air Pollution and the Forests of Developing and Rapidly Industrializing Countries. DCABI Publishing, Wallingford, UK, 262pp, 2000.
7. M.R. Ashmore, F.M. Marshall, Ozone impacts on agriculture: an issue of global concern, Advances in Botanical Research, 29: 32-49, 1999.
8. L. Peñarrubia, J. Moreno, Molecular mechanisms of plant responses to elevated levels of tropospheric ozone, [In:] Pessarakli, M., eds. Handbook of Plant and Crop Stress, 2nd ed. Taylor & Francis, New York, p.769-793, 1999.
9. L. Coetzee, H.H. du Preez, J.H.J. van Vuren, Metal concentrations in Clarias gariepinus and Labeo umbratus from the Olifants and Klein Olifants River, Mpumalanga, South Africa: Zinc, copper, manganese, lead, chromium, nickel, aluminium and iron, ISSN 0378-4738 = Water SA Vol. 28, No. 4, October 2002.
10. P. Ashton, D. Love, H. Mahachi, P. Dirks, An Overview of the Impact of Mining and Mineral Processing Operations on Water Resources and Water Quality in the Zambezi, Limpopo and Olifants Catchments in Southern Africa. Report to Minerals, Mining and Sustainable Development Project, Southern Africa, p338, 2001.
11. B. Davies, J. & Day, Vanishing waters. Cape Town: University of Cape Town Press, 1998.
12. E. M. Fagbote and E.O. Olanipekun, American-Eurasian Journal of Scientific Research, 5, 4, 241, 2010.
13. T. Oyelola and A. I. Baatunde, International Journal of Pure and Applied Sciences, 2, 1, 17, 2008.
14. R.P. Rorich, J.S. Galpin, Air Quality in the Mpumalanga Highveld region, South Africa, South African Journal of Science, 94: 109-114, 1998.
15. Lauri Laakso, Johan Paul Beukes, Pieter Gideon Van Zyl, Jacobus J. Pienaar, Miroslav Josipovic, Andrew Venter, Kerneels Jaars, Ville Vakkari, Casper Labuschagne, Kgaugelo Chiloane and Juha-Pekka Tuovinen, Ozone Concentrations and Their Potential Impacts on Vegetation in Southern Africa, Developments in Environmental Science, Global Dimension of Air Pollution as Part of Climate Change, Vol. 13, Chapter 20, Elsevier, 2013.
16. N.L. Lacasse, M. Treshow, Diagnosing Vegetation Injury Caused by Air Pollution. U.S. Environmental Protection Agency Handbook, 1976.
17. M.C. Scholes, K.A. Olbrich, E. van Rensburg, The environ-mental impact of atmospheric pollution in the industrial Highveld and adjacent regions: crops, indigenous vegetation and commercial forests. [In:] Held, G., Gore, B.J., Surridge, A.D., Tosen, G.R., Turner., C.R., & Walmsey, R.D. eds. Air pollution and its impacts on the South-African Highveld, Environmental Scientific Association, Cleveland, 1996.
18. A.D. Maynard, Nanotechnology: A Research Strategy for Addressing Risk.Woodrow Wilson International Center for Scholars,Washington, DC, 2006.

19. B. Nowack, T.D. Bucheli, Occurrence, behavior and effects of nanoparticles in the environment, Environmental Pollution, 150, 5-22, 2007.
20. J.J. Rottman, Fundamentals and application of porous media filtration for the removal of nanoparticles from industrial wastewater, PhD thesis, University of Arizona, 2012.
21. F. Gottschalk, R.W. Scholz, B. Nowack, Probabilistic material flow modeling for assessing the environmental exposure to compounds: Methodology and an application to engineered nano-TiO_2 particles, Environmental Modelling & Software, 25, 320–332, 2010.
22. T.J. battin, F. v.d. Kramer, A. Sweilhartner, S. Ottofuelling, T. Hofmann, nanostructured TiO_2: Transport behavior and effects on aquatic microbial communities under environmental conditions, Environmental Modelling & Software, 28, 102–220, 2010.
23. K. Schmid, M. Riediker Use of nanoparticles in Swiss industry: a targeted survey, Environmental Science and Technology, 42, 7, 2253–2260, 2008.
24. L.K. Limbach, R. Bereiter, E. Müller, R. Krebs, R. Galli, W.J. Stark, Removal of oxide nanoparticles in a model wastewater treatment plant: influence of agglomeration and surfactants on clearing efficiency, Environmental Science and Technology, 42 (15), 5828–5833, 2008.
25. T. Yadav, A.A. Mungray, A.K. Mungray, Fabricated Nanoparticles: Current Status and Potential Phytotoxic Threats, D.M. Whitacre (ed.), Reviews of Environmental Contamination and Toxicology, volume 230, Reviews of Environmental Contamination and Toxicology, 230, Springer International Publishing ,Switzerland, 2014.
26. M. Khus, W. Gernjak, P.F. Ibanez, S.M. Rodriguez, J.B. Galvez, S. Icli, A comparative study of supported TiO_2 as photocatalyst in water decontamination at solar pilot plant scale, Journal of Solar Energy, 128:331–337, 2006.
27. F. Aslani, S Bagheri, N. Julkapli, A.S. Juraimi, F.S.G. Hashemi, A. Baghdadi, Effects of Engineered Nanomaterials on Plants Growth: An Overview, The Scientific World Journal, Article ID 641759, Volume 2014.
28. G. Abdi, H. Salehi, M. Khosh-Khui, "Nano silver: a novel nanomaterial for removal of bacterial contaminants in valerian (*Valeriana officinalis* L.) tissue culture," Acta Physiologiae Plantarum, vol. 30, no. 5, pp. 709–714, 2008.
29. S. Mishra, R.S. Dubey, Heavy metal toxicity induced alterations photosynthetic metabolism in plants, Handbook of photosynthesis, Chapter 44, Taylor and Francis group, LLC, 2005.
30. H.J. Bohnert, D.L. Nelson, R.G. Jensen, Adaptations to environmental stress, Plant Cell, 7:1099–1111, 1995.
31. E.D. Schulze, E. Beck, K. Müller-Hohenstein, Plant Ecology, p.702-708, 2005.
32. Y. Gong, L. Rao, D. Yu, Abiotic Stress in Plants, Chapter 6, p.113-151, In Tech, 2013.
33. C.H. Foyer, G. Noctor, Redox sensing and signalling associated with reactive oxygen in chloroplasts, peroxisomes and mitochondria, Physiologia Plantarum, 119, 3, 355-364, 2003.

34. R.C. Bortolin, F.F. Caregnato, A.M. Divan Jr., F.H. Reginatto, D.P. Gelain, J.C.F. Moreira, Effects of chronic elevated ozone concentration on the redox state and fruit yield of red pepper plant Capsicum baccatum, Ecotoxicology and Environmental Safety, 100-114, 2014.
35. M.M. Chaves, J.P. Maroco, J.S. Pereira, Understanding plant responses to drought — from genes to the whole plant, Functional Plant Biology, 30, 239–264, 2003.
36. M.M. Chaves, J.M. Costa, N.J. Madeira Saibo, Recent Advances in Photosynthesis Under Drought and Salinity, in: Turkan, I. (Eds.), Plant Responses to Drought and Salinity Stress: Developments in a Post-Genomic Era, Academic Press Ltd-Elsevier Science Ltd, London, pp. 49–104, 2011.
37. Handbook of Photosynthesis, Taylor and Francis, 2nd ed., edited by M. Pessarakli, CRC press, 2005.
38. F.F. Caregnato, R.C. Bortolin, A.M.D. Junior, J.C.F. Moreira, Exposure to elevated ozone levels differentially affects the antioxidant capacity and the redox homeostasis of two subtropical *Phaseolus vulgaris L.* varieties, Chemosphere, 93, 320–330, 2013.
39. E.H. Kim , X.P. Li, R. Razeghifard, J.M. Anderson, K.K. Niyogi, B.J. Pogson, W.S. Chow, The multiple roles of light-harvesting chlorophyll a/b-protein complexes define structure and optimize function of *Arabidopsis* chloroplasts: a study using two chlorophyll b-less mutants, Biochimica Biophysica Acta, 1787(8):973-84, 2009.
40. P. Albertsson, A quantitative model of the domain structure of the photosynthetic membrane, Trends in Plant Science, 6, 349–358, 2001.
41. P.A. Albertsson, The structure and function of the chloroplast photosynthetic membrane, a model for the domain organization, Photosynthetic Research, 46, 141–149, 1995.
42. H. Kirchhoff, S. Haferkamp, J.F. Allen, D.B.A. Epstein, C.W. Mullineaux, Protein Diffusion and Macromolecular Crowding in Thylakoid Membranes, Plant Physiology, 146, 1571–1578, 2008.
43. L. Jin, P. Smith, C.J. Noble, R. Stranger, G.R. Hanson, R.J. Pace, Electronic structure of the oxygen evolving complex in photosystem II, as revealed by 55 Mn Davies ENDOR studies at 2.5 K, Physical Chemistry Chemical Physics, 16, 7799–7812, 2014.
44. A. Stirbet, Govindjee, On relation between the Kautsky effect (chlorophyll *a* fluorescence induction) and Photosystem II: Basics and applications of the OJIP fluorescence transient, Journal of Photochemistry and Photobiology B, 104 (1-2):236-57, 2011.
45. J.P. Whitelegge, H. Zhang, R. Aguilera, R.M. Taylor, W.A. Cramer, Full subunit coverage liquid chromatography electrospray ionization mass spectrometry (LCMS+) of an 302 oligomeric membrane protein: cytochrome b_6f complex from spinach and the *cyanobacterium Mastigocladus laminosus*, Molecular and Cellular Proteomics, MCP 1, 816–827, 2002.
46. D. Arnon, M. Allen, F. Whatley, Photosynthesis by isolated chloroplasts, Nature, 174, 394–396, 1954.

47. G.N. Johnson, Cyclic electron transport in C_3 plants: fact or artefact? Journal of Experimental Botany, 56, 407–416, 2005.
48. T. Joët, B. Genty, E.M. Josse, M. Kuntz, L. Cournac, G. Peltier, Involvement of a plastid terminal oxidase in plastoquinone oxidation as evidenced by expression of the Arabidopsis thaliana enzyme in tobacco, Journal of Biological Chemistry, 277, 31623–31630, 2002.
49. U. Heber, D. Walker, Concerning a Dual Function of Coupled Cyclic Electron Transport in Leaves, Plant Physiology, 100, 1621–1626, 1992.
50. Y. Munekage, M. Hashimoto, C. Miyake, K. Tomizawa, T. Endo, M. Tasaka, T. Shikanai, Cyclic electron flow around photosystem I is essential for photosynthesis. Nature 429, 579–582, 2004.
51. T. Shikanai, Central role of cyclic electron transport around photosystem I in the regulation of photosynthesis. Current Opinion in Biotechnology, Food biotechnology Plant biotechnology 26, 25–30, 2014.
52. S.P. Long, C.J. Bernacchi, Gas exchange measurements, what can they tell us about the underlying limitations to photosynthesis? Procedures and sources of error, Journal of Experimental Botany, Vol. 54, No. 392, pp. 2393-2401, November 2003.
53. R.C. Leegood, Strategies for engineering C_4-photosynthesis, Journal of Plant Physiology, 170, 378– 388, 2013.
54. J.R. Ehleringer, R.K. Monson, Evolutionary and ecological aspects of photosynthetic pathway variation, Annual Review of Ecolology, Evolution and Systematics, 24:411–39, 1993.
55. A.E. McDonald, A.G. Ivanov, R. Bode, D.P. Maxwell, S.R. Rodermel, N.P.A. Hüner, Flexibility in photosynthetic electron transport: The physiological role of plastoquinol terminal oxidase (PTOX), Biochimica et Biophysica Acta, 1807, 954–967, 2011.
56. C.H. Foyer, G. Noctor, Photosynthetic nitrogen assimilation: inter-pathway control and signalling, in: C.H. Foyer, G. Noctor (Eds.), Advances in Photosynthesis and Respiration. Photosynthetic Nitrogen Assimilation and Associated Carbon Respiratory Metabolism, Kluwer Academic Publishers, Dordrecht, pp. 1–22, 2002.
57. P. Streb, W. Shang, J. Feierabend, R. Bligny, Divergent strategies of photoprotection in high-mountain plants, Planta, 207, 313–324, 1998.
58. A. Wingler, P.J. Lea, W.P. Quick, R.C. Leegood, Photorespiration: metabolic pathways and their role in stress protection, Philosofical Transactions of the Royal Society London, B 355, 1517–1529, 2000.
59. K. Asada, The water–water cycle in chloroplasts: scavenging of active oxygen and dissipation of excess photons, Annual Reviews of Plant Physiology and Plant Molecular Biology, 50, 601–639, 2000.
60. H. Kautsky, A. Hirsch, Neue Versuche zur Kohlensaure assimilation, Naturwissenschaften, 19 964, 1931.

61. A.D. Stirbet, Govindjee, B.J. Strasser, R.J. Strasser, Chlorophyll *a* fluorescence induction in higher plants: Modelling and numerical simulation, Journal of theoretical Biology, 193: 131-151, 1998.
62. G.C. Papageorgiou and Govindjee (eds): Chlorophyll Fluorescence: A Signature of Photosynthesis, pp 1–42, Kluwer Academic Publishers. Printed in The Netherlands, 2004.
63. Neil R. Baker, Chlorophyll Fluorescence: A Probe of Photosynthesis *In Vivo*, Annuual Reviews of Plant Biology, 59:89–113, 2008.
64. R.J. Strasser, M. Tsimilli-Michael, A. Srivastava, Analysis of the Chlorophyll *a* Fluorescence Transient, in: Chlorophyll Fluorescence: A Signature of Photosynthesis, George C. Papageorgiou and Govindjee (eds): Kluwer Academic Publishers. Printed in The Netherlands, pp. 342–391, 2004.
65. Govindjee, Sixty-three years since Kautsky: chlorophyll *a* fluorescence, Australian Journal of Plant Physiology, 22, 131–160, 1995.
66. G. Schansker, S.Z. Toth, R.J. Strasser, Methylviologen and dibromothymoquinone treatments of pea leale reveal the role of photosystem I in the Chl a fluorescence rise OJIP, Biochimica et Biophysica Acta, 1706, 250–261, 2005.
67. P.D.R. Van Heerden, J.W. Swanepoel, G.H.J. Krüger, Modulation of photosynthesis by drought in two desert scrub species exhibiting C_3-mode CO_2-assimilation, Environmental and Experimental Botany, 61,124–136, 2007.
68. F. Bussotti, R. Desotgiu, C. Cascio, M. Pollastrini, E. Gravano, G. Gerosa, R. Marzuoli, C. Nali, G. Lorenzini, E. Salvatori, F. Manes, M. Schaub, R.J. Strasser, Ozone stress in woody plants assessed with chlorophyll a fluorescence. A critical reassessment of existing data, Environmental and Experimental Botany, 73, 19–30, 2011.
69. R.J. Strasser, M. Tsimilli-Michael, S. Qiang, V. Goltsev, Simultaneous in vivo recording of prompt and delayed fluorescence and 820 nm reflection changes during drying and after rehydration of the resurrection plant Haberlea rhodopensis. Biochimica Biophysica Acta, 1797: 122–122, 2010.
70. E. Salvatori, L. Fusaro, E. Gottaradini, M. Pollastrini, V. Goltsev, R.J. Strasser, F. Bussotti, Plant stress analysis: applications of Prompt, Delayed Chlorophyll Fluorescence and 820 nm Modulated Reflectance. Insights from independent experiments, Plant Physiology and Biochemistry, In Press, 2014.
71. G.D. Farquhar, T.D. Sharkey, Stomatal conductance and photosynthesis, Annuual Reviews of Plant Physiology, 33: 317–345, 1982.
72. S.S. Mulkey, M. Smith, Measurement of photosynthesis by Infra-Red Gas Analysis, IN: Bioinstrumentation, C.T. Lange, (ed). 79-84, Publication of the American Biology Teachers Association, 1988.
73. G.H.J. Kruger, 3rd year practical student guide, North-West University, Potchefstroom, 2014.

74. G.D. Farquhar, S. von Caemmerer, J.A. Berry, A biochemical model of photosynthetic CO_2-assimilation in leaves of C_3 species, Planta, 149:78–90, 1980.
75. N.W. Pammenter, Research letter, Clarification of an apparent anomaly in the supply function associated with the response of carbon assimilation to carbon dioxide determined using conventional field equipment, South African Journal of Science, 85:271-272, 1989.
76. S. von Caemmerer, & R.T. Furbank, Modeling C_4-photosynthesis. C_4 Plant Biology (eds. R. F. Sage & R. K. Monson), Academic Press, San Diego, 1999.
77. D. Pimental, X. Huang, A. Cordova, M. Pimental, Impact of population growth on food supplies and environment, Population and Environment, 19: 9-14, 1997.
78. Bureau U-C, Global population at a glance: 2002 and beyond. In International Brief, Washington, DC: US Census Bureau, 2004.
79. T.J. Marchione, E. Messer, Food Aid and the World Hunger Solution: Why the U.S. Should Use a Human Rights Approach, Food and Foodways: Explorations in the History and Culture, 18: 10-27, 2010.
80. G.R. Cramer, K. Urano, S. Delrot, M. Pezzotti and K. Shinozaki, Effects of abiotic stress on plants: a systems biology perspective, BMC Plant Biology, 11:163, 2011.
81. J.S. Boyer, Plant productivity and environment, Science, 218, 4571, 443-448, 1982.
82. M.R. Ashmore, J.N.B Bell, The role of ozone in global change, Annals of Botany, 67: 39-48, 1991.

Chapter 2

Evaluation of the photosynthetic electron transport performance of a South African maize cultivar (IMP 52-11) under varying copper, manganese, iron and zinc concentrations

Chapter 2

Evaluation of the photosynthetic electron transport performance of a South African maize cultivar (IMP 52-11) under varying copper, manganese, iron and zinc concentrations

2.1.1 Introduction

Industrialization plays a vital role in sustaining a nation's economy and improving the wellbeing of its citizens. However, industrialization also has a negative impact, particularly in terms of the release by industrial processing plants of unwanted by-products into the ecological system. These abiotic stressors include toxic metal concentrations from metal smelters and continuous fertilizer programs, high salinity from irrigation water as well as various green-house gasses from several industries. Also, the long-term effects of industrial pollution on the environment may be disastrous for not only people but for all living organisms if not carefully controlled. This explains the current awareness among researchers of the need to monitor the activities of process industries, especially those that discharge heavy metals into the environment. Heavy metals occur naturally in the ecosystem, with large variations in concentration. In modern times, anthropogenic sources of heavy metals, that is, man-made pollution, have also been introduced to the ecosystem. The resultant build-up of heavy metals and sediments in the soil has caused acute concern in environmentalists. The main issues include the potential toxicity to plants and wildlife which an overload of heavy metals may cause, and the inherent problems of biomagnification that may occur at several levels in the biological food chain. The concentration of heavy metals retained in soils varies widely. These differences are brought about by the surrounding geological environment, and by the anthropogenic and natural activities taking place in that area. Heavy metal transport is mainly dependent on the physical and chemical properties of soil and waterbodies, i.e. the pH, mineralogical composition as well as the clay and organic content.[3]

2.1.2 Heavy metal pollution in a South African context

South Africa is rich in mineral resources and is one of the leading mineral raw and processed material exporters in the world. The main mineral raw materials are gold, diamonds, platinum, chromium, vanadium, manganese, uranium, iron ore and coal (USGS, 2009).[4] Pollution from mining activities is probably the most direct cause of groundwater contamination in the country. Despite the prolific mining activities, there is still little information available in South Africa on pollution and the fate of trace metals in surface waters or sediments. This has been attributed to relatively few studies that have been undertaken to establish the levels of heavy metals and primarily because of lack of enforcement of stringent regulatory guidelines in the past.[5] The dewatering processes of the mines and disposal of

wastes contribute to environmental heavy metal pollution. One of the potential hazards of mining operations is that as water flows through settlements around mining operations, heavy metals are dispersed in the environment. Some parts of the country (Highveld priority area), where there are more of these mining operations, experience poor water quality, which is likely to impact the fresh water resources on long term basis.[5] For example, an impact assessment study on the dewatering of mine waters in the East Rand Blesbokspruit, reported traces of metal concentration higher than the world average concentrations measured in rivers.[5] Mining processes such as acid mine drainage (AMD) also play a major role in metal contamination. Please refer to Chapter 1 (Section 1.2.2.1) for a review the AMD process and mechanisms with which it causes pollution. If left unchecked, AMD will continue to contribute to increased concentrations of dissolved salts, metal ions and, in some instances, radionuclides to the already stressed river and reservoir systems. Low pH values in AMD areas will increase the solubility of trace metals locked up in sediments and release these into the overlying water. The Witwatersrand region in South Africa is famous for its gold production. The groundwater within the mining district is heavily contaminated, has elevated concentrations of heavy metals and is acidified as a result of oxidation of pyrite (FeS_2) contained in waste rock and tailings dumps. The polluted groundwater is discharged into streams in the area and contributes up to 20% of total stream discharge, causing a lowering of pH in the stream water while most of the metal load is precipitated. The type and concentration of metal pollutants vary greatly, depending on the geology, pH, soil texture (and cation exchange capacity) as well as the distance from the pollution source. Trace metals have little degradation potential and they tend to accumulate in sediments which form metal-rich deposits and with continued accumulation of metals in the sediment, the environmental threshold is often exceeded causing toxicity.[4,5] Concentrations up to an average of 40 $mg.L^{-1}$ in water sources adjacent to the mining areas have been reported.[4,5] Furthermore, a change in oxidation state can easily remobilize sequestered trace metals, causing an up-concentrating effect of metal-rich deposits that could reach concebtrations up to 1-2 mM in the soil, resulting in a potential long term source of metal pollution.[3-5] This results in the bioaccumulation of metals, which moves up the food and causes genotoxicity among living organisms.[4]

2.1.3 Metals in plants

Due to the complexity of a plant's metabolism, it is possible that the same abiotic stress can affect various metabolic pathways simultaneously.[1] The influence of metal stress on plants has been studied intensively during the last few decades due the impact it has had on crop production. Metal stress can essentially be divided into two sub-catagories; i) toxic heavy metals including cadmium (Cd), lead (Pb), arsenic (As) and mercury (Hg) which have no known role in plant metabolism and ii) transition metals such as copper (Cu), manganese (Mn), iron (Fe) and zinc (Zn) that play a vital role in plant metabolism.[2] Deficiencies of the latter can significantly limit the functionality of various biochemical

pathways within the plant. One such process where various transition metals play an important role is photosynthesis. The role of these micronutrients in photosynthesis can either be directly involved in photosynthetic electron transport, as co-factors of enzymes involved in photosynthesis or in free radical detoxification. Although these metals are essential for plant metabolism (micronutrients), excess amounts of these metals adversely affect the metabolism of a plant.[2,3]

The importance and location of these metals will be briefly discussed in Section 2.1.4, while Section 2.1.5 will focus on the possible toxicities of these metals. For a more comprehensive review of most known plant enzymes/proteins where copper, manganese, iron and zinc are thought to be involved in, see Hansch *et. al* 2009.[13]

2.1.4 Biochemical role of transition metals in plant metabolism, with the emphasis on photosynthesis and its role in the protection of photosynthetic integrity

Manganese is located on the PSII donor side as part of the OEC. Copper forms part of plastocyanin (PC) which transfers electrons from the Cytochrome b_6f complex to PSI electron acceptors. Iron in its non-heme form, is bound to a bicarbonate ion located between Q_A and Q_B. An iron-sulphur protein (FeS) known as the Rieske FeS forms part of the Cytochrome b_6f (Cyt b_6f) complex. Furthermore, iron is also located as part of PSI in the form of three iron-sulphur centres (F_x, F_A and F_B) and as part of Ferredoxin (Fd) (of which there are more than one).[14] The positions of the transition metals involved in photosynthesis are given in Figure 2.1.

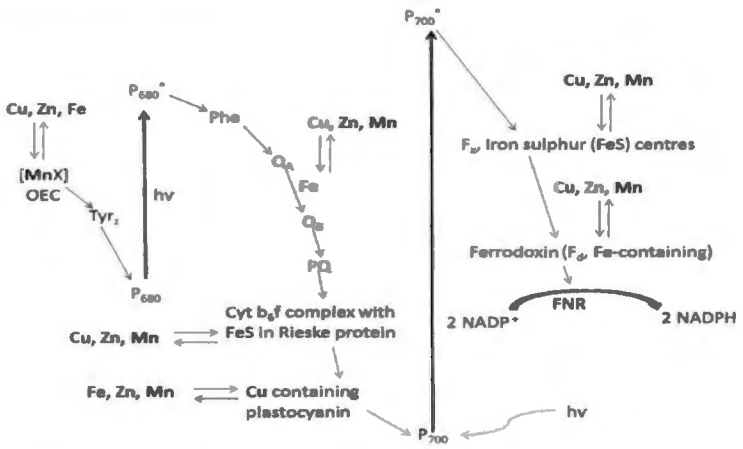

Figure 2.1: A modified Z-Scheme for electron transport in photosynthesis showing the localities of the various transition metals within the electron transport chain and the possible metal interactions with the metal containing centres.[14]

2.1.4.1 Copper (Cu)

Copper is an important transition metal in many cellular processes. It is used as a co-factor in various enzymatic reactions, for example as prosthetic group of the chloroplastic antioxidant enzyme Cu/Zn superoxide dismutase (Cu/Zn-SOD).[2] The function of this enzyme is the conversion of O_2^- radicals (formed via the Mehler reaction) to H_2O_2 and O_2.[6] This is a critical enzyme reaction which protects cellular constituents from oxidative damage (ROS). Cu/Zn superoxide dismutase is found throughout the plant cell and has been shown to be localized in the cytoplasm, peroxisomes and chloroplasts. Figure 2.2 is a schematic demonstration of the protective mechanism and location of Cu/Zn-SOD.[10]

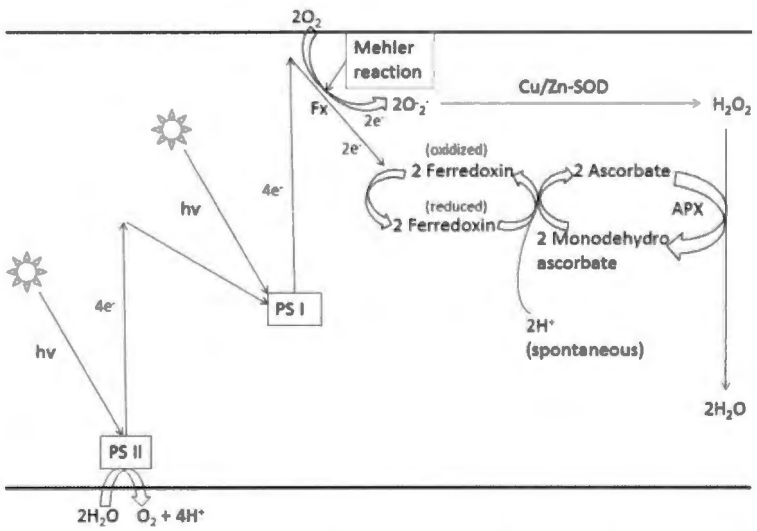

Figure 2.2: Scheme, showing the functionality of Cu/Zn-SOD during the Mehler reaction in photosynthetic electron transport.[2]

However, most of the copper that enters the plant is located within the chloroplast as part of the structure of plastocyanin which is a 10-kDa copper-containing mobile protein coupling electron transfer from photosystem II to photosystem I (PSII to PSI).[2,8] It is located in the thylakoid lumen and transfers electrons between the reduced cytochrome of the b_6f complex and the photo-oxidized P700 of PSI.[2,8] Figure 2.1 shows the location of the copper containing plastocyanin (PC) protein in the electron transport chain.

2.1.4.2 Manganese (Mn)

Manganese is essential to the functioning of photosynthesis in plant systems as it is a critical component of the oxygen evolving complex (OEC) which produces electrons, protons and molecular oxygen through the catalytic splitting of water (see Figure 2.1).[2] The OEC is a tetra-nuclear manganese cluster that is closely associated with the water splitting reaction centre and it is stabilized

by a number of extrinsic polypeptides as well as calcium and chloride ions. Two water molecules bind to the cluster complex producing the four oxidizing equivalents required for their oxidation through five so-called S-states (S_0 to S_4).[2] Without manganese to catalyse the water splitting reaction, no electrons would thus be able to be extracted from water to drive PSII activity.

Similar to copper, manganese also acts as a co-factor for another superoxide dismutase enzyme (Mn-SOD), which also protects the cellular constituents from ROS. Manganese superoxide dismutase is localized in mitochondria and peroxisomes in plant cells.[10] Manganese also plays a role in ATP synthesis, in RuBP carboxylase reactions and the biosynthesis of fatty acids, acyl lipids and proteins. In addition, manganese plays a primary role in the activation and as co-factor of various other enzymes in plants (~ 35) such as: Mn-catalase, pyruvate carboxylase and phospho-enolpyruvate carboxykinase.[11] Manganese is essential for the biosynthesis of chlorophyll (through the activation of specific enzymes), aromatic amino acids (tyrosine) and secondary products such as lignin and flavonoids. Furthermore, it participates in the biosynthetic pathway of isoprenoids and the assimilation of nitrates.[11]

2.1.4.3 Iron (Fe)

Iron is another essential transition metal that has several important functions in a plants' metabolism. Iron is essential for chlorophyll synthesis and deficiency in iron has been shown to cause dramatic decreases in chlorophyll concentration.[12] Depending on the function, type of ligand and location within the plant, iron can be divided into three subgroups; i) proteins with iron–sulphur clusters (Fe–S), ii) heme-containing proteins and iii) other iron proteins (known as non-heme proteins).[13] The highest concentration of iron within the plant is located within the chloroplasts, which suggests its importance in photosynthesis. Iron-sulphur (Fe-S) proteins play a vital role in the electron transport process where various iron localities have been previously demonstrated (see Figure 2.1). Whilst the heme proteins are pivotal to photosynthesis and electron transport, [13] some non-heme proteins play a role in cellular detoxification and protection against ROS. One such form of protein is iron superoxide dismutase (Fe-SOD), which has been shown to be localized within chloroplasts.[10]

2.1.4.4 Zinc (Zn)

Zinc is an important component of several enzymes within a plant, for example as a cofactor in the enzymes involved in protein synthesis and energy production.[13] Most of the zinc enzymes are involved in the regulation of DNA-transcription, RNA-processing and translation. Several proteolytic active enzymes within the chloroplast have also been found to be zinc dependent.[13] One such example is the repair of photo-damaged PSII by turning over the damaged D1 protein. Furthermore, net

photosynthesis is also affected by zinc deficiencies due to the limiting of the activity of carbonic anhydrase (involved in CO_2 fixation) and Cu/Zn-SOD, which plays a major role in the elimination of chloroplastic ROS formed during electron transport. See Figure 2.2 for a schematic illustration of the involvement of Cu/Zn-SOD in ROS elimination.

2.1.5 Transition metal toxicity on plant metabolism and photosynthetic behaviour

In the sections above, the importance of the transition metals Cu, Mn, Fe and Zn in plants have been highlighted but it is important to note that excess concentrations of these metals can be detrimental to plant health. Recent research has more specifically explored the effect of excess amounts of essential metals on photosynthesis.[1-3, 1, 19, 21,23, 25, 29] According to Ernst *et al.*, 1992 approximately 10% of excess metals that enters the plant accumulates in the leaves while only 1% enters the chloroplasts.[15] Since the mode and site of toxicity is dependent on the type of metal, the toxicity due to Cu, Mn, Fe and Zn will be briefly discussed in the following sections.[2, 16]

2.1.5.1 Copper toxicity

While copper is an essential part of many enzymes and photosynthesis, excess copper can be detrimental to plant health and development. Several sites of copper toxicity have been reported in the literature with reference to photosynthesis.[2] According to the literature, four effects of copper toxicity on photosynthesis have been reported; i) Ultrastructural changes in chloroplasts, ii) effect on PSII efficiency and chlorophyll status, iii) effect on electron transport and ribulose-1,5-bisphosphate carboxylase/oxygenase (Rubisco) activity and iv) formation of ROS which damage the photosynthetic apparatus.[2]

i) Effect of excess Cu on ultrastructural changes in chloroplasts

Several publications have reported that excess copper cause structural changes to the thylakoid membrane.[17,18] In a study by Patsikka *et al*, 2001, Cu-treated plants showed a lower level of acyl lipids as structural constituents of the thylakoid membranes, which was especially evident in the decrease of monogalactosyl diacylglycerol (MGDG).[19] Any increase in the unsaturated fatty acid level in membrane lipids will invariably cause destabilisation of reaction centres, which will ultimately lead to inhibition of PSII.[17] Studies of possible alterations on the PSI structure are not often cited in the literature. Copper induced structural changes in the photosynthetic apparatus have also been reported due to deficiencies of other transition metals, seeing that the uptake and translocation of the various metals are often in competition.[20]

ii) Effect of excess Cu on PSII efficiency and chlorophyll status

The susceptibility of PSII to copper damage is well documented. *In vitro* studies have shown that PSII is more sensitive to excessive copper than PSI.[21] Copper has also been reported to decrease chlorophyll bio-synthesis, which could be a result of an indirect effect, given that copper is in competition with other metals (Fe, Mn, Zn, etc.) because of their similar charge and ionic radius.[22]

iii) Effect of excess Cu on electron transport and Rubisco activity

The debate as to where the exact inhibiting location of electron transport as a result of copper toxicity, remains controversial.[2] On the PSII reducing side, the Q_B binding site and the Pheo-Fe-Q_A domain have been reported as the most sensitive sites for Cu^{2+} toxicity.[2] Some studies show inhibition at both the donor and acceptor side of PSII. Maksymiec *et al.*,1997 argued that inhibition of the Calvin cycle (and subsequent down regulation of electron transport) was the main reason why PSII activity decreased in the presence of excess copper.[2,23] The non-heme iron between Q_A and Q_B has also been suggested as a possible site for copper interaction through the exchange of the non-heme iron with copper.[2,24-26] Studies have shown an imbalance between Q_A reduction by PSII activity and the re-oxidation of Q_A by PSI activity, which invariably points to a 'break in the chain' between PSII acceptors and PSI acceptors.[2] Copper inhibition of the binding site of Q_B has also been reported through a non-competitive action with DCMU (which block Q_B binding sites).[2,32] The presence of high concentrations of copper within chloroplasts has been implicated in the destabilisation of the OEC complex through exchange of both Mn and Ca from the OEC, causing the OEC to dissociate.[2,27-29] Similarly, plants grown in excess copper have been shown to have a decreased Rubisco activity.[2,21] Figure 2.1 shows the proposed main sites of action of copper toxicity on PSII and PSI electron transport.

iv) Effect of excess Cu on ROS formation and cellular damage

Redox active metals such as Cu and Fe can cause direct formation of ROS through the Fenton and Haber-Weiss reactions. Reactive oxygen species have been extensively shown to cause damage to almost all cellular components, including the photosynthetic apparatus.[2,3]

2.1.5.2 Manganese toxicity

Depending on soil conditions, excess manganese in the soil can have several adverse effects on crop production. Research has shown that low soil pH can exaggerate the effect of high manganese levels in the soil, due to the higher solubility of the manganese ions at low pH values.[33] The effects of

manganese toxicity have been described in the literature, with its inhibiting effects ascribed to various metabolic systems of which only a few will be discussed below:

i) Effect of excess Mn on chlorophyll concentration

Manganese dependent enzymes have been shown to be involved in chlorophyll bio-synthesis. Therefore, manganese deficiencies and excess directly influences the concentration of chlorophyll.[2] Several studies have reported decreased chlorophyll levels under excess manganese conditions.[34,35] These studies have shown that manganese toxicity not only lowers chlorophyll biosynthesis, but also causes increased chlorophyll degradation.[2,34,35] Some authors have attributed the chlorophyll degradation to photo-oxidation caused by oxidised manganese species within the chloroplast,[36] whilst others have attributed a reduced chlorophyll biosynthesis to the possible ion exchange between Mg^{2+} and Mn^{2+} within the chlorophyll structure.[35]

ii) Effect of excess Mn on CO_2-assimilation and Rubisco activity

Studies have shown that the reduction in photosynthetic activity in the presence of increased manganese concentrations preceded the onset of chlorophyll degradation.[37] Houtz *et al.*, 1988 found a significant decline in photosynthetic activity due to the inhibitory effect of high concentrations of Mn, which they ascribed to a Mn induced modification of the Rubisco kinetics.[38] A more recent study by Li *et al.*, 2010 indicated that CO_2-assimilation was severely decreased in *Citrus grandis* seedlings under excess Mn conditions due to a reduction in the activity of the whole photosynthetic electron transport chain from the donor side of PSII to the reduction of end acceptors of PSI, thus limiting the production of reducing equivalents and hence the rate of CO_2-assimilation.[39]

iii) Effect of excess Mn reactive oxygen species (ROS) formation

Excess manganese concentrations have been shown to cause the formation of ROS in the Fenton type reaction.[39]

iv) Effect of excess Mn on electron transport through PSI and PSII

Photosystem sensitivity to manganese toxicity has been studied extensively during the last few decades. Despite these extensive studies, various conflicting opinions exist surrounding their mode of action, location of inhibition and differential inhibiting response on PSI, PSII or the intersystem electron transporters such as the Cyt b_6f-complex. Most recent studies using chlorophyll *a* fluorescence have shown a definite decrease in the quantum efficiency of PSII due to manganese

toxicity.[39,40] Doncheva *et al.,* 2009 reported that a decrease in various electron transport parameters in Mn-sensitive *Zea mays L.* under excess manganese concentrations.[41] Li *et al.* performed a chlorophyll *a* fluorescence study on *Citrus grandis* seedlings under excess Mn conditions in which they reported a decrease in various electron transport parameters as well as the overall photosynthetic performance index.[39] They also reported an increase in non-photochemical energy dissipation due to an increased amount of closed reaction centres.

2.1.5.3 Iron toxicity

Although reports on Fe toxicities are rare, some studies have been published on the effects of excess iron on plant metabolism. Acidic and water logged soil have been shown to promote the effect of Fe toxicity due to the high solubility of Fe at a low pH.[2] As elevated levels of other transition metals can cause Fe deficiency, excess amounts of Fe can also cause deficiencies of transition metals such as Cu, Mn and Zn (due to similar uptake mechanisms based on ionic radii).[2] Furthermore, excess Fe has been shown to have several adverse effects on plants. Only a few of these effects will be discussed below:

i) Effect of excess Fe on chlorophyll concentration

Although Fe is a well-known co-factor in the bio-synthesis of chlorophyll, excess amounts of Fe have been shown to decrease chlorophyll bio-synthesis while causing degradation of existing chlorophyll molecules.[43]

ii) Effect of excess Fe on ROS formation

As mentioned earlier (under copper and manganese), redox active metals such as Fe and Cu have the ability to catalyse ROS forming reactions due to their ability to accept and donate electrons from their valence orbitals. Examples of these reactions are the catalytic reaction of O_2^- and H_2O_2 to form highly reactive OH^- species (Fenton and Haber-Weiss reactions).[2,3]

iii) Effect of excess Fe on photosynthesis and electron transport parameters

Limited published data is available on the effect of Fe toxicity on photosynthetic electron transport in comparison to the effect of Fe deficiency.[44] In one such study, Pereira *et al.,* 2013 showed a significant decrease in the maximum quantum yield of the primary photochemistry (F_v/F_m) under excess Fe concentrations in rice cultivars.[44] An increase in non-photochemical reactions was also observed which is indicative of inefficient electron transfer, while closure of reaction centres was indicated by increasing F_0 values with increasing Fe concentrations.[44] In studies with *Nicotiana*

plumbaginifolia, it was found that excess Fe resulted in a decrease of the photosynthetic rate by 40%, an increased oxido-reduction of PSII and higher thylakoid energization.[2]

2.1.5.4 Zinc toxicity

Although Zn is crucial for the normal functioning of plant metabolism, excess concentrations can lead to severe adverse effects. The toxicity threshold of Zn is however relatively heterogeneous in nature, with large differences in Zn tolerance between different plant species and even different cultivars within the same species.[45]

i) Effect of excess Zn on chlorophyll concentration

Zinc has been implicated in replacing Mg^{2+} in the chlorophyll structure, thereby impairing the function of LHCII.[45] A possible obstruction in the transport of Fe to the chloroplasts seems to cause a lowering in the chlorophyll content in the leaves.[45] Zinc excess can also cause Fe deficiencies due to uptake and transport competition (similar ionic radii).

ii) Effect of excess Zn on the Hill reaction and Rubisco activity

Several studies have associated a Zn excess with impaired function of the water oxidizing complex (OEC). A possible explanation of this phenomenon is based on the theory of the competition between Zn^{2+} and Mn^{2+} for a coordination place within the OEC at excess zinc concentrations.[2] This would in turn cause the structure OEC to change and even dissociate. An active Zn^{2+} inhibitory site on the donor side of the PSII has also been reported by Rashid *et al.*, 1991 proposing that Zn^{2+} directly modifies the Q_B site, affecting the reduction of Q_A without changing the re-oxidation properties and disturbing the conformation of the PSII core complex, which also affects the acceptor side of the photosystem II.[46-48] Some authors have suggested that electron transport inhibition due to Zn toxicity was induced by changes in the thylakoid membrane structure.[45] Several studies have shown a definite inhibition of PSII activity due to rapid declines in F_v/F_m under increasing Zn concentrations.[45] Mallick *et al.*, 2003 reported increases in the F_0 values of chlorophyll *a* fluorescence, which was ascribed to the inactivation of reaction centres (RCs) due to Zn toxicity.[49] They also reported inactivation of OEC due to Mn^{2+} replacement by Zn^{2+} from the OEC.[47] Although bivalent cations play a major role in the activation of Rubisco and in the equilibrium between CO_2 and O_2 binding,[50] certain transition metals such as Zn^{2+} displace Mg^{2+} in the structure of Rubisco causing deterioration of its structure and subsequent loss of activity.[51] Nevertheless, Zn mostly inhibits the carboxylase activity of this enzyme without affecting its oxygenase function.[52]

iii) Effect of excess Zn in ROS formation and associated cellular damage

Zinc is not classified as a redox-active metal, due to its inability to perform one electron oxido-reduction reactions.[45] Due to this fact, Zn is unable to catalyse Fenton and Haber-Weiss type reactions. Despite this inability, Lopes-Milan *et al.*, 2005 found that excess amounts of Zn caused the formation of damaging ROS species such as O_2^- and H_2O_2.[53] The exact mechanism of ROS formation under excess Zn conditions is still uncertain, but the most probable cause is thought to be due to its inhibitory effect on electron transport. Inhibition of one part of the electron transport chain (ETC) leads to over-reduction of another part, which in turn causes electron leakages and ultimately ROS formation.[54]

2.1.6 Aim

The aim of this study was to evaluate the photosynthetic whole electron transport response of a South African hybrid maize cultivar (IMP 52-11) to different concentrations (deficiency to excess) of heavy metals (copper, manganese, iron and zinc) using non-invasive chlorophyll *a* fluorescence and modulated 820 nm reflection measuring techniques. These non-invasive techniques were chosen in an attempt to establish a fast and reliable method to evaluate the response of crop plants (such as maize) to cultivation in metal contaminated soils. Furthermore, the treated maize plants were also evaluated with regard to biomass accumulation and root to shoot biomass ratio.

2.2 Methods

2.2.1 Plant culture and metal treatments

The study was conducted between October and December 2013 at the Faculty for Enviromental Sciences, School for Botany at the North-West University in Potchefstroom, South Africa. *Zea mays L.* seeds were germinated in vermiculite in plastic planting trays in a growth chamber. Two weeks after germination, seedlings of similar stature and health (visually selected) were carefully transplanted into 6 L plastic pots containing only vermiculite medium, which once again remained in the growth chamber at day and night temperatures of 27°C and 19°C, respectively. Sixty five pots were used with 1 seedling planted in each pot. Every 3 weeks, 300 mL of a nutrient solution was given to each pot. The nutrient solution contained the following nutrients: Macronutrients (in mM); 1.25 mM KNO_3; 1 mM $Ca(NO_3)_2$; 1 mM $(NH_4)H_2PO_4$; 0.5 mM $MgSO_4$ and 0.1 mM KCl, whilst the micronutrients (in µM) were varied depending on the different treatments as shown in Table 2.1. The plants were watered with 300 mL deionized water every 3rd day.

Table 2.1: Varying metal concentrations per treatment.

Treatment	H_3BO_3 (µM)	$Na_2MoO_4.2H_2O$ (µM)	Fe-EDTA (µM)	$MnSO_4$ (µM)	$CuSO_4$ (µM)	$ZnSO_4$ (µM)	Number of Replicates
Control	10	0.065	5	5	5	5	5
Cu-deficient	10	0.065	5	5	0	5	5
Cu-0.05 mM	10	0.065	5	5	50	5	5
Cu-1 mM	10	0.065	5	5	1000	5	5
Mn-deficient	10	0.065	5	0	5	5	5
Mn-0.05 mM	10	0.065	5	50	5	5	5
Mn-1 mM	10	0.065	5	1000	5	5	5
Fe- deficient	10	0.065	0	5	5	5	5
Fe-0.05 mM	10	0.065	50	5	5	5	5
Fe-1 mM	10	0.065	1000	5	5	5	5
Zn-deficient	10	0.065	5	5	5	0	5
Zn-0.05 mM	10	0.065	5	5	5	50	5
Zn-1 mM	10	0.065	5	5	5	1000	5

From Table 2.1 it can be seen that in each treatment, the concentration of one metal (Cu, Mn, Fe or Zn) was changed. Each metal concentration varied between an optimum value (control), which was determined beforehand by 8 sets of 4 week mini trials where the biomass accumulation and plant height was monitored closely, deficient level (0 mM), an intermediate toxic level (0.05 mM) and a highly toxic level (1 mM) of a specific metal. These specific metal concentrations were chosen in an attempt to mimic reported concentrations of these metals in contaminated soils (See section 1.2.2.1 in Chapter 1). Six weeks after the seedlings were transplanted into the 6 L pots, chlorophyll *a* fluorescence measurements (see Section 2.3) were taken and the plants were harvested to determine the respective root- and shoot biomass for each treatment.

2.2.2 Biomass accumulation

After harvest, the plants were separated into root and shoot partitions. The shoots and roots were placed into paper envelopes and dried at 80°C for 72 hours. Thereafter the dry weight of the individual roots and shoots of each plant was measured.

2.2.3 Chlorophyll *a* fluorescence transient and modulated 820 nm reflection measurements

The measurements were conducted using a multifunctional plant efficiency analyser (M-PEA, Hansatech, UK), which was designed and well described by Strasser *et al.*, 2010.[55] The modulated reflection change near 820 nm was monitored as a convenient way to follow the redox state of PSI (reaction center + plastocyanin). This instrument was designed and well described by Strasser *et al.*, 2010.[55] In this study, leaves were dark adapted for 60 min, by keeping the plants in total darkness, before they were illuminated with a 1 s pulse of a continuous red light (627 nm, 5000 μmol photons $m^{-2}s^{-1}$) while recording the chlorophyll *a* fluorescence and modulated 820 nm reflection. The declined amplitude of the modulated 820 nm reflection intensity due to PSI redox change is indicative of the PSI photochemical capacity.[53,54] In addition, the fast fluorescence transients were analysed and the JIP-parameters were quantified according to the JIP-test.[42] The following data points on the transients were taken: (1) fluorescence intensity at 30 ms (F_o, when all reaction centres of PSII are open); (2) the maximum fluorescence intensity (F_m, when all reaction centres of PSII are closed) and (3) fluorescence intensities at 300 μs (K step), 3 ms (J step), 30 ms (I step) an 300 ms (P step). These original data points were taken and JIP-parameters describing the structure and functionality of PSII were calculated using the formulas described in Table 1.5 (Chapter 1).

2.2.4 Statistical analysis

The experiments were arranged in a completely randomised block design with 5 replicates for each treatment and 5 replicates for the control treatment. Statistical variance analysis was done using one-way ANOVA with least significant differences (LSD) at the 5% level.

2.3 Results

2.3.1 Biomass accumulation

In Table 2.2 the changes in the biomass as a function of the micronutrient concentration is presented. As seen in Table 2.2, the greatest decrease in root biomass was seen at the highest metal concentrations. One mM of copper, manganese, iron and zinc treatments caused a decrease in root biomass compared to control plants of 35%, 22.5%, 34.6% and 23.9% respectively. The same trend was observed for the shoot biomass at 1 mM of copper, manganese, iron and zinc, which showed a respective decrease of 55.5%, 34.8%, 51.1% and 28.9% compared to control plants. All of these differences were statistically significant at $p \leq 0.05$. High levels of iron and copper showed similar toxic effects towards biomass development, whereas the effect of manganese and zinc appeared to be less pronounced. The reason that copper and iron show greater toxicity (than manganese and zinc)

may be that the copper and iron are high redox-active metals, which can contribute to the production of reactive oxygen species (ROS), causing damage to many physiological systems and structures.[2,3] At intermediate toxic levels (0.05 mM), all of the metals showed significant decreases ($p \leq 0.05$) in root and shoot biomass accumulation, compared to control plants, although the effect was much less pronounced. Excluding the effect of copper deficiency on root development, the effects on both root and shoot biomass accumulation decreased statistically significantly ($p \leq 0.05$) for all the metals compared to control plants, under metal deficiency conditions.

Table 2.2: The influence of different metal treatments on the root and shoot DW as well as on the root/shoot DW ratio.

Treatment	Root DW (g.plant^{-1})	Shoot DW (g.plant^{-1})	Root DW/Shoot DW
Control	48.8 ± 1.3 a	69.1 ± 1.5 a	0.70 ± 0.02 a
Cu-deficient	45.2 ± 0.3 a	53.1 ± 0.3 b	0.73 ± 0.01 a
Cu-0.05 mM	35.2 ± 1.6 b	56.3 ± 1.5 b	0.67 ± 0.03 a
Cu-1 mM	21.7 ± 1.6 c	40.1 ± 1.3 c	0.54 ± 0.02 b
Mn- deficient	43.9 ± 2.3 a	54.2 ± 2.2 b	0.72 ± 0.04 a
Mn-0.05 mM	43.1 ± 1.4 a	64.5 ± 1.3 a	0.67 ± 0.02 a
Mn-1 mM	31.8 ± 0.5 b	49.4 ± 0.8 bc	0.64 ± 0.01 a
Fe- deficient	35.1 ± 1.3 b	47.1 ± 1.5 b	0.68 ± 0.02 a
Fe-0.05 mM	43.1 ± 2.2 a	64.5 ± 2.3 a	0.67 ± 0.03 a
Fe-1 mM	23.9 ± 1.3 c	40.3 ± 1.1 bc	0.60 ± 0.02 b
Zn- deficient	37.4 ± 1.3 b	51.4 ± 1.5 b	0.70 ± 0.02 a
Zn-0.05 mM	44.5 ± 1.2 a	63.1 ± 1.3 a	0.69 ± 0.02 a
Zn-1 mM	32.1 ± 1.1 bc	49.1 ± 1.5 bc	0.65 ± 0.02 a
LSD ($p \leq 0.05$)	5.82	8.52	0.09

Data are means ± standard errors (n = 5). Within a column, values followed by different letters are significantly different at $P \leq 0.05$.

Compared to control plants, the root/shoot ratio decreased significantly ($p \leq 0.05$) at the highest treatment concentrations (1 mM) for copper, manganese, iron and zinc. These decreases (compared to control plants) were again more pronounced under high copper and iron toxic concentrations,

compared to the same concentrations of manganese and zinc. Copper and iron showed a decrease in root/shoot ratio of 22.8% and 14.2% (compared to control), whilst manganese and zinc only showed a decrease of 8.5% and 7.1% respectively. According to Nishizono *et al.*, 1989 the phenomenon of reduced root/shoot ratio was due to a natural plant response of reduced metal translocation to plant shoots under excess metal concentrations.[57] The data in the present study supported the hypothesis of Nishizono *et al.*, 1989 and Mahmood *et al.*, 2005 who reported decreases in root/shoot ratio under high copper concentrations.[57, 58] None of the metals caused a significant change in root/shoot ratio under deficiency conditions.

2.3.2 Influence of different metal concentrations on the chlorophyll *a* fluorescence transient and modulated 820 nm reflection

2.3.2.1 Influence of metal concentrations on apparent PSII activity quantified by the fast kinetics chlorophyll *a* fluorescence transients

Relative variable (V) fluorescence (OP normalization, V_{OP}) and difference in variable fluorescence (ΔV) bands (ΔV_{OJ}, ΔV_{JH}, ΔV_{OK}, ΔV_{KJ}, ΔV_{JI}, ΔV_{IH}, ΔV_{Kn}, ΔV_{Jn}, ΔV_{In} and ΔV_{Hn} (n = narrow)) were constructed (F_0 chosen at 30 µs) for all the respective metal treatments. The H-band appears at the same time interval as the P-phase of the fluorescence transient. The term H-band is used only to distinguish between the P-phase in the OJIP induction curve (at exactly 300 ms) and a distinct band (H-band) that appears over a time range that includes the P-phase at 300 ms. In Figures 2.3-2.8 an illustrative example of the various normalizations using the respective copper treatments is given. In Figure 2.3, the change in chlorophyll *a* fluorescence (single normalized at 0.03ms) with varying copper concentrations is shown. Figure 2.4 A shows the relative variable fluorescence, V_{OP}, for the different copper treatments. The differential relative variable fluorescence phases; ΔV_{OP}, ΔV_{OJ}, ΔV_{JH}, ΔV_{OK}, ΔV_{KJ}, ΔV_{JI}, ΔV_{IH}, ΔV_{Kn}, ΔV_{Jn}, ΔV_{In} and ΔV_{Hn} for the different copper treatments are shown in Figures 2.4-2.8. Figure 2.8 A-D gives the maximal/minimal amplitudes of the differential normalizations (ΔV) of all the respective metal treatments relative to control treatments. The validation of V and ΔV in variable fluorescence phases and peaks obtained by the various normalizations to obtain these peaks, have previously been described in detail.[42] A short summary of how these normalization peaks are obtained is depicted in Figure 1.13 and their meanings are given in Table 1.4 (Chapter 1).

Only the copper differential variable fluorescence phases will be shown graphically as illustration in Figures 2.5-2.7, whereas the averages of the maximum and minimal amplitudes of these bands will be shown for all the heavy metal treatments in Figures 2.8 A-D.

In Figure 2.3 the changes in the single normalized (at 0.03 ms) fast chlorophyll *a* fluorescence transient at different copper concentrations is shown, displaying the characteristic steps (O-J-I-P steps) in the fluorescence transient.[42]

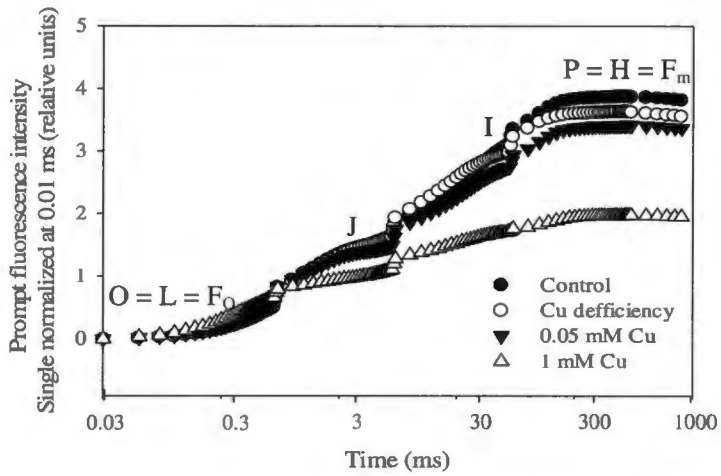

Figure 2.3: Change in chlorophyll *a* fluorescence (single normalized at 0.03ms) with varying copper concentrations.

In Figure 2.4 A the changes in the variable fluorescence, V_{OP}, (normalized at 0.03 ms and 300 ms) fast chlorophyll *a* fluorescence transient at different copper concentrations is shown, whilst Figure 2.4 B shows the difference in variable fluorescence ($\Delta V = V_{treatment} - V_{control}$), ΔV_{OP}, for the various copper treatments.

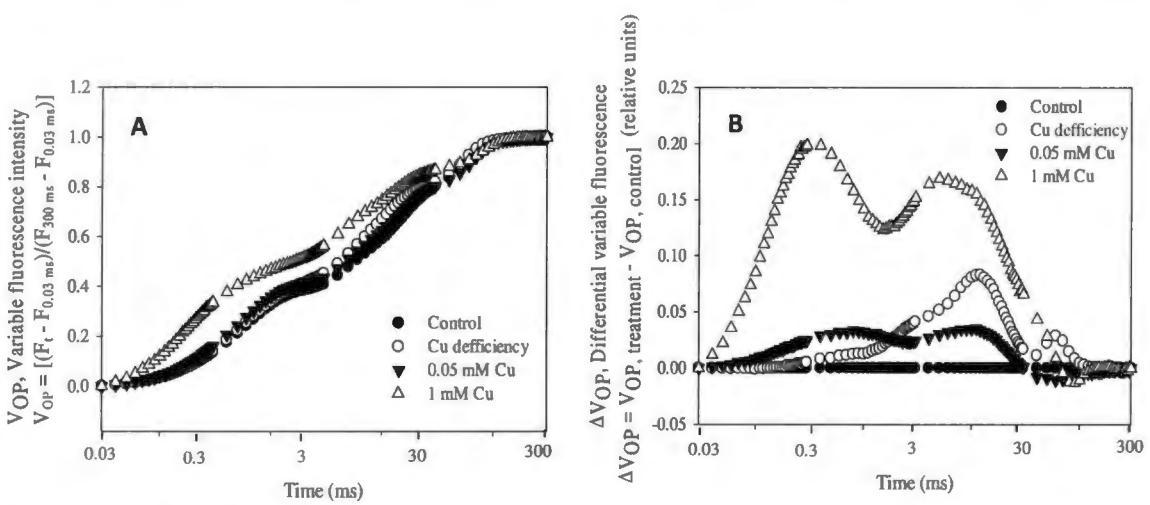

Figure 2.4 A & B: Variable fluorescence (A) and differential variable fluorescence (B) ($\Delta V_{OP} = V_{OP, treatment} - V_{OP, control}$) between the O (0.03 ms) and P (300 ms) steps in the fluorescence transient for the various copper treatments.

The O (0.03 ms) to J (3 ms) part of the transient curve refers to the single turnover range (i.e. primary quinone acceptor (Q_A) is only reduced once) and therefore reflects mainly photochemical reactions resulting in the reduction of the electron acceptor Q_A, whereas the J (3 ms) to H (300 ms) steps in the fluorescence transient is related to the multiple turnover region (post Q_A reduction). Multi-differential normalizations between O and J as well as J and H steps in the fluorescence transient revealed the K- and I-bands respectively (Figure 2.5).

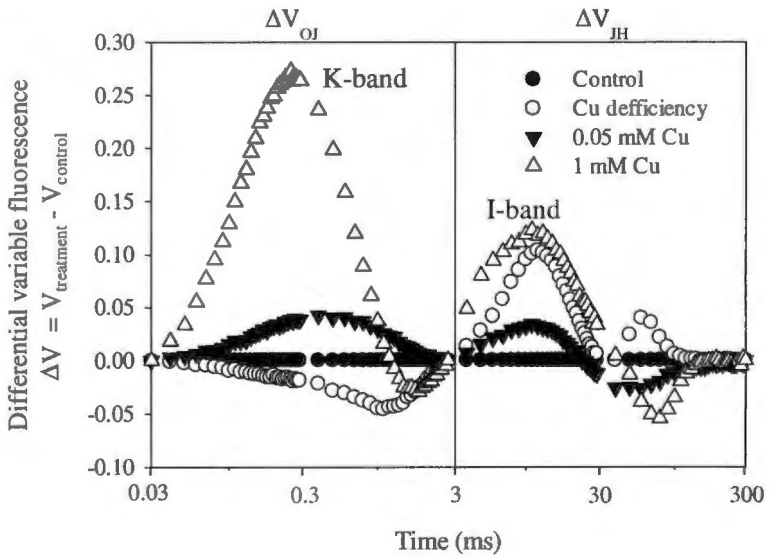

Figure 2.5: Differential variable fluorescence ($\Delta V = V_{treatment} - V_{control}$) between the O (0.03 ms) and J (3 ms) as well as J (3 ms) and H (300 ms) steps in the fluorescence transient for the various copper treatments.

Differential normalization between O (0.03 ms) and K (0.3 ms) steps is the fluorescence transient revealed the ΔV_L-band (Figure 2.6) for the different copper treatments.

Other differential normalizations shown in Figure 2.6 are the ΔV_{KJ}, ΔV_{JI} and ΔV_{IP} phases which stretch over the single and multiple turnover phases of the electron transport events.

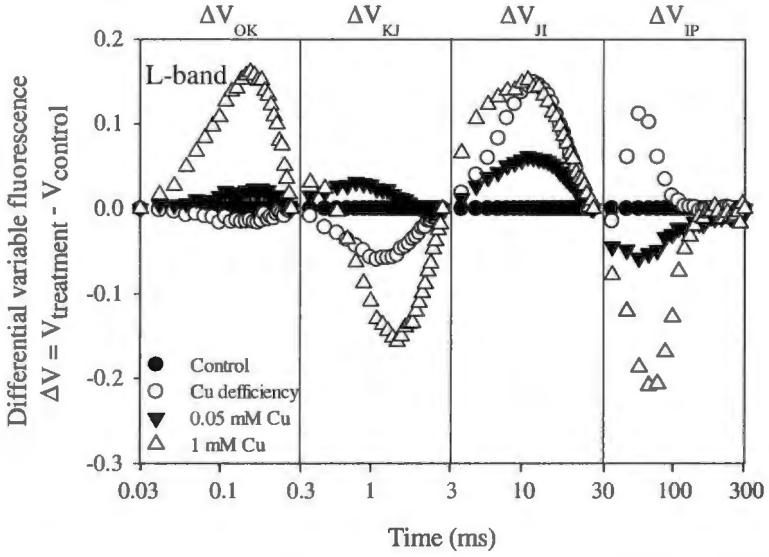

Figure 2.6: Differential variable fluorescence ($\Delta V = V_{treatment} - V_{control}$) between the L (0.03 ms) and K (0.3 ms), K (0.3 ms) and J (3 ms), J (3 ms) and I (30 ms) as well as I (30 ms) and H (300 ms) steps in the fluorescence transient for the various copper treatments.

Further ('narrower') normalization is thus needed to isolate the influence of the respective events (processes). These narrower normalizations were constructed for all of the metal treatments, but once again only the copper treatments are shown graphically in Figure 2.7 (to illustrate how such narrower bands are obtained). The normalizations were made at 0.1 ms, 1 ms, 10 ms, 100 ms and 300 ms in log time. Only the maximal/minimal amplitudes (relative to control) of these normalizations are shown for the other metal treatments (Figure 2.8 A-D).

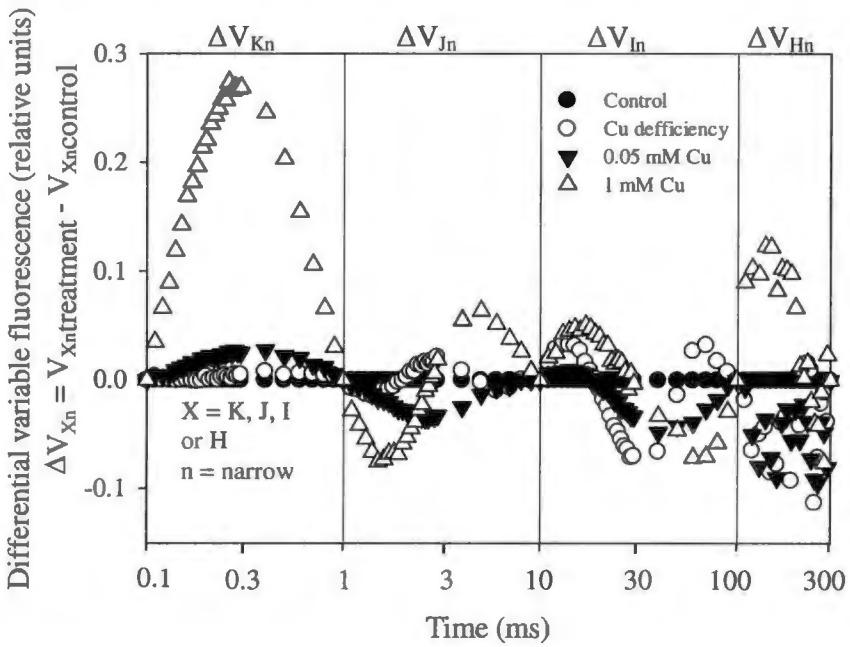

Figure 2.7: Differential variable fluorescence ($\Delta V_{Xn} = V_{Xn,\ treatment} - V_{Xn,\ control}$) between 0.1 ms and 1 ms, 1 ms and 10 ms, 10 ms and 100 ms, as well as 100 ms and 300 ms time intervals in the fluorescence transient for the various copper treatments. These normalizations reveal the K_n, J_n, I_n and H_n-bands, respectively.

Figures 2.8 A-D are composite graphs that show the maximal/minimal amplitudes of the 'narrow bands' (relative to control) that resulted from the respective normalizations discussed above for all the metal treatments.

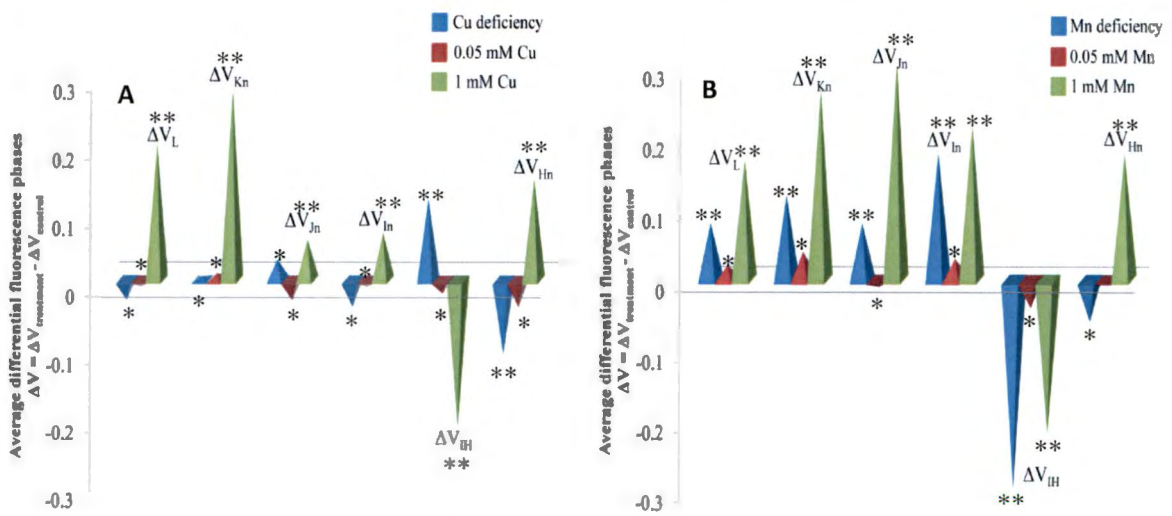

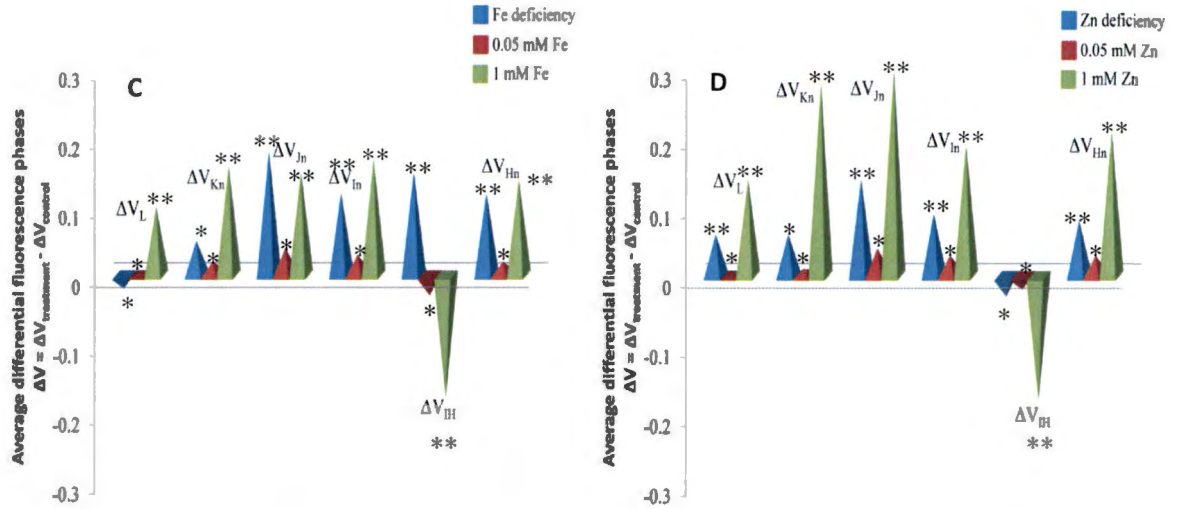

Figure 2.8 A-D: Averages of the maximal/minimal amplitudes of the differential normalizations (ΔV) obtained for copper (A), manganese (B), iron (C) and zinc (D) relative to control treatments. All values are given as average values of 20 measurements (4 measurements per plant x 5 replicates per treatment. ** indicates significance and * indicates non-significance at $p \leq 0.05$ (LSD = 0.073) relative to control.

Substantial narrow bands appeared following the respective normalizations as seen in Figure 2.8 A-D. Significant positive ΔV_L-bands ($p \leq 0.05$) were seen at the highest concentration treatments (1 mM) for all of the respective metal treatments, which suggest a decrease in antennae cooperativity at such high metal concentrations. Furthermore, significant ($p \leq 0.05$) positive ΔV_L-bands were also seen in the manganese- and zinc deficiency treatments.

Normalization between 0.1 ms and 1 ms revealed sharper ΔV_{Kn}-band (n = narrow) bands (at ~ 0.3 ms), which is a more accurate representation of the ΔV_K-band, as the influence of antennae cooperativity is not taken into account. Significant positive ($p \leq 0.05$) ΔV_{Kn}-bands were seen at the highest concentrations of all the metal types and at the manganese and zinc deficiency treatments, which suggests degradation of the OEC and/or an increase in antenna size due to the inactivation of functional RCs.[59]

Normalization between 1 ms and 10 ms revealed significant ($p \leq 0.05$) sharper ΔV_{Jn}-bands (at ~ 2-3ms) at the highest concentration for all metal types. Additionally significant ($p \leq 0.05$) positive ΔV_{Jn}-bands were also seen for the manganese, iron and zinc deficiency treatments (Figure 2.8 B-D), where the iron deficiency caused the greatest ΔV_{Jn}-band (Figure 2.8 C) amongst the deficiency treatments, which points to a decrease in electron transport past Q_A.

In Figure 2.8 A-D the presence of ΔV_{In}-bands became evident at ~ 20-30 ms. The ΔV_{In}-bands (narrower ΔV_I-band) is a more accurate representation of the intersystem electron transport events, because it inherently excludes the influence of Q_A and end electron acceptor reduction, because of the timeframe at which these bands appear. Significant ($p \leq 0.05$) positive ΔV_{In}-bands could be seen at the highest copper, manganese, iron and zinc concentrations, which suggest strong inhibition of electron transport before the PSI acceptor side, causing an accumulation of reduced intersystem electron carriers (a 'traffic jam' of electrons at the intersystem electron transporters). Furthermore, significant ($p \leq 0.05$) positive ΔV_{In}-bands were also seen for the deficiency manganese, iron and zinc treatments, which interestingly also suggests accumulation of reduced intersystem electron carriers at these metal deficient conditions.

Differential normalization between the IH (or IP) phase brought about significant ($p \leq 0.05$) differences in ΔV_{IH}-bands amongst the respective treatments with respect to the control treatments (at ~ 100 ms), which points to different influences on the reduction of PSI end electron acceptors, since this phase has previously been suggested to be related to PSI end electron acceptor reduction.[39] At the highest concentration, significant ($p \leq 0.05$) negative ΔV_{IH}-bands can be seen for all of the metal types (Figure 2.8 A-D). These bands suggest strong decreases in electron transport toward PSI end electron acceptors. Inversely, large positive ΔV_{IH}-bands were seen for the copper- and iron deficiency treatments, suggesting a build-up of electrons between intersystem electron carriers before PSI end electron acceptors. Interestingly, the manganese deficiency treatment also resulted in a significant ($p \leq 0.05$) negative ΔV_{IH}-band.

2.3.2.2 Influence of different metal concentrations on PSII biophysical parameters derived by JIP-equations

Strasser *et al.*, 2000 translated the OJIP transients into biophysical parameters, which describe quantum yields of photon capture used for Q_A reduction (φ_{Po}), electron transport probabilities (φ_{Eo}, φ_{Ro} and δ_{Ro}), specific activities per reaction centre (RC), phenomenological fluxes per leaf cross section (CS), as well as the two performance indexes PI_{ABS} and PI_{total}.[42] The derivation and meanings of these JIP-parameters are given and described in Table 1.5. These values were calculated and selected parameters were normalized to those of controls and plotted on radar graphs, to demonstrate the effect of different metal types and concentrations on the selected parameters (Figure 2.9 A-D).

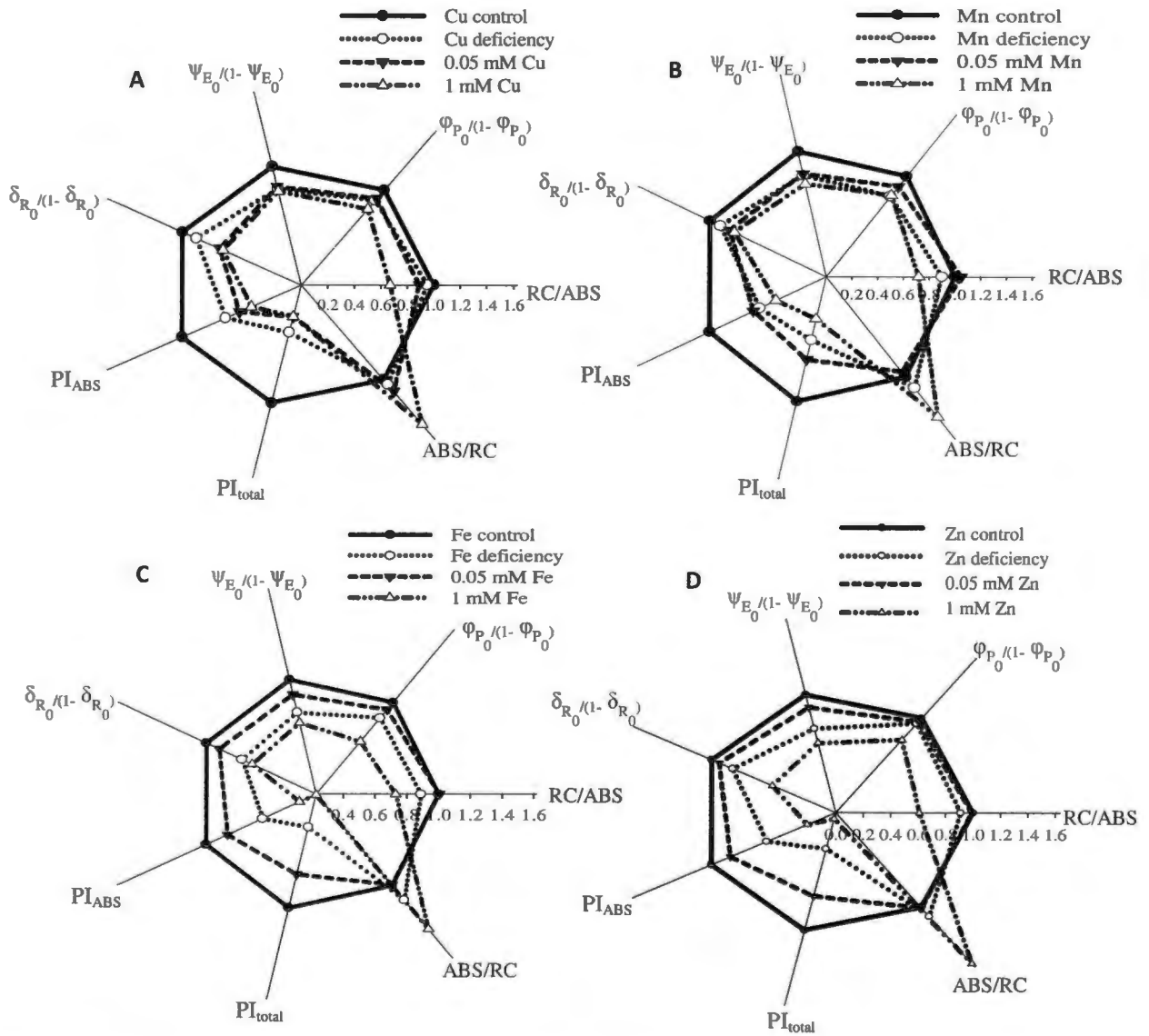

Figure 2.9 A-D: Radar graphs showing the influence (relative to control) of the various copper (A), manganese (B), iron (C) and zinc (D) concentrations on key parameters in the electron transport chain (see Table 1.4). Significance was determined at $p \leq 0.05$ (LSD = 0.104).

An increase in the ABS/RC parameter in Figures 2.10 A-D can be used to ascertain whether the functional antenna size increased.[59] At the highest metal concentrations (for all metal types), significant ($p \leq 0.05$) increases in ABS/RC can be seen, with a 47%, 40%, 36% and 63% increase (compared to control) for the copper, manganese, iron and zinc treatments, respectively. Significant ($p \leq 0.05$) increases of 30% and 12% in this parameter can also be seen for the manganese and iron deficiency treatments (Figure 2.9 B & C). The reciprocal of ABS/RC is RC/ABS (Figure 2.9 A-D), which is indicative of the amount of active reaction centres (RC's) per chlorophyll antennae. Given that RC/ABS is the reciprocal of ABS/RC, the highest metal concentrations caused a significant

($p \leq 0.05$) decrease in RC/ABS, with a 33%, 28%, 23% and 40% decrease (compared to control) for the copper, manganese, iron and zinc treatments, respectively. Likewise, a significant ($p \leq 0.05$) decrease in RC/ABS can also be seen for the manganese (33%) and iron (27%) deficiency treatments (Figure 2.9 B & C).

A parameter that can be used to evaluate the reduction of Q_A is $\varphi_{Po}/(1- \varphi_{Po})$, which is a measure of the quantum yield of primary photochemistry, or to put it in another way, the amount of photochemical energy used to reduce Q_A (seen in Figure 2.9 A-D).[42,60] Again, the highest metal concentrations had the greatest effect on this parameter. The copper, manganese, iron and zinc treatments caused significant ($p \leq 0.05$) decreases of 20%, 19%, 36% and 22% in $\varphi_{Po}/(1- \varphi_{Po})$ (compared to control). The manganese and iron deficiency treatments also caused significant ($p \leq 0.05$) decreases of 15% and 11%, respectively. These decreases at the highest concentration and deficiency treatments suggests a considerable decrease in the quantum yield of photochemistry, i.e. a substantial amount of excitation energy was not used for Q_A reduction. This excitation energy is mostly lost in the form of heat dissipation.

The probability that an electron moves beyond Q_A^- to the intersystem electron carriers is given by the $\psi_{Eo}/(1- \psi_{Eo})$ parameter.[42,60] Considerable changes in this parameter was seen for the different treatments. The highest metal concentrations caused significant ($p \leq 0.05$) decreases of 21%, 26%, 29% and 41% for the copper, manganese, iron and zinc treatments, respectively. The $\psi_{Eo}/(1- \psi_{Eo})$ parameter seemed relatively unaffected by the intermediately high metal concentration (0.05 mM) treatments, except for the 0.05 mM copper treatment, which reduced significantly ($p \leq 0.05$) by 17% compared to the control treatment (Figure 2.9 A). The copper, iron and zinc deficiency treatments also caused marked changes in $\psi_{Eo}/(1- \psi_{Eo})$, with significant ($p \leq 0.05$) decreases of 17%, 22% and 29% (Figure 2.9 B, C & D), respectively.

The efficiency of electron movement from the reduced intersystem electron acceptors to the PSI end electron acceptors (Ferredoxin and $NADP^+$) is described by $\delta_{Ro}/(1- \delta_{Ro})$.[42,60] A decrease in $\delta_{Ro}/(1- \delta_{Ro})$ is thus indicative of electron accumulation/losses before these $NADP^+$. Once more the highest metal concentrations caused the greatest decrease in this parameter, which is indicative of electron flow disruption at such high metal concentrations. Corresponding significant ($p \leq 0.05$) decreases of 34%, 31%, 36% and 44% was seen for the 1 mM copper, manganese, iron and zinc treatments. Of the intermediately high (0.05mM) concentration treatments, only the iron treatment caused a significant ($p \leq 0.05$) decrease of 11% in $\delta_{Ro}/(1- \delta_{Ro})$. Additionally, a significant ($p \leq 0.05$) decline in $\delta_{Ro}/(1- \delta_{Ro})$ of 21%, 25% and 17% was seen for the copper, iron and zinc deficiency treatments, underlining the importance of these metals for efficient photosynthetic electron transport.

Two other parameters often used to describe energy conservation (electron transport) are PI_{ABS} and PI_{total}. These two parameters are multi-parametric expressions describing energy conservation from photon absorption to different parts of the electron transport process. Table 1.5 (Chapter 1) describes the derivation and meaning of these parameters. The performance index for energy conservation from photons absorbed to the reduction of intersystem electron acceptors, PI_{ABS}, essentially refers to the efficiency with which photons are absorbed, the efficiency with which these photons are used for photochemical energy generation and finally the efficiency with which photochemically generated electrons are transported through PSII. The performance index for energy conservation from photons absorbed to the reduction of PSI end electron acceptors, PI_{total}, contains the identical information to PI_{ABS}, but in addition it also includes the efficiency of PSI end electron acceptor reduction, which inherently means that PI_{total} provides information on the total electron transport process.[42,60] The following significant ($p \leq 0.05$) decreases (compared to control) were seen for the respective metal treatments. A 28%, 13% and 56% decrease in PI_{ABS} and a 41%, 16% and 70% decrease in PI_{total} were seen at the copper deficiency, 0.05 mM and 1 mM copper treatments, respectively (Figure 2.9 A). A 25%, 16% and 49% decrease in PI_{ABS} and a 29%, 21% and 71% decrease in PI_{total} could be seen for the manganese deficiency, 0.05 mM and 1 mM manganese treatments, respectively (Figure 2.9 B). A 40%, 35% and 65% decrease in PI_{ABS} and a 55%, 25% and 76% decrease in PI_{total} could be seen for the iron deficiency, 0.05 mM and 1 mM iron treatments, respectively (Figure 2.9 C). A 29%, 15% and 72% decrease in PI_{ABS} was seen and a 44 %, 27 % and 80% decrease in PI_{total} could be seen for the zinc deficiency, 0.05 mM and 1 mM zinc treatments, respectively (Figure 2.9 D). Marked reduction in these parameters is clearly indicative of electron transport inhibition in all of the treatments compared to the control plants. Despite the fact that not all of the parameters decreased in all of the treatments, the accumulative decline in photon capture and electron transport efficiency caused by the various treatments, are emphasized by these two performance indexes.

2.3.2.3 PSI and plastocyanin (PC) electron transport activity quantified by modulated 820 nm reflection

During the 1 s illumination of the dark-adapted leaves with a pulse of continuous red light (627 nm, 5000 µmol photons $m^{-2}s^{-1}$) modulated 820 nm reflection was also recorded. Figure 2.10 A-D are normalized (at 500 ms) $MR_{820\ nm}$ curves that show the influence of varying metal concentrations on the light induced photochemical reactions of PSI and PC. Characteristic sections of these curves were used to calculate/elucidate changes in the oxidation-, re-reduction rate and maximum size of the oxidized PSI-pool. Figures 2.11 A-D show the normalized $MR_{820\ nm}$ reflection kinetics in response to 5000 µmol photons $m^{-2}s^{-1}$ red actinic light. The curves show an initial oxidation of P700 and PC (v_{ox}) followed by a re-reduction of $P700^+$ by arriving electrons from PSII (v_{red}).[62]

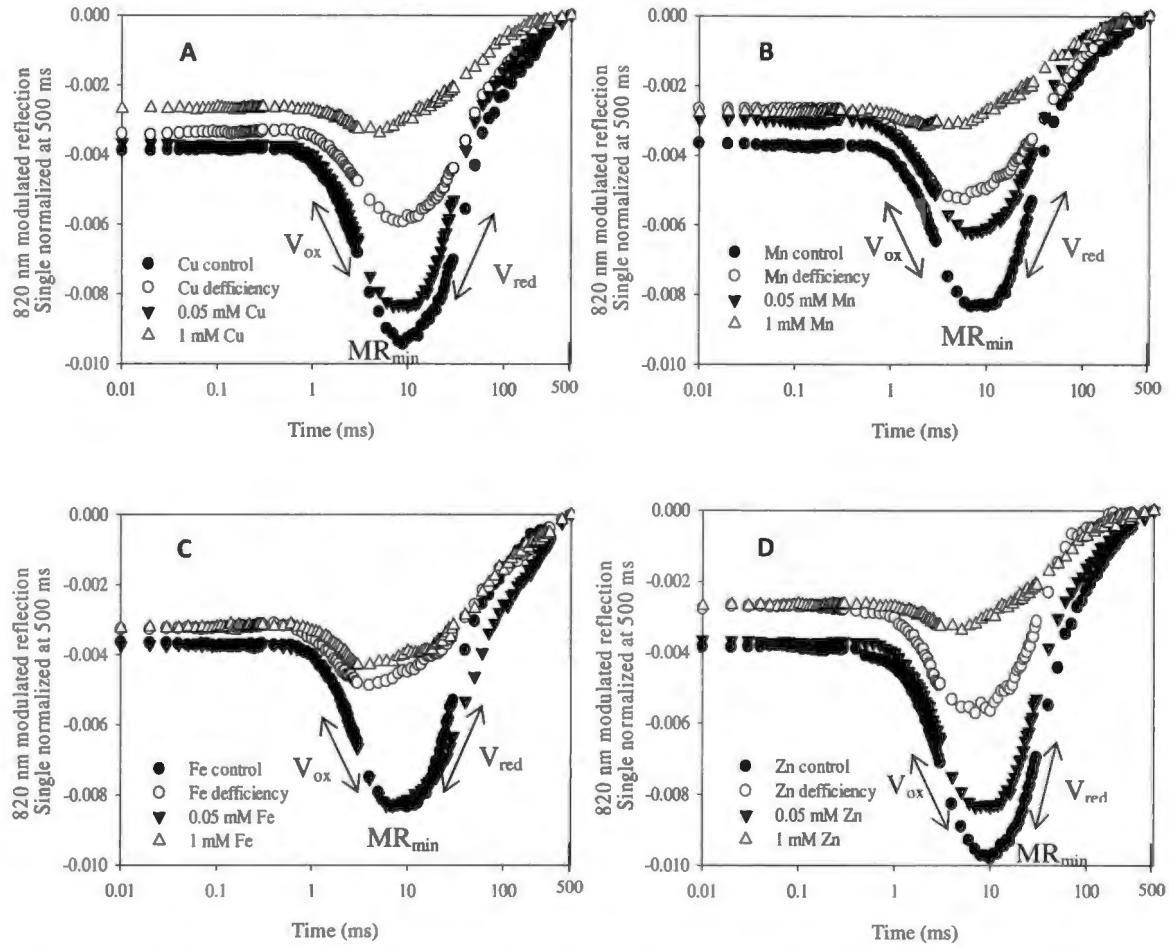

Figure 2.10 A-D: Normalized (at 500 ms) light induced $MR_{820\ nm}$ changes for the various copper (A), manganese (B), iron (C) and zinc (D) concentrations.

The minima of the MR curves (MR_{min} in Figure 2.10 A-D) can be used to deduce the maximum oxidation state of PSI, or in other words the maximum amount of electron flow through PSI before electrons from PSII arrives. MR_{min} was significantly ($p \leq 0.05$) higher for all deficiency and 1 mM copper, manganese, iron and zinc treatments (compared to control; Figure 2.10 A-D), whereas only the 0.05 mM manganese treatment resulted in a significant ($p \leq 0.05$) increase in MR_{min} (Figure 2.10 B). This can be attributed to the fact that v_{ox} (Figure 2.11 C) was down-regulated to a greater extent than v_{red} (Figure 2.11 D) at the 0.05 mM manganese treatment, subsequently leading to a decreased P700 oxidized state (MR_{min}), because of the difference in kinetics of the fast (v_{ox}) and slow (v_{red}) phase electron transport.

The initial decay (slope) of MR_{820nm} reflection intensity, due to PSI redox change, represents the rate of PC and P700 (PSI) photochemical oxidation (v_{ox}), whilst the secondary slope reflects the re-reduction rate of PC and $P700^+$ (PSI) by PSII.[62] A change in v_{ox} can thus be interpreted as a change in the rate at which electrons move through PC and PSI, whereas v_{red} reflects the rate with which PC and

PSI is re-reduced by arriving electrons from PSII.[60,61] Changes in v_{ox} and v_{red} with varying metal concentrations (relative to control) are shown in Figure 2.11 A-H.

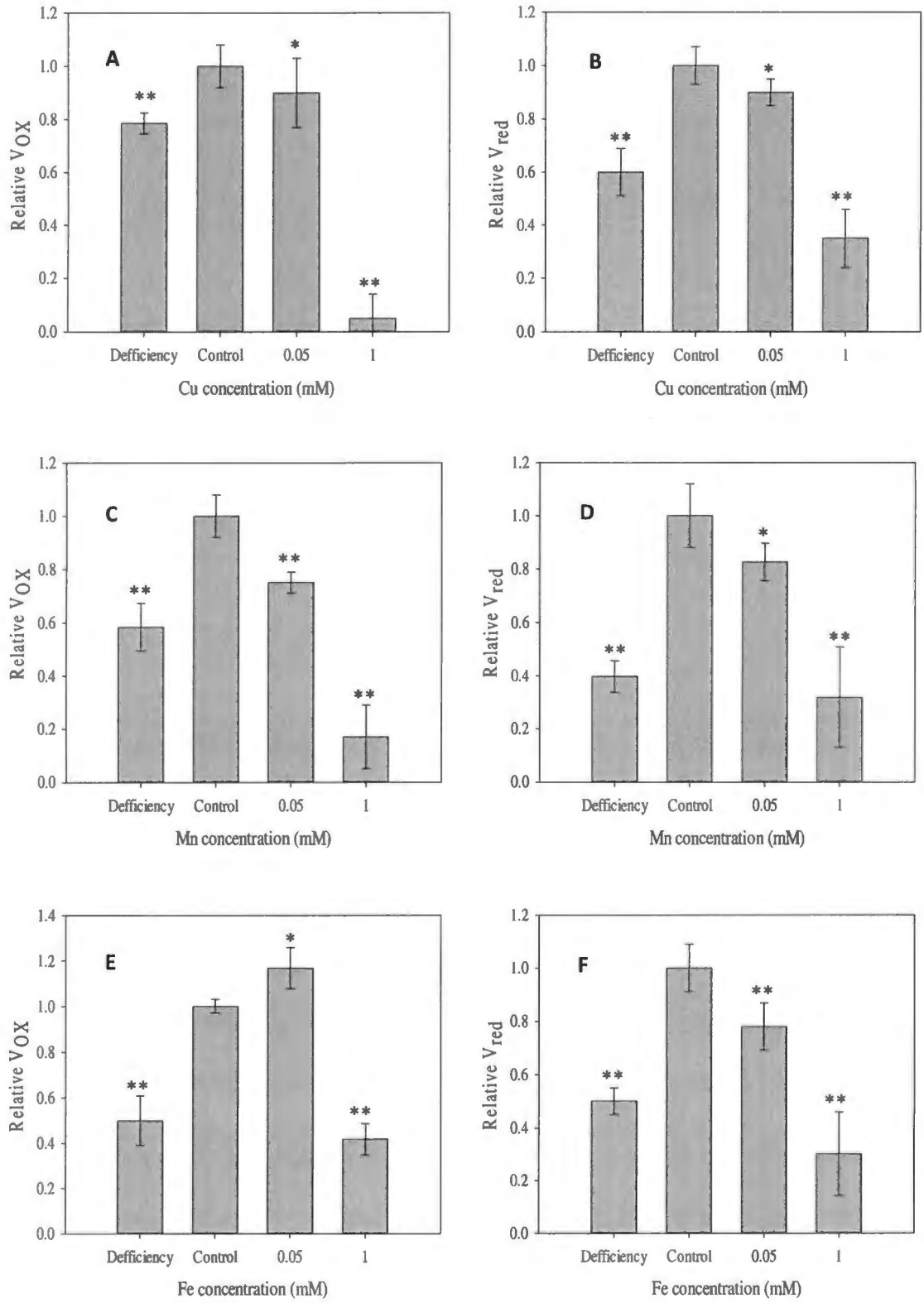

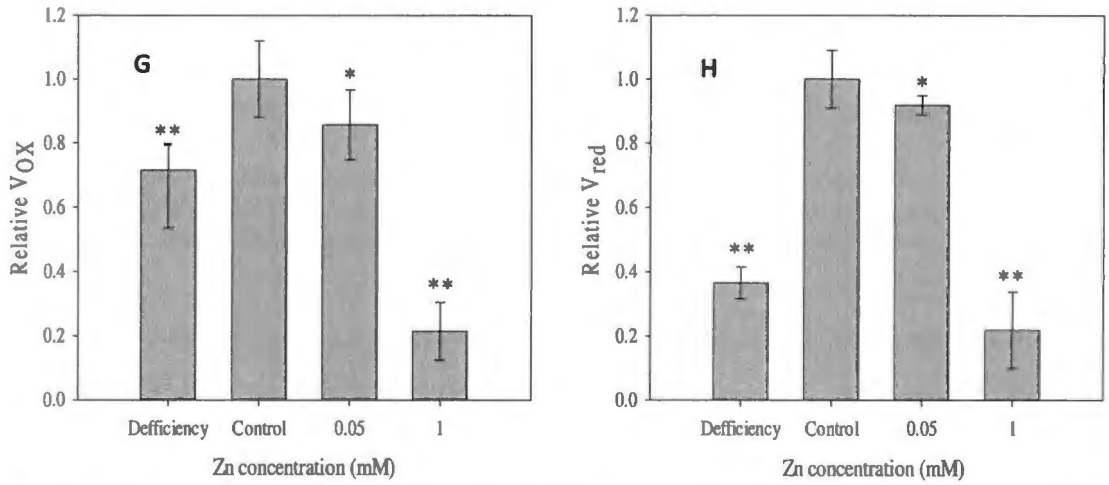

Figure 2.11 A-H: Figure 2.11 A-H reflects the maximal slopes, relative to control, of the kinetics of photo-induced MR_{820nm} changes. Figure 2.11 A, C, E, G gives the relative oxidation rate (v_{ox}) of electron movement through PSI, before electrons from PSII arrive to re-reduce oxidized PSI, whilst Figure 2.11 B, D, F & H gives the relative re-reduction rate of the combined flow of electrons pumped by PSI and PSII (v_{red}). Significance relative to control was determined at $p \leq 0.05$ (LSD = 0.21). * indicates non-significant and ** indicates significant differences from control.

The relative v_{ox} (Figure 2.11 A) decreased significantly ($p \leq 0.05$) by 22% and 92% at the deficiency and 1 mM copper treatments respectively, whist the relative v_{red} (Figure 2.11 B) decreased significantly ($p \leq 0.05$) by 40% and 65% for the deficiency and 1 mM copper treatments, with no significant ($p \leq 0.05$) change in either v_{ox} and v_{red} at the 0.05 mM copper treatment. In Figure 2.11 C, the relative v_{ox} of the deficiency, 0.05 mM and 1 mM manganese treatments decreased significantly ($p \leq 0.05$) by 42%, 25% and 83% respectively, whereas the relative v_{red} (Figure 2.11 D) significantly ($p \leq 0.05$) decreased by 60% and 69% at only the deficiency and 1 mM manganese treatments, which suggests that PC and PSI oxidation seemed to be more sensitive to excess manganese concentrations than PC and PSI re-reduction. The relative v_{ox} of the deficiency and 1 mM iron treatments (Figure 2.11 E) decreased significantly ($p \leq 0.05$) by 50% and 59%, whilst the relative v_{ox} increased by 16% at the 0.05 mM iron treatment (compared to control), but this increase was not significant ($p \leq 0.05$). The relative v_{red} (Figure 2.11 F) decreased significantly ($p \leq 0.05$) by 50%, 22% and 70% at the deficiency, 0.05 mM and 1 mM iron treatments, respectively. This data suggests that PC and PSI re-reduction appears to be more sensitive to excess iron compared to PC and PSI oxidation. In the case of the zinc treatments, the relative v_{ox} of the deficiency and 1 mM zinc treatments (Figure 2.11 G) decreased significantly ($p \leq 0.05$) by 29% and 79%, whereas the relative v_{red} significantly ($p \leq 0.05$) declined by 64% and 79% for the zinc deficiency and 1 mM zinc treatments (Figure 2.11 H). A clear difference in

the down-regulation of PC and PSI oxidation and re-reduction can be seen under zinc deficient conditions, suggesting differential sensitivity between the two processes to zinc deficiency.

2.4 Discussions

2.4.1 Influence of different metal concentrations on biomass accumulation

Several of the different metal treatments caused significant ($p \leq 0.05$) reductions in both root and shoot biomass. The highest metal concentrations caused the largest decrease in the biomass of the respective treatment plants. The greatest decreases were seen at the highest copper and iron treatments. The reason that copper and iron show greater toxicity (than manganese and zinc) is due to the fact that the copper and iron are highly redox-active metals, which are known contributers in the production of reactive oxygen species (ROS).[2,3] At intermediate toxic levels (0.05 mM), only the copper treatment showed significant ($p \leq 0.05$) decreases in root and shoot biomass accumulation, compared to control plants, highlighting the toxic effect of the redox active copper ion. Excluding the effect of copper and manganese deficiency on root development, the effects on both root and shoot biomass accumulation decreased statistically significantly ($p \leq 0.05$) for all the metals compared to control plants, under metal deficiency conditions. This serves as concrete proof of the importance of these transition metals in normal plant development and functioning.

2.4.2 Influence of different metal concentrations on photosynthetic electron transport

2.4.2.1 Metal deficiency

Under copper deficient conditions, the only ΔV-bands that differed significantly ($p \leq 0.05$) in Figure 2.8 A were positive ΔV_{Jn} and ΔV_{IH}-bands. Because no band appears at ΔV_{Jn}, we could deduce that the build-up of electrons were beyond Q_A in the electron transport chain. The appearance of positive ΔV_{Hn} and ΔV_{IH}-bands suggested a build-up of electrons between intersystem carriers and PSI end electron acceptors (Figure 2.8 A).[39,60] A possible reason for the build-up of electrons at the intersystem electron carriers and a decrease in the reduction of electron end acceptors (on the PSI acceptor side) can be the inability to synthesize the plastocyanin (PC) complex (Figure 2.2), in which copper is a key constituent. This would result in a build-up of electrons and intensified positive and ΔV_{IH}-bands. The copper deficiency treatment also caused a significant ($p \leq 0.05$) decrease in $\psi_{Eo}/(1-\psi_{Eo})$ (Figure 2.9 A), which is indicative build-up ('traffic jam') of intersystem electrons, supporting the hypothesis of lower PC synthesis due to insufficient copper availability. The lower v_{ox} of PC and PSI at copper deficient conditions (Figure 2.11 A) is also in agreement with the hypothesis of insufficient PC synthesis, resulting in decreased electron movement through PC and PSI (see also

Figure 2.1). Furthermore, the decline in v_{red} (Figure 2.11 B) at the copper deficiency treatment, is in agreement with the fast kinetics chlorophyll *a* fluorescence data presented in Section 2.3.2.1, where a decrease in $\delta_{Ro}/(1- \delta_{Ro})$ (efficiency of electron transport from PSII to end electron acceptors) was observed (Figure 2.9 A). Significant ($p \leq 0.05$) reductions in PI_{ABS} and PI_{total} (Figure 2.9 A) could be seen for the copper deficiency treatments, which is indicative of a decrease in total electron transport efficiency.

Under manganese deficient conditions, the ΔV-bands that differed significantly in Figure 2.4 B were positive ΔV_L, ΔV_{Kn}, ΔV_{Jn} and ΔV_{In}-bands, as well as a negative ΔV_{IH}-band. The reason for the appearance of a positive ΔV_L-band is not know at this point in time, but it suggests a decrease in antenna cooperativity. The appearance of a positive and ΔV_{Kn}-band is due to the inability of the OEC (of which manganese is an essential part of) to function properly under manganese deficient conditions, causing a loss of structural integrity and subsequent electron donation by non-water electron donating entities. A decrease in the number of active RCs' can be deduced by a decrease in RC/ABS (Figure 2.9 B. The ABS/RC in Figure 2.9 B increased (being the reciprocal of RC/ABS), which is indicative of increased antennae size, in an effort to compensate for the loss of functional RCs'.

A positive ΔV_{Jn}-band is indicative of a kinetic 'bottleneck' of the electron transport around Q_A, i.e. the reduction rate of Q_A exceeds the re-oxidation rate of Q_A^-. Over-reduction of one part of the electron transport chain has been shown to result in ROS formation, causing more structural damage, which results in further dow-regulation of electron transport.[2,10,13] The down-regulation of electron transport past Q_A^- was confirmed by the decrease in $\psi_{Eo}/(1- \psi_{Eo})$ in Figure 2.9 B. The presence of a negative ΔV_{IH}-band and a decrease in $\delta_{Ro}/(1- \delta_{Ro})$ in Figure 2.9 B is an indication of a decrease in the efficiency of electron movement from the reduced intersystem electron acceptors to the PSI end electron acceptors. The lower v_{ox} suggests that manganese deficient conditions (Figure 2.11 C) caused significant ($p \leq 0.05$) decreased electron movement through PC and PSI. Furthermore, the decline in v_{red} (Figure 2.11 D) at the manganese deficiency treatment is in agreement with the fast kinetics chlorophyll *a* fluorescence data presented in Section 2.3.2.1, where a decrease in $\delta_{Ro}/(1- \delta_{Ro})$ and a large negative ΔV_{IH}-band were observed in Figure 2.9 B and Figure 2.8 B, respectively. A decline in $\varphi_{Po}/(1- \varphi_{Po})$ points at a lowering in the efficiency with which absorbed energy is converted to photochemical energy (Figure 2.9 B). This means that a significant amount of energy is dissipated as heat (heat sink centres), which acts as a mechanism to minimize photo-inhibition by non-photochemical quenching, as a result of a decrease in the number of active RCs (supported by a decrease in RC/ABS in Figure 2.9 B). Significant ($p \leq 0.05$) reductions in PI_{ABS} and PI_{total} suggest a decrease in whole electron transport efficiency under manganese deficient conditions.

Under iron deficient conditions, the ΔV-bands that differed significantly ($p \leq 0.05$) in Figure 2.8 C were positive ΔV_{Jn}, ΔV_{In}, ΔV_{IH} and ΔV_{Hn}-bands. The appearance of a positive ΔV_{Jn}-band can be due to the instability of the key non-heme iron unit between Q_A and Q_B in iron deficient conditions, ultimately leading to lower electron transport past Q_A (see Figure 2.1). A study by Kalaji *et al.*, 2014 reported similar results under iron deficient conditions in tomato and maize plants.[66] Lower electron transport beyond Q_A is also indicated by the decrease in $\psi_{Eo}/(1-\psi_{Eo})$ in Figure 2.9 C. A large positive ΔV_{In}-band (Figure 2.8 C) is indicative of accumulation of reduced intersystem electrons before end PSI acceptors. The lack of iron for the synthesis of iron-containing Cyt b_6f complex causes the build-up of electron at this site. Furthermore, the appearance of a positive ΔV_{IH} and ΔV_{Hn}-bands (Figure 2.8 C) also points to the accumulation of electrons between intersystem electron transporters and PSI end electron acceptors (Ferredoxin and $NADP^+$). This can once again be attributed to the loss of structural integrity of iron-containing PSI-carriers on PSI acceptor and donor side (Figure 2.1), also seen as a significant ($p \leq 0.05$) decrease in lowering in $\delta_{Ro}/(1-\delta_{Ro})$ in Figure 2.9 C. The absorption per reaction centre (ABS/RC) in Figure 2.9 C increased significantly ($p \leq 0.05$), which again is indicative of an increase in antenna size. Inversely, a decrease in the number of active RCs' can be deduced from a decrease in RC/ABS (Figure 2.9 C). A significant ($p \leq 0.05$) decrease in the relative v_{ox} and v_{red} was also seen (Figure 2.11 E & F) in the MR_{820nm} signal, supporting the fast kinetics chlorophyll *a* fluorescence data, suggesting a lowering in the electron transport through PSI (PSI-oxidation) and the ensuing re-reduction of PSI by arriving electrons from PSII. The decrease in the efficiency with which absorbed energy is converted to photochemical energy was also apparent, because of the decline in $\varphi_{Po}/(1-\varphi_{Po})$ in Figure 2.9 C. This means that a significant amount of energy is dissipated as heat (heat sink centres). Moreover, the decrease in effective energy conversion and electron transport efficiency resulted in the significant ($p \leq 0.05$) reduction in the multi-parametric PI_{ABS} and PI_{total} parameters (Figure 2.9 C). The appearance of the respective ΔV-bands, changes in the calculated JIP-parameters and decreases in v_{ox} and v_{red} correlate well with a recent study, where the effect of iron deficiencies on maize and tomato plant was also evaluated.[68]

Under zinc deficient conditions, significant ΔV_{Jn}, ΔV_{In} and ΔV_{Hn}-bands can be seen in Figure 2.8 D. Increased ROS formation have repeatedly been reported under zinc deficient conditions, which has been ascribed to lower Cu/Zn-SOD prevalence and activity (Figure 2.2).[2,10,13,69,70] The appearance of positive ΔV_{Jn} and ΔV_{In}-bands (Figure 2.8 D) are indicative of electron transport inhibition in single turnover region as well as at the intersystem electron carriers. This was supported by a marked decrease in $\psi_{Eo}/(1-\psi_{Eo})$ in Figure 2.9 D. Decreased end electron reduction can also be caused by the accumulation of NADPH (reduced NADP) as a result of lower CO_2-fixation, under zinc deficient conditions. This phenomenon can be ascribed to the role of zinc as a constituent of carbonic anhydrase (involved in CO_2-fixation). A decrease in the NADPH-demand function can cause electron accumulation upstream (before NADP) at the PSI end electron acceptors. Similar results have

previously been reported by Busotti *et al.*, 2011 and Burkart *et al.* 2013 under ozone stress, where a decoupling between electron transport and CO_2-assimilation was suggested.[65,66] This was confirmed by a significant ($p \leq 0.05$) positive ΔV_{Hn}-band (Figure 2.8 D) at the zinc deficiency treatment. In Figure 2.9 D, $\delta_{Ro}/(1-\delta_{Ro})$ was also significantly ($p \leq 0.05$) decreased, indicating a decrease in the efficiency of electron movement to PSI end electron acceptors. The MR_{820nm} data showed that a significant ($p \leq 0.05$) decline in v_{ox}, whilst a significant ($p \leq 0.05$) decrease in v_{red} was also seen (Figure 2.11 G & H). A greater decline in v_{red} compared to v_{ox} suggested that the arriving electrons from PSII were inhibited to a greater extent compared to the actual electron movement through PSI (oxidation). A significant ($p \leq 0.05$) reduction in the multi-parametric PI_{ABS} and PI_{total} parameters (Figure 2.9 D) at the zinc deficiency treatment was also seen pointing at overall down-regulation of light driven photosynthetic processes.

2.4.2.2 Excess metals

The data suggested that the increasingly higher metal concentrations had an increasingly down-regulatory effect on the photosynthetic electron transport. In this current study, the highest copper concentration (1 mM), resulted in far greater disruption of electron transport, where ΔV_L, ΔV_{Kn}, ΔV_{Jn}, ΔV_{In}, ΔV_{Hn} and ΔV_{IH}-bands were observed in Figure 2.8 A. The positive ΔV_L-band is indicative of a decrease in cooperativity between the chlorphyll antennae, possibly due to the high redox active metal (M^{2+}, diavlaent metal; Cu^{2+}, Mn^{2+}, Fe^{2+} or Zn^{2+}) concentrations. High copper and iron concentrations have been proved to cause large amounts of ROS through the Fenton and Haber-Weiss reaction.[2,3] The occurrence of a ΔV_{Kn}-band points to OEC inactivation in response to high metal concentrations, because of cation exchange between the Mn^{2+} and the Cu^{2+} divalent ion. Increases in functional antenna size was suggested by increases in ABS/RC in Figure 2.9 A-D at the highest metal concentrations. The reciprocal of the ABS/RC, RC/ABS, decreased significantly ($p \leq 0.05$), indicating RC deactivation during the 1 mM metal treatments. Positive ΔV_{Jn}- bands seen in Figure 2.5 A has also been reported in the literature in response to high metal concentration conditions.[2] This can be attributed to cation exchange of the non-heme iron between Q_A and Q_B (Figure 2.1), which will inhibit electron transport past Q_A. Marked decreases in $\psi_{Eo}/(1-\psi_{Eo})$ also suggests post Q_A electron transport inhibition (Figure 2.9 A-D). The presence of a prominent positive ΔV_{Hn}-bands and negative ΔV_{IH}-bands indicate the inhibition of the reduction of electron end receptors. This supports previous studies that suggested cation exchange of metals with the iron-containing intersystem electron carriers in the Cyt b_6f complex and the iron-containing sulphur centres and Ferrodoxin at the end acceptor PSI side (Figure 2.1).[37, 62] Marked decreases in $\delta_{Ro}/(1-\delta_{Ro})$ in Figure 2.9 A-D at high metal concentrations are also indicative of strong inhibition of PSI end acceptor reduction. Significant ($p \leq 0.05$) reductions in PI_{ABS} and PI_{total} could be seen at both the 0.05 mM and 1 mM metal treatments, which is indicative of a decrease in electron transport efficiency. A negative ΔV_{IH}-band (Figure 2.8 A-D) is a result of

reduced electron flow to the end electron acceptors because of an accumulation of reduced intersystem electron carriers. Studies have also shown that an imbalance between Q_A reduction by PSII activity and the re-oxidation of Q_A by PSI activity (also seen by the presence of positive ΔV_{In}-bands and negative ΔV_{IH}-bands) points to a 'break in the chain' between PSII acceptors and PSI acceptors.[2] This is seen as a decrease in the amplitude of the IP-phase (ΔV_{IH}), which can be interpreted as a decrease in the amount and reduction rate of reduced end acceptors at the PSI acceptor side. This was also seen by decreases in $\delta_{Ro}/(1-\delta_{Ro})$ in Figure 2.9 A-D.

Furthermore, a decrease in v_{ox} was also seen at increasing metal concentrations (Figure 2.11 A, C, E & G) becoming significant significant ($p \leq 0.05$) at the 1 mM treatments. This may have been caused by the displacement of Cu^{2+} in PC and Fe^{2+} in PSI transporters and Ferredoxin, by excess amounts of non-iron metal ions (Figure 2.1). The decline in v_{ox} may also have been as a result of decreased electron demand from the carboxylation reactions, which may have been inhibited to an extent by ROS damage to carboxylation enzymes. This phenomenon has been reported in previous studies under ozone stress.[65,66] The progressive decline in v_{red} (Figure 2.11 B, D, F & G) at increasing metal concentrations suggest down-regulation in the re-reduction rate of PSI by arriving PSII electrons. This is in agreement with the fast kinetics chlorophyll *a* fluorescence data presented in Section 2.3.2.1, where a decrease in $\delta_{Ro}/(1-\delta_{Ro})$ at high metal concentrations (efficiency of electron transport from PSII to end electron acceptors) was observed in Figure 2.9 A-D. A co-regulating mechanism between PSII and PSI is also possible, manifesting as a decline in v_{red}, as a result of decreased v_{ox}, in an attempt to minimize PSI over-reduction and subsequent ROS formation. Such a co-regulation mechanism was also reported by Busotti *et al.*, 2011 in woody plants under ozone stress.[65]

2.5 Conclusions

Trace (heavy) metals such as copper, manganese, iron and zinc play a vital role in whole plant metabolism. It often plays an important role as metal co-factors in the synthesis of vital enzymes, cellular and membrane components. Furthermore, it also plays a vital role in the process of photosynthesis, as a structural component of chlorophyll, functional and structural components of OEC responsible for water splitting, structural and functional components of electron carriers in the electron transport chain in PSII, intersystem carriers and PSI. In the present study, different trace metals deficiencies were found to differentially down-regulate specific parts of the electron transport process in a way which seems to correlate with the known positions of the respective metals within the electron transport chain.

Excess amounts of these trace metals were also found to impose a significant strain on the photosynthetic process of the IMP 52-11 maize cultivar. According to the results, the OEC, Q_A and intersystem electron transporters all appeared to be sensitive parts of PSII electron transport under

high metal concentrations (see Figure 2.9 A-D). This was attributed to the cation exchange of the M^{2+} with the Mn^{2+} in the OEC, Fe^{2+} in iron containing intersystem electron carriers between Q_A and PSI acceptor side and Cu^{2+} in the copper containing PC (see Figure 2.1 for proposed exchange sites). Damage to the chlorophyll antennae, OEC and intersystem transporters resulted in a decreased electron transport rate. Moreover, the highest metal concentration was found to cause a marked decrease in both v_{ox} and v_{red} for all metal types, which suggests definitive evidence of down-regulated PSI activity.

In this current study, the decreases in biomass accumulation with regard to dry root and shoot mass, compared well to the trends observed in the fast kinetics chlorophyll *a* fluorescence and MR_{820nm} data. The highest metal concentrations (1 mM) caused the greatest decrease in biomass, followed by a smaller but still significant ($p \leq 0.05$) decrease in the deficiency treatments. Metal deficiency conditions are also relevant in metal toxicity studies, seeing that plants absorp metals in a competitive fashion. Only in a few cases significant ($p \leq 0.05$) changes in either root or shoot biomass at the 0.05 mM treatments were observed (relative to control). The reduction in photosynthetic capacity under metal stress thus clearly translated into reduced growth in the IMP 52-11 maize cultivar. Furthermore, metal toxicity also depends on the form and its oxidation state.

In conclusion, the negative effect of the various metal types and concentrations on the growth and photosynthetic capacity of the IMP 52-11 maize plants could be successfully evaluated using the non-invasive (*in vivo*) chlorophyll *a* fluorescence and modulated 820 nm reflection techniques. Using these techniques, it was possible to pinpoint and suggest different areas and possible modes of inhibition and sensitivity in both the PSI and PSII electron transport phases, which has not been presented before for such a range of metal types and concentrations in maize. The severity of toxicity of the metals in maize depended on their relative level of exposure and type of element. According to the results of this study metal contaminated soils are potentially toxic at sufficiently high concentrations (>0.05 mM) and this will have a definite negative effect on maize crop production in the affected areas, such as AMD and other contaminated water runoff sites. Therefore, it is imperitive that the concentration of metals in heavily industrialized and mining areas be monitored closely; to make sure that exposure limits are not exceeded.

2.6 References

1. G.R. Cramer, K. Urano, S. Delrot, M. Pezzotti, Kazuo Shinozaki, Effects of abiotic stress on plants: a systems biology perspective, BMC Plant Biology, 11:163, 2011.
2. S. Mishra, R.S. Dubey, Heavy metal toxicity induced alterations photosynthetic metabolism in plants, Handbook of photosynthesis, Chapter 44, Taylor and Francis group, LLC, 2005.
3. J.L. Hall, Cellular mechanisms for heavy metal detoxification and tolerance, Journal of Experimental Botany, 53: 1-11, 2002.
4. United States Geological Survey (USGS), Mineral year book: South Africa, 2005.
5. D.J. Roux, J.E. Badenhorst, H.H. du Preez, G.J. Steyn, Note on the occurrence of selected trace metals and organic compounds in water, sediments and biota of the Crocodile river, Eastern Transvaal, SA, Water South Africa, 20: 333-339, 1994.
6. W. Maksymiec, Effect of copper in cellular processes in higher plants, Photosynthetica, 34(3), 321-342, 1997.
7. A. Aggarwal, I. Sharma, B.N. Tripathi, A.K. Munjal, M. Baunthiyal and V. Sharma Photosynthesis: Overviews on Recent Progress & Future Perspective, Chapter 16, I.K. International Publication, 2012.
8. W. Haehnel, T. Jansen, K. Gause, R.B. Klosgen, B. Stahl, D. Michl, B. Huvermann, M. Karas, R.G. Herrmann. Electron transfer from plastocyanin to photosystem I, The EMBO Journal, 13:1028–1038, 1994.
9. S. Chen, C. Yin, R.J. Strasser, Govindjee, C. Yang, S. Qiang, Reactive oxygen species from chloroplasts contribute to 3-acetyl-5-isopropyltetramic acid-induced leaf necrosis of *Arabidopsis thaliana*, Plant Physiology and Biochemistry, 52, 38-51, 2012.
10. R.G. Alscher, N. Erturk, L.S. Heath, Role of superoxide dismutase (SOD's) in controlling oxidative stress in plants, Journal of experimental Botany, Antioxidants and reactive oxygen species in plants special issue, 53:372, 1331-1341, 2002.
11. R. Millaleo, M. Reyes-Diaz, A.G. Ivanov, M.L. Mora, and M. Alberdi, Manganese as essential and toxic element for plants: transport, accumulation and resistance mechanisms, Journal of soil science and plant nutrition, 10 (4): 470 – 481, 2010.
12. G.W. Miller, I.J. Huang, G.W. Welkie, J.C. Pushnik, Function of Iron in plants with special emphasis on chloroplasts and photosynthetic activity, J. Abadla, Iron nutrition in soils and plants, 19-28, 1995.
13. R. Hansch and R.R. Mendel, Physiological functions of mineral micronutrients (Cu, Zn, Mn, Fe, Ni, Mo, B, Cl), Current Opinion in Plant Biology, 12:259–266, 2009.
14. A. Stirbet, Govindjee, On relation between the Kautsky effect (chlorophyll *a* fluorescence induction) and Photosystem II: Basics and applications of the OJIP fluorescence transient, Journal of Photochemistry and Photobiology B, 104(1-2):236-57, 2011.

15. W.H.O Ernst, J.A.C. Verkleij, H. Schat, Metal tolerance in plants. Acta Botanica Neerlandica, 41:229–248, 1992.
16. S.K. Yadav, Heavy metals toxicity in plants: An overview on the role of glutathione and phytochelatins in heavy metal stress tolerance of plants, South African Journal of Botany, 76, 167–179, 2010.
17. H. Clijsters, F. Van Assche, L. Gora, Physiological responses of higher plants to soil contamination with metals. In : J. Rozema, J.A.C. Verkleij eds. Ecological Responses to Environmental Stresses, Dordrecht: Kluwer Academic Publishers, ISBN 0-7923- 0762-3., 49, 1991.
18. G. Ouzounidou, The use of photoacoustic spectroscopy in assessing leaf photosynthesis under copper stress: correlation of energy storage to photosystem II fluorescence parameters and redox change of P700, Plant Science, 113:229–237, 1996.
19. E. Patsikka, E.M. Aro, E. Tyystjrvi, Mechanism of copper-enhanced photoinhibition of thylakoid membranes, Physiologia Plantarum, 113:142–150, 2001.
20. F.C. Lidon, S.F. Henriques, Effects of excess copper on the photosynthetic pigments in rice plants, Botanical Bulletin of Academia Sinica, 33:141–149, 1992.
21. M. Baron, J.B. Arellano, J.L. Gorge, Copper and photosystem II: a controversial relationship, Physiologica Plantarum, 94:174–180, 1995.
22. F.C. Lidon, S.F. Henriques, Limiting step on photosynthesis of rice plants treated with varying copper levels, Journal of Plant Physiology, 138:115–118, 1991.
23. W. Maksymiec, R. Russa, T. Urbanik-Sypniewska, Baszynski, Effect of excess Cu on the photosynthetic apparatus of runner bean leaves at two different growth stages, Physiologica Plantarum, 91:715–721, 1994.
24. J.B. Arellano, J.J. Lazaro, J. Lopez Gorge, M. Baron, The donor side of photosystem II as the copper-inhibitory binding site, Photosynthetic Research, 45:127–134, 1995.
25. N. Mohanty, I. Vass, S. Demeter, Copper toxicity affects photosystem II electron transport at the secondary quinone acceptor (Q_B), Plant Physiology, 90:175–179, 1989.
26. M. Ciscato, R. Valcke , K. Van Loven, H. Clijsters, F. Navari-Izzo, Effects of *in vivo* copper treatment on the photosynthetic apparatus of two *Triticum durum* cultivars with different stress sensitivity, Plant Physiology, 100:901–908, 1997.
27. I. Yruela, M. Alfonso, M. Baron, R. Picorel, Copper effect on the protein composition of photosystem II, Plant Physiology, 110 :551–557, 2000.
28. F. Vacha, D.M. Joseph, J.R. Durrent, A. Tefler, D.R. Klug, G. Porter, J. Barber, Photochemistry and spectroscopy of a five-chlorophyll reaction center of photosystem II isolated by using a Cu affinity column, Procedings of the National Academy of Sciences of the United States of America, 92:2929–2933, 1995.

29. S.C. Sabat, Copper ion inhibition of electron transport activity in sodium chloride washed photosystem II particle is partially prevented by calcium ion. Z. Naturforsch, 51c: 179–184, 1996.
30. W. Maksymiec, T. Baszynski, The role of Ca^{2+} ions in modulating changes induced in bean plants by an excess of Cu^{2+} ions, Chlorophyll fluorescence measurements, Physiologica Plantarum, 105:562–568, 1999.
31. C. Schafer, H. Simper, B. Hofmann, Glucose feeding results in coordinated changes of chlorophyll content, ribulose-1,5-biphosphate carboxylase-oxygenase activity and photosynthetic potential in photoautrophic suspension cultured cells of *Chenopodium rubrum*, Plant Cell and Environment, 15:343–350, 1992.
32. G. Oquist, R. Wass A portable microprocessor operated instrument for measuring chlorophyll fluorescence kinetics in stress physiology, Physiologica Plantarum, 73:211–217, 1988.
33. I.J. Fernandez, Effects of acidic precipitation on soil productivity. In: Adriano DC, Johnson AH, eds. Acidic Precipitation. Vol. 2. Biological and Ecological Effects. New York: Springer-Verlag, 61–83, ISBN 0-387-97000-2, 1989.
34. K. Ohki, Manganese deficiency and toxicity effects on photosynthesis, chlorophyll and transpiration in wheat, Crop Science, 25:187–191, 1985.
35. K.B. Clairmont, W.G. Hagar, E.A. Davis, Manganese toxicity to chlorophyll synthesis in tobacco callus, Plant Physiology, 80:291–293, 1986.
36. T. Horiguchi, Mechanisms of manganese toxicity and tolerance of plants. VII. Effect of light intensity on manganese-induced chlorosis, Journal of Plant Nutrition, 11:235–246, 1988.
37. R.O. Nable, R.L. Houtz, G.M. Cheniae: Early inhibition of photosynthesis during development of Mn toxicity in tobacco, Plant Physiology, 86:1136-1142, 1988.
38. R. Houtz, R.O. Nable, G.M. Cheniae, Evidence for effects on the in vivo activity of ribulose-bisphosphate carboxylase/oxygenase during development of Mn toxicity in tobacco, Plant Physiology, 86:1143-1149, 1988.
39. Q. Li, L. Chen, H. Jiang, N. Tang, L. Yang, Z. Lin, Y. Li, G. Yang, Effects of manganese-excess on CO_2-assimilation, ribulose-1,5-bisphosphate carboxylase/oxygenase, carbohydrates and photosynthetic electron transport of leaves, and antioxidant systems of leaves and roots in *Citrus grandis* seedlings, BMC Plant Biology, 10:42, 2010.
40. J.P. Feng, Q.H. Shi, X.F. Wang, Effects of exogenous silicon on photosynthetic capacity and antioxidant enzyme activities in chloroplast of cucumber seedlings under excess manganese. Agricultural Science China, 8:40-50, 2009.
41. S. Doncheva, C. Poschenrieder, Z. Stoyanova, K. Georgieva, M. Velichkova, J. Barceló, Silicon amelioration of manganese toxicity in Mn-sensitive and Mn-tolerant maize varieties, Environmental and Experimental Botany, 65:189-197, 2009.
42. R.J. Strasser, A. Srivastava, M. Tsimilli-Michael, The fluorescence transient as a tool to characterize the situation photosynthetic samples. In M Yunus, U Pathre, P Mohanty, eds.

Probing photosynthesis: mechanisms, regulation and adaptation, Taylor & Francis, London, UK, pp. 445–483, 2000.

43. E.G. Pereira, M.A. Oliva, L. Rosado-Souza, G.C. Mendes, D.S. Colares, C.H. Stopato, A.M. Almeida, Iron excess affects rice photosynthesis through stomatal and non-stomatal limitations, Plant Science, 201-202:81-92, 2013.
44. E.G. Pereira, M.A. Oliva, L. Rosado-Souza, G.C. Mendes, D.S. Colares, C.H. Stopato, A.M. Almeida, Iron excess affects rice photosynthesis through stomatal and non-stomatal limitations, Plant Science, 201– 202, 81– 92, 2013.
45. T. Tsonev, F. J. Cebola Lidon, Zinc in plants - An overview, Emirates Journal of Food and Agriculture, 24 (4): 322-333, 2012.
46. A. Rashid, M. Bernier, L. Pazdernick, R. Carpentier, Interaction of Zn^{2+} with donor side of photosystem II, Photosynthetic. Research, 30:123-130, 1991.
47. N. Mohanty, I. Vass, S. Demeter, Impairment of photosystem II activity at the level of secondary quinone electron acceptor in chloroplasts treated with cobalt, nickel and zinc ions, Physiologica Plantarum, 76:386-390, 1989.
48. M. Ciscato, J. Vangronsveld, R. Valeke, Effects of heavy metals on the fast chlorophyll fluorescence induction kinetics of photosystem II: a comparative study. Z. Naturforsch. C. 54c:735-739, 1999.
49. N. Mallick, F. H. Mohn, Use of chlorophyll fluorescence in metal-stress research: A case study with the green microalga *Scenedesmus*, Ecotoxicology and Environmental Safety, 55(1):64-69, 2003.
50. G. H. Lorimer, The carboxylation and oxygenation of ribulose 1,5-bisphosphate: The primary events in photosynthesis and photorespiration, Annual Review of Plant Physiology, 32:349-388, 1981.
51. E. Mateos-Naranjo, S. Redondo-Gó mez, J. Cambrollé, T. Luque and M. E. Figueroa, Growth and photosynthetic responses to zinc stress of an invasive cordgrass, *Spartina densiflora*, Plant Biology, 10:754–762, 2008.
52. F. Van Assche, H. Clijsters, Inhibition of photosynthesis in *Phaseolus vulgaris* by treatment with toxic concentration of Zn: effects on electron transport and photophosphorylation, Physiologica Plantarum, 66:717-721, 1986.
53. A.F. López-Millán, D. R. Ellis, M. A. Grusak, Effect of zinc and manganese supply on the activities of superoxide dismutase and carbonic anhydrase in *Medicago truncatula* wild type and *raz* mutant plants, Plant Science, 168:1015-1022, 2005.
54. F. Morina, L. Jovanovic, M. Mojovic, M. Vidovic, D. Pankovic and S. Veljovic Jovanovic. Zinc-induced oxidative stress in *Verbascumthapsus* is caused by an accumulation of reactive oxygen species and quinhydrone in the cell wall, Physiologica Plantarum, 140:209-224, 2010.

55. R.J. Strasser, M. Tsimilli-Michael, S. Qiang, V. Goltsev, Simultaneous in vivo recording of prompt and delayed fluorescence and 820 nm reflection changes during drying and after rehydration of the resurrection plant Haberlea rhodopensis, Biochimica Biophysica Acta, 1797: 122–122, 2010.
56. K. Yan, P. Chen, H.B. Shao, S.J. Zhao, L.H. Zhang, Photosynthetic characterization of Jerusalem artichoke during leaf expansion, Acta Physiologiae Plantarum, 34: 353–360, 2012.
57. H. Nishizono, K. Kubta and S. Suzuki, Accumulation of heavy metals in cell walls of Polygonum cuspidatum roots from metalliferous habitats, Plant and Cell Physiology, 30, 595-598, 1989.
58. S. Mahmood, A. Hussain, Z. Saeed and M. Athar, Germination and seedling growth of corn (Zea mays l.) under varying levels of copper and zinc, International Journal of Environmental Science and Technology, Vol. 2, No. 3, pp. 269-274, 2005.
59. M.A. Yusuf, D. Kumar, R. Rajwanshi, R.J. Strasser, M, Tsimilli-Michael, Govindjee and N.B. Sarin, Overexpression of γ-tocopherol methyl transferase gene in transgenic *Brassica juncea* plants alleviates abiotic stress: physiological and chlorophyll *a* fluorescence measurements, Biochimica et Biophysica Acta, 1797:1428-1438, 2010.
60. E. Heyneke, A.J. Strauss, R.J. Strasser, G.H.J. Kruger, Open-top chamber facility to study air pollution impacts in South Africa. Part II: SO_2-drought interactions on yield, photosynthesis and symbiotic nitrogen fixation in soybean, South African Journal of Plantand Soil, 29(1):9-23, 2012b.
61. T. Baszynsk, A. Tukendorf, M. Ruszkowska, E. Skorzynska, & W. Maksymiec, Characteristics of the photosynthetic apparatus of copper non tolerant spinach exposed to excess copper, Journal of Plant Physiology, 132:708-713, 1988.
62. A. Oikarroum, V. Goltsev, R.J. Strasser, Temperature effects on pea plants probed by simultaneous measurements of the kinetics of prompt fluorescence, delayed fluorescence and modulated 820 nm reflection, PLoS ONE, 8 (3), e59433, 2013.
63. R. Millaleo, M. Reyes-Diaz, M Alberdi, A.G. Ivanov, M. Krol, P.A. Huner, Excess manganese differentially inhibits photosystem I versus II in *Arabidopsis thaliana*, Journal of Experimental Botany, 64, 1, p. 343-354, 2013.
64. C.W. Scheepers, R.J. Strasser, G.H.J. Kruger, Effect of Ozone on Photosynthesis and Seed Yield of Sensitive (S156) and Resistant (R123) *Phaseolus Vulgaris* L. Genotypes in Open-Top Chambers, T. Kuang *et al.*, Photosynthesis Research for Food, Fuel and the Future, Zhejiang University Press, Hangzhou and Springer-Verlag Berlin Heidelberg, 2013.
65. F. Bussotti, R. Desotgiu, C. Cascio, M. Pollastrini, E. Gravano, G. Gerosa, R. Marzuoli, C. Nali, G. Lorenzini, E. Salvatori, F. Manes, M. Schaub, R.J. Strasser, Ozone stress in woody plants assessed with chlorophyll *a* fluorescence, A critical reassessment of existing data, Environmental and Experimental Botany, 73, 19–30, 2011.

66. S. Burkart, J. Bender, B. Tarkotta, S. Faust, A. Castagna, A. Ranieri, H.J. Weigel, Effects of Ozone on Leaf Senescence, Photochemical Efficiency and Grain Yield in Two Winter Wheat Cultivars, Journal of Agronomy and Crop Science, ISSN 0931-2250, 2013.
67. R. Hajiboland and N. Beiramzadeh, Growth, gas exchange and function of antioxidant defense system in two contrasting rice genotypes under Zn and Fe deficiency and hypoxia, Acta Biologica Szegediensis, 52(2):283-294, 2008.
68. H.M. Kalaji, A. Oukarroum, V. Alexandrov, M. Kouzmanova, M. Brestic, M. Zivcak, I.A. Samborska, M.D. Cetner, S.I Allakhverdiev, V. Goltsev, Identification of nutrient deficiency in maize and tomato plants by in vivo chlorophyll *a* fluorescence measurements, Plant Physiology and Biochemistry, 81, 16-25, 2014.
69. M. Afsharnia, N. Aliazgharzad, R.Hajiboland, S.Oustan, The Effect of Light intensity and Zinc Deficiency on Antioxidant Enzyme Activity, Photosynthesis of Corn, International Journal of Agronomy and Plant Production, 4 (3), 425-428, 2013.
70. H. Wang and J.Y. Jin, Photosynthetic rate, chlorophyll fluorescence parameters and lipid peroxidation of maize leaves as affected by zinc deficiency, Photosynthetica, 43 (4): 591-596, 2005.

Chapter 3

Evaluation of the photosynthetic response of two South African maize cultivars IMP 52-11 and PAN 6114 under varying O_3 concentrations in Open-top chamber conditions

Chapter 3

Evaluation of the photosynthetic response of two South African maize cultivars IMP 52-11 and PAN 6114 under varying O_3 concentrations in Open-top chamber conditions

3.1 Introduction

3.1.1 Atmosheric pollution in South Africa

South Africa has an approximate population of 55 million people, which is concentrated mainly in the south and east coast, as well as in the north-eastern interior.[6] The densely populated areas are often relatively polluted, especially during the local winter, due to the presence of pronounced atmospheric inversion layers, combined with a regional high-pressure system that can trap pollutants in a large anti-cyclonic vortex covering the interior of southern Africa.[7] During the last years, three specific industrial areas in South Africa, all located within 200 km from Johannesburg, have been declared as national air pollution priority areas by the South African government. This declaration implies that emission abatement measures have to be put into place by the government to mitigate air pollution. The Vaal Triangle Air-shed Priority Area incorporates most of the petrochemical-related industries, pyrometallurgical smelters, coal-fired power plants and other industrial activities. In 2007, the Highveld Priority Area in the western Mpumalanga, a part of the Free State and a small part of the Gauteng province, with the large coal-fired power plants, a large petrochemical plant and several pyrometallurgical smelters, was declared a priority area.[8] In southern Africa there is a growing concern that the concentration of atmospheric pollutants may adversely affect natural vegetation, forests and crops.[8]

3.1.2 Ozone (O_3) as a threat to crop production in South Africa

Ozone is one of the most important pollutants in South Africa. Ozone in particular has been identified as a common gas pollutant and its concentration has been reported to reach up to 130 ppb in severly industrialized areas (such as the Highveld Priority Area mentioned above).[8] During 2013 and 2014, all of the monitoring sites in the Vaal Triangle and Highveld priority areas were out of compliance with the National Ambient Air Quality Standards for ozone in terms of the number of reported exceedances.[3,7,8] In South Africa, the focus of concern relating to ambient ozone has largely been in relation to human health, however, it has long been known that high levels of ambient ozone have a large detrimental effect on agricultural productivity.[10]

As stated in Chapter 1 (Section 1.2.1), the most important crop in these highly affected areas is maize. Maize production not only plays a vital role with regard to food security in South Africa, but it is also of vital importance to the South African economy in terms of being one of its principle export products. According to a market value chain report by the South African Department of Agriculture, Forestry and Fisheries, the maize is mainly exported to Africa, Europe and Asia.[9] From 2002-2011 the estimated average export volume of maize was reported to be in the order of 2.5 million tons per annum.[9] In 2011, roughly 48% of the maize production in South Africa was produced in the affected priority area.[9]

Any limiting factors (including an atmospheric pollution such as O_3) on maize production in the priority area must thus be carefully evaluated to ensure maximal production capacity. Differences in genotype (cultivar) sensitivity are one of the avenues that need to be explored, in order to find the most suitable genotype for a given set of conditions. Figure 3.1 shows the mean monthly (in 2010) O_3 concentrations measured at 5 different locations in the affected priority area (North West Province, Gauteng and Mpumalanga), by making use of 37 passive sampler systems.[8] From the data in Figure 3.1, it can be seen that the monthly maximum mean levels measured was about 100 ppb O_3 and the annual average was 62 ppb O_3.[8] According to the results (data not shown), the hourly means reached O_3 levels of up to 130 ppb.[8]

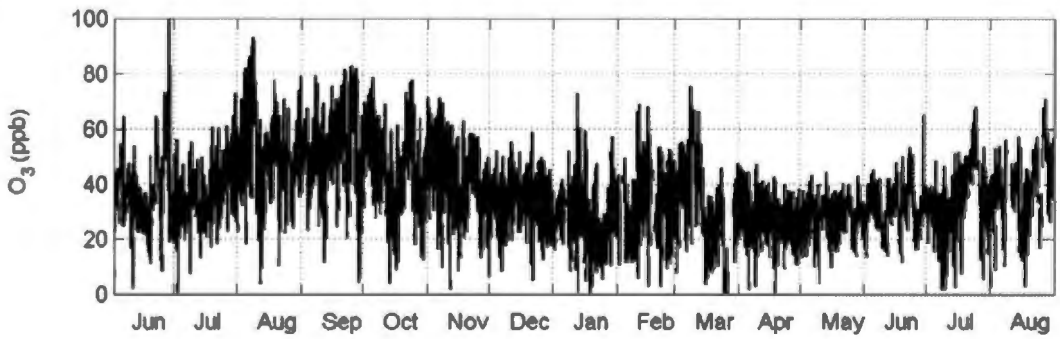

Figure 3.1: The mean monthly average O_3 concentrations (in 2010) measured at 5 different locations in the affected priority area, by making use of 37 passive sampler systems.[8]

Ozone has previously been shown to significantly reduce agricultural yield, which can have severe economic implications. Economic losses due to a decrease in crop yield, as well as a decrease in product quality (visual injury of product), have been reported.[11] Reports of losses in the billion dollar range per annum, due to the negative impact of O_3, certainly warrants further investigation into its (O_3's) effect on crop production in South Africa.[8,11,12]

3.1.3 Effect of O_3 on plants

Ozone has been shown previously to affect plant physiology and modulating processes such as photosynthesis and stomatal regulation.[3] A common experimental tool for such studies has been Open Top Chambers (OTCs), which were specifically designed for the purpose of studying atmospheric gas pollution. OTCs allow controlled O_3 (or other gas) fumigations at near field conditions. Ozone symptoms characteristically occur on the upper surface of affected leaves and appear as a flecking, bronzing or bleaching of the leaf tissues. Although yield reductions are usually coupled with visible foliar injury, crop loss can also occur without any sign of pollutant stress. Susceptibility to ozone injury is influenced by many environmental and plant growth factors. High relative humidity, sub-optimum soil-nitrogen levels and water availability increase susceptibility. Injury development on leaves is also influenced by the stage of maturity. The youngest leaves are more resistant. With expansion, they become successively susceptible at the middle and basal portions. The leaves become resistant again at complete maturation.[2,3]

Plants can deal with O_3 in one, or both, of two ways. Firstly, stomatal control of O_3 uptake can be seen as the ability of a plant to avoid stress by closing its stomata, hence stress avoidance. Stomatal closure in response to O_3 can be regarded as a protective mechanism, which limits the dose/concentration delivered to the intercellular space.[3] Differences in stomatal frequency or response have been related to differences in plant sensitivity to O_3. Secondly, when O_3 penetrates leaves through the stomata, it can be dissolved in the apoplastic fluid, where it can react with cell structures to form reactive oxygen species (ROS), such as hydrogen peroxide (H_2O_2), as well as hydroxyl ($OH^{\cdot}$) and superoxide (O_2^{-}) radicals, which can cause structural damage to cell and enzymatic components. As a result, plants have developed complex detoxification systems to deal with ROS induced stress. Enzymatic and non-enzymatic strategies are employed by plants to control ROS levels.[4] Enzymatic systems involved in ROS detoxification include superoxide dismutase (SOD), (which is found in almost all cellular components), catalase (CAT), ascorbate peroxidase (APX) and glutathione peroxidase (GPX).[4] Non-enzymatic antioxidants include ascorbate, tocopherol and glutathione.[4] These ROS defence systems are usually sufficient to protect plants from ROS damage, but when external stressors are imposed on the plant, more ROS are produced than these defence systems can handle. While it is well-known that O_3 affects stomatal conductance and photosynthetic CO_2-fixation, the magnitude thereof varies widely among plant species due to varying capacities for absorbing and detoxifying O_3.[5]

Since photosynthesis is regarded as one of the most sensitive indicators of stress in a plants' metabolism, numerous studies have been conducted to evaluate the response of different plant species to O_3-induced limitation on photosynthesis. Stomatal conductance (g_s) can be used effectively as a measure of stomatal health under stress conditions. Numerous authors have reported stomatal closure

under O_3-stress conditions. Stomata function by regulating simultaneously the absorption of CO_2 and the loss of water through transpiration. Under no or low stress conditions the stomatal conductance decreases when there is sufficient CO_2 in the stomatal cavity, in an attempt to limit water loss through transpiration. Under stress conditions, it has been shown that stomata can become damaged or more closed as a result of a stress avoidance mechanism (for example in case of elevated atmospheric gasses such as O_3, SO_2 etc.).[21,28]

3.1.4 Using photosynthesis to evaluate O_3 sensitivity

Whilst elevated background levels of O_3 are often insufficient to produce visible injury, lower photosynthesis is often reported, which makes it an excellent tool to use to evaluate O_3 sensitivity. Because of the sensitivity of photosynthesis to changes in O_3 concentration, it even becomes possible to differentiate between intergenotype O_3-sensitivities.[12,36] Both the electron transport and CO_2-fixation processes of photosynthesis have previously been identified as target sites for O_3-induced damage.[12] Ozone-induced reduction in photosynthesis rate has been attributed to two factors: (i) stomatal and (ii) non-stomatal limitation. A reduction in the maximal rate of carboxylation (V_{cmax}) by either ribulose 1,5-bisphosphate carboxylase/oxygenase (C_3 plants) or phosphoenol-pyruvate carboxylase (C_4 plants) is considered to be the primary effect of O_3 on photosynthesis, which induces stomatal closure *via* an increase in intercellular CO_2 concentration (C_i). As mentioned earlier, stomatal regulation in itself is also considered as a very important factor in controlling the ozone sensitivity of plants and O_3 uptake. Furthermore, studies have also suggested the decoupling of stomatal conductance and photosynthesis under O_3-stressed conditions.[28] Ozone can also alter photosynthetic process at the level of the electron transport, such as decreases in leaf Chl content, reduction in the efficiency of excitation capture in plants, reduced numbers of intact or open photosystem II (PSII) reaction centers or damage individual transport constituents within the electron transport chain which increases the dissipation of energy through alternative means such as heat. Recently, a few studies have also reported lower photosystem I (PSI) electron transport activity in response to chronic O_3 exposure, although such studies are still relatively scarce, due to the availability of reliable technology and the lack of expertise to interpret such data.[36,46,47]

The influence of O_3 on CO_2-fixation and electron transport can be monitored efficiently by using photosynthetic gas exchange and chlorophyll *a* fluorescence, respectively. Although extensive research has been done in Europe concerning the impact of elevated O_3 concentrations on different food crop species (particularly maize), the sensitivity of South African genotypes to O_3-induced responses remains somewhat unclear.

3.1.5 Aim of this study

The aim of the present investigation was to compare the photosynthetic response of two popular South African maize cultivars (IMP 52-11 and PAN 6114) to different O_3-levels. Photosynthetic gas exchange was monitored using an infrared gas analysis system and the function of the photosynthetic electron transport chain was examined, by measuring simultaneously the kinetics of prompt fluorescence (JIP-test), modulated light reflection at 820 nm and far-red irradiation at 735 nm. In this chapter we deemed it necessary to measure both the photosynthetic gas exchange and electron transport properties, seeing that they are both directly influenced by O_3-stress. As mentioned earlier, the decoupling of stomatal conductance and photosynthesis has been reported. In this current study we will also attempt to construct an electron flux model, in an effort to demonstrate increased decoupling (with increase in O_3-stress severity) between the electron transport chain (at PSI donor side) and electron transport used for CO_2-assimilation.

3.2 Materials and Methods

3.2.1 Plant cultivation and O_3 treatment

Pots (12 L in volume) were filled with sterilized soil and two seeds of two widely used South African maize genotypes IMP 52-11 (Agricol) and PAN 6114 (Pannar) were planted in the respective pots. These specific genotypes were also chosen because of their known drought resistence charactersitics, which is important in the relatively low annual rainfall Highveld priority area. The experiment was conducted in Open-top Chambers (OTCs) located at the North-West University, Potchefstroom campus, South Africa (S26°41.033' E27°06.237'). The pots were well watered every second day. Every 2 weeks, 500 mL of a nutrient solution was given to each pot. The nutrient solution contained the following nutrients: macronutrients (in mM): 1.25 KNO_3, 1 $Ca(NO3)_2$, 0.25 $(NH_4)H_2PO_4$, 0.5 $MgSO_4$, 0.1 KCl, & micronutrients (in µM): 15 H_3BO_3, 0.065 $Na_2MoO_4.2H_2O$, 20 Fe-EDTA, 5 $MnSO_4$, 2 $CuSO_4$ and 5 $ZnSO_4$. The 48 pots were divided into 8 open top chambers (OTCs) (3 pots of each cultivar in each OTC). Chronic O_3-fumigation of the OTCs commenced two weeks after emergence. Fumigation lasted 10 day light hours (to match the main period of photosynthesis) each day for a period of 6 weeks. The chronic O_3 treatments were as follows: OTC 1 & 2 = ambient O_3 (varied between 5 - 12 ppb O_3), OTC 3 & 4 = 40 ppb O_3, OTC 5 & 6 = 80 ppb O_3, OTC 7 & 8 = 120 ppb O_3. The ozone levels were monitored daily using a 2B Technologies Model 202 Ozone Monitor (UV absorption at 254 nm).

3.2.2 Meteriological data in OTC

The temperature and humidity inside the OTCs were monitored using a RHT03 (also known as a DHT-22) humidity and temperature sensor with a single wire digital interface. It provides a voltage output that is linearly proportional to the Celsius temperature and relative humidity (RH). Photon flux density was measured using a photosynthetically active radiation (PAR) meter from Vernier.

3.2.3 Photosynthetic gas exchange

After 6 weeks' of fumigation, the leaf level photosynthetic gas exchange was measured under varying leaf surface concentrations of CO_2 (0, 25, 50 75, 100, 200, 350, 500, 750, 1000, 1250 and 1500 ppm), using a portable infrared gas exchange analyser (IRGA) system (CIRAS-2, PP-systems, Hitchin, UK). The gas exchange measurements were used to plot the net CO_2-assimilation rate (A) versus intercellular CO_2 concentration (C_i) (so called A:C_i curves) and these curves were analysed according to the C_4-plant model of Von Caemmerer and Furbank 1999, which is a derivation of the original model by Farquhar and Sharkey 1982 for C_3-plants.[13,14] The C_4-plant model of Von Caemmerer and Furbank 1999 was used to estimate the maximal rate of phosphoenol-pyruvate carboxylase (PEPc) activity, V_{pmax}. The regeneration rate of PEPc (C_4 plants) and maximal electron transport rate (J_{max}) was also estimated.[13] The parameters are fitted to determine the photosynthetic response to O_3. Values of C_i were estimated from stomatal conductance to CO_2 transfer, g_s, and the ambient CO_2 concentration external to the leaf, C_a. The stomatal conductance (g_s) was also plotted against C_i, which was used to assess the stomatal response as a result of the various O_3 treatments. The water use efficiency (WUE) of the plants was calculated (at 360 ppm CO_2) through the assimilation (A) and transpiration (E) data, using the well-known equation of: WUE = A/E.[16]

3.2.4 Chlorophyll *a* fluorescence, modulated 820 nm reflection and far-red illumination

Fast chlorophyll *a* fluorescence kinetics was measured after 1 hour dark adaptation of the test plants, using a multichannel multifunctional plant efficiency analyser (M-PEA, Hansatech, UK). Dark-adapted leaves were illuminated for 1 s pulse with continuous red light (627 nm, 5000 µmol photons. $m^{-2}s^{-1}$) followed by a 15 s illumination using far-red light (735 nm, 200 µmol photons $m^{-2}.s^{-1}$). During the 1 s illumination, chlorophyll *a* fluorescence (prompt fluorescence – PF) and modulated 820 nm reflection (MR) were recorded. The PF was used to monitor the redox reactions around photosystem II (PSII), whereas the modulated 820 nm reflection was used to monitor the redox state of PSI and plastocyanin (PC).[17] Far-red light was used to fully oxidize the reaction centres of PSI. The entire prompt fluorescence kinetics series is called the OJIP-fluorescence transient.[18] For an illustrative

example of the characteristic steps (O-J-I-P) of a typical prompt fluorescence transient please refer to Figure 1.13.

During the actinic illumination, the following data points on the transients were extracted and used for the calculation of several photosynthetic parameters (Review: Strasser *et al.,* 2000)[18]: F_o at 30 μs (when all reaction centres of PSII are open), F_L between 30 and 300 μs, F_K at about 300 μs, F_J at 2-3ms, F_I at 20-30 ms and F_H at 300 ms, which often coincides with the maximum of the fluorescence transient, F_P. These original data points were used and the JIP-parameters describing the structure and functionality of PSII were calculated using the formulas shown in Table 1.5. The time at which these peaks appear in the fluorescence transient, can be related to a certain point/process within the electron transport chain. 'Narrower' fluorescence fragments again allowed for more accurate representation of the processes represented by specific timeframes within fluorescent transients. In Figures 3.7-3.11 the changes in the relative (relative to control) variable fluorescence and fractions of the variable fluorescence phases are shown graphically to illustrate the change in these transients measured on plants grown under different ozone concentrations. Please refer to equations i-xi (Chapter 1, p51) on how the various relative variable fluorescence phases were obtained.

3.2.5 The link between PSI electron transport and CO_2-assimilation

In C_4-photosynthesis, electrons leaving PSI end electron acceptors can be used to regenerate PEPc in the C_4-cycle. The relative electron transport rate through PSI (from the modulated 820 nm reflection data) can be correlated to J_{max}, because electrons moving through PSI are used for PEPc regeneration. The relationship between the PSI electron transport rate and J_{max} will be termed 'coupling' in this thesis. This relationship was obtained by by plotting the data shown in Figures 3.3 B vs 3.13 A. The relationship together with a coupled (elctron flux or 'ideality') model, which was constructed by plotting relative PSI oxidation rate against its identical values, was also constructed and is shown in Figure 3.16 A & B.

3.2.6 Statistical analysis

The experiments were arranged by placing the 48 pots into 8 open top chambers (OTCs) (3 pots of each cultivar in each OTC), which equates to 2 replicates and 6 pseudo-replicates per treatment. Statistical variance analysis was done using one-way ANOVA ($p \leq 0.05$) with least significant differences (LSD) at the 5% level. Although there were only 2 replicates (2 OTCs) and 6 pseudo-replicates for each treatment, the statistics suggested that no significant differences (LSD) were seen within groups (i.e. within the same O_3-concentration treatments), which gives some assurance as to the validility of the differences between groups (between the different O_3-concentration treatments).

3.3 Results

In the following sections the results showing the influence of the various O_3 concentrations on the two maize cultivar types will be given. In Section 3.3.1 the metereological data is shown whilst the results on the influence on photosynthetic gas exchange properties are given in Section 3.3.2, followed by the influence of the various O_3 concentrations on the electron transport parameters of the two maize cultivar types in Section 3.3.3.

3.3.1 Metereological data

Figure 3.2 A-C shows the daily averages of the meteorolical data inside the OTCs (average of all OTCs) over the total 6 week fumigation period.

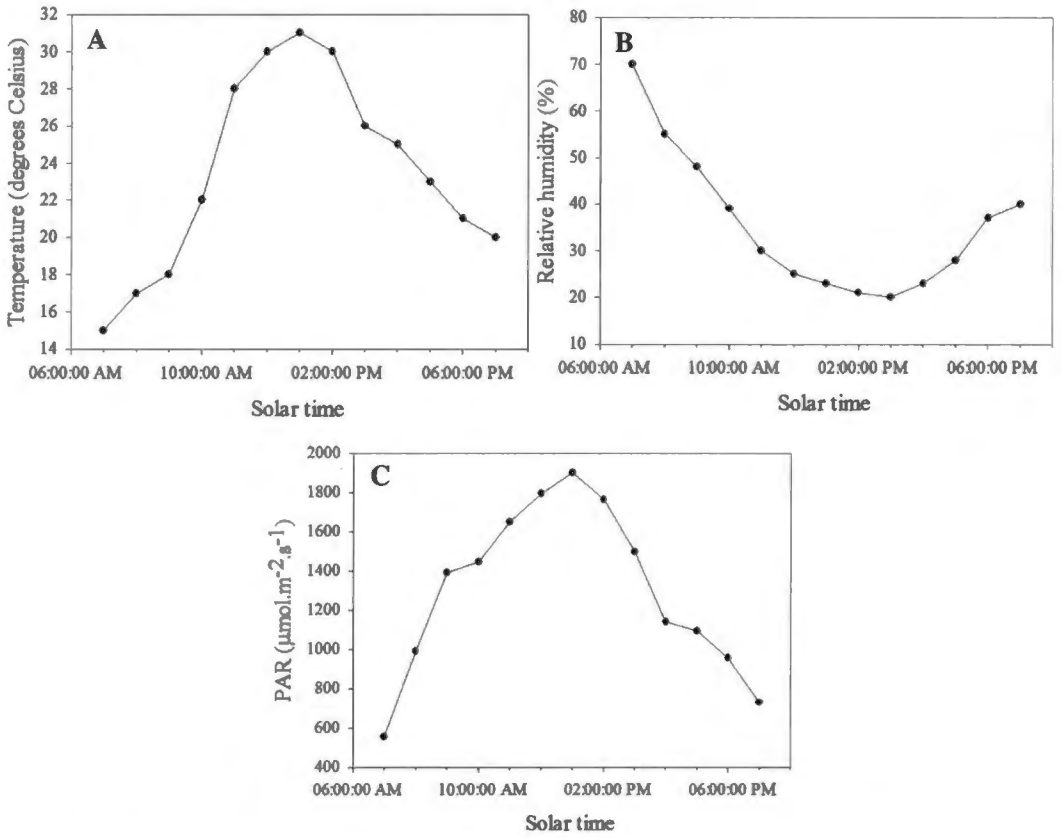

Figure 3.2 A-C: Typical daily averages of the meteorological data (A = Temperature, B = relative humidity, C = PAR) in the OTCs.

3.3.2 Photosynthetic gas exchange

3.3.2.1 CO_2-assimilation

As mentioned in Chapter 1, the primary carboxylation enzyme involved in C_4-photosynthesis during CO_2-fixation in the cytosol of the mesophyll cells is phosphoenol-pyruvate carboxylase (PEPc). Figure 3.3 A & B shows the A:Ci curves, which was attained by plotting the net CO_2-assimilation rate (A) versus intercellular CO_2 concentration (C_i) for various O_3-fumigation treatments for IMP 52-11 (A) and PAN 6411 (B). From these A:C_i curves, data relating to the influence of O_3 on the carboxylation activity (mesophyll limitation in Section 3.3.2.1), stomatal behaviour (stomatal limitation Section 3.3.2.2) and water use efficiency (Section 3.3.2.3) could be obtained.

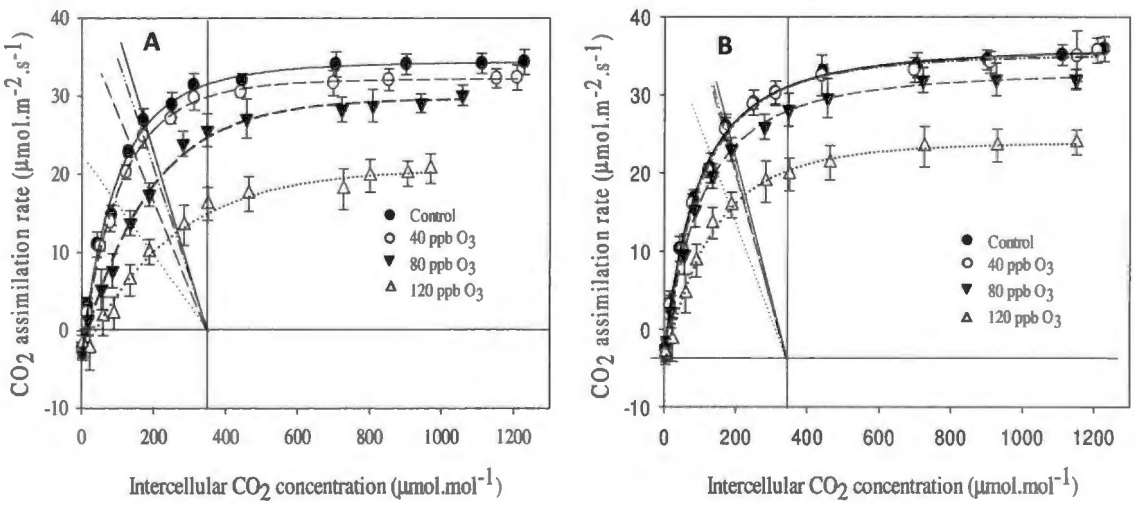

Figure 3.3 A & B: A:C_i curves of the net CO_2-assimilation rate (A) versus intercellular CO_2 concentration (C_i) for various O_3-fumigation treatments for IMP 52-11 (A) and PAN 6411 (B). The supply function [$A = g_{CO2}(C_a - C_i)$], corresponding to the demand function [$A = CE(C_a - \Gamma)$], was drawn by simply joining the value of $C_i - C_a = 360$ ppm on the abscissa to the point giving A_{360} at this value of C_a, where $CE = V_{pmax}$.[61]

3.3.2.2 Mesophyll limitation

Using the model of Farquhar *et al.*, 1982 and Von Caemmerer and Furbank (1999) described in Chapter 1, the maximal carboxylation rate of PEPc, V_{pmax}, can be approximated by the initial slope of the linear part of the assimilation versus intercellular CO_2 concentration (A:C_i) plots, i.e. the demand function. (Figure 3.3 A & B).[13,14]

The results showing the change in V_{pmax} at varying O_3 concentrations for the two maize cultivars (IMP 52-11 and PAN 6411) relative to the control are given in Figure 3.4 A. Significant decreases ($p \leq 0.05$) (compared to control) of 41% and 60% in the V_{pmax} were seen at the 80 ppb and 120 ppb O_3 treatments for IMP 52-11, whilst significant ($p \leq 0.05$) decreases of 20% and 33% decrease in the V_{pmax} were seen for the 80 ppb and 120 ppb O_3 treatments for PAN 6411. This is already indicative of a difference in O_3 sensitivity between the two cultivars. This is of great importance seeing that the O_3 levels often exceeded 80 ppb according to the data presented by Laakso *et. al*, 2013.[8] The model of Von Caemmerer and Furbank was also used to estimate the maximal rate of PEPc regeneration capacity and electron transport, J_{max}.[14,20] A significant ($p \leq 0.05$) decrease in the J_{max} of 22% and 39% (Figure 3.4 B) could be seen for the IMP 52-11 cultivar at the 80 ppb and 120 ppb treatments respectively (compared to control), whereas the PAN 6411 only showed a significant ($p \leq 0.05$) reduction of 32% at the 120 ppb treatment. These results suggested differential O_3 sensitivity with regard to PEPc regeneration capacity and electron transport between the two cultivars. A decrease in the V_{pmax} and J_{max} parameters is indicative of mesophyll limitation on photosynthesis.

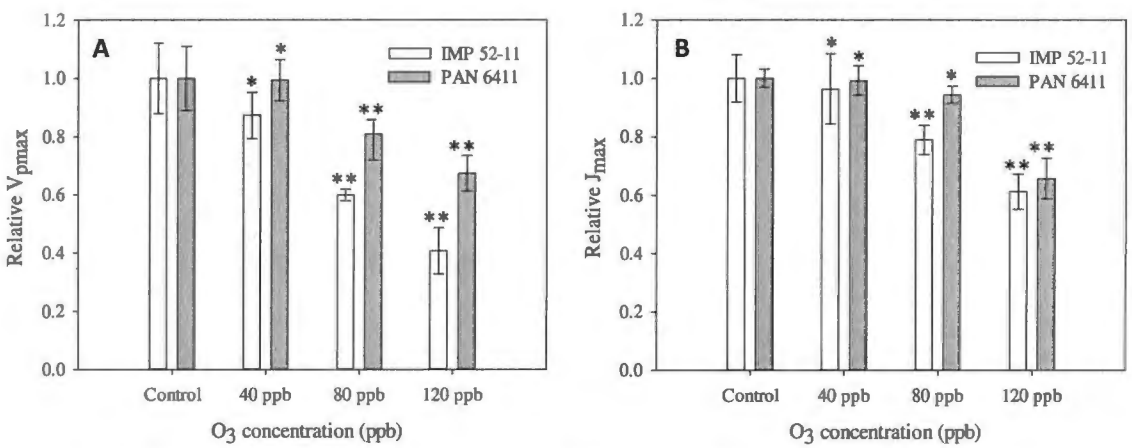

Figure 3.4 A & B: Relative PEPc activity (A) and relative maximal rate of PEPc regeneration capacity and electron transport (B) with varying O_3 concentrations. Significance relative to control was determined by a one way anova at $p \leq 0.05$ (V_{pmax}; LSD = 0.19 and J_{max}; LSD = 0.17). Data marked with '*' indicates non-significant and '**' indicates significant changes relative to control.

3.3.2.3 Stomatal limitation

Given this normal physiological response of stomatal closure (conductance) under elevated internal CO_2 concentrations (C_i), the stomatal conductance data were plotted from the various measurements against C_i, for the respective treatments (Figure 3.5 A & B), which is indicative of the physical state of the stomata (i.e. whether or not stomatal damage/closure may or may not have occurred). A clear tendency of decreasing maximal g_s with increasing O_3 concentrations was evident, becoming

significant ($p \leq 0.05$) at the 80 ppb and 120 ppb treatments for both cultivars. This suggests a decreased stomatal opening (supported by decreased transpiration – data not shown) and subsequent stomatal limitation on photosynthesis.

According to the data in Figure 3.5 A & B, the g_s of PAN 6411 appeared to be less sensitive to O_3 stress compared to IMP 52-11. Significant ($p \leq 0.05$) decreases of 10% and 24% (relative to control) in the maximal g_s were seen for IMP 52-11 at the 80 ppb and 120 ppb O_3 treatments, whilst the maximal g_s only decreased by 6% (not significant ($p \leq 0.05$)) and 19% (significant ($p \leq 0.05$)) for PAN 6411 at the 80 ppb and 120 ppb O_3 treatments. The generally applied equation of $l = [(A_0 - A) / A_0] \times 100$ was used to calculate the true stomatal limitation, where A is the assimilation rate at ambient atmospheric [CO_2] (360 ppm) and A_0 is the assimilation rate when no stomatal limitation existed, i.e. $C_i = C_a$.[14] The data shown in Figure 3.3 A & B was used to calculate the stomatal limitation. A significant ($p \leq 0.05$) decrease (relative to control) of 9.5% and 22.8% in l could be seen at the 80 ppb and 120 ppb treatments for IMP 52-11, whilst PAN 6411 only showed a decrease of 3% (not significant ($p \leq 0.05$)) and 15.5% (significant ($p \leq 0.05$)) in l at the 80 ppb and 120 ppb treatments, respectively. These values correlated well with the decrease in maximal g_s in Figure 3.5 A & B, indicating differential stomatal limitation in the two cultivars. The phenomenon of differential photosynthetic O_3 sensitivity in different cultivars of the same species has been reported previously in the literature.

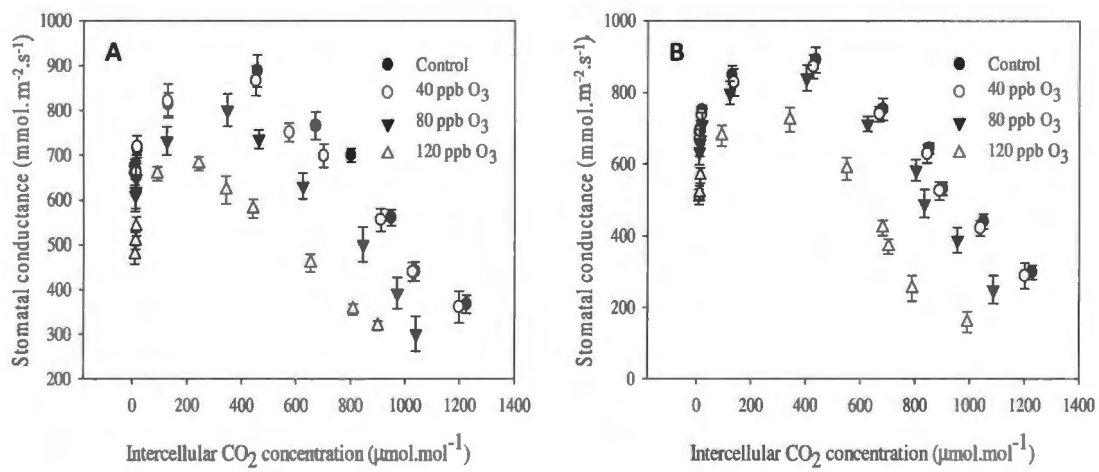

Figure 3.5 A & B: Change in stomatal conductance with change in C_i under varying O_3 concentrations for IMP 52-11 (A) and PAN 6411 (B). Significance relative to control ($\frac{g_s treatment}{g_s control} X \frac{100}{1}$) was determined by a one way anova at $p \leq 0.05$ (LSD = 9.04).

3.3.2.4 Water use efficiency

In Figure 3.6 the relative change in the WUE for the two cultivars as a function of the O_3 concentration is presented.

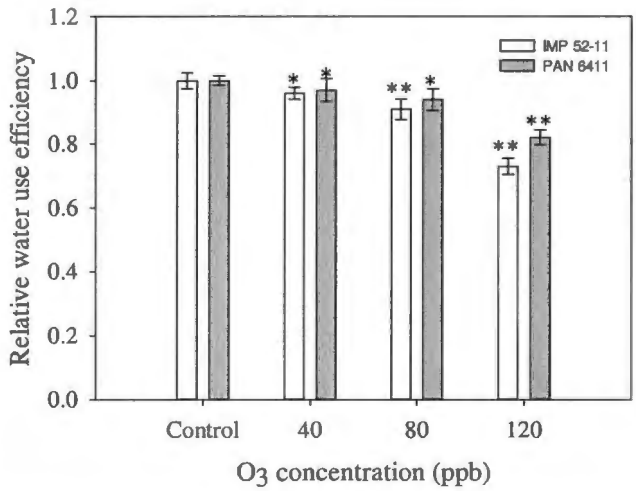

Figure 3.6: Relative change in water use efficiency (WUE) with varying O_3 concentrations. Significance relative to control was determined by a one way anova at $p \leq 0.05$ (LSD = 0.15). Non-significant differences (from control) are indicated by '*', whilst '**' indicates significant differences (from control).

A significant decrease in the water use efficiency for both IMP 52-11 and PAN 6411 occurred at the 80 ppb and 120 ppb treatments. A 11% and 20% decrease was seen for IMP 52-11 (80 ppb and 120 ppb), whilst PAN 6411 decreased by 12% and 17% for the respective treatments (Figure 3.6), which means that only the 120 ppb O_3 treatments in both cultivars showed significant ($p \leq 0.05$) reductions in the WUE.

3.3.3 Chlorophyll *a* fluorescence, modulated 820 nm reflection and far-red illumination

In Figure 3.7 A & B the change in the fast kinetics chlorophyll *a* fluorescence (PF) with varying O_3 concentrations for IMP 52-11 (A) and PAN 6411 (B) are shown, whilst Figure 3.7 C & D shows the change in the modulated 820 nm reflection ($MR_{820\ nm}$) curves with varying O_3 concentrations for both IMP 52-11 (A) and PAN 6411 (B). From the PF curves (Figure 3.7 A & B), information on the processes of light absorption, energy conversion (photochemical and non-photochemical) and electron transport could be obtained, by making use of characteristic points in the time progression on the PF curve, through calculated biophysical parameters and the construction of various variable fluorescence phases (normalizations). The maximal slopes of the kinetic curves of the photo-induced

MR changes in Figure 3.7 C & D were used to calculate the rates of P700 and PC oxidation and subsequent re-reduction.

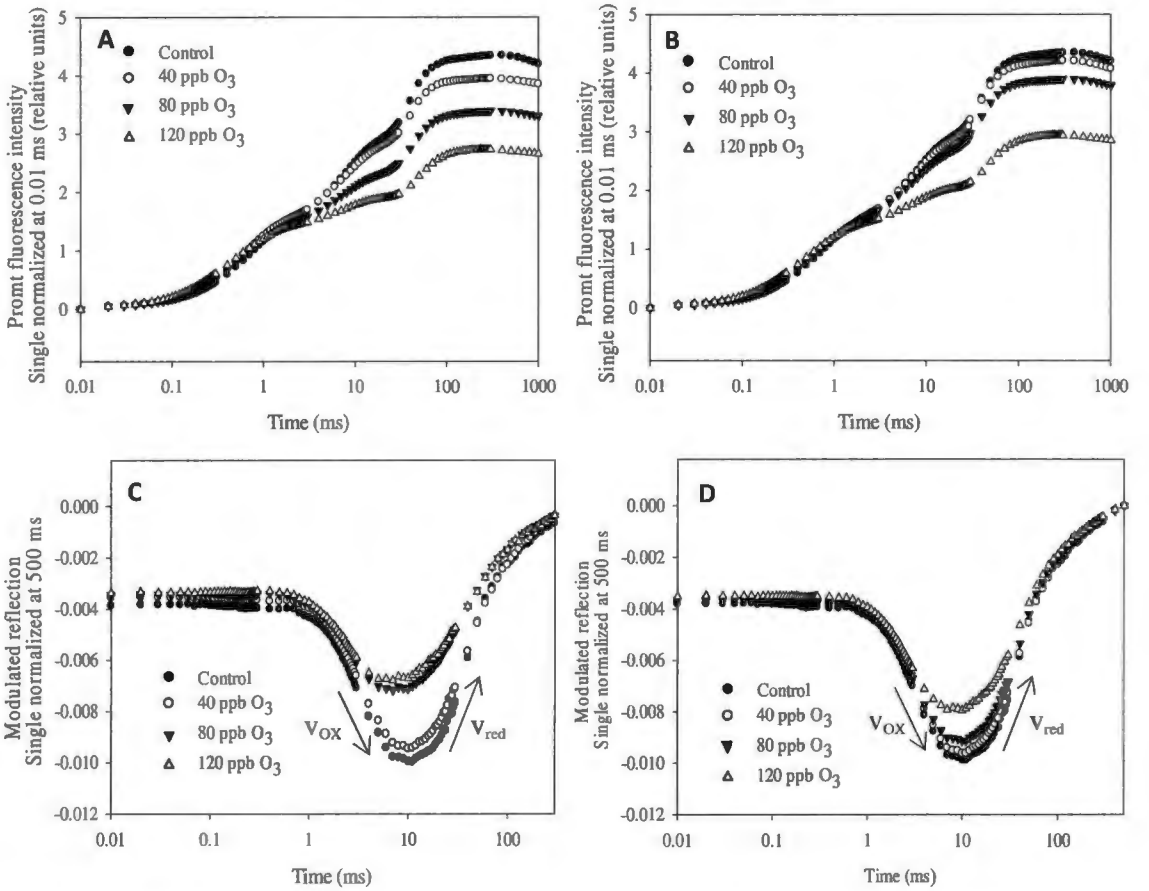

Figure 3.7 A-D: Change in prompt chlorophyll *a* fluorescence kinetics (PF) and modulated 820 nm reflection ($MR_{820\ nm}$) with varying O_3 concentrations for IMP 52-11 (A & C) and PAN 6411 (B & D).

3.3.3.1 Influence of O_3 on apparent PSII activity

Differential normalization ($\Delta V = \Delta V_{treatment} - \Delta V_{control}$) between the F_L (0.03 ms) and F_K (0.3 ms) revealed the ΔV_L-band (Figure 3.7 A & B). A positive ΔV_L-band is indicative of a loss in cooperation between chlorophyll antennae due to less photon capturing active antennae.[18]

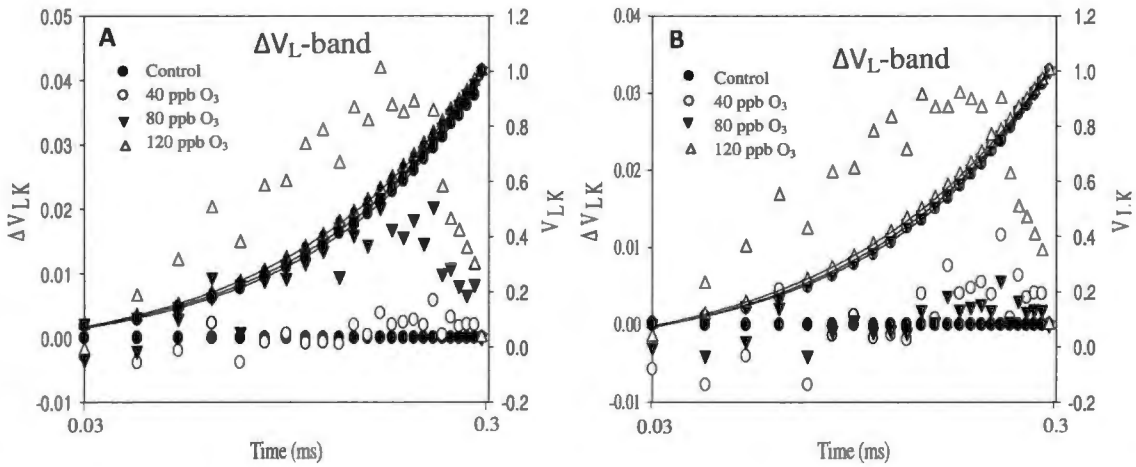

Figure 3.8 A & B: Fluorescence transients normalized between steps L (0.03 ms) and K (0.3 ms). Both these partial transients were also plotted as difference kinetics, $\Delta V_{LK} = V_{LK,\ treatment} - V_{LK,\ control}$. **A** = IMP 52-11, **B** = PAN 6411. Significance relative to control was determined by a one way anova at $p \leq 0.05$ (LSD = 0.015).

A significant ($p \leq 0.05$) positive ΔV_L-band was seen at the 80 ppb and 120 ppb O_3 treatments for IMP 52-11 (Figure 3.8 A), whereas only the 120 ppb O_3 treatment resulted in the appearance of a significant ($p \leq 0.05$) ΔV_L-band for PAN 6411 (Figure 3.8 B). This suggests differential sensitivity between the two cultivars.

The O (30 μs) to J (2-3 ms) part of the transient curve refers to the single turnover range (i.e. primary quinone acceptor (Q_A) is only reduced once) and therefore reflects mainly photochemical reactions resulting in the reduction of the electron acceptor Q_A. Differential normalization between F_0 and F_J amplifies the ΔV_K-band, which can be observed around 0.3 ms. Accumulation of electrons around Q_A results from this, giving rise to a short-lived positive ΔV_K-band. A positive ΔV_K-band is suggestive of an increase in functional antenna size (competitive inhibition). Focusing normalization between $F_{0.1\ ms}$ and $F_{1\ ms}$ reveals an intensified sharper resolution ΔVK_n-band.

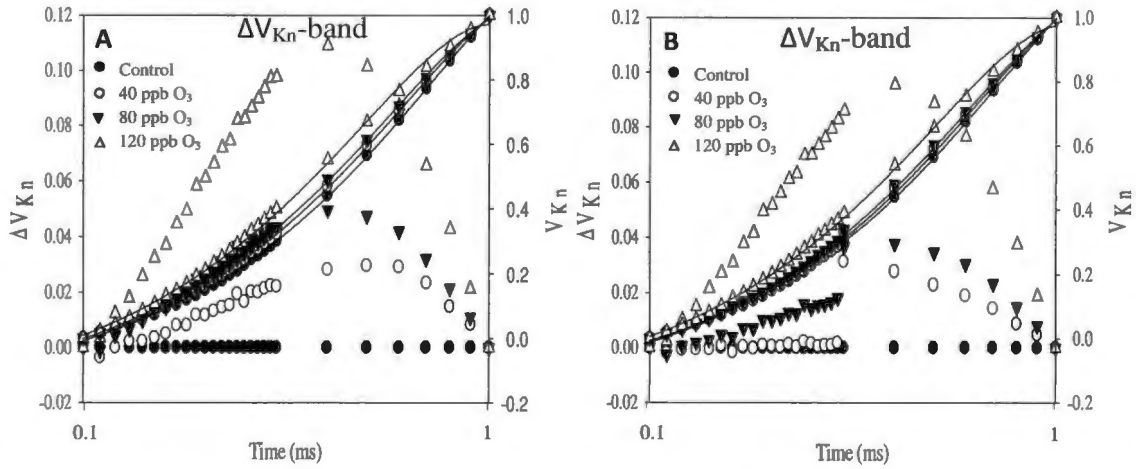

Figure 3.9 A & B: Fluorescence transients normalized between steps $F_{0.1ms}$ and F_{1ms}. Both these partial transients were also plotted as difference kinetics, $\Delta V_{Kn} = V_{Kn,\ treatment} - V_{Kn,\ control}$.
A = IMP 52-11, **B** = PAN 6411. Significance relative to control was determined by a one way anova at $p \leq 0.05$ (LSD = 0.036).

The ΔVK_n-band is a more accurate representation of these phenomena, because it excludes the impact of antenna cooperativity (ΔV_L) and Q_A-reduction. In Figure 3.9 A & B, significant ($p \leq 0.05$) positive ΔVK_n-bands can be seen at the 80 ppb and 120 ppb O_3 treatments for both cultivars, which underlines the sensitivity of the OEC and RCs to O_3 induced oxidative stress.

Differential normalization between F_0 (0.03 ms) and F_I (30 ms) amplifies the ΔV_J-band, which can be observed around 2-3 ms. A positive ΔV_J-band can be attributed to the accumulation of reduced Q_A (Q_A^-) and is indicative of decreased electron transport beyond Q_A. Further normalization between F_0 (1 ms) and F_I (10 ms) revealed a sharper ΔV_{Jn}-band (Figure 3.10 A & B), which only contains a more accurate representation of electron transport around Q_A (single turnover region).

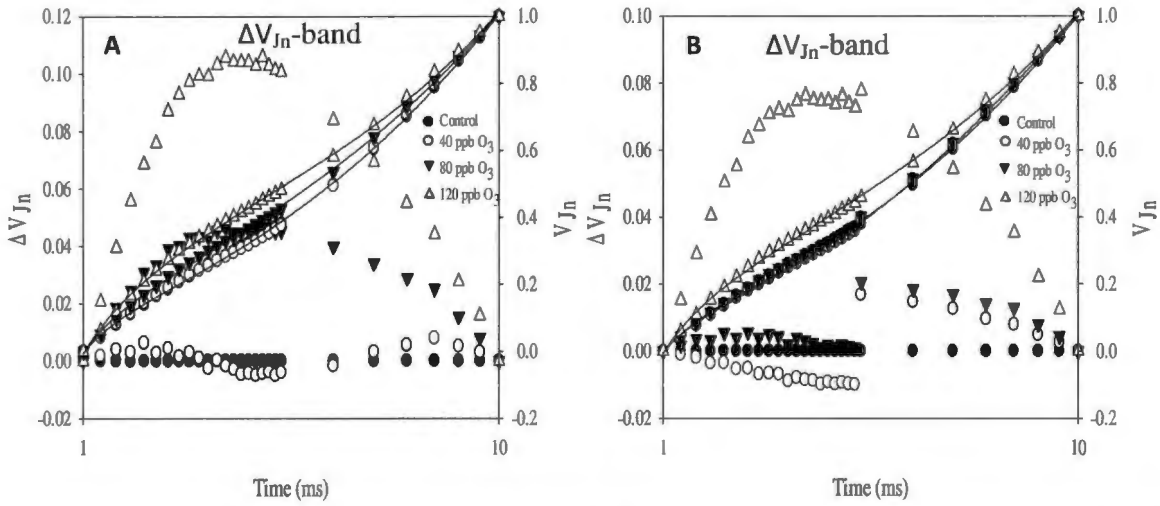

Figure 3.10 A & B: Fluorescence transients normalized between steps $F_{1\ ms}$ and $F_{10\ ms}$. Both these partial transients were also plotted as difference kinetics, $\Delta V_{Jn} = V_{Jn,\ treatment} - V_{Jn,\ control}$.
A = IMP 52-11, **B** = PAN 6411. Significance relative to control was determined by a one way anova at $p \leq 0.05$ (LSD = 0.018).

Significant ($p \leq 0.05$) positive ΔV_{Jn}-bands could be seen at the 80 ppb and 120 ppb treatments for both cultivars (Figure 3.10 A & B). Although both cultivars exhibited similar sensitivity to these levels of O_3, a clear difference in maximum ΔV_{Jn}-amplitude between the two cultivars was observed. If the amplitude is directly proportional to the amount of Q_A^-, then PAN 6411 (Figure 3.9 B) appeared to be less sensitive to O_3 in terms of this parameter (PAN 6411 having a smaller ΔV_{Jn}-band).

Differential normalization between F_J (3 ms) and F_P (300 ms) amplifies the ΔV_I-band, which can be observed around 30 ms. This region of the fluorescence transient coincides with the multiple turnover events of electron transport and has been suggested to reflect the velocity of ferredoxin reduction beyond PSI.[40] The I–P phase reflects the rate of electron transport through PSI.[32, 40] Many authors have ascribed a decrease in the amplitude of the ΔV_{IP} phase as a decrease in the flow of electrons to the PSI end electron acceptors (NADP, ferredoxin-$NADP^+$-reductase (FNR), ferredoxin (Fd)).[32, 37, 40] The IP-phase contains distinct information with regard to electron transport through the intersystem electron carriers (between Q_A and PSI acceptors) to PSI end electron acceptors. With further normalization between $F_{10\ ms}$ and $F_{100\ ms}$ a sharper ΔV_{In}-band was obtained (Figure 3.11 A & B), which only contains information of electron transport up to the PSII end acceptors (before plastocyanin (PC)), effectively excluding the influence of PSI activity.

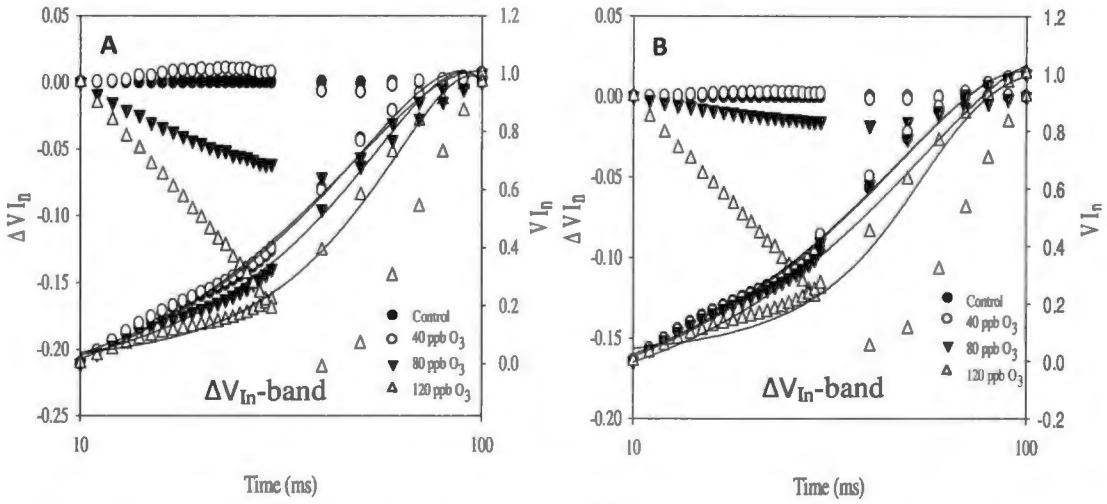

Figure 3.11 A & B: Fluorescence transients normalized between steps $F_{10\ ms}$ and $F_{100\ ms}$. Both these partial transients were also plotted as difference kinetics, $\Delta V_{In} = V_{In,\ treatment} - V_{In,\ control}$.
A = IMP 52-11, **B** = PAN 6411. Significance relative to control was determined by a one way anova at $p \leq 0.05$ (LSD = 0.06).

A significant ($p \leq 0.05$) decrease in the amplitude of the ΔV_{In}-band was seen at the 80 ppb and 120 ppb treatments for IMP 52-11 (Figure 3.11 A), whilst only the 120 ppb treatment showed a significantly ($p \leq 0.05$) reduced ΔV_{In}-band for PAN 6411 (Figure 3.11 B). This again points to differential sensitivity of the two cultivars. A decrease in the amplitude of the ΔV_{In}-band is to be expected, given the accumulation ('traffic jam') of Q_A^-, which points to decreased Q_A^- re-oxidation by intersystem electron carriers.

Using an additional normalization between $F_{100\ ms}$ to $F_{300\ ms}$, information on the second part of the IP-phase can be obtained (ΔV_{Hn}-band). The second part is termed the H-band.[17] This distinct phase in the fluorescence transient exclusively provides PSI electron transport information up to the PSI end electron acceptors. Increased ΔV_{Hn} amplitudes can be interpreted as an accumulation of reduced PSI electron carriers before $NADP^+$ and Ferredoxin (Fd).

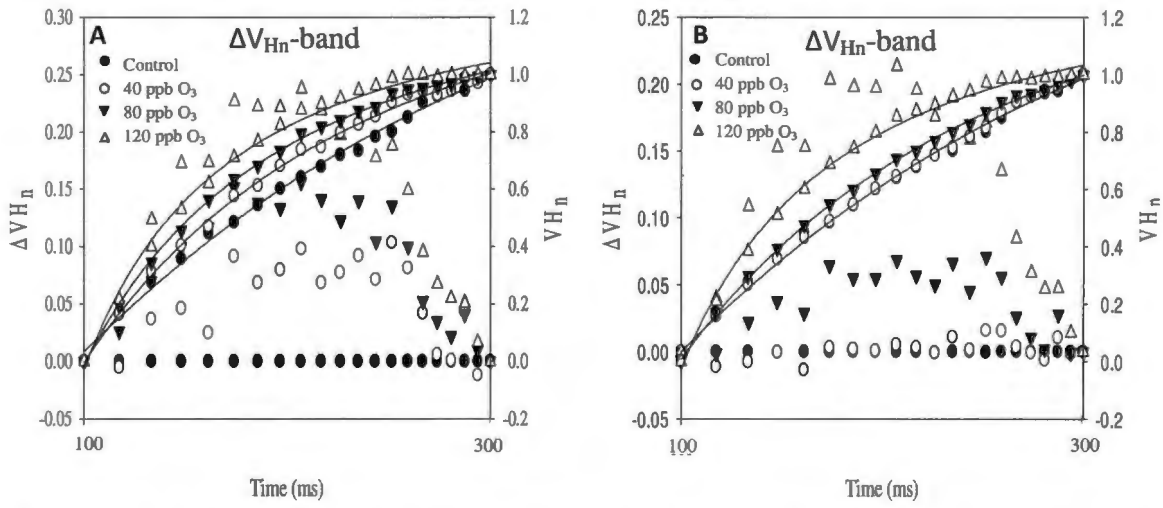

Figure 3.12 A & B: Fluorescence transients normalized between steps $F_{100\ ms}$ and $F_{300\ ms}$. Both these partial transients were also plotted as difference kinetics, $\Delta V_{Hn} = V_{Hn,\ treatment} - V_{Hn,\ control}$.
A = IMP 52-11, **B** = PAN 6411. Significance relative to control was determined by a one way anova at $p \leq 0.05$ (LSD = 0.05).

A significant ($p \leq 0.05$) increase in the amplitude of the ΔV_{Hn}-band was seen at all of the O_3 treatments for IMP 52-11 (Figure 3.12 A), highlighting the sensitivity of this part of its electron transport process to O_3-stress. Whilst both the 80 ppb and 120 ppb O_3 treatments for PAN 6411 (Figure 3.12 B) showed a significant ($p \leq 0.05$) increase in the ΔV_{Hn} amplitude, the increase was less pronounced. This is further supporting evidence of differential O_3 sensitivity of the two cultivars.

3.3.3.2 Influence of O_3 on apparent PSI activity

Few studies on the direct measurement of O_3 effects on PSI activity have been reported in the literature. Mazarura 2012 used electron paramagnetic resonance (EPR) to study the effect of O_3 on PSI and PSII activity in Foxtail grass species. He reported that O_3 caused down-regulation of electron flow through PSI and PSII.[42] A number of *in vitro* studies on the sensitivity of PSI to ROS have been reported in the literature. For a review of PSI photo-inhibition under various stress conditions (including ROS stress) see Sonoike 1996.[43]

In this study, far-red light (735 nm, 200 µmol photons $m^{-2}.s^{-1}$) was used to differentially stimulate PSI activity, effectively causing complete oxidation of PSI (as PSI re-reduction by PSII cannot take place), thereby emptying all electrons from the dark adapted PSI red-ox equilibrium state, allowing the true maximum oxidation capacity of PSI ($PSI_{max\text{-}ox}$) for the given sample to be determined. These

values are estimated from global minima of the far-red illumination induction curves. In Figure 3.13, PSI_{max-ox} of the various treatments can be seen as values normalised to the control.

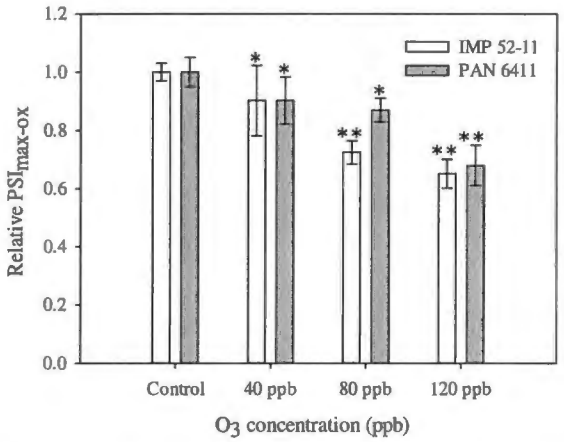

Figure 3.13: Relative PSI maximum oxidation activity, expressed as PSI_{max-ox}, under varying O_3 concentrations for IMP 52-11 and PAN 6411. Significance relative to control was determined by a one way anova at $p \leq 0.05$ (LSD = 0.19). Non-significant differences are indicated by '*', whilst '**' indicates significant differences (from control).

In Figure 3.13, significant ($p \leq 0.05$) decreases of 28% and 40% compared to control samples were observed at the 80 ppb and 120 ppb O_3 treatments for IMP 52-11, whilst PAN 6411 only showed a significant ($p \leq 0.05$) decrease of 32% at the 120 ppb O_3 treatments. According to the data PSI oxidation of IMP 52-11 is more sensitive to O_3 stress compared to PAN 6411. These decreases in PSI_{max-ox} can be interpreted as a decreased flow of electrons through PSI electron end acceptors, which indicates down-regulation in the activity of electron carriers in PSI and/or PSI reaction centre deactivation.

From the maximal slopes of the photo-induced MR changes (Figure 3.7 C & D), the v_{ox} and v_{red} was calculated, reflecting the changes in the rate of PSI oxidation and re-reduction, respectively. The results of these calculated slopes are shown in Figure 3.14 A & B.

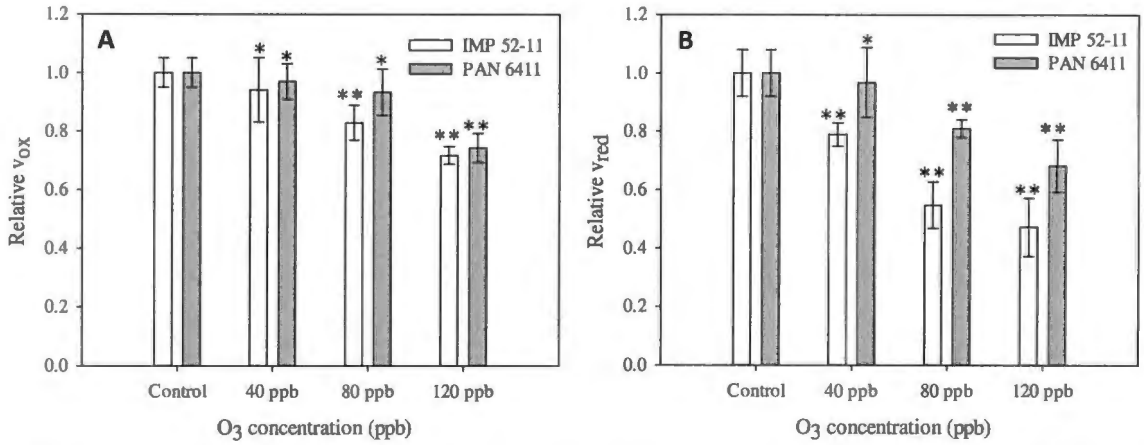

Figure 3.14 A & B: Relative P700 (PSI) oxidation kinetics (A) and relative re-reduction kinetics of $P700^+$ (B) of IMP 52-11 and PAN 6411 under varying O_3 concentrations. P700 oxidation kinetics reflects reduction rate, RE, of end electron acceptors of PSI (Ferredoxin and NADP), whilst the re-reduction kinetics of $P700^+$ reflects the rate of re-reduction of oxidized PSI and PC by PSII. Significance relative to control was determined by a one way anova at $p \leq 0.05$ (LSD = 0.16). Non-significant differences are indicated by '*', whilst '**' indicates significant differences (from control).

Significant ($p \leq 0.05$) decreases in the relative v_{ox} of PC and PSI of 17% and 29% could be seen at the 80 ppb and 120 ppb O_3 treatments for IMP 52-11, whilst PAN 6411 only showed a significant ($p \leq 0.05$) decrease of 27% at the highest (120 ppb) O_3 treatment (Figure 3.14 A). These decreases in PSI relative v_{ox} are indicative of inhibition of electron flow through PSI, which was most likely caused by oxidative damage to PSI electron carriers or were a result of a decreased electron demand by the carboxylation reactions. Guidi *et al.*, 2000 ascribed decreased Rubisco activity to lower NADPH and ATP formation, which was a result of a reduction in electron transport.[30] In Figure 3.14 B decreases in the relative (relative to control) v_{red} of PC and PSI are shown. Significant ($p \leq 0.05$) decreases of 21%, 47% and 54% could be seen for IMP 52-11 at the 40 ppb, 80 ppb and 120 ppb O_3 treatments, whilst PAN 6411 exhibited significant ($p \leq 0.05$) decreases of 19% and 34% at the 80 ppb and 120 ppb treatments. This is indicative of a breakdown in the flow of electrons between the two photosystems.

3.3.3.3 Influence of O_3 on PSII biophysical parameters derived by JIP-equations

The OJIP transients can be translated into biophysical parameters, which describe quantum yields of photon capture used for Q_A reduction (φ_{Po}), electron transport probabilities (φ_{Eo}, φ_{Ro} and δ_{Ro}), specific activities per reaction centre (RC), phenomenological fluxes per leaf cross section (CS), as well as the two performance indexes PI_{ABS} and PI_{total}.[45] The derivation and meanings of these JIP-parameters are given and described in Table 1.5 (Chapter 1). These values were calculated and selected parameters

were normalized to those of controls and plotted on radar graphs to demonstrate O_3 effects relative to control plants (Figure 3.15 A & B). The ABS/RC parameter has been described as a measure of the apparent antenna size.[45] Significant increases in ABS/RC were seen at the 80 ppb and 120 ppb O_3 treatments for both IMP 52-11 and PAN 6411. IMP 52-11 showed significant ($p \leq 0.05$) increases of 19% and 36%, whilst PAN 6411 showed significant ($p \leq 0.05$) increases of 9% and 20% at the 80 ppb and 120 ppb treatments respectively.

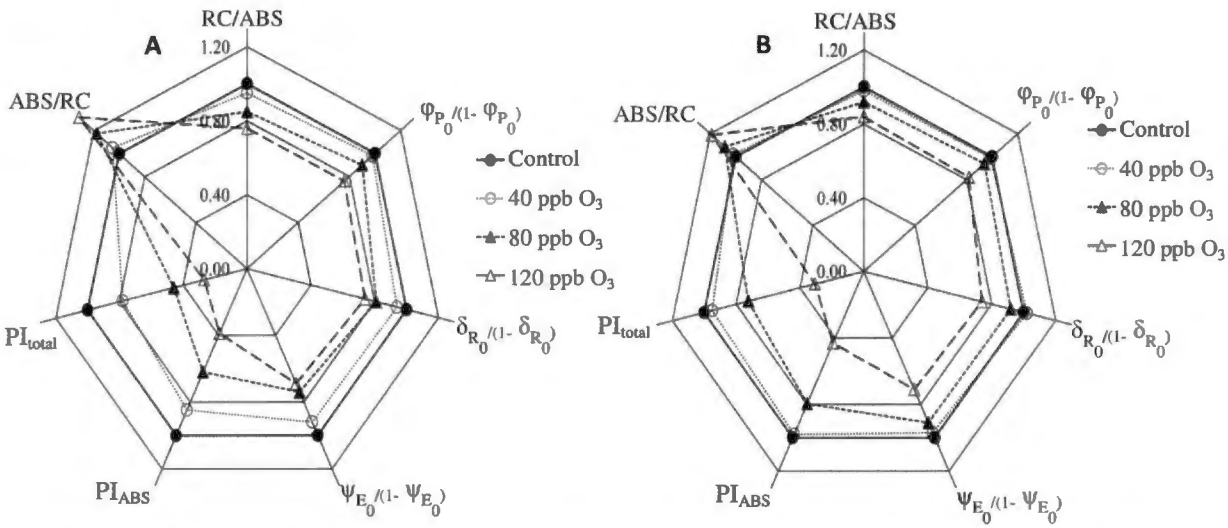

Figure 3.15 A & B: Multi-parametric (radar) plots showing the influence of the various O_3 concentrations on key photochemical and electron transport parameters for IMP 52-11 (A) and PAN 6411 (B). Significance relative to control was determined by a one way anova at $p \leq 0.05$ (LSD = 0.08).

The maximum yield of primary photochemistry, $\varphi_{Po}/(1-\varphi_{Po}) = F_v/F_m$, is defined as the probability that an absorbed photon is trapped by a PSII RC and used for Q_A reduction. In the present study IMP 52-11 showed significant ($p \leq 0.05$) decreases of 9% and 22% at the 80 ppb and 120 ppb treatments, whilst PAN 6411 only showed a significant ($p \leq 0.05$) decrease 19% at the 120 ppb O_3 treatment. The probability that a trapped excitation moves an electron into the electron transport chain beyond Q_A is given by described as $\psi_{Eo}/(1-\psi_{Eo})$. Significant ($p \leq 0.05$) decreases in $\psi_{Eo}/(1-\psi_{Eo})$ of 19% and 26% were observed for IMP 52-11 at the 80 ppb and 120 ppb O_3 treatments, whislt PAN 6411 only showed a significant ($p \leq 0.05$) decrease of 22% at the 120 ppb O_3 treatment. An accumulation of reduced Q_A and subsequent lowering of electron transport past Q_A^- has frequently been described in literature.[36-39] Electron transport to PSI end electron acceptors are quantified by the parameter $\delta_{Ro}/(1-\delta_{Ro})$. Down-regulation of electron transport from intersystem transporters up to PSI end acceptors have also been reported under O_3 stress conditions. It has mostly been reported as changes in the amplitude of the J-I-P-phase of the fluorescence transient.[38, 39, 46] Significant ($p \leq 0.05$) decreases of 24% and 28% decrease in $\delta_{Ro}/(1-\delta_{Ro})$ was seen at the 80 ppb and 120 ppb O_3 treatments for IMP 52-11, whilst PAN 6411

only showed significant ($p \leq 0.05$) decreases of 9% and 24% at the 80 ppb and 120 ppb O_3. A clear difference between the two cultivars in the sensitivity in PSI reduction by electrons from PSII is again apparent.

Two multi-parametric performance index expressions, namely PI_{ABS} and PI_{total}, described in Chaper 1 and 2. The performance index for energy conservation from photons absorbed to the reduction of intersystem electron acceptors (PI_{ABS}) significantly ($p \leq 0.05$) decreased by 17%, 38% and 60% at the 40 ppb, 80 ppb and 120 ppb O_3 for IMP 52-11. Significant ($p \leq 0.05$) reductions of 19% and 54% in PI_{ABS} were also seen for PAN 6411 at the 80 ppb and 120 ppb O_3 treatments, respectively. Significantly smaller decreases in PI_{ABS} (at 80 ppb and 120 ppb) coupled with a statistically insignificant ($p \leq 0.05$) decrease at 40 ppb O_3 for PAN 6411, suggested lower PSII sensitivity to O_3 of PAN 6411 compared to IMP 52-11. The PI_{total} decreased significantly ($p \leq 0.05$) by 21%, 53% and 76% at the 40 ppb, 80 ppb and 120 ppb O_3 for IMP 52-11, whilst PAN 6411 showed significant ($p \leq 0.05$) decreases of 23% and 66% at the 80 ppb and 120 ppb O_3 treatments. Larger decreases for PI_{total} compared to PI_{ABS} are indicative of significant PSI inhibition, seeing that the only difference in the two parameters is that PI_{total} in addition reflects the probability of PSI end acceptor reduction ($\delta_{Ro}/(1-\delta_{Ro})$). Markedly smaller decreases in the PI_{total} for PAN 6411 compared to IMP 52-11 also points to inter-cultivar differences in PSI electron transport sensitivity under O_3 stress.

3.3.4 The link between PSI electron transport and CO_2-assimilation

The relative (to control) relationship between v_{OX} and J_{max} and a decoupling (elctron flux or 'ideality') model, is shown in Figure 3.16 A & B.

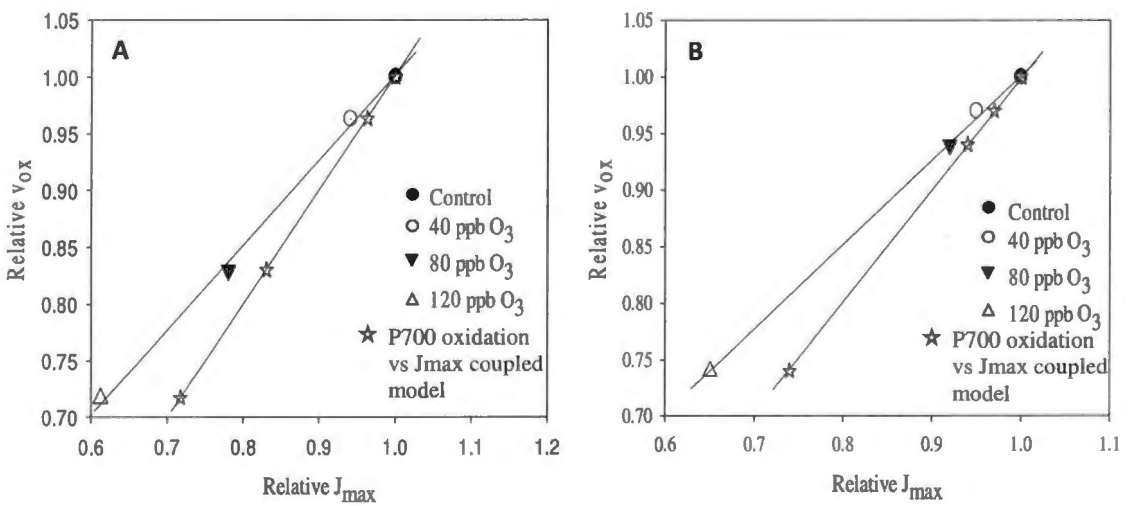

Figure 3.16 A & B: An electron flux model showing the correlation between relative P700 oxidation rate (v_{ox}) and relative PEPc regeneration or electron transport rate (J_{max}) as a fraction of the control.

Open stars depict a model of the ideal coupling correlation if 100% of PSI reduced NADPH were used for ATP formation and CO_2-assimilation. **A** = IMP 52-11, **B** = PAN 6411.

The % deviation from the electron flux (coupled) model (ε) for each treatment can be calculated using eqation 3.1 below.

$$\varepsilon = \left(1 - \left(\frac{J_{max,relative}}{v_{OX,relative}}\right)_{measured}\right) \text{ X } \frac{100}{1} \qquad 3.1$$

The ratio between J_{max} and v_{OX} for the model will always be 1 (i.e. no electrons are lost in ideal conditions). Although the authors of this paper are well aware that such ideality is not likely or possible, the model is only shown as a reference point, to show increased ε with increasing stress severity. Significant deviation from the electron flux (coupled) model (ε) was determined by a one way anova at $p \leq 0.05$ (LSD = 0.07). An insignificant ($p \leq 0.05$) decrease in ε (relative to control) was seen the 40 ppb O_3 treatments for both the IMP 52-11 and PAN 6411 cultivars, suggesting that the coupling phenomenon between electron transport and CO_2-assimilation remained relatively unchanged at these O_3 treatments. At the 80 ppb O_3 treatment, only the IMP 52-11 cultivar showed a significant ($p \leq 0.05$) increase of 9% in ε. At the 120 ppb O_3 treatment, both the IMP 52-11 and PAN 6411 cultivars showed significant ($p \leq 0.05$) increases (relative to control) of 16% and 13% in ε, respectively.

3.4 Discussion

In the OTC fumigation, the aim was to investigate the photosynthetic response (*in vivo*) of two popular South African maize cultivars (IMP 52-11 and PAN 6411) at various levels of O_3, in an attempt to elucidate whether differences in sensitivity between the two cultivars could be seen.

In this present study plants were chronically exposed to O_3 over a 6 week growth period. Various differences with regard to O_3 sensitivity between the two cultivars could be seen in both the photosynthetic gas exchange and electron transport measurements. These results confirmed previously reported O_3-induced CO_2-assimilation and electron transport responses.[4-5, 24-26, 49, 54]

3.4.1 Photosynthetic gas exchange

Photosynthetic gas exchange measurements were used to evaluate the CO_2-assimilation and stomatal response to the O_3 treatment, by making use of the C_4-plant model of Von Caemmerer and Furbank 1999, by which A:C_i curves were constructed and analysed.[13]

A reduction in the maximum net assimilation rate (A) was also observed in both cultivars, particularly at O_3 concentrations of 80 ppb and above. The maximum assimilation rate (V_{pmax}) of the primary carboxylation C_4-plant enzyme (PEPc) of both cultivars appeared to be relatively insensitive to O_3 levels of 40 ppb, whilst the V_{pmax} decreased significantly ($p \leq 0.05$) for both cultivars at the 80 ppb and 120 ppb O_3 treatments. This is also in agreement with data reported by Leitao *et al.*, 2007, where they found that similar concentrations (80 ppb) of ozone induced at least a 40% decrease (compared to control plants) in the PEPc activity in juvenile maize.[26] They attributed this to a loss of carboxylation activity due to ozone induced oxidative damage. Clebsch *et al.*, 2009 ascribed decreased Rubisco activity under increased ozone concentrations to oxidative damage caused by ROS forming O_3 in five cultivars of the C_3-plant, *Phaseolus vulgaris L.*[27] In this study, the V_{pmax} of IMP 52-11 seemed to be more sensitive to O_3 compared to PAN 6411 (Figure 3.4 A). This clearly points to differential O_3 sensitivity with regard to CO_2-assimilation between the two cultivars.

In the present study, the CO_2-response curve-deduced parameters indicated a decrease in the maximal electron transport and PEPc regeneration rate, J_{max}, for both cultivars (Figure 3.4 B). Once again both cultivars did not show a significant ($p \leq 0.05$) decrease in J_{max} at the 40 ppb treatment. Interestingly, only IMP 52-11 showed a significant ($p \leq 0.05$) decrease at the 80 ppb O_3 treatment, whilst the 120 ppb treatment showed a strong inhibitory (significant at $p \leq 0.05$) effect on J_{max} for both IMP 52-11 and PAN 6411 (Figure 3.4 B). This phenomenon also suggests differential sensitivity of the electron transport and subsequent PEPc regeneration processes between the two cultivars. The fact that V_{pmax} and J_{max} decreased with increasing O_3 concentration, suggested that strong mesophyll limitation were imposed by the treatments.

The main route of O_3 uptake by plants is by diffusion through stomata. Therefore the first line of defence of plants against O_3 damage is stomatal uptake limitation. The stomatal response under O_3 stress has been shown to be species- and cultivar specific, depending on the inherent resistance of the specific species and/or cultivar.[3, 12, 27, 31] Differences in g_s (Figure 3.5 A & B) and l was indeed observed between the PAN 6411 and IMP 52-11 cultivars. A decrease in g_s (Figure 3.5 A & B) with increasing O_3 concentration was found to be almost linearly proportional to O_3 concentration for IMP 52-11, but not for PAN 6411 (data not shown). Although both cultivars showed a decrease in g_s an l with increasing O_3 concentration, the decrease was only significant ($p \leq 0.05$) for IMP 52-11 at the 80 ppb O_3 treatment. Both cultivars showed significant ($p \leq 0.05$) reductions in g_s and l at the 120 ppb O_3 treatment. These variances indicate marked differences between IMP 52-11 and PAN 6411 with regard to O_3-induced stomatal limitation. Salvatori *et al.*, 2013 ascribed a difference in stomatal conductance to O_3 as one of the reasons for differences in O_3 sensitivity between resistant and sensitive snap bean genotypes.[47]

The water use efficiency (WUE) only decreased significantly ($p \leq 0.05$) at the highest O_3 treatment for both cultivars, with no difference in WUE response between the two cultivars (Figure 3.6). Similar decreases in the WUE under O_3-stress have been reported in the literature.[33] The decrease was not as prominent as had been expected, which could possibly be due to a possible negative feedback mechanism which regulates stomatal conductance, and subsequent transpiration, under downregulated CO_2-assimilation conditions.

3.4.2 Chlorophyll *a* fluorescence, modulated 820 nm reflection and far-red illumination

Fast kinetics chlorophyll *a* fluorescence (PF) coupled with modulated reflection ($MR_{820\ nm}$) and far-red illumination was used to investigate the PSII and PSI electron transport response to different O_3 concentration treatments in both maize cultivars.

From the PF, $MR_{820\ nm}$ and far-red illumination measurements (Figure 3.7 A-D), various structural and functional PSII and PSI electron transport parameters were obtained. Damage to chlorophyll antennae and reaction centres became evident, especially at the highest O_3 concentrations (120 ppb). A positive ΔV_L-band could be seen at the highest O_3 treatment (Figure 3.8 A & B), which is indicative of a loss of antennae cooperativity. The JIP parameter, ABS/RC, which is related to the functional antenna size, also increased, suggesting an increased antenna size due to losses in functional antennae or RC deactivation. Significant ($p \leq 0.05$) differences in ABS/RC compared to control could be seen for both cultivars at 80 ppb and 120 ppb O_3 treatments (Figure 3.15 A & B). IMP 52-11 exhibited larger increases in ABS/RC (versus control) compared to PAN 6411, indicating lower O_3 sensitivity in PAN 6411. Increased antenna size under O_3 stress has previously been attributed to damage to chlorophyll antennae by ROS species.[46] This O_3 induced phenomenon has been described in a full review by Bussotti *et al.*, 2007.[46]

Reaction centre (RC) deactivation could also be seen from the a decrease in the quantum yield of primary photochemistry ($\varphi_{Po}/(1- \varphi_{Po})$), i.e. the efficiency with which photons absorbed by active RCs are converted to photochemical energy for the reduction of Q_A. According to Strasser *et al.*, 2004, RC deactivation results in a decrease in the fraction of fully active RCs (Q_A and Q_B reducing centres) in favour of an increase of the fraction of heat sink centres (non Q_A reducing centres or silent centres).[45] This is considered a down-regulation mechanism to dissipate excess absorbed light in a controlled way. Photosystem II (PSII) thus switches from a process of converting light energy into biochemical energy storage to an energy conversion process that transforms absorbed light energy into heat dissipation. Significant ($p \leq 0.05$) decreases in $\varphi_{Po}/(1- \varphi_{Po})$ were seen for both IMP 52-11 and PAN 6411 at the 80 ppb and 120 ppb O_3 treatments (Figure 3.15 A & B). This is in agreement with data of most documented studies, where a marked decrease in the quantum yield of photochemistry under O_3

stress was reported.[5, 24, 34, 37] A greater decline in $\varphi_{Po}/(1- \varphi_{Po})$ (Figure 3.15 A & B) was seen in the IMP 52-11 cultivar (compared to the PAN 6411 cultivar) suggesting stronger inhibition in this cultivar. The presence of a positive ΔV_{Kn}-band (Figure 3.9 A & B) was seen for all O_3 treatments for both cultivars. This corroborates the reported sensitivity of the OEC to O_3 stress (ROS damage) in various previous studies by Scheepers *et al.*, 2013 and Bussotti *et al.*, 2011.[36, 37] In the present study, no significant ($p \leq 0.05$) distinction in the intensity of the ΔV_{Kn}-band between the two cultivars could be made after O_3 stress.

According to the literature, another sensitive part of electron transport to O_3 induced ROS, is the single turnover events involving Q_A reduction and Q_A^- re-oxidation. A positive ΔV_{Jn}-band can be interpreted as an accumulation of Q_A^-, resulting from inhibited electron transport beyond Q_A. The appearance of positive ΔV_{Jn}-bands is shown in Figure 3.10 A & B. The amplitudes of the ΔV_{Jn}-bands were greater in the IMP 52-11 cultivar compared to PAN 6411, which points at larger post Q_A electron transport inhibition in IMP 52-11. A positive ΔV_J-band induced by high O_3 levels was also observed by Bussotti *et al.*, 2011, Scheepers *et al.*, 2013, Cascio *et al.*, 2010 and Nussbaum *et al.*, 2001, where decreased electron transport past Q_A was reported.[36-39] A decrease in the probability that a trapped excitation moves an electron into the electron transport chain beyond Q_A, $(\psi_{Eo}/(1- \psi_{Eo})$, also suggests such a response. A differential inhibition in the two cultivars is also suggested by this $\psi_{Eo}/(1- \psi_{Eo})$ parameter as shown in Figure 3.15 A & B.

A decrease in the amplitude of ΔV_{IP} phase has been attributed to a reduction in electron transport to PSI end acceptors.[32] By differentiating between the ΔV_I and ΔV_P phases through normalization, it becomes possible to distinguish between the transport events around the intersystem electron carriers and electron transport through PSI to the end acceptors of PSI. The ΔV_{In}-band (Figure 3.11 A & B) can be interpreted as the electron transport around the intersystem electron carriers or the size of the reduced plastoquinone pool. The data showed a significant ($p \leq 0.05$) decrease in the amplitude of the ΔV_{In}-band at the 80 ppb and 120 ppb O_3 treatments for IMP 52-11, whilst PAN 6411 only showed a significant ($p \leq 0.05$) decrease at the 120 ppb O_3 treatment, suggesting differential sensitivity.

Changes in the ΔV_{Hn} amplitude can be associated with changes in the PSI end acceptor reduction. An increase in the ΔV_{Hn} amplitude (Figure 3.12 A & B) is indicative of an accumulation of reduced PSI iron containing electron carriers before NADP. CO_2-assimilation is the major sink for the reducing equivalents and energy produced by the primary photochemical reactions. Therefore, a diminished CO_2-fixation will induce a decreased demand for ATP and NADPH, and consequently, may lead to an over-reduction (electron accumulation) of PSI and PSII. A down-regulated electron demand function by an O_3-induced decrease in CO_2-assimilation reactions may be responsible for this phenomenon. A similar co-regulatory modulation of electron transport and carboxylation reactions has previously been reported for other abiotic stresses.[37, 55-58] In the present study, significant ($p \leq 0.05$) decreases in

the amount of electrons transported to PSI end electron acceptors ($\delta_{Ro}/(1-\delta_{Ro})$) were seen for both cultivars at the 80 ppb and 120 ppb O_3 treatments, with more prominent decreases in IMP 52-11 (Figure 3.15 A & B).

Far-red light (735 nm, 200 µmol photons $m^{-2}.s^{-1}$) was used to differentially stimulate PSI activity, effectively causing complete oxidation of PSI (as PSI re-reduction by PSII cannot take place). Emptying all electrons from the dark adapted PSI red-ox equilibrium state allowed us to deduce the true maximum oxidation capacity of PSI (PSI_{max-ox}) for the given sample. The data suggested greater down-regulation in the activity of electron carriers in PSI and/or PSI reaction centre deactivation in IMP 52-11 at high O_3 concentrations (≥ 80 ppb), compared to PAN 6411 (Figure 3.13).

The use of MR_{820nm} allowed us to monitor the redox reactions around PSI. By analysing the modulated reflection curves, the maximum rate of PC and P700 oxidation (v_{ox}) and $P700^+$ re-reduction (v_{red}) could be obtained from the respective maximum slopes of the curves (See Figures 3.7 C & D and Figure 3.14 A & B). Figure 3.14 A indicates the O_3-induced decrease in the v_{ox} of PSI which occurred. This can be interpreted as a decrease in the rate at which electrons move through PSI to PSI end acceptors. The v_{ox} of IMP 52-11 was significantly ($p \leq 0.05$) lower at the 80 ppb and 120 ppb O_3 treatments, whereas the v_{ox} for PAN 6411 only decreased significantly ($p \leq 0.05$) at the 120 ppb O_3 treatment. Several authors have described the influence of O_3 induced damage on the flow of electrons between PSII and PSI. Mereua *et al.,* 2011 attributed the decreased electron transport between PSII and PSI to a build-up of the reduced primary electron acceptors (Q_A), which subsequently means a decreased reduction of other electron carriers towards the end electron acceptors on the PSI acceptor side.[31] Furthermore, the accumulation of electrons in PSII and PSI can also be ascribed to a decrease in the efficiency of the carboxylation reactions (suggested by the decreased V_{pmax} and J_{max} in Figure 3.4 A & B), which subsequently lead to a lower ATP and NADPH demand (which caused electron accumulation).

Moreover, a decrease in the relative $P700^+$ re-reduction capacity (v_{red}) (Figure 3.14 B) was in agreement with the data obtained from the PF data, both suggesting a decreased rate of re-reduction of oxidized PSI and PC by PSII (decreased electron flow). The decrease in v_{red} was more prominent in IMP 52-11 compared to PAN 6411, which correlates well with the PF data. Strong decreases in the multi-parametric JIP-parameters, PI_{ABS} and PI_{total} is also indicative of electron transport down-regulation in both PSI and PSII. Once again IMP 52-11 exhibited a stronger decrease in these parameters than PAN 6411.

An increase in the decoupling (ε) was observed at the 80 ppb and 120 ppb O_3 treatments for IMP 52-11 and the 120 ppb O_3 treatment for PAN 6411 (Figures 3.16 A & B). The increase in ε with increasing stress severity is indicative of an increase in electrons lost to alternative electron acceptors.

The loss of electrons to alternative electron acceptors (O_2 etc.) and the subsequent activity of the Mehler ascorbate peroxidase pathway may explain the deviation from the coupled model in Figures 3.16 A & B. Several authors have suggested decoupling between CO_2-assimilation and electron transport under severe stress conditions.[59, 60, 63] Aldea *et al.*, 2005 and Freyer *et al.*, 1998 suggested that it is possible that the transient activity of an alternative electron sink (such as O_2) can uncouple electron transport from primary carbon assimilation.[59, 63] Deviation from the model at the 120 ppb O_3 treatment becomes apparent for both cultivars, with the IMP 52-11 showing a greater deviation compared to PAN 6411. Whether or not the differences in antioxidant activity between the two cultivars were in part responsible for the difference in the amount of deviation in the coupled model remains to be checked (by measuring the antioxidant activity of both cultivars). Although this was not done in this chapter, inter-species and cultivar genetic variances in antioxidant activity are well-known reasons for differential abiotic stress (including O_3) sensitivity.[47-51, 53] This has been documented in various studies with a number of species and cultivars. Genetic variance in the prevalence and activity of detoxifying entities has been suggested as the main reason for differential sensitivities to ROS stress caused by elevated O_3 exposure. Turcsanyi *et al.*, 2000 found a decrease in apoplastic ascorbate under O_3 fumigation compared to control ROS.[48] Caregnato *et al.*, 2014 suggested that the difference in catalase activity exhibited by two varieties of ***Phaseolus vulgaris L.*** under O_3 fumigation was responsible for their differences in O_3 responses.[49] The one variety that showed greater catalase activity had far greater O_3-damage resistance because of its enhanced detoxifying capability. Eltayeb *et al.*, 2005 found that overexpression of monodehydroascorbate reductase in a transgenic tobacco cultivar was responsible for its tolerance to various abiotic stresses, which included O_3 stress.[50] Calatayud *et al.*, 2003, Gillespie *et al.*, 2011 and Mishra *et al.*, 2013 all found an increase in CAT, APX and SOD under O_3-induced stress.[51-53] In light of the numerous studies in the literature, it is reasonable to speculate that a difference in the antioxidant capacity may, in part at least, be responsible for the differences in sensitivity between the IMP 52-11 and PAN 6411 maize cultivars used in this study. Measurement of specific antioxidant activities of both cultivars is needed to confirm this hypothesis. An increase in antioxidant activity and an increase in the deviation in the coupled model (with increasing stress conditions) were indeed observed in the following chapter (Chapter 4).

3.5 Conclusions

According to the data obtained, the O_3 treatments imposed a variety of limitations on primary photochemistry and CO_2-assimilation. These limitations were found to be strongly concentration dependent. For the most part, decreases in the measured and calculated parameters were only significant ($p \leq 0.05$) at the 80 ppb and 120 ppb O_3 treatments, suggesting that the O_3 toxicity threshold of the test plants was higher than the lowest O_3 treatment (40 ppb). Keeping in mind that the O_3 levels

measured by Laakso *e. al,* 2013 surpassed the proposed toxicity threshold (>80 ppb), it is reasonable to suggest that the using the PAN 6411 maize cultivar would be preferred to the IMP 52-11 cultivar in the affected priority area in terms of O_3 tolerability. The photosynthetic limitations were as follows:

1. Stomatal limitation occurred due to a compensatory mechanism to limit O_3 uptake.
2. Mesophyll limitation occurred as a result of a decrease in the carboxylation efficiency of PEPc (V_{pmax}) and rate of PEPc regeneration (maximum electron transport rate, J_{max}).
3. Possible structural damage to the chlorophyll antennae and electron carriers.
4. Down-regulation in the quantum yield of primary photochemistry occurred, suggesting damage to PSII RCs and a subsequent decrease in the efficiency with which absorbed photons are converted to photochemical energy for Q_A reduction.
5. Decreased efficiency of electron transport in PSII (single turnover region), between PSII and PSI (multiple turnover region) as well as in PSI itself.
6. Decreased P700 oxidation and $P700^+$ re-reduction rate.
7. Increased decoupling (ε) between electron transport and CO_2-assimilation at the 80 ppb and 120 ppb O_3 treatments for IMP 52-11 and the 120 ppb treatment for PAN 6411.

In conclusion, it was found that the presence of O_3 caused limitations on all of the major processes involved in photosynthesis. Differential limitation of photosynthesis was seen between the IMP 52-11 and PAN 6411 cultivars, which were clearly shown by measuring the photosynthetic gas exchange and electron transport parameters. Clear differences with regard to stomatal behaviour, PEPc activity and electron transport efficiency pointed to a difference in O_3 sensitivity between the two cultivars, in which PAN 6411 seemed to be more resistant to O_3 stress than IMP 52-11. Intergration of the data from indirect measurement techniques (Chlorophyll *a* fluorescence and MR 820nm refelction) and a direct measurement technique (photosynthetic gas exchange) made it possible to introduce for the first time the concept of % decoupling (ε) between PSI electron transport (v_{OX}) and PEPc regeneration (J_{max}). Measurement of ROS markers and antioxidant activities are required to establish whether the process of ROS formation is is involved in the apparent increase in ε.

3.6 References

1. W.R. Stockwell, F. Kirchner, M. Kuhn, and S. Seefeld, A new mechanism for regional atmospheric chemistry modelling, Journal of Geophysical Research-Atmospheres, 102, 25847–25879, 1997.
2. L. Grunhage, H.J. Jager, H.D. Haenel, F.J. Lopmeier and K. Hanewald, The European critical levels for ozone: improving their usage, Environmental Pollution, 105, 163–173, 1999.
3. A.M. Betzelberger, K.M. Gillespie, J.M. MCgrath, R.P. Koester, R.L. Nelson & E.A. Ainsworth, Effects of chronic elevated ozone concentration on antioxidant capacity, photosynthesis and seed yield of 10 soybean cultivars, Plant, Cell and Environment, 33, 1569–1581, 2010.
4. R.C. Bortolin, F.F. Caregnato, A.M. Divan Jr., F.H. Reginatto, D.P. Gelain, J.C.F. Moreira, Effects of chronic elevated ozone concentration on the redox state and fruit yield of red pepper plant *Capsicum baccatum*, Ecotoxicology and Environmental Safety, 100, 114–121, 2014.
5. R.C. Musselman, W.J. Massman, Ozone flux to vegetation and its relationship to plant response and ambient air quality standards, Atmospheric Environment, 33: 65–73, 1999.
6. Center for International Earth Science Information Network (CIESIN), Columbia University, United Nations Food and Agriculture Programme (FAO), and Centro Internacional de Agricultura Tropical (CIAT), 2005, Gridded Population of the World: Future Estimates (GPWFE). Socioeconomic Data and Applications Center (SEDAC), Columbia University, Palisades, NY. http://sedac.ciesin.columbia.edu/gpw, 2010.
7. M. Garstang, M. Tyson, R. Swap, M. Edwards, P. Kallberg, J.A. Lindesay, Horizontal and vertical transport of air over southern Africa, Journal of Geophysical Research, 101, 23721–23736, 1996.
8. L. Laakso, J.P. Beukes, P.G. Van Zyl, J.J. Pienaar, M. Josipovic, A. Venter, K. Jaars, V. Vakkari, C. Labuschagne, K. Chiloane and J. Tuovinen, Ozone Concentrations and Their Potential Impacts on Vegetation in Southern Africa, Developments in Environmental Science, Global Dimension of Air Pollution as Part of Climate Change, Vol. 13, Chapter 20, Elsevier, 2013.
9. South African Department of Agriculture, Forestry and Fisheries, Maize market value chain profile, 2012.
10. A.P.K. Tai, M.V. Martin, C.L. Heald, Threat to future global food security from climate change and ozone air pollution. Nature Climate Change, (July), pp.2–6, 2014.
11. J. Sibiya, P. Tongoona, J. Derera, I. Makanda, Farmers' desired traits and selection criteria for maize varieties and their implications for maize breeding: A case study from KwaZulu-Natal Province, South Africa, Journal of Agriculture and Rural Development in the Tropics and Subtropics, Vol. 114 No. 1 39–49, 2013.

12. E.A. Ainsworth, C.R. Yendrek, S. Sitch, W.J. Collins, L.D. Emberson, The effect of tropospheric ozone on net primary productivity and implications for climate change, Annual Reviews of Plant Biology, 63, 637-661, 2012.
13. S. von Caemmerer, & R.T. Furbank, Modeling C_4-photosynthesis. C_4 Plant Biology (eds R. F. Sage & R. K. Monson), Academic Press, San Diego, 1999.
14. G.D. Farquhar, T.D. Sharkey, Stomatal Conductance and Photosynthesis, Annual Review of Plant Physiology, 33: 317-345, 1982.
15. G.D. Farquhar, S. von Caemmerer and J.A. Berry, A biochemical model of photosynthetic CO_2-assimilation in leaves of C_3 species, Planta, 149:78–90, 1980.
16. A.K. Knapp, W.K. Smith, Effects of water stress on stomatal and photosynthetic responses in Subalpine plants to cloud patterns, American Journal of Botany, 75(6): 851-858, 1988.
17. R.J. Strasser, M. Tsimilli-Michael, S. Qiang, V. Goltsev, Simultaneous *in vivo* recording of prompt and delayed fluorescence and 820 nm reflection changes during drying and after rehydration of the resurrection plant *Haberlea rhodopensis*, Biochimica Biophysica Acta, 1797: 122–122, 2010.
18. R.J. Strasser, A. Srivastava, M. Tsimilli-Michael, The fluorescence transient as a tool to characterize the situation photosynthetic samples. In M Yunus, U Pathre, P Mohanty, eds., Probing photosynthesis: mechanisms, regulation and adaptation, Taylor & Francis, London, UK, pp. 445–483, 2000.
19. R.C. Leegood, Strategies for engineering C_4-photosynthesis, Journal of Plant Physiology, 170, 378– 388, 2013.
20. R.J.C. Markelz, R.S. Strellner and A.D.B. Leakey, Impairment of C_4-photosynthesis by drought is exacerbated by limiting nitrogen and ameliorated by elevated [CO_2] in maize, Journal of Experimental Botany, Vol. 62, No. 9, pp. 3235–3246, 2011.
21. E.L. Fiscus, Booker F.L., Burkey, Crop responses to ozone: uptake, modes of action, carbon assimilation and partitioning, Plant, Cell and Environment, 28, 997-1011, 2005.
22. E.J. Pell, C.D. Schlagnhaufer, R.N. Arteca, Ozone-induced oxidative stress: mechanisms of action and reaction, Physiology Planta, 100, 267-273, 1997.
23. P.B. Reich, Quantifying plant response to ozone: a unifying theory, Tree Physiology, 3, 63-91, 1987.
24. C. Angeles, J.W. Ramirez, D.J. Iglesias, E.Barreno, Effects of ozone on photosynthetic CO_2 exchange, chlorophyll *a* fluorescence and antioxidant systems in lettuce leaves, Physiologia Plantarum, 116, 308–316, 2002.
25. L. Leitao, E. Delacoˆte, P. Dizengremel, D. Le Thiec, J. Biolley, Assessment of the impact of increasing concentrations of ozone on photosynthetic components of maize (*Zea mays* L.), a C_4 plant, Environmental Pollution, 146, 5-8, 2007.

26. L. Leitao, O. Bethenod, J. Biolley, The Impact of Ozone on Juvenile Maize (*Zea mays* L.) Plant Photosynthesis: Effects on Vegetative Biomass, Pigmentation and Carboxylases (PEPc and Rubisco), Plant Biology, 9, 478–488, 2007.
27. C.C. Clebsch, A.M. Divan Junior, P.L. Oliveira, N.Márcio, Physiological disturbances promoted by ozone in five cultivars of *Phaseolus vulgaris L.*, Brazilian Journal of Plant Physiology, 21, 4, 319-329, 2009.
28. D. Lombardozzi, J.P. Sparks, G. Bonan, S. Levis, Ozone exposure causes a decoupling of conductance and photosynthesis: implications for the Ball-Berry stomatal conductance model, Oecologia, 169:651–659, 2012.
29. A.Oikarroum, V.Goltsev, R.J.Strasser, Temperature effects on pea plants probed by simultaneous measurements of the kinetics of prompt fluorescence, delayed fluorescence and modulated 820 nm reflection, PLoS ONE 8 (3), e59433, 2013.
30. L. Guidi, M. Tonini, G.F. Soldatini, Effects of high light and ozone fumigation on photosynthesis in *Phaseolus vulgaris*, Plant Physiology and Biochemistry, 38, 717-725, 2000.
31. S. Mereua, G. Gerosac, R. Marzuolic, L. Fusaroe, Salvatori E., Fincoc A., Spanoa D., Manese F., Gas exchange and JIP-test parameters of two Mediterranean maquis species are affected by sea spray and ozone interaction, Environmental and Experimental Botany, 73, 80–88, 2011.
32. P.D.R. Van Heerden, J.W. Swanepoel, G.H.J. Krüger, Modulation of photosynthesis by drought in two desert scrub species exhibiting C_3-mode CO_2-assimilation, Environmental and Experimental Botany, 61, 124–136, 2007.
33. E.J. Oksanen, Environmental pollution and function of plant leaves, Physiology and Maintenance, Vol. V, Chapter 25, Encyclopaedia of life support systems, 2005.
34. A.J. Clark, W. Landolt, J. Bucher, R.J. Strasser, The response of *Fagus sylvatica* to elevated CO_2 and ozone probed by the JIP-test, based on the chlorophyll fluorescence rise: OJIP. In: De Kok LJ, Stulen I (eds) Responses of Plant Metabolism to Air Pollution and Global Change, Backhuys Publishers, Leiden, The Netherlands, pp 283–286, 1998.
35. M.A. Yusuf, D. Kumar, R. Rajwanshi, R.J. Strasser, M, Tsimilli-Michael, Govindjee and N.B. Sarin, Overexpression of γ-tocopherol methyl transferase gene in transgenic *Brassica juncea* plants alleviates abiotic stress: physiological and chlorophyll *a* fluorescence measurements, Biochimica et Biophysica Acta, 1797:1428-1438, 2010.
36. C.W. Scheepers, R.J. Strasser, G.H.J. Kruger, Effect of Ozone on Photosynthesis and Seed Yield of Sensitive (S156) and Resistant (R123) *Phaseolus Vulgaris* L. Genotypes in Open-Top Chambers, T. Kuang *et al.*, Photosynthesis Research for Food, Fuel and the Future, Zhejiang University Press, Hangzhou and Springer-Verlag Berlin Heidelberg, 2013.
37. F. Bussotti, R. Desotgiu, C. Cascio, M. Pollastrini, E. Gravano, G. Gerosa, R. Marzuoli, C. Nali, G. Lorenzini, E. Salvatori, F. Manes, M. Schaub, R.J. Strasser, Ozone stress in woody plants

assessed with chlorophyll *a* fluorescence. A critical reassessment of existing data, Environmental and Experimental Botany, 73, 19–30, 2011.

38. S. Nussbaum, M. Geissmann, P. Eggenberg, R.J. Strasser, J. Fuhrer, Ozone sensitivity in herbaceous species as assessed by direct and modulated chlorophyll fluorescence techniques, Journal of Plant Physiology, 158, 757–766, 2001.
39. C. Cascio, M. Schaub, K. Novak, R. Desotgiu, F. Bussotti, R. J. Strasser, Foliar responses to ozone of *Fagus sylvatica L.* seedlings grown in shaded and in full sunlight conditions, Environmental and Experimental Botany, 68, 188–197, 2010.
40. G. Schansker, S.Z. Toth, R.J. Strasser, Methylviologen and dibromothymoquinone treatments of pea leale reveal the role of photosystem I in the Chlorophyll *a* fluorescence rise OJIP, Biochimica et Biophysica Acta, 1706, 250–261, 2005.
41. H. Eichelmann, E. Talts, V. Oja, E. Padu and A. Laisk, Rubisco in planta kcat is regulated in balance with photosynthetic electron transport, Journal of Experimental Botany, Vol. 60, No. 14, pp. 4077–4088, 2009.
42. U. Mazarura, Effects of ozone exposure on free radical signals in photosystem I and on chlorophyll fluorescence in green foxtail, *Setaria viridis Beauv.*, Journal of Agricultural Technology, Vol. 8(7): 2409-2421, 2012.
43. K. Sonoike, Photoinhibition of Photosystem I: Its Physiological Significance in the Chilling Sensitivity of Plants, Plant Cell Physiology, 37(3): 239-247, 1996.
44. R. Millaleo, M. Reyes-Diaz, M Alberdi, A.G. Ivanov, M. Krol, P.A. Huner, Excess manganese differentially inhibits photosystem I versus II in *Arabidopsis thaliana*, Journal of experimental Botany, 64, 1, p. 343-354, 2013.
45. R.J. Strasser, M. Tsimilli –Michael, A. Srivastava, Analysis of the chlorophyll *a* fluorescence transient. In: G. Papageorgiou, Govindjee (Eds.), Advances in Photosynthesis and Respiration. Chlorophyll *a* fluorescence: a Signature of Photosynthesis. Springer, Dordrecht, The Netherlands, pp 321-362, 2004.
46. F. Bussotti, R.J. Strasser, M. Schaub, Photosynthetic behavior of woody species under high ozone exposure probed with the JIP-test: A review, Environmental Pollution, 147, 430-437, 2007.
47. E. Salvatori, L. Fusaro, S. Mereu, A. Bernardini, G. Puppi, F. Manes, Different O_3 response of sensitive and resistant snap bean genotypes (*Phaseolus vulgaris L.*): The key role of growth stage, stomatal conductance, and PSI activity, Environmental and Experimental Botany, 87, 79– 91, 2013.
48. E. Turcsanyi, T. Lyons, M. Plöchl, J. Barnes, Does ascorbate in the mesophyll cell walls form the first line of defense against ozone? Testing the concept using broad bean (*Vicia faba L.*), Journal of Experimental Botany, Vol. 51, 346, pp. 901-910, 2000.

49. F.F. Caregnato, R.C. Bortolin, A.M.D. Junior, J.C.F. Moreira, Exposure to elevated ozone levels differentially affects the antioxidant capacity and the redox homeostasis of two subtropical *Phaseolus vulgaris L.* varieties, Chemosphere 93, 320–330, 2013.
50. A.E. Eltayeb, N. Kawano, G.H. Badawi, H. Kaminaka, T. Sanekata, T. Shibahara, S. Inanaga, K. Tanaka, Overexpression of monodehydroascorbate reductase in transgenic tobacco confers enhanced tolerance to ozone, salt and polyethylene glycol stresses, Planta, 225, 1255-1264, 2005.
51. A. Calatayud, D.J. Iglesias, M. Talón, E. Barreno, Effects of 2-month ozone exposure in spinach leaves on photosynthesis, antioxidant systems and lipid peroxidation, Plant Physiology and Biochemistry, PPB/Société françaisede physiologie végétale 41, 839–845, 2003.
52. K.M. Gillespie, A. Rogers, E.A. Ainsworth, Growth at elevated ozone or elevated carbon dioxide concentration alters antioxidant capacity and response to acute oxidative stress in soybean (*Glycine max*), Journal of Experimental Botany, 62, 2667–2678, 2011.
53. A.K. Mishra, R. Rai, S.B. Agrawal, Individual and interactive effects of elevated carbon dioxide and ozone on tropical wheat (*Triticum aestivum L.*) cultivars with special emphasis on ROS generation and activation of antioxidant defence system, Indian Journal of Biochemistry & Biophysics, 50, 139–149, 2013.
54. S. Singh Gill, N. Tuteja, Reactive oxygen species and antioxidant machinery in abiotic stress tolerance in crop plants, Plant Physiology and Biochemistry, 48, 909-930, 2010.
55. S. Burkart, J. Bender, B. Tarkotta, S. Faust, A. Castagna, A. Ranieri, H.J. Weigel, Effects of Ozone on Leaf Senescence, Photochemical Efficiency and Grain Yield in Two Winter Wheat Cultivars, Journal of Agro Crop Science, ISSN 0931-2250, 2013.
56. B. Genty, J.M. Briantais, N.R. Baker, The relationship between the quantum yield of photosynthetic electron transport and quenching of chlorophyll fluorescence, Biochimica et Biophysica Acta, 990: 87–92, 1989.
57. F. Loreto, D. Tricoli, G. Di Marco, On the relationship between electron transport rate and photosynthesis in leaves of the C_4 plant *Sorghum bicolor* exposed to water stress, temperature changes and carbon metabolism inhibition, Australian Journal of Plant Physiology, 22: 885–892, 1995.
58. A. Lal, G.E. Edwards, Analysis of inhibition of photosynthesis under water stress in the C_4 species *Amaranthus cruentus* and *Zea mays*: electron transport, CO_2-fixation and carboxylation capacity, Australian Journal of Plant Physiology, 23: 403–412, 1996.
59. M. Aldea, J.G. Hamilton, J.P. Resti, A.R. Zangerl, M.R. Berenbaum, E.H. DeLucia, Indirect effects of insect herbivory on leaf gas exchange in soybean, Plant, Cell and Environment, 28: 402–411, 2005.
60. D.R. Ort & N.R. Baker, A photoprotective role for O_2 as an alternative electron sink in photosynthesis, Current Opinion in Plant Biology, 5, 193–198, 2002.

61. N.W. Pammenter, Research letter, Clarification of an apparent anomaly in the supply function associated with the response of carbon assimilation to carbon dioxide determined using conventional field equipment, South African Journal of Science, 85:271-272, 1989.
62. E. Salvatori, L. Fusaro, E. Gottaradini, M. Pollastrini, V. Goltsef, R.J. Strasser, F. Bussotti, Plant stress analysis: applications of Prompt, Delayed Chlorophyll Fluorescence and 820 nm Modulated Reflectance. Insights from independent experiments, Plant Physiology and Biochemistry, In Press, 2014.
63. M.J. Fryer, J.R. Andrews, K. Oxborough, D.A. Blowers, N.R. Baker, Relationship between CO_2-Assimilation, Photosynthetic Electron Transport and Active O_2 Metabolism in Leaves of Maize in the Field during Periods of Low Temperature, Plant Physiology,116: 571–580, 1998.

Chapter 4

Evaluation of the photosynthetic response of *Zea mays L.* to TiO_2 and SiO_2 nano-particulate foliar exposure using photosynthetic gas exchange and chlorophyll *a* fluorescence

Chapter 4

Evaluation of the photosynthetic response of *Zea mays L.* to TiO_2 and SiO_2 nano-particulate foliar exposure using photosynthetic gas exchange and chlorophyll *a* fluorescence

4.1 Introduction

4.1.1 Particulate matter

Particulate matter (PM) in the atmosphere is defined as particles between 0.1 and 10 μm in size. Approximately 25% of all particulate matter is based on carbon and associated with exhaust from all kinds of gas and coal engines.[2,30] Emissions of PM caused by anthropogenic activities arise primarily from four source categories: fuel combustion, industrial processes (mining, construction), non-industrial fugitive sources (roadway dust from paved and unpaved roads, biomass burning, wind erosion of cropland, agricultural activities) and transportation sources. The total amount of PM of most major cities often register values above 50 $mg.m^{-3}$.[2,30] Various metals often make up a substaintial amount of the particulate fractions in areas that are close to heavy metal industries, such as mines, processing and manufacturing plants. A whole range of base metals and other heavy metals such as mercury are currently being monitored closely, especially in populated areas surrounding these industries.[30] The southern African region has been recognised as a major source of aerosols in the southern hemisphere and it is known to be significant in the production and transportation of aerosols with urban and industrial areas as major sources. Aeolian dust and industrial sulphur are the major constituents of the inorganic fraction of the aerosols in the haze layer in areas downwind of the major urban and industrial areas of the Highveld plateau of South Africa. Emissions from biomass burning contribute a relatively insignificant fraction to the total aerosol loading of the major transport plume that transports materials out of the subcontinental sector to the Indian Ocean. The industrial Highveld region accounts for approximately 90% of South Africa's scheduled emissions of particulate matter, SO_2 and NO_x.[7]

The most distinguishing characteristics of PM are the particle size and the chemical composition. Particle size has the greatest influence on the behaviour of PM in the atmosphere with smaller particles tending to have longer residence times than larger ones. Particle matter is categorised according to particle size into total suspended particulates (TSP), PM_{10} and $PM_{2.5}$. The subscripts denote the size size of the PM (in μm), in which 90% of the particles are smaller or equal to that size.[7] Figure 4.1 shows the yearly average of PM in the atmosphere in the Highveld area from 1994-2012 as measured by the National Ambient Air Quality Standards authority (NAAQS).

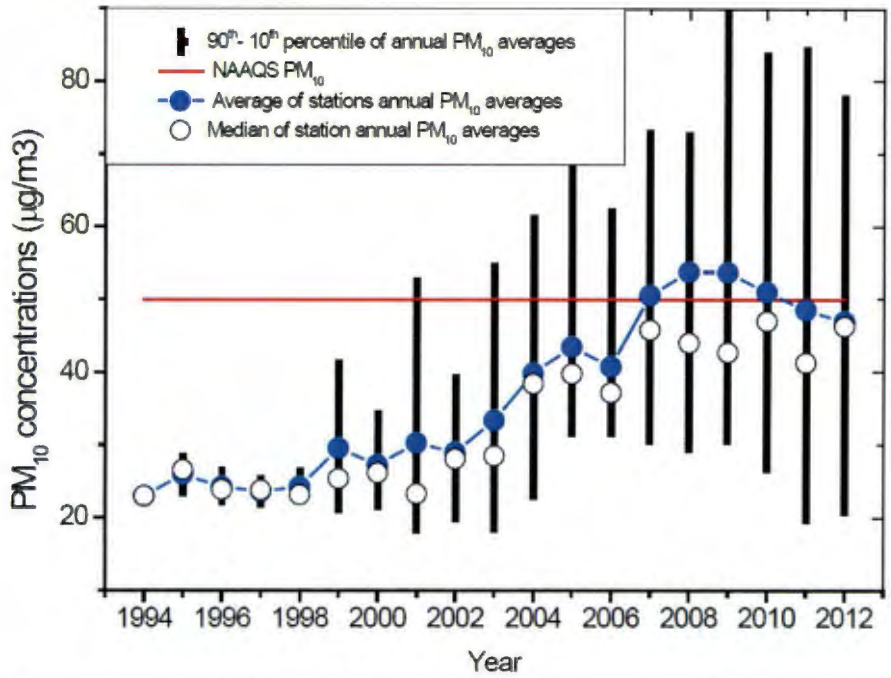

Figure 4.1: Yearly average of PM in the atmosphere in the Highveld area from 1994-2012.[7]

An alarming increase in PM is seen from 1996-2012 in the Highveld priority area. Although the current levels are below the NAAQS standard for human helth, the impact on vegetation has been shown to be significant.[7]

4.1.2 Engineered nanomaterials (ENMs)

Anthropogenic emissions are not the only source of PM entering the biosphere. Nanotechnology refers to the manipulation of materials at the nanoscale. The possibilities of this research field were envisioned by Richard Feynman in a famous talk in 1959. Later, between 1981 and 1992 the term nanotechnology was popularized and the scanning tunnelling microscope and the atomic force microscope became well established, leading to the research field we know today.[6,30] Yet the field of nanotechnology continues to grow with increased application of nanomaterials in consumer products. The main reason that materials at the nano-scale are of specific interest, are the changes in physical and chemical properties, which are different at the nano-scale compared to the bulk material. These changes are mostly related to the increase in surface area to volume ratio, resulting in changes in physico-chemical properties related to color, solubility, conductivity and catalytic activity of engineered nanomaterials (ENMs).[2,7] Increasing quantities of materials of this small size are being produced. Although nanomaterials have many benefits, the implications of large quantities of these types of materials entering the environment is not yet fully understood.[2,3] While this is generally the case when novel chemicals are developed, the question remains whether current guidelines for risk assessment of novel chemicals, such as implemented in the registration, evaluation, authorisation and

restriction of chemical substances are adequate for ENMs.[7] Risk assessment of chemicals is based on both exposure and effect assessment. The exposure assessment is based on a good understanding of the environmental behavior of chemicals combined with quantification of the fate processes by making use of modeling tools. Using such tools, the predicted exposure concentrations are estimated from the physico-chemical characteristics of the aquatic system and chemical in question. Nanoparticles are characterised as a particle with at least one dimension less than 100 nm in diameter.[2] Engineered nanomaterials have been explored for applications in various industries including catalysis, pharmacology, electronics, lubricants and cosmetics. Because of the unique characteristics of ENMs (physical and chemical), special care should be taken that these nanoparticles do not end up in ecosystems because of the potential risk of ecotoxic reactions. Although extensive research has been done in recent years with numerous reviews published on the ecotoxic implications of engineered nanoparticles, little is known about the mechanisms of this induced toxicology.[2,3]

4.1.3 Engineered nanomaterials stability in the environment

Nanomaterials can stay in solid particle form and aggregate together or even attach themselves to natural surfaces like colloids, which then sediments, only to be suspended again if enough turbulace is experienced.[6] Furthermore, depending on the solubility of the type of particle, it can also dissolve under natural conditions. The chemical composition of ENMs, specifically at the interface between the solid and liquid phase, is the basis for dissolution behavior.[6] Carbon ENMs are generally considered to be insoluble in water. However, in some cases the individual carbon particles in the water phase can be considered as dissolved, e.g. derivatized C_{60} or nano-crystals of C_{60} in water (termed nC_{60}). On the other hand, metal oxide ENMs show a great range in degree of solubility. Metal oxide nanoparticles like TiO_2 and SiO_2 are practically insoluble, whereas ZnO, CuO and Al_2O_3 can dissolve under natural conditions. Although not much is known about the dissolution kinetics of metal nanoparticles, several metals are known to dissolve to some extent.[3,6]

4.1.4 Engineered nanomaterials concentration models

Gottschalk *et* al., 2009 calculated environmental concentrations of NPs based on a probabilistic material flow analysis from a life-cycle perspective of ENMs containing products.[9] They found the simulated models ranged from 0.003 $ng.L^{-1}$ (fullerenes) to 21 $ng.L^{-1}$ (nano-TiO_2) for surface waters, and from 4 $ng.L^{-1}$ (fullerenes) to 4 $\mu g.L^{-1}$ (nano-TiO_2) for sewage treatment effluents. In addition, Mueller and Nowack used a life-cycle perspective to model the quantities of three NPs in the environment; nano-Ag, nano-TiO_2 and CNT.[10] They use variables such as estimated worldwide production volume, location, particle release and flow coefficient. They found that only in the case of TiO_2 the expected concentration in water (70-160 $\mu g.L^{-1}$) was close to or higher than the predicted

inhibitory concentration (<100 $\mu g.L^{-1}$).[10] This suggests that more detailed studies are required to predict the effects of TiO_2 in the environment. So far, most of the studies on fate and transport of NPs in terrestrial ecosystems lead to the conclusion that increased entry into the soil of engineered and anthropogenic NPs raises concern about the impact it will have once it reaches sufficient concentrations to cause harm to plants and other organisms. For the purpose of this study, only the impact of ENMs on plants will shortly be discussedin Section 4.1.7.

4.1.5 Factors determining the toxicology of engineered nanomaterials

Ecotoxicological tests were mostly developed for aquatic test organisms and water-soluble chemical compounds. Thus, aquatic toxicity testing of nanoparticles (NPs) is definitely a challenge. However, whatever the apparent route of exposure and the mechanisms of toxicity, bioavailability remains a key factor for the hazard evaluation of synthetic NPs. Bioavailability is a dynamic concept that considers physical, chemical and biological processes of contaminant exposure and dose.[8] Bioavailability incorporates concepts of environmental chemistry and ecotoxicology, integrating contaminant concentration, fate, and an organism's behavior in the given environment.[7,8] Bioavailability of NPs depends on the: (i) physicochemical properties of the particles (aggregation, solubility), (ii) on nanoparticle-organism contact environment, but also (iii) on the target organism (particle-ingesting or not). Thus, environmental risk assessment of synthetic NPs requires thorough characterization of NPs before, during and after exposure. Many methods still need development and optimization, especially for new types of NPs, but extensive experience can be gained from environmental chemistry.[8]

4.1.6 Uptake of engineered nanomaterials by plants

One of the major research gaps on the uptake mechanism of nanomaterials towards plants is the absence of consistent and broadly applicable information.[9] Most information revealed that ENMs could adhere to plant roots and exert chemical or physical uptake upon plants.[11] Recently, there are an increasing number of publications emerging on the interaction of ENMs with plants.[10,11] The uptake, accumulation and build-up of nanoparticles vary, and these factors largely depend on the type, size and the composition of the plant. Indeed, the verification on the uptake mechanism of ENMs is limited and is focused on stock solutions rather than the actual concentration. The stock solution is prepared either from a series of dilution or media renewable periods. As such, most methods being reported might not produce similar results for different shapes, sizes and forms of nanomaterials. NPs are adsorbed to plant surfaces and taken up through natural nano- or micrometer-scale plant openings.[11,34] Several pathways exist or are predicted for NP association and uptake in plants and are shown below. The aboveground surface of plant shoots usually exceeds ground area and facilitates the deposition of airborne NPs on plant shoot surfaces. NP uptake into the plant body can use different

paths. Uptake rates will depend on the size and surface properties of the NPs. The outer surfaces of leaves, fruits and epidermal cells are mostly covered by cuticle. Very small and lipophilic NPs can be incorporated into apolar fluid areas of the cuticle, which contains apolar and polar pathways for uptake. Permeation properties differ between cuticles on the epidermal cells and trichomes or stomata. Physical and, thus, biomechanical properties of the cuticle also change with temperature. The physical interaction and penetration of NPs into the cuticle have not been analyzed. Larger NPs can penetrate through cuticle-free areas, such as hydathodes, the stigma of flowers and stomates.[34] Apertures of opened stomates reach values of 10 μm in diameter in mesophytic plants, such as *Vicia faba* leaves exposed to high light. Penetration of NPs into leaves via stomates is therefore a real possibility. Most primary roots that develop in soil have a suberinized exodermis as well as a suberinized endodermis. The exodermis prevents apoplastic bypass flow of solutes and water from the soil to the central cylinder. However, in the more basal root zone of lateral root development, the newly formed lateral roots break through the cortex and apoplastic bypass is rendered possible.[34] Thus, at the site of lateral root formation, NPs could enter the xylem via the cortex and the central cylinder. Several avenues for the uptake of nanomaterials by plant cells are proposed. Some of the data suggested that the nanomaterials could enter plant cells by being bound to a carrier protein, through aquaporin, ion channels, or endocytosis via the creation of new pores and entry by being bound to organic chemicals.[10] This phenomenon is preferred in the case of carbon nanotubes rather than other types of nanomaterials.[9,11,34] Meanwhile, the greater surface area-to-mass ratio of the nanoparticle compared to the bulk metals, induces higher reactivities compared to the surroundings. Consequently, the nanomaterials may form complexes with membrane transporters or root exudates before being transported into the plants. Most metal based nanomaterials that have been reported as being taken up by plants include elements for which ion transporters have been identified. Once the nanomaterials enter the plant cells, it may be transported either apoplastically or symplastically from one cell to another via plasmodesmata.[11] However, the relation between the selectivity of the uptake of nanomaterial and the type of plant remains unknown and is open to exploration. Some studies suggested that the gradual increase in ENM uptake was observed with a reduction in granule size.[9-11] Figure 4.2 shows some reported ENMs routes of entry into plants.

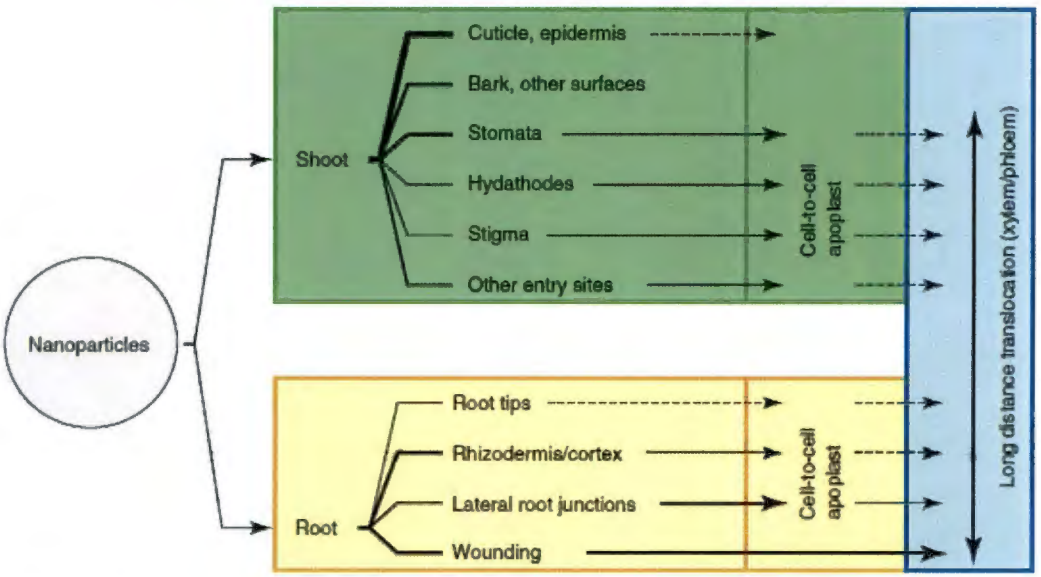

Figure 4.2: Suggested and reported routes of entry of nanoparticles into plants.[34]

4.1.7 Toxicity of engineered nanomaterials on plants

Phytotoxicity studies using higher plants are an important criterion for understanding the toxicity of ENMs. The vast majority of research dedicated to the potential toxicity of ENMs to plants, where negative, positive or inconsequential effects have been reported.[7,8,9] The majority of the reports available in the literature indicate the phytotoxicity of ENMs.[9,10] As the size of the particles decreases, its surface area increases, allowing a greater proportion of its atoms or molecules to be displayed on the surface rather than the interior of the ENMs.[9] The increase of surface area determines the potential number of reactive groups on the particles' surface. The change in the structural and physicochemical properties of ENMs, with a decrease in size, could be responsible for a number of material interactions that could result in toxicological effects. Figure 4.3 shows some of the key reported toxicological nanoparticle plant interactions.

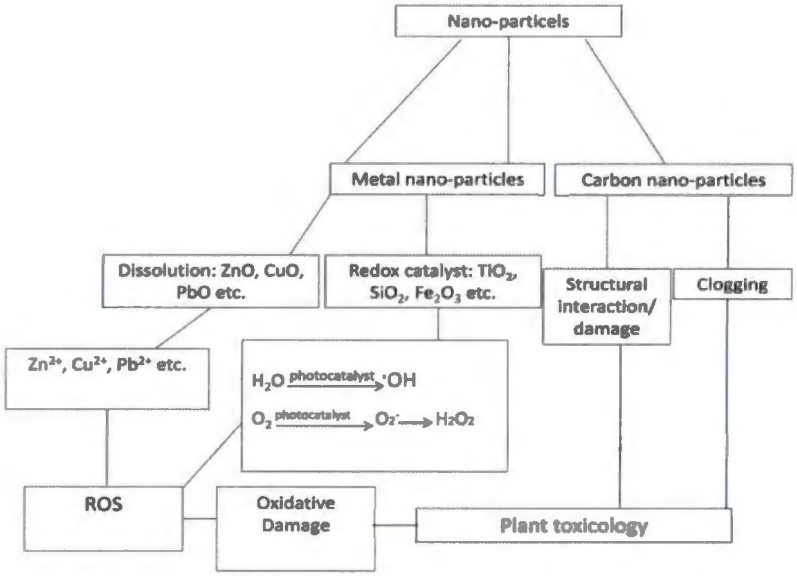

Figure 4.3: Schematic diagram showing the key reported nanoparticle interactions leading to plant toxicology.[34]

4.1.8 Effect of engineered nanomaterials on photosynthesis

One of the most sensitive processes to environmental stressors in nature is the process of photosynthesis. Photosynthesis has been shown to be extremely sensitive to all kinds of abiotic stressors, which include drought, salinity, sub-optimal temperatures, heavy metals and greenhouse gasses.[4] There is some literature on the effect of engineered nanoparticles on photosynthesis of higher plants, but the description of the exact limitations on photosynthesis remains vague and unclear.[7,9] Regardless of this fact, various studies have looked at a range of different nanoparticles which includes carbon-, metal- and metal oxide nanoparticles.[6,12] It was shown that the toxicity of nano-materials are dependent on its chemical and physical properties.[13] In previous studies, emphasis has been placed on the size, morphology and dissolution properties of such nanoparticles. The amount of cellular uptake has been shown to decrease with an increase in particle size. The smaller the particles, the greater the tendency to enter subcellular organelles based solely on their sizes.[15-17] Most research on nanoparticle toxicology has been done using metal NPs, which includes TiO_2, CeO_2, Fe_3O_4, ZnO, Au, Ag, Cu, and Fe, which is probably due to the many industrial activities in which these metal-type particles are produced (mining etc.).

One nanoparticle produced in high quantities is titanium dioxide (TiO_2). Titanium dioxide nanoparticles are widely used as food additives, drug delivery agents, personal care products, paints, plastics and cosmetics.[14] Nano-TiO_2 has excellent optical and biological properties and has recently caught the attention of plant physiologists.

Titanium dioxide is a well-known photocatalyst because of its relatively small band gap of 3.2 eV, which is capabale of producing highly reactive O_2^-, OH^- and H_2O_2 species under normal physiological pH and UV-light conditions, by donating an electron to molecular oxygen. Furthermore, TiO_2 can also mediate a water splitting reaction to form highly reactive hydroxyl radicals.[55] These species can all react with organic compounds to cause oxidative degradation of protein and membrane compounds. In Figure 4.4 the photocatalytic induced toxicologic mechanism of TiO_2 is shown.

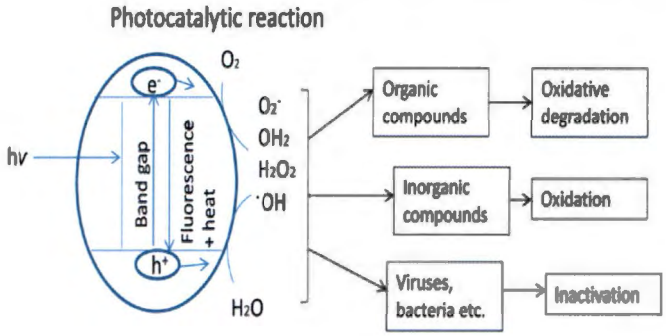

Figure 4.4: Photo-catalytic action of TiO_2 which can lead to ROS formation and subsequent interactions of these ROS with organic and inorganic compounds.[55]

Zheng *et al.*, 2005 reported that 2.5% rutile nano-TiO_2 promoted the germination of spinach seeds, whereas 0.25% rutile nano-TiO_2 was found to enhance spinach photosynthesis by promoting cyclic and linear photophosphorylation.[19] This promotion was suggested to be closely related to Mg^{2+}-ATPase activity.[20] Rutile nano-TiO_2 was suggested to positively affect spinach by protecting the chloroplast membrane structure from reactive oxygen species, thus increasing the activity of antioxidant enzymes such as SOD, CAT and peroxidase (POD).[21] Gao *et al.*, 2006 reported that nano-anatase TiO_2 can enhance spinach Rubiso activase activity by significantly promoting the expression of Rubiso activase mRNA.[22] Key antioxidant enzyme reactions where these antioxidant enzymes play a critical role are shown in Figure 4.5.

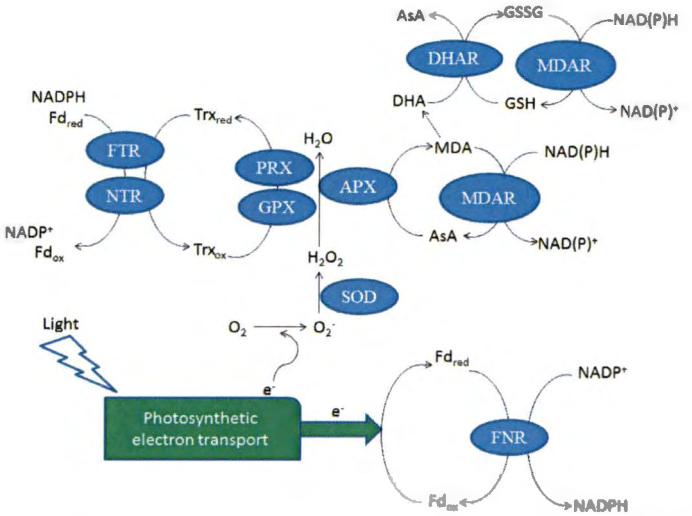

Figure 4.5: Scheme, showing the locations and mechanisms of key detoxifying enzymes.[55]

Whilst such up-regulation of photosynthesis was reported by these authors, other *in vivo* studies have shown that TiO_2 imposed significant toxic effects on various plant species. A study by Wang *et al.*, 2010 found that nano-TiO_2 exerted toxic effects by inducing an increase in the lipid peroxidation product, malondialdehyde (MDA).[23] X-ray fluorescence micro-spectroscopy showed that nano-TiO_2 can attach to the *Vicia faba* root surface in 48 h, thus resulting in the inhibition of plant growth.[24] Nano-TiO_2 particles were found to only penetrate wheat roots below a threshold diameter size of 36 nm.[25,26] Li *et al.*, 2012 found that the effect of nano-TiO_2 on *Gymnodinium breve* was more significant, as was shown by the LC50 (median lethal concentration) of 9.7 $mg.L^{-1}$ in 72 h.[27] In their study the activities of superoxide dismutase (SOD), catalase (CAT) and MDA reached their maximum after 12 h, whereas that of the hydroxyl radical (OH^-) significantly increased after 48 h. The disruption of the free radical and antioxidant system was suggested as the mechanism of growth suppression in *G. breve*.[23] Gao *et al.*, 2013 showed significant inhibiting effects of TiO_2 on *Ulmus elongata* seedlings, with regard to electron transport and photosynthetic gas exchange parameters.[28]

Another nanoparticle produced in high quantities is silica dioxide (SiO_2). Siilicon dioxide is mostly used in electronic and medical applications. Akhtar *et al.*, 2010 reported that silica nanoparticles induced cytotoxicity and resultant oxidative stress in a dose dependent manner, mediated by the induction of reactive oxygen species (ROS) and lipid peroxidation in the cell membrane in mammalian cells.[29] However, several authors have reported on the improvement in drought and salinity tolerance of higher plants with nano-SiO_2 treatment, which has mostly been attributed to decreased transpiration because of a decrease in stomatal conductance.[31-33]

Although reported data on the effect of different nanoparticles on different plant species are often conflicting, most authors agree that any cytotoxic effects are a result of the formation of ROS induced

damage. In Figure 4.3, the key reported reactions that produce ROS induced cytotoxic effects on plants are shown. The aim of this study was to evaluate the effect of different concentrations of nano-TiO_2 and nano-SiO_2 with respect to popular ROS markers (H_2O_2 and MDA concentration), key antioxidant activities, photosynthetic gas exchange and photosynthetic electron transport in a South African maize cultivar (IMP 52-11). Photosynthetic gas exchange and photosynthetic electron transport was monitored using an infrared gas analysis system and chlorophyll *a* fluorescence induction kinetics, respectively.

4.2 Materials and Methods

4.2.1 Plant cultivation and treatments

In early December 2013, 35 (12 L in volume) pots were filled with sterilized soil and two seeds of a popular South African hybrid maize cultivar (IMP 52-11, Agricol) were planted in each pot. The pots were arranged in a completely randomized block design within a greenhouse with a day/night temperature of 26/17 °C. The location of the experiment was Potchefstroom, North-West Province, South Africa. (S26°41.033' E27°06.237') The pots were well watered every second day. Every 3 weeks, 500 mL of a nutrient solution was given to each pot. The nutrient solution contained the following nutrients: macronutrients (in mM): 1.25 KNO_3, 1 $Ca(NO3)_2$, 0.25 $(NH_4)H_2PO_4$, 0.5 $MgSO_4$, 0.1 KCl, & micronutrients (in µM): 15 H_3BO_3, 0.065 $Na_2MoO_4.2H_2O$, 20 Fe-EDTA, 5 $MnSO_4$, 2 $CuSO_4$ and 5 $ZnSO_4$. After four weeks, each maize plant was foliarly sprayed until runoff with 250 mL of pre-determined concentrations of TiO_2 and SiO_2 nanoparticle containing spray solutions (see Table 4.1). The TiO_2 (rutile, D_{90} of 21 nm) was procured from Merck (Germany), whilst the SiO_2 (fumed silica, D_{90} of 13 nm) was procured from Evonik chemical company (Germany). The nanoparticles were used without any further modification. The respective spray solution concentrations were made up using deionized water with the addition of a fixed amount of surfactant (Tween 20), which was added to reduce the surface tension between the leaf surface and solution droplets, ensuring higher nanoparticle absorption. The control plants were sprayed with deionized water containing only the surfactant.

Table 4.1: Treatments and concentrations of TiO_2 and SiO_2 nanoparticle solutions.

Treatment	SiO_2 concentration (mass %)	TiO_2 concentration (mass %)	Replicates
Control	0	0	5
1	0.05	0	5
2	0.5	0	5
3	2	0	5
4	0	0.05	5
5	0	0.5	5
6	0	2	5

4.2.2 Photosynthetic gas exchange

Four weeks after the spray treatment, leaf photosynthetic gas exchange was measured under varying leaf surface concentrations of CO_2 (0, 25, 50 75, 100, 200, 350, 500, 750, 1000, 1250 and 1500 ppm), using a portable infrared gas exchange analyser (IRGA) system (CIRAS-2, PP-systems, Hitchin, UK). The gas exchange measurements were used to plot the net CO_2-assimilation rate (A) versus intercellular CO_2 concentration (C_i) (A:C_i curves) and these curves were analysed according to the C_4-plant model of Von Caemmerer and Furbank 1999, which is a derivation of the original model by Farquhar and Sharkey 1982 for C_3-plants.[35,36] The C_4-plant model of Von Caemmerer and Furbank 1999 was used to estimate the maximal rate of phosphoenolpyruvate carboxylase (PEPc) activity, V_{pmax}. The same model was used to estimate J_{max}, which can be related to the regeneration rate of PEPc (C_4 plants) and maximal electron transport rate.[34] These parameters were fitted to determine the photosynthetic response to the various concentrations of nano-TiO_2 and nano-SiO_2. Values of C_i were estimated from stomatal conductance to CO_2 transfer, g_s, and the ambient CO_2 concentration external to the leaf, C_a. The stomatal conductance (g_s) was also plotted against C_i, which was used to assess the stomatal response to different treatments nano-TiO_2 and nano-SiO_2. The water use efficiency (WUE) of the plants was calculated (at 360 ppm CO_2) through the assimilation (A) and transpiration (E) data, using the well-known equation of: WUE = A/E.[37]

4.2.3 Chlorophyll *a* fluorescence and Modulated 820 nm reflection

The fast kinetics chlorophyll *a* fluorescence was measured after 1 hour dark adaptation of the test plants, using a multichannel multifunctional plant efficiency analyser (M-PEA, Hansatech, UK). Dark-adapted leaves were illuminated with a 1 s pulse of continuous red light (627 nm, 5000 µmol photons $m^{-2}s^{-1}$) during which chlorophyll *a* fluorescence (prompt fluorescence – PF) and modulated 820 nm reflection (MR) were recorded. The PF is used to monitor the redox reactions around

photosystem II (PSII) whilst modulated 820 nm reflection has been shown to be related to the redox state of PSI and plastocyanin (PC).[37] From the reflected MR signal, the ratio MR_t/MR_0, where MR_t indicates the modulated 820 nm reflection intensity at time t, and MR_0 the value of the 820 nm reflection of the sample at the onset of the actinic illumination, was calculated. The MR_t/MR_0 ratio is descriptive of the redox state of P700 and PC.[53,54] The first part of the curve is representative of the oxidation reactions around P700 and PC (slow phase), after which a steady state is reached in the second part of the curve (minimal MR_t/MR_0). At this point, the oxidation rate of P700 and PC is equal to the re-reduction rate of $P700^+$ and PC^+ (from electrons arriving from PSII). The global minima at the steady state are termed MR_{min}.[38] The point in time where MR_{min} occurs is in the range of the J-I phase of PF. The last part of the curve reflects a change in the difference in PSII electron arrival rate (fast phase) and the rate at which oxidized PSI electron carriers can accept these arriving electrons (slow phase).[52,53] During the actinic illumination, the same data points (at characteristic time intervals) on the transients were extracted (as in Chapter 2 and Chapter 3) and used for the calculation of several parameters using equations i-xi in Chapter 1. F_o was chosen as 30 µs. Furthermore, the JIP-parameters describing the structure and functionality of PSII were calculated using the formulae shown in Table 1.5. Variable fluorescence and fractions of the relative (relative to control) in variable fluorescence phases (ΔV_{LK}, ΔV_{Kn}, ΔV_{Jn}, ΔV_{In} and ΔV_{Hn}) were also constructed. The changes in relative variable fluorescence and fractions of the variable fluorescence phases are given to illustrate the change in these transients measured on plants grown under different types and nanoparticle concentrations. The validation of relative variable fluorescence phases and their differences (relatively to control samples which were normalized to zero) that form bands due to various normalizations, are described in detail by Strasser *et al.*, 2000.[39] The bands were revealed using the fragments of variable fluorescence phases of time segments, over four, two and one decades of time (Figures 4.10-4.13).

4.2.4 Determination of ROS markers

4.2.4.1 Hydrogen peroxide

Once all the measurements were taken (4 weeks after the treatments), the third and fourth youngest leaves were collected, vacuum sealed and frozen in a -80°C freezer for 48h. Thereafter, the foliar hydrogen peroxide content was estimated according to the method of Brennan and Frenkel 1977.[40] One hundred mg of chilled leaf tissue was macerated in 4 mL cold acetone and the homogenate was filtered through a Whatman No.1 filter paper. Two mL of this filtrate were treated with 1 mL of titanium reagent (20% titanium tetrachloride in concentrated HCl, 32% v/v) and 1 mL of concentrated ammonia solution to precipitate the titanium–hydroperoxide complex. After centrifugation (at 5000 × g for 30 min) the precipitate was dissolved in 2 N H_2SO_4 and the absorbance was obtained at 415 nm.

The H_2O_2 content was calculated from a standard curve prepared in a similar way and expressed as $\mu mol.g^{-1}fm$ (fm = fresh mass).

4.2.4.2 Malondialdehyde (MDA)

The malondialdehyde concentration was determined according to the procedure of Hodges *et al.*, 1999.[41] Frozen leaf tissue was homogenized in 80% cold ethanol and centrifuged to pellet debris. Different aliquots of the supernatant were mixed either with 20% tri-chloroacetic acid or with a mixture of 20% tri-chloroacetic acid (TCA) and 0.5% thio-barbituric acid (TBA). Both mixtures were allowed to react in a water bath at 90°C for 1h. Subsequently, the samples were cooled in an ice bath and centrifuged. Absorbance of the supernatant was determined at 440, 532 and 600 nm against a blank sample. Calculation of the MDA concentration was done using equations 1-3:

$$A = [(Abs\ 532nm_{+TBA/TCA\ sol}) - (Abs\ 600nm_{+TBA/TCA\ solution}) - (Abs\ 532nm_{-TBA/TCA\ sol} - Abs\ 600nm_{-TBA/TCA\ solution})] \quad (1)$$

$$B = [(Abs\ 440nm_{+TBA/TCA\ sol} - Abs\ 600nm_{+TBA/TCA\ sol}) \times 0.0571] \quad (2)$$

$$MDA\ concentration\ (nmol.g^{-1}fm) = (A-B/157000)106 \quad (3)$$

4.2.5 Extraction of antioxidant enzymes

Frozen (-80°C) leaf tissue (0.5g) was homogenized in 1.5 mL of a 50 mM potassium phosphate buffer (PBS, pH 7.8) containing 1 mM EDTA, 1mM di-thiotreitol (DTT) and 2% (w/v) poly-vinylpyrrolidone (PVP) using a chilled mortar and pestle kept on ice. The homogenate was centrifuged at 15,000 × g at 4°C for 30 min. The clear supernatant was used for superoxide dismutase, glutathione reductase, dehydro-ascorbate reductase and mono-dehydroascorbate reductase enzyme assays. For measuring ascorbate peroxidase activity, the tissue was separately ground in 50 mM PBS (pH 7.8) supplemented with 2.0 mM ascorbate, 1mM EDTA, 1 mM DTT and 2% (w/v) PVP. All assays were done at 25°C.

Soluble protein content was determined according to Bradford 1976 using BSA as standard.[42] The Bradford reagent was diluted 5 times with dH_2O and kept at 4°C. Twenty µL of the protein extract was mixed with 1 mL of the diluted Bradford reagent. The light absorption of blue color that formed was spectrofotometrically measured at 595 nm. A serial dilution series of 0.1-1 $mg.mL^{-1}$ of the BSA standard was made up in the PBS buffer. The absorption of the BSA dilution series was used to create a standard curve of known protein content, which was thereafter used to elucidate the unknown

protein concentration in the samples. The All spectrophotometric analyses were conducted using an UV/VIS spectrophotometer-Genesis 10 S UV–vis (Thermo Scientific).

4.2.5.1 Ascorbate peroxidase (APX)

Ascorbate peroxidase activity was assayed according to the method of Nakano and Asada 1981.[43] This was done by taking 3 mL of a reaction mixture (described above) containing 50 mM potassium phosphate buffer (pH 7.0), 0.1 mM EDTA, 0.5 mM ascorbate, 0.1 mM H_2O_2 and 0.1 ml enzyme extract and following the hydrogen peroxide-dependent oxidation of ascorbate by measuring the decrease in the absorbance at 290 nm (ε = 2.8 mM^{-1} cm^{-1}). Ascorbate peroxidase activity was expressed as µmol ascorbate oxidized.min^{-1}.mg^{-1} protein.

4.2.6 Antioxidant enzyme essays

4.2.6.1 Superoxide dismutase (SOD)

Superoxide dismutase activity was determined by the nitro blue tetrazolium (NBT) photochemical assay according to Beyer and Fridovich 1987.[44] One mL of solution containing 50 mM potassium phosphate buffer (pH 7.8), 9.9 mM l-methionine, 57 µM NBT, 0.025 % triton-X-100 was added into small glass tubes followed by 20 µL of the sample. The reaction was started by adding 10 µL of riboflavin solution (4.4 mg/100 mL) followed by incubating the tubes in an aluminium foil-lined box having two 20-W fluorescent lamps (12 cm distance between sample and light source) for 15 min. A parallel control (blank 1) was run where a phosphate buffer was used instead of the sample. After illumination, the absorbance of the solution was measured at 560 nm. A complete reaction mixture that had not been exposed to light was used as blank 2. The SOD activity was expressed as U.mg^{-1} protein. One unit of SOD was equal to that amount which caused a 50% decrease of SOD-inhibitable NBT reduction. The calculation of the SOD activity was done as follows:

% inhibition = ($Abs_{control}$-Abs_{sample}) / Absorbance control × 100 × df

Unit enzyme = 1 unit inhibit 50% reduction rate of NBT

SOD specific activity (mU.mg^{-1} protein) = Inhibition percentage (%) / V × [protein] × t

df = dilution factor, V = enzyme volume (mL), [protein] = protein concentration (mg.mL^{-1}), t = time (minutes).

4.2.6.2 Glutathione reductase (GR)

Glutathione reductase activity was determined by monitoring the glutathione dependant oxidation of NADPH, as described by Carlberg and Mannervik (1985).[45] In a 1 mL cuvette, 0.75 mL 0.2 M potassium phosphate buffer (pH 7) containing 2 mM EDTA, 75 µL NADPH (2 mM), 75 µL oxidized glutathione (20 mM) were mixed. The reaction was initiated by adding 0.1 mL of the enzyme extract to the cuvette and the decrease in absorbance at 340 nm was monitored for 2 min. GR activity was calculated using the extinction coefficient for NADPH of 6.2 $mM^{-1}.cm^{-1}$ and expressed as µmol NADPH oxidized min^{-1} mg^{-1} protein. The GR activity was calculated as follows:

$\varepsilon = 6.2\ mM^{-1}cm^{-1}$ and pathlength = 1 cm;

Then:

µmol NADPH oxidized min^{-1} mg^{-1} protein = $(Abs_{340}.min^{-1})/\varepsilon$,

4.2.7 Statistical analysis

The experiments were arranged in a completely randomised block design with 5 replicates for each treatment and 5 replicates for the control treatment. Statistical variance analysis was done using one-way ANOVA ($p \leq 0.05$) with least significant differences (LSD) at the 5% level.

4.3 Results

4.3.1 Photosynthetic gas exchange

4.3.1.1 Mesophyll limitation

Using the model of Farquhar *et al.*, 1982, the maximal carboxylation rate of PEPc, V_{pmax}, can be approximated by the slope of the linear part of the assimilation versus internal CO_2 ($A:C_i$) plots (Figure 4.6 A & B).[35]

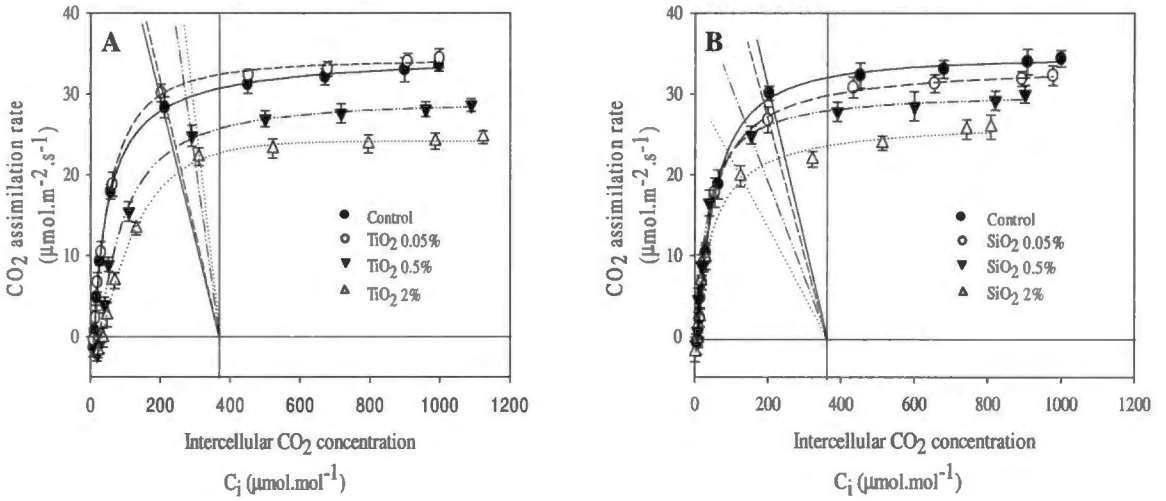

Figure 4.6 A & B: A:C_i curves of the net CO_2-assimilation rate (A) versus intercellular CO_2 concentration (C_i) for various nano-TiO_2 (Figure 4.6 A) and nano-SiO_2 (Figure 4.6 B) treatments for *Zea mays L.* The supply function was drawn by simply joining the value of $C_i - C_a$ at 360 ppm on the abscissa to the point giving A_{360} at this value of C_a (Pammenter 1989).[45] ($CE = V_{pmax}$)

Supply function: $A = g_s(C_a - C_i)$

Demand function: $A = V_{pmax}(C_i - \Gamma)$

The results showing the change in V_{pmax} with varying nano-TiO_2 and nano-SiO_2 concentrations relative to the control, obtained from the A:C_i curves (using the model of Von Caemmerer and Furbank 1999 in Figure 4.6 A & B)[35], are given in Figures 4.7 A & B respectively. In Figure 4.7 A, a slight increase of 8.5% (relative to control) in the V_{pmax} was seen at the 0.05% nano-TiO_2 treatment, although this increase was not statistically significant. At higher TiO_2 concentrations, significant ($p \leq 0.05$) reductions of 22% and 41% in V_{pmax} was seen for the 0.5% and 2% nano-TiO_2 treatments, respectively, which is indicative of some kind of toxicity threshold (Figure 4.7 A). As seen from the data in Figure 4.7 B, only the 2% nano-SiO_2 treatment caused a significant decrease of 29% in V_{pmax}. The results suggest a differential sensitivity of PEPc with regard to nano-TiO_2 and nano-SiO_2.

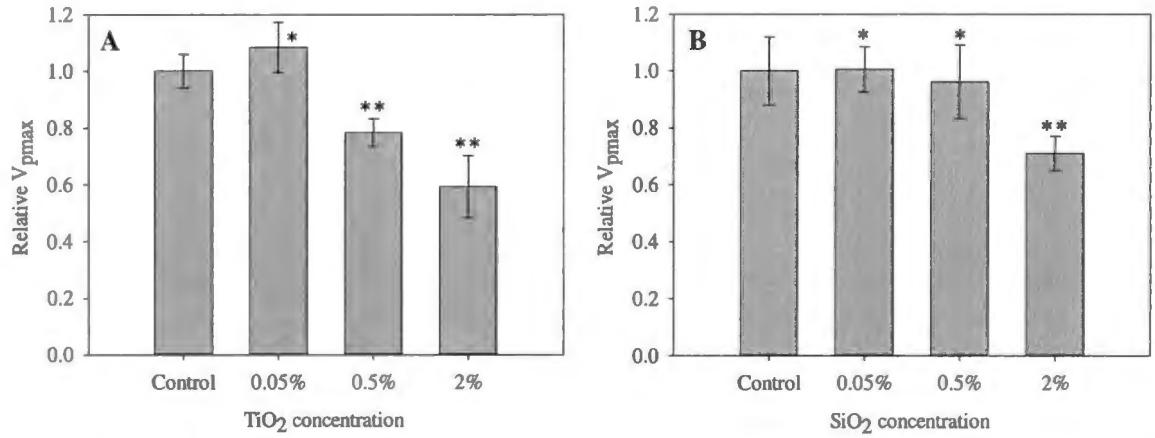

Figure 4.7 A & B: Relative PEPc activity under varying nano-TiO_2 (A) and nano-SiO_2 (B) concentrations. Significance relative to control was determined by a one way anova at $p \leq 0.05$; LSD = 0.21. Data marked with '*' indicates non-significant and '**' indicates significant changes relative to control.

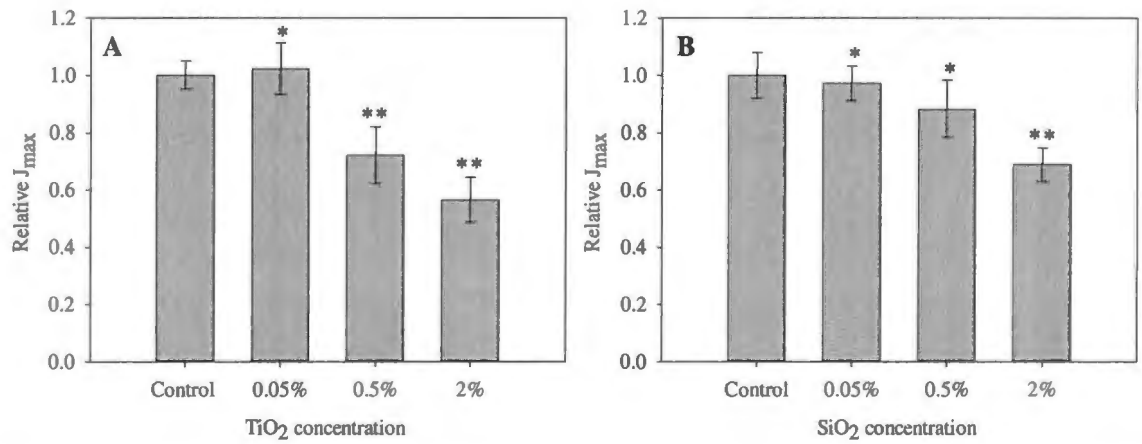

Figure 4.8 A & B: Relative maximal rate of PEPc regeneration capacity and electron transport with varying nano-TiO_2 (A) and nano-SiO_2 (B) concentrations. Significance relative to control was determined by a one way anova at $p \leq 0.05$; LSD = 0.18. Data marked with '*' indicates non-significant and '**' indicates significant changes relative to control.

The model of Von Caemmerer and Furbank 1999 in Figure 4.6 A & B was also used to estimate the maximal rate of PEPc regeneration capacity and electron transport, J_{max} (as presented in Figure 4.8 A & B).[35] In this study, significant decreases of 28% and 44% in the relative J_{max} were seen at the 0.5% and 2% nano-TiO_2 treatments respectively. The highest nano-SiO_2 treatment also had an effect on J_{max} parameter, as a significant decrease of 34% in relative J_{max} was seen at 2% nano-SiO_2 treatment (Figure 4.8 B).

4.3.1.2 Stomatal limitation

In Figure 4.6 A, a marked increase in the slope of the supply function, $A = g_s(C_a - C_i)$, relative to control can be seen at the 0.5% and 2% nano-TiO_2 treatments, which is indicative of a decrease in stomatal limitation. On the other hand the 0.5% and 2% nano-SiO_2 treatments (Figure 4.6 B) showed a marked decrease in the slope of supply function, which suggests increased stomatal limitation. Moreover, given the normal physiological response of stomatal closure (conductance) under elevated internal CO_2 concentrations (C_i), the stomatal conductance data from the various measurements were plotted against C_i, for the respective treatments (Figure 4.9 A & B).

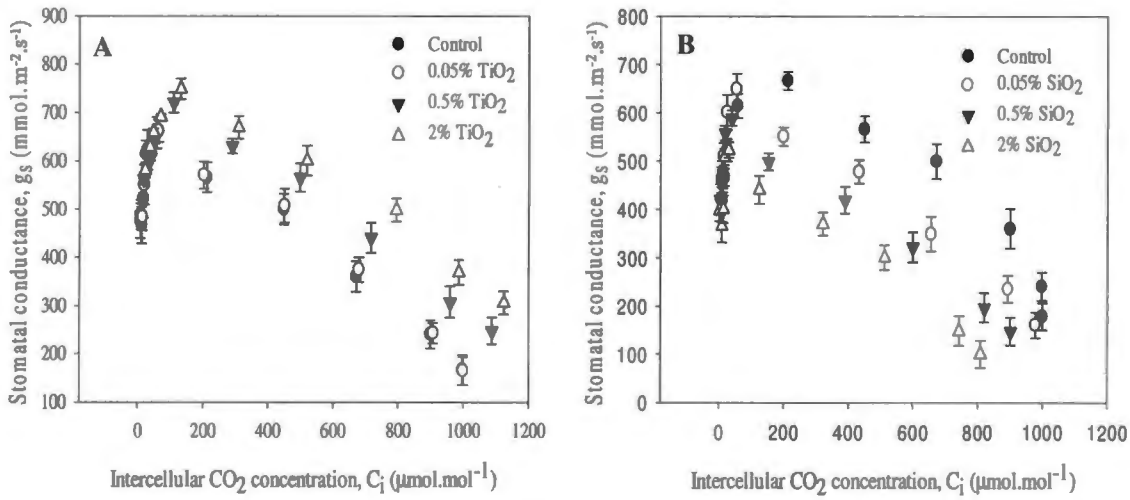

Figure 4.9 A & B: Change in stomatal conductance (g_s; $mmol.m^2.s^{-1}$) with change in C_i under nano-TiO_2 (A) and nano-SiO_2 (B) concentrations. Significance relative to control ($\frac{g_s treatment}{g_s control} X \frac{100}{1}$) was determined by a one way anova at $p \leq 0.05$ (LSD = 14.7).

Using the data from Figure 4.9 A & B, the change in the physical state and behaviour of the stomata under increasing nano-TiO_2 and nano-SiO_2 concentrations becomes apparent. A clear tendency of increased g_s with increasing nano-TiO_2 concentrations was evident (compared to control at all C_i concentrations), becoming significant ($p \leq 0.05$) at the 0.5% and 2% nano-TiO_2 treatments, with increases of 16% and 23%, respectively. This indicated increased stomatal opening (supported by increased transpiration (data not shown) and increases in C_i in the supply function). Inversely, significant ($p \leq 0.05$) decreases in g_s of 24% and 29% were seen at the 0.5% and 2% nano-SiO_2 treatments (compared to control at all C_i concentrations), which indicates decreased stomatal opening (supported by decreased transpiration (data not shown) and decreases in C_i in the supply function).

The well-known equation of $l = [(A_0 - A) / A_0] \times 100$ (Farqhuar and Sharkey 1982) was used to calculate the true stomatal limitation, where A is the assimilation rate at ambient atmospheric ($[CO_2]$

360 ppm) and A_0 is the assimilation rate when no stomatal limitation existed, i.e. C_a=C_i=360 ppm CO_2.[36] The data in Figure 4.6 A & B was used to calculate the stomatal limitation (please refer to Figure 1.9 in Chapter 1 to see how A and A_0, that was used to calculate *l*, was obtained from Figure 4.6 A & B). Marked decreases (relative to control) of 20% and 21.8% in *l* could be seen for the 0.5% and 2% nano-TiO_2 treatments, whereas the 0.5% and 2% nano-SiO_2 showed an increase of 15% and 22% in *l*.

Furthermore, the observed changes in the calculated *l* values correlated well with the changes in g_s (Figure 4.9 A & B). This is to be expected; given that *l* is a function of the assimilation rate (A) and the assimilation rate is a function of stomatal conductance g_s ($A = g_s(C_a - C_i)$). The differences in the changes in stomatal parameters induced by nano-TiO_2 and nano-SiO_2 strongly suggest that the two types of nanoparticles have different influences on stomatal regulation.

4.3.1.3 Water use efficiency (WUE)

Significant ($p \leq 0.05$) decreases of 27% and 31% in the relative WUE were seen for the 0.5% and 2% nano-TiO_2 treatments (Figure 4.10 A), whereas the 0.5% nano-SiO_2 treatment showed a significant ($p \leq 0.05$) increase of 15% in relative WUE.

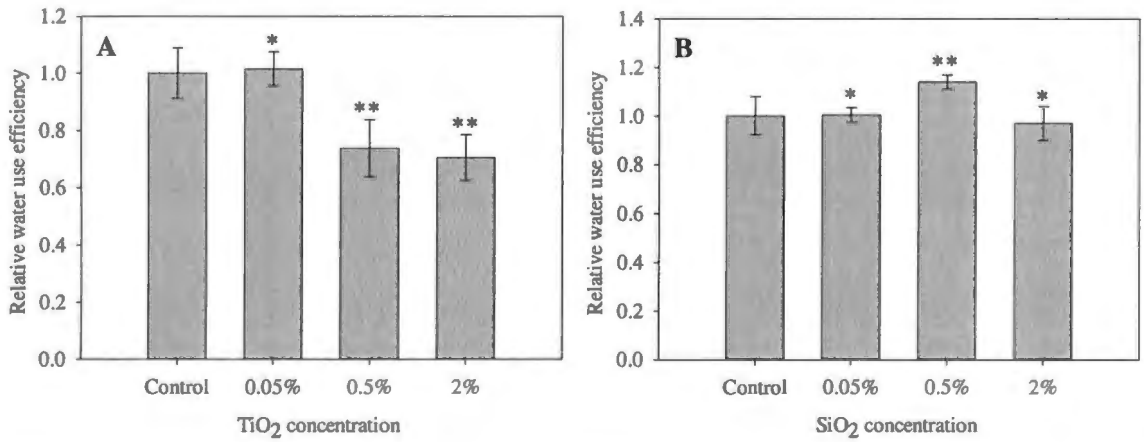

Figure 4.10 A & B: Relative change in water use efficiency (WUE) with varying nano-TiO_2 (A) and nano-SiO_2 (B) concentrations. Significance relative to control was determined by a one way anova at $p \leq 0.05$; LSD = 0.14. Data marked with '*' indicates non-significant and '**' indicates significant changes relative to control.

4.3.2 Chlorophyll *a* fluorescence and modulated 820 nm reflection

In the following sections the data obtained from the chlorophyll *a* fluorescence and modulated 820 nm reflection measurements are given and briefly discussed. Firstly, the 'raw' data curves of these two

distinct signals are shown in Figure 4.11 A & B. Various normalizations within particular time intervals (related to specific absorption and electron transport processes) of the chlorophyll *a* fluorescence curves are shown, in an attempt to illustrate the changes in the fluorescence signals, resulting from the various nano-TiO_2 (A) and nano-SiO_2 treatments (Figures 4.12-4.15). The changes in the JIP-parameters (relative to control), calculated using equations i-xi (Chapter 1), are shown in Table 4.2. Moreover, the changes in PSI activities, that were calculated and deduced from the modulated 820 nm reflection curves (Figure 4.11 A & B), are given in Table 4.3.

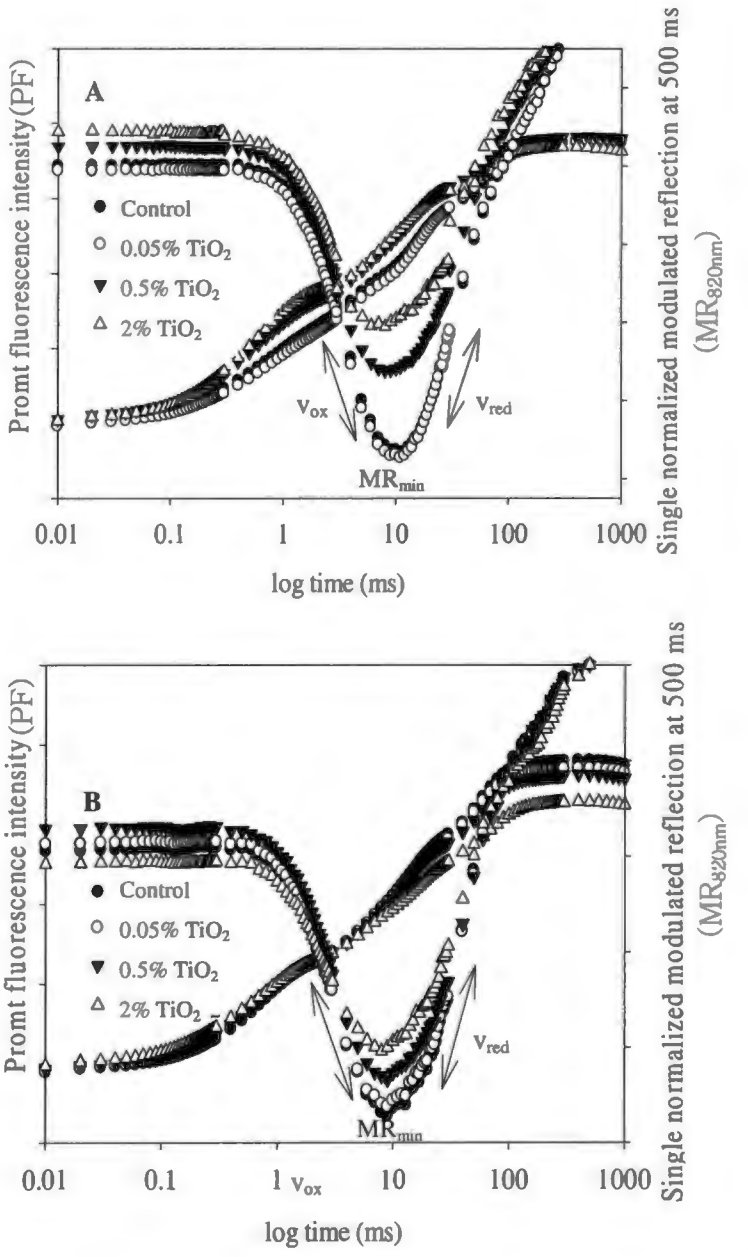

Figure 4.11 A & B: Change in fast kinetics chlorophyll a fluorescence (PF) and modulated 820 nm reflection ($MR_{820\,nm}$) with varying nano-TiO_2 (A) and nano-SiO_2 (B) concentrations.

4.3.2.1 Influence of varying nano-TiO_2 and nano-SiO_2 concentrations on apparent PSII activity

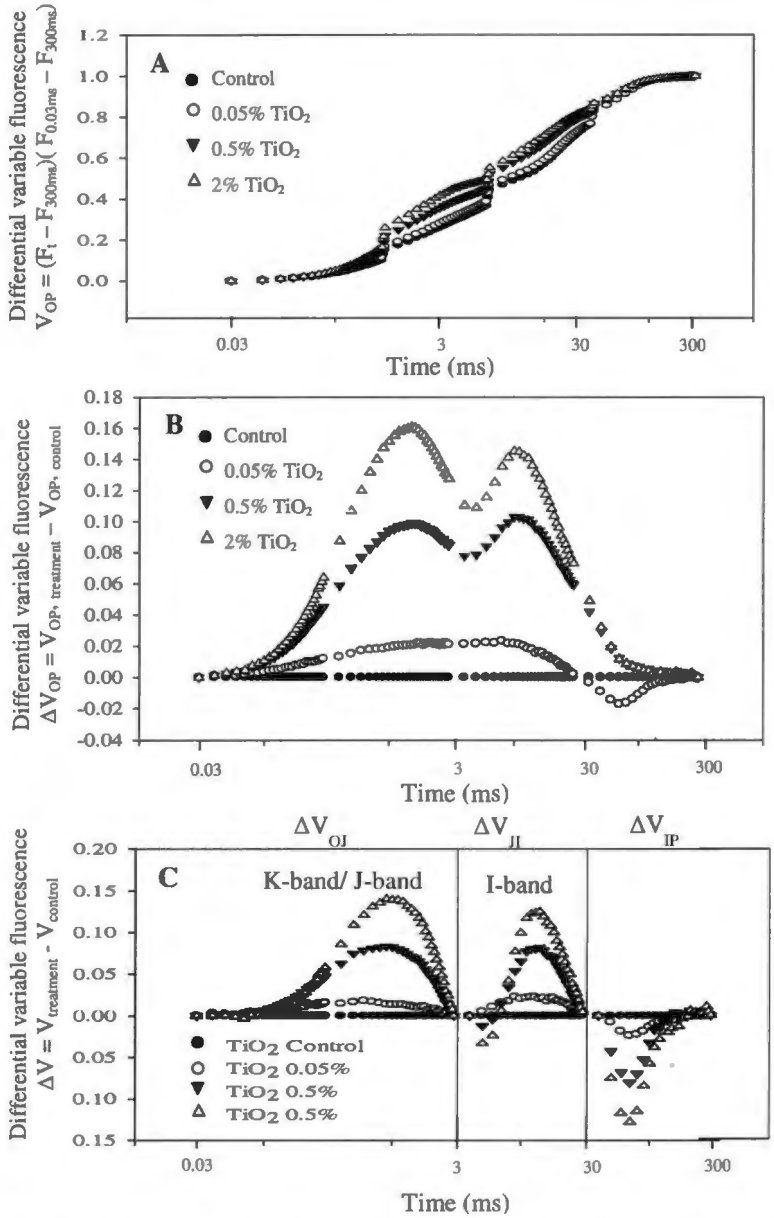

Figure 4.12 A-C: Normalisation between points O and P in PF transient, V_{OP} (Figure 4.12 A) for the different TiO_2 concentrations. Differential variable fluorescence normalized (normalized to control) between points O and P, ΔV_{OP} (Figure 4.12 B) for the different TiO_2 concentrations. Figure 4.12 A & B are both over 4 decades in time ($F_{0.03\ ms}$ to F_{300ms}). Differential normalizations between OJ, JI and IP in the PF transient are shown in Figure 4.12 C for the various TiO_2 concentrations. These are shown as a composite figure to illustrate the normalisations in 1 decade time progression ($F_{0.03\ ms}$ to $F_{3\ ms}$, $F_{3\ ms}$ to $F_{30\ ms}$ and $F_{30\ ms}$ to $F_{300\ ms}$).

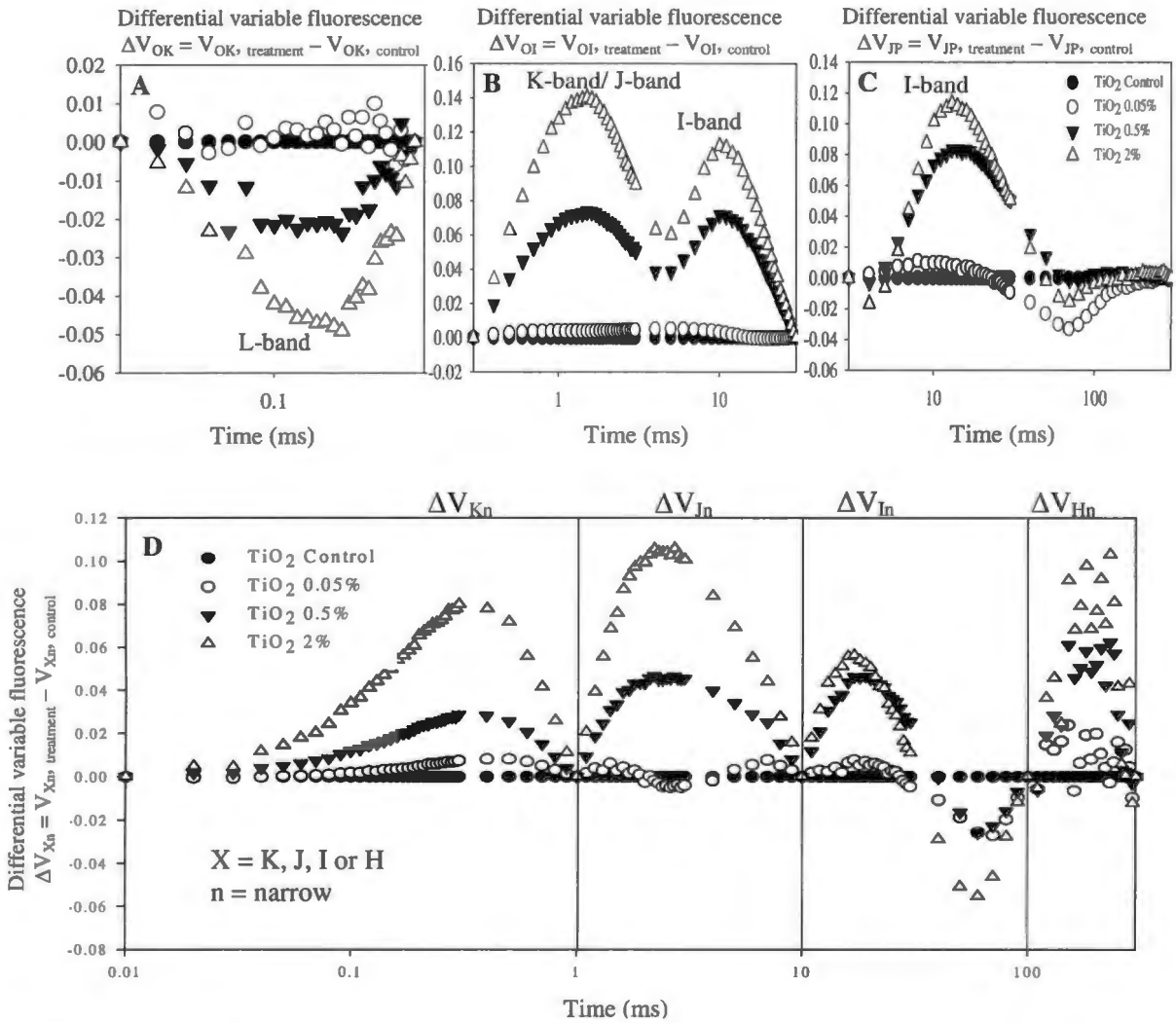

Figure 4.13 A-D: Differential variable fluorescence normalized between points OK, OI and JP (Figure 4.13 A-C) to show ΔV_{OK}, ΔV_{OI} and ΔV_{JP} for the various TiO_2 concentrations. Figure 4.13 A is over 1 decade in time ($F_{0.03\ ms}$ to $F_{0.3\ ms}$), whilst Figures 4.13 B & C are over 2 decades in time ($F_{0.03\ ms}$ to $F_{30\ ms}$ and $F_{3\ ms}$ to $F_{300\ ms}$). Differential normalizations between $F_{0.01\ ms}$ to $F_{1\ ms}$, $F_{1\ ms}$ to $F_{10\ ms}$, $F_{10\ ms}$ to $F_{100\ ms}$ and $F_{100\ ms}$ to $F_{300\ ms}$ in the PF transient are shown in Figure 4.13 D for the various TiO_2 concentrations. These are shown as a composite figure to illustrate the normalisations in a 1 decade time progression. Significance relative to control was determined by a one way anova at $p \leq 0.05$ (LSD = 0.023).

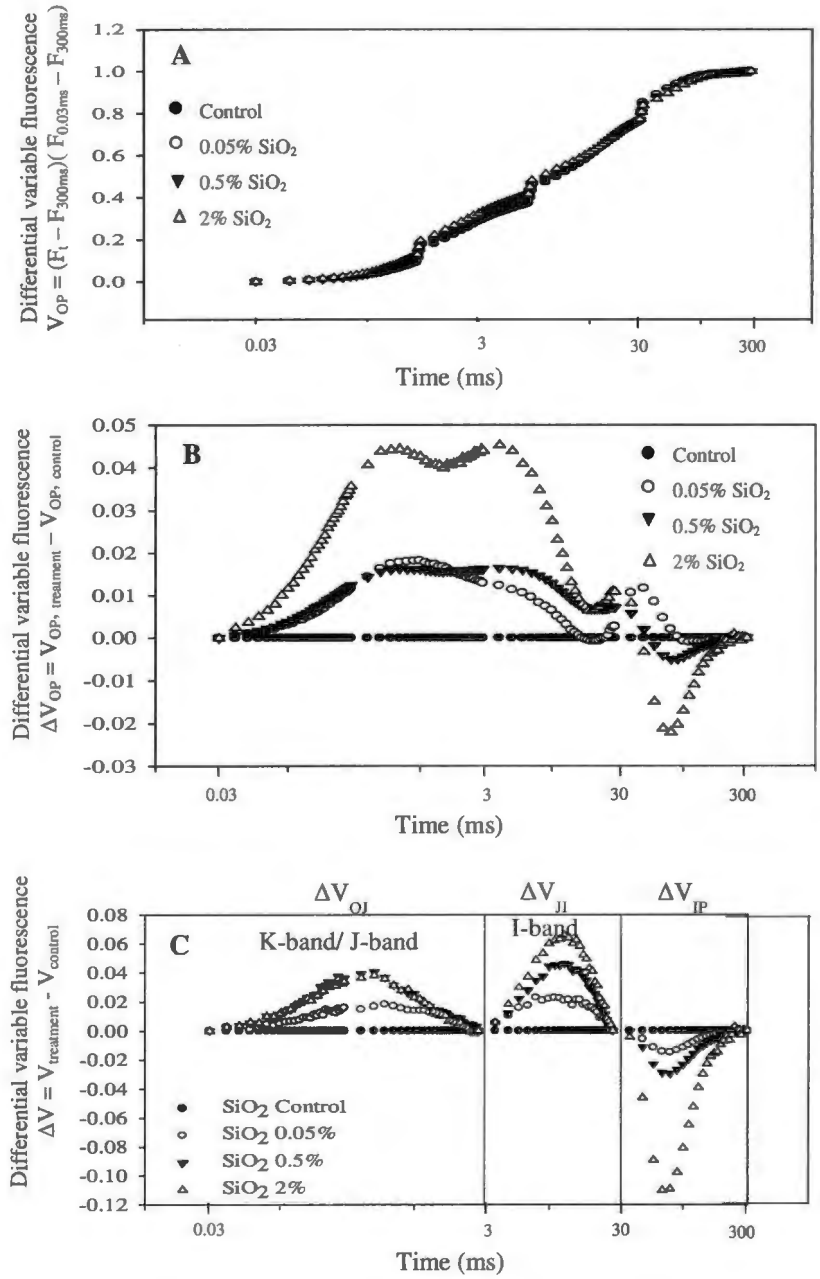

Figure 4.14 A-C: Normalisation between points O and P in PF transient, V_{OP} (Figure 4.14 A) for the different SiO_2 concentrations. Differential variable fluorescence normalized (normalized to control) between points O and P, ΔV_{OP} (Figure 4.14 B) for the different SiO_2 concentrations. Figure 4.14 A & B are both over 4 decades in time ($F_{0.03\ ms}$ to $F_{300\ ms}$). Differential normalizations between OJ, JI and IP in the PF transient are shown in Figure 4.14 C for the various SiO_2 concentrations. These are shown as a composite figure to illustrate the normalisations in 1 decade time progression ($F_{0.03\ ms}$ to $F_{3\ ms}$, $F_{3\ ms}$ to $F_{30\ ms}$ and $F_{30\ ms}$ to $F_{300\ ms}$)

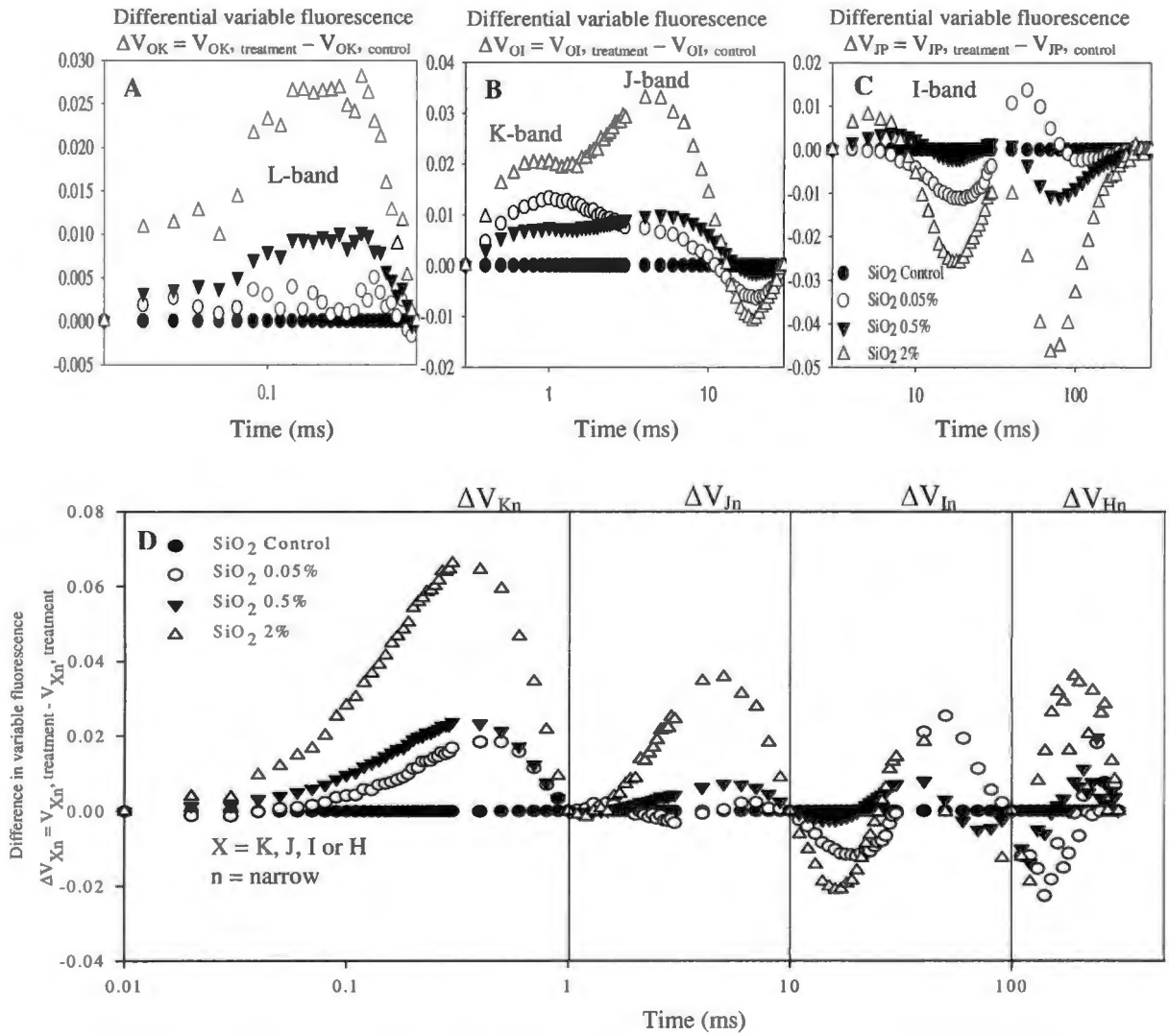

Figure 4.15 A-D: Differential variable fluorescence normalized between points OK, OI and JP (Figure 4.15 A-C) to show ΔV_{OK}, ΔV_{OI} and ΔV_{JP} for the various SiO_2 concentrations. Figure 4.15 A is over 1 decade in time ($F_{0.03\ ms}$ to $F_{0.3\ ms}$), whilst Figures 4.15 B & C are over 2 decades in time ($F_{0.03\ ms}$ to $F_{30\ ms}$ and $F_{3\ ms}$ to $F_{300\ ms}$). Differential normalizations between $F_{0.01\ ms}$ to $F_{1\ ms}$, $F_{1\ ms}$ to $F_{10\ ms}$, $F_{10\ ms}$ to $F_{100\ ms}$ and $F_{100\ ms}$ to $F_{300\ ms}$ in the PF transient are shown in Figure 4.15 D for the various SiO_2 concentrations. These are shown as a composite figure to illustrate the normalisations in 1 decade time progression. Significance relative to control was determined by a one way anova at $p \leq 0.05$ (LSD = 0.019).

Differential normalization ($\Delta V = \Delta V_{treatment} - \Delta V_{control}$) between the F_O (0.03 ms) and F_K (0.3 ms) reveals the ΔV_L-band. In Figures 4.13 A and 4.15 A, the appearance of significant ΔV_L-bands were observed for both the nano-TiO_2 and nano-SiO_2 treatments at the highest concentrations (2%). A significant ($p \leq 0.05$) positive ΔV_L-band was observed at the 2% nano-SiO_2 treatment (Figure 4.15 A).

Furthermore, a significant ($p \leq 0.05$) negative ΔV_L-band was also observed at the 2% nano-TiO_2 treatment (Figure 4.13 A).

Differential normalization between F_0 and F_J amplifies the ΔV_K-band, appearing around 0.3 ms. Further normalization between $F_{0.1\ ms}$ and $F_{1\ ms}$ revealed an intensified sharper resolution of the ΔV_K-band, which we have termed the ΔV_{Kn}-band (n = narrow). The ΔV_{Kn}-band is a more accurate representation of these phenomena, because it excludes the impact of antenna cooperativity (ΔV_L) and the Q_A-reduction. Well defined ΔV_{Kn}-bands for both the nano-TiO_2 (Figure 4.13 D) and nano-SiO_2 (Figure 4.15 D) treatments were observed, becoming significant ($p \leq 0.05$) at the 0.5% and 2% treatments of both types of nanoparticles.

The J-step in the fluorescence transient has been suggested to represent the reactions around the reduction of Q_A.[50, 53,54] Differential normalization between F_0 (0.03 ms) and F_I (30 ms) amplifies the ΔV_J-band, which can be observed around 2-3 ms. To better highlight the changes in the single turnover region around Q_A (with changes in nanoparticle type and concentration), intensified sharper resolution curves of the ΔV_{Jn}-band were constructed by differentially normalizing between $F_{1\ ms}$ and $F_{10\ ms}$ in the fluorescence transients. The results of this study indicated significant ($p \leq 0.05$) increases in the ΔV_{Jn}-bands for both the 0.5% and 2% nano-TiO_2 treatments (Figure 4.13 D), whilst only the 2% nano-SiO_2 treatment (Figure 4.15 D) showed a significant ($p \leq 0.05$) increase in the ΔV_{Jn} amplitude relative to the control. The nano-TiO_2 treatment appeared to have a greater impact on the electron transport events around Q_A, compared to the effect of the nano-SiO_2 treatments.

Differential normalization between F_J (3 ms) and F_P (300 ms) amplifies the ΔV_I-band, which forms part of the multiple turnover region of electron transport in the fluorescence transient. The ΔV_I-band can be observed around 30 ms and has been described as the redox state of the reduced intersystem electron carriers or size of the reduced plastiquinone pool. With further normalization between $F_{10\ ms}$ and $F_{100\ ms}$ a sharper ΔV_{In}-band was obtained, which only contains information of electron transport up to the PSII end acceptors (before plastocyanin (PC)), effectively excluding the influence of PSI activity. Significant ($p \leq 0.05$) increases in the amplitude of the ΔV_{In}-bands were seen at the 0.5% and 2% nano-TiO_2 treatments (Figure 4.13 D), whilst at the highest nano-SiO_2 concentration (Figure 4.15 D) a significant ($p \leq 0.05$) decrease in the ΔV_{In} amplitude was seen relative to the control. This is indicative of differential sensitivity/inhibitory mechanisms between the two types of nanoparticles.

The F_H phase at 300 ms often coincides with the maximum fluorescence intensity peak, F_P or F_m. Differential normalization between $F_{100\ ms}$ to $F_{300\ ms}$ brings about the appearance of a ΔV_{Hn}-band which can be interpreted as the redox state of PSI electron carriers before NADP and Ferredoxin (Fd). In this study, significant positive ΔV_{Hn}-bands were obtained at the 0.5% and 2% nano-TiO_2 treatments (Figure 4.13 D), whereas only the 2% caused a substantial increase in the ΔV_{Hn} amplitude (Figure 4.15 D).

4.3.2.2 Influence of varying nano-TiO_2 and nano-SiO_2 concentrations on biophysical parameters derived by JIP-equations

The OJIP transients can be translated into biophysical parameters. These parameters describe quantum yields of photon capture used for Q_A reduction (φ_{Po}), electron transport probabilities (φ_{Eo}, φ_{Ro} and δ_{Ro}), specific activities per reaction centre (RC) and performance indexes, PI_{ABS} and PI_{total}.[51] The derivation and meanings of these JIP-parameters are given and described in Table 1.5 (Chapter 1). The calculated values of selected parameters were normalized to those of controls and given in Table 4.1. No significant ($p \leq 0.05$) changes in the parameters were seen at the 0.05% concentration for both the nano-TiO_2 and nano-SiO_2 treatments. However, significant ($p \leq 0.05$) changes in all parameters were seen for the 0.5% and 2% nano-TiO_2 treatments, with the most significant ($p \leq 0.05$) changes at the 2% treatment, suggesting concentration dependence for the inhibition phenomenon. Although most of the parameters decreased for the 0.5% nano-SiO_2 treatment, only the PI_{total} decreased significantly ($p \leq 0.05$) at this treatment concentration. This is because of the accumulative effect of the down regulation of the parameters used in the calculation of PI_{total} ($PI_{total} = \varphi_{Eo} \cdot \varphi_{Ro} \cdot \delta_{Ro}$). At the 2% nano-$SiO_2$ treatment, significant ($p \leq 0.05$) changes in all parameters were observed, although the changes were not as substantial as the 2% nano-TiO_2 treatment.

Table 4.2: Calculated biophysical parameters and probabilities derived by JIP-equations; given as values relative to control.

Treatment	ABS/RC	DI_0/RC	$\varphi_{Po}/(1-\varphi_{Po})$	$\psi_{Eo}/(1-\psi_{Eo})$	$\delta_{Ro}/(1-\delta_{Ro})$	PI_{ABS}	PI_{total}
Control	1±0.12	1±0.12	1±0.10	1±0.06	1±0.05	1±0.09	1±0.08
0.05% TiO_2	1.03±0.09	1.05±0.16	1.09±0.08	1.1±0.08	0.91±0.15	1.2±0.15	1.16±0.06
0. 5% TiO_2	**1.65±0.24**	**1.37±0.09**	**0.79±0.08**	**0.74±0.09**	**0.79±0.11**	**0.58±0.12**	**0.46±0.09**
2% TiO_2	**2.05±0.32**	**1.58±0.21**	**0.71±0.08**	**0.58±0.16**	**0.41±0.13**	**0.41±0.09**	**0.17±0.08**
0.05% SiO_2	1.05±0.12	1.02±0.08	0.99±0.22	0.96±0.10	0.98±0.12	0.95±0.05	0.93±0.15
0.5% SiO_2	1.08±0.17	1.08±0.11	0.94±0.13	0.90±0.04	0.89±0.08	0.84±0.12	**0.75±0.12**
2% SiO_2	**1.34±0.15**	**1.21±0.06**	**0.77±0.10**	**0.79±0.15**	**0.61±21**	**0.60±0.19**	**0.37±0.22**
LSD ($p \leq 0.05$)	0.16	0.09	0.15	0.18	0.12	0.15	0.20

Results of one-way ANOVA analysis for each parameter. Significantly ($p \leq 0.05$) different (to control) values are marked in bold. Mean±S.E., n = 8 measurements.

Furthermore, the data of the relative parameters in Table 4.2 were used to calculate the total driving force ($DF_{total} = \log(PI_{total})$). The DF_{total} can be considered as the total driving force for the photochemical activity of the observed system and is equal to the sum of the partial driving forces for the events involved in the OJIP fluorescence rise, from light absorption up to PSI end acceptor

reduction.[48] The DF_{total} can be calculated by adding the log of the partial process efficiencies/probabilities. This DF_{total} (relative to control) was calculated using the following equation:

$$DF_{total(relative)} = \log(PI_{total(relative)}) = \{1 + \log(RC/ABS)_{relative}\} + \{1 + \log[(\varphi_{Po}/(1-\varphi_{Po})]_{relative}\} + \{1 + \log[(\psi_{Eo}/(1-\psi_{Eo})]_{relative}\} + \{1 + \log[(\delta_{Ro}/(1-\delta_{Ro})]_{relative}\} \quad 4.1$$

where log(RC/ABS) is the driving force for light absorption (photon capture), $\log[(\varphi_{Po}/(1-\varphi_{Po})]$ is the driving force for Q_A-reduction, $\log[(\psi_{Eo}/(1-\psi_{Eo})]$ is the driving force for electron transport past Q_A (to intersystem carriers) and $\log[(\delta_{Ro}/(1-\delta_{Ro})]$ is the driving force for the reduction of PSI end electron acceptors. One (1) is added to the log term in each part of the equation to obtain the relative change in the individual driving forces compared to the control, in order to see which partial processes were down-regulated the most. Figure 4.16 shows the changes in the relative $DF_{total(relative)}$ and the relative partial driving forces at the different nanoparticle concentrations.

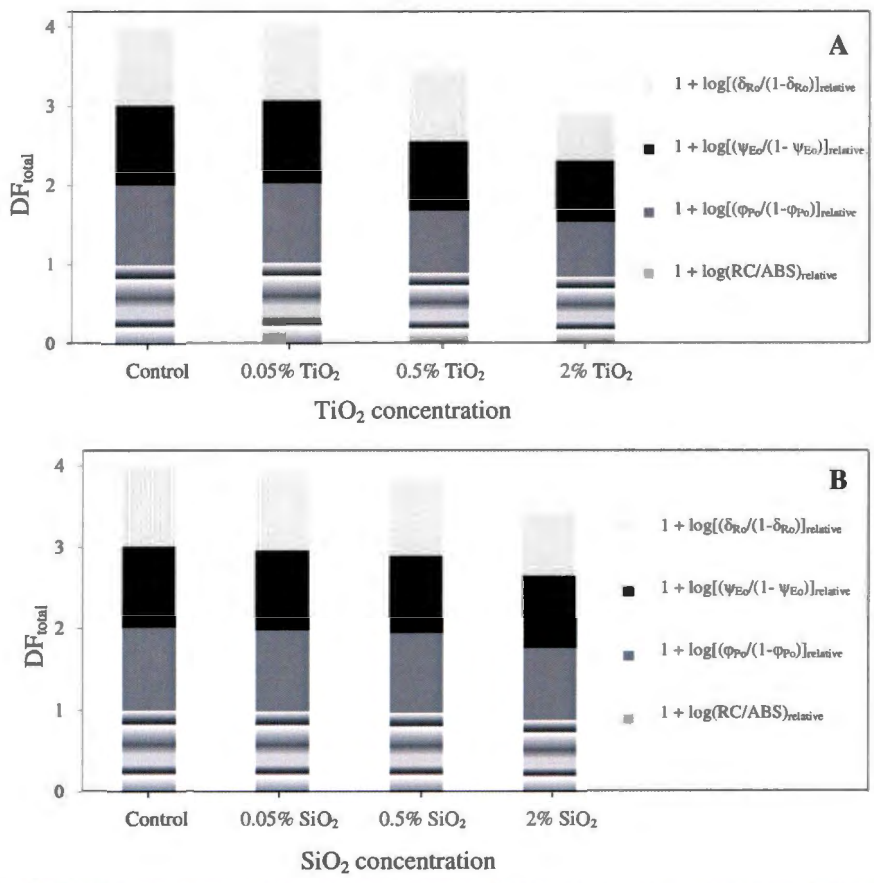

Figure 4.16 A & B: Changes in relative partial driving force processes and accumulative relative total driving force (DF_{total}) at different nano-TiO_2 (A) and nano-SiO_2 (B) concentrations.

According to Figure 4.16 A, the driving forces for Q_A-reduction, post Q_A electron transport and PSI end electron acceptor reduction appeared to be more sensitive than the driving force for light

absorption with increasing nano-TiO_2 concentrations. In Figure 4.16 B, the most sensitive partial driving force under the highest nano-SiO_2 concentration was the partial driving force for PSI end electron acceptor reduction. This suggests differential sensitivity and different limitation modes of down-regulation.

4.3.2.3 Influence of varying nano-TiO_2 and nano-SiO_2 concentrations on apparent PSI activity

From the maximal slopes of the kinetic curves of photo-induced MR changes in Figures 4.11 A & B, the rates of P700 and PC oxidation (v_{ox}) followed by the subsequent re-reduction of $P700^+$ and PC (v_{red}) could be calculated.

The results in Table 4.3 suggest different PSI sensitivities with regard to the type and concentration of the nanoparticle treatments. The maximum re-reduction rate of $P700^+$ and PC (v_{red}) appeared to be more sensitive to the treatments than P700 and PC oxidation (v_{ox}). This implies an inherent limitation on electron transport between PSII and PSI. Decreases in MR_{min} suggest a decline in the maximum pool size of the oxidized PSI carriers. Even though v_{red} decreased to a greater extent than v_{ox}, the MR_{min} still declined significantly, which can be attributed to the difference in the fast and slow phase electron transport. Put in another way, a small change in v_{ox} (slow phase) will cause a greater change in MR_{min} than a relatively large change in v_{red}. Furthermore, nano-TiO_2 caused a greater decrease in all of the parameters compared to nano-SiO_2, mostly becoming significant ($p \leq 0.05$) at the 0.5% and 2% treatments for both nanoparticle types.

Table 4.3: Calculated P700 and PC oxidation (v_{ox}) and $P700^+$ re-reduction (v_{red}) parameters as well as MR_{min} values from 820 nm reflection induction curves.

Treatment	Relative V_{ox} (Relative to control)	Relative V_{red} (Relative to control)	Relative MR_{min} (Relative to control)
Control	1±0.08	1±0.07	1±0.07
0.05% nano-TiO_2	1.02±0.07	1.09±0.06	1.05±0.06
0.5% nano-TiO_2	**0.81±0.03**	**0.73±0.04**	**0.78±0.04**
2% nano-TiO_2	**0.71±0.05**	**0.62±0.09**	**0.70±0.05**
0.05% nano-SiO_2	1.05±0.06	0.98±0.04	0.97±0.03
0.5% nano-SiO_2	0.95±0.09	0.88±0.06	0.91±0.02
2% nano-SiO_2	**0.77±0.1**	**0.73±0.09**	**0.79±0.06**
LSD ($p \leq 0.05$)	0.15	0.17	0.15

Results of one-way ANOVA for each parameter. Significantly ($p \leq 0.05$) different (to control) values are marked in bold. Mean ±S.E., n = 8 measurements.

4.3.3 ROS markers and enzyme activities

According to the results presented in Table 4.4, the 0.05% nano-TiO_2 and nano-SiO_2 did not cause a significant ($p \leq 0.05$) increase (relative to control) in the measured H_2O_2 concentration. However, at the 0.5% and 2% nano-TiO_2 treatments, a significant ($p \leq 0.05$) increase (~ 2.5 fold) in the H_2O_2 concentration was observed. A significant ($p \leq 0.05$) increase in the H_2O_2 concentration was also observed for the 2% nano-SiO_2 treatment.

Table 4.4: Changes in the concentrations of ROS markers and activities of key antioxidant enzymes at different nano-TiO_2 and nano-SiO_2 concentrations.

Treatment	H_2O_2 ($\mu mol.g^{-1}$) *Fm	MDA ($nmol.g^{-1}$) *Fm	APX ($\mu mol\ ASC.min^{-1}mg^{-1}$) *PT	SOD ($U.mg^{-1}$)	GR ($\mu molNADPH.min^{-1}.mg$) *PT
Control	8.2±1.1	47.3±6.9	214.7±24.2	38.9±8.9	19.8±3.9
0.05% TiO_2	8.5±1.8	55.8±5.1	222.3±21.5	41.9±5.1	21.9±5.1
0. 5% TiO_2	**21.8±2.1**	**86.7±6.9**	**272.5±15.6**	**79.3±4.9**	**41.5±5.7**
2% TiO_2	**23.2±1.2**	**93.4±5.6**	**293.0±35.6**	**87.6±8.6**	**62.6±2.2**
0.05% SiO_2	8.1±0.8	47.3±3.6	213.2±24.2	37±9.0	16.8±3.1
0.5% SiO_2	10.1±1.9	48.5±11.2	231.3±12.3	49.4±2.6	**25.9±0.8**
2% SiO_2	**18.9±1.1**	**70.8±8.5**	**276.5±15.1**	**76.6±7.1**	**44.0±6.2**
LSD ($p \leq 0.05$)	7.6	19.9	54.3	30.1	5.4

Results of one-way ANOVA analysis for each parameter. Significantly ($p \leq 0.05$) different (to control) values are marked in bold. Mean ±S.E., n = 6 measurements; *Fm = fresh mass; *PT = protein.

The MDA concentration is often used as a measure to follow lipid membrane oxidative damage.[50] An increase in MDA is thus indicative of increased membrane damage. The 0.5% and 2% nano-TiO_2 treatments showed ~2 fold increases in the measured MDA concentration (Table 4.4), with the largest increase observed at the highest nano-TiO_2 treatment (2% nano-TiO_2). The only nano-SiO_2 treatment that induced significant ($p \leq 0.05$) changes in the MDA concentration was the 2% nano-SiO_2 treatment, which showed a ~1.4 fold increase (Table 4.4).

In Table 4.4, a significant ($p \leq 0.05$) increase in the APX activity was observed at the 0.5% and 2% nano-TiO_2 treatments. The activity was found to be ~ 1.4 times higher than that of the control treatments. A significant ($p \leq 0.05$) increase in APX activity (relative to control) was only observed in the highest nano-SiO_2 treatment, where a ~ 1.2 fold increase was observed (Table 4.4). Ascorbate peroxidase (APX) plays an important role in ROS detoxification as part of the ascorbate-glutathione cycle and an increase in APX activity suggests a definite increase in ROS formation.

Superoxide dismutase (SOD) activity was significantly ($p \leq 0.05$) enhanced by the 0.05% and 2% nano-TiO_2 treatments, with a ~2 fold and a ~ 2.2 fold increase respectively (Table 4.4). Again, only the highest nano-SiO_2 treatment (2%) showed a significant ($p \leq 0.05$) increase relative to control treatments (Table 4.4). Increased SOD activity is also indicative of increased ROS formation, given its role in detoxifying hydroxyl radicals (OH^-) via the Haber-Weiss reaction to form H_2O_2, which is then further detoxified by APX etc. More information on these mechanisms and how they interact is discussed in the discussion section (Section 4.4).

Significant ($p \leq 0.05$) increases in GR activity were observed for the 0.5% and 2% nano-TiO_2 treatments (Table 4.4). At the 0.5% nano-TiO_2 treatment, the GR activity was ~2 times higher than that of the control treatment, whilst the 2% nano-TiO_2 treatment plants exhibited more than 3 times the GR activity compared to that of the control treatment (Table 4.4). The 0.5% and 2% nano-SiO_2 treatments also showed significant ($p \leq 0.05$) increases in the GR activity, with a ~1.5 and ~2.2 fold increase at the 0.5% and 2% nano-SiO_2 treatments, respectively.

4.3.4 Coupling between PSI electron transport and CO_2-assimilation

When plotting the relative J_{max} data shown in Figures 4.8 A & B vs the relative v_{ox} values in Table 4.3 and comparing it to a coupled model, that was constructed by plotting the relative PSI oxidation rate (v_{ox}) against its identical values (to simulate a situation where 100% of the PSI electrons are used for $NADP^+$-reduction and subsequent carbon assimilation), an increase in decoupling (ε) could be seen with increasing nanoparticle concentration (Figure 4.17 A & B). As stated in Chapter 3, 100% efficiency is highly unlikely (due to other electron withdrawing reactions, such as nitrogen and sulphur reduction etc.). The model was again constructed not to obtain absolute ratio values, but rather to show increased ε under amplified stress conditions. The relative (to control) relationship between v_{OX} and J_{max} and the coupled (elctron flux or 'ideality') model, is shown in Figure 4.17 A & B.

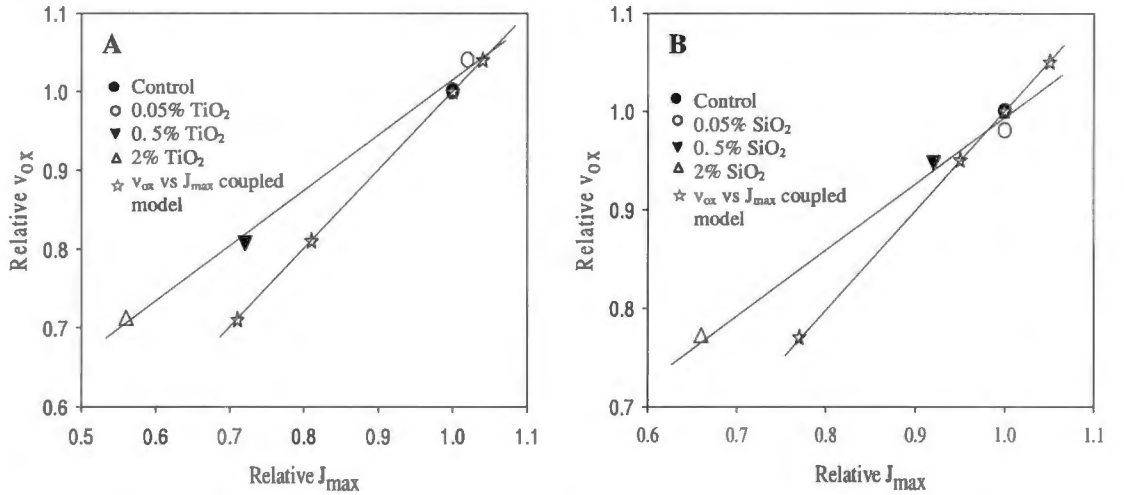

Figure 4.17 A & B: An electron flux model showing the correlation between relative P700 oxidation rate (v_{ox}) and relative PEPc regeneration or electron transport rate (J_{max}) as a fraction of the control. Open stars depict a model of the ideal coupling correlation if 100% of PSI reduced NADPH were used for ATP formation and CO_2-assimilation (i.e. $\varepsilon = 0$). Significant deviation from the electron flux (coupled) model (ε) was determined by a one way anova at $p \leq 0.05$ (LSD = 0.07). **A** = nano-TiO_2, **B** = nano-SiO_2.

The % deviation from the electron flux (coupled) model (ε) for each treatment can be calculated using eqation 3.1 (Chapter 3). At the 0.05% nano-treatments, no significant ($p \leq 0.05$) deviation in ε (relative to control) could be seen, suggesting that the coupling phenomenon between electron transport and CO_2-assimilation remained relatively unchanged at these nanoparticle treatments. At the 2% SiO_2 (Figure 4.17 A), 0.5% and 2% TiO_2 treatments (Figure 4.17 B), significant ($p \leq 0.05$) increases of 14%, 16% and 25% in ε could be seen. This points to increased decoupling between PSI electron transport and PEPc regeneration with increasing nanoparticle (stress) conditions.

4.4 Discussion

The aim of this study was to investigate the photosynthetic response of *Zea mays L.* (cultivar IMP 52-11) to different concentrations of nano-TiO_2 and nano-SiO_2 applied as a foliar spray. Gas exchange measurements were used to evaluate the CO_2-assimilation and stomatal response to the nanoparticle treatments, by making use of the C_4-plant model of Von Caemmerer and Furbank 1999, by which A:C_i curves were constructed and analysed (Figure 4.6 A & B). Fast kinetics chlorophyll *a* fluorescence (PF) coupled with modulated reflection ($MR_{820\ nm}$) was used to quantify the response of PSII and PSI electron transport to the nanoparticle treatments. Furthermore, important ROS markers

and activities of key antioxidant enzymes were also monitored to assess whether there was a change in the amount of ROS species formed during the various treatments.

The maximum assimilation rate (V_{pmax}) of the primary carboxylation C_4-plant enzyme (PEPc) has previously been reported to decrease with nanoparticle treatments. Up-regulation of the carboxylation enzyme activity was also reported by Gao *et al.,* 2006 and Zheng *et al.,* 2005, whom both reported increased Rubisco activity in spinach under nano-TiO_2 treatment.[19,22] As observed in this study, spraying specific concentrations of nano-TiO_2 solutions on the leaf, reduced the V_{pmax}, in which seems to be a concentration dependent manner (Figure 4.7 A). The decrease in V_{pmax} at the 0.5% and 2% nano-TiO_2 treatments coupled with the increase in water loss (increased transpiration) is indicative of decreased carboxylation activity. The CO_2 response curve deduced parameters also indicated a decrease in the maximal electron transport and PEPc regeneration rate, J_{max}. An insignificant ($p \leq 0.05$) increase in J_{max} was observed at the 0.05% nano-TiO_2 treatment (Figure 4.8 A). Both the 0.5% and 2% treatments showed a significant ($p \leq 0.05$) decrease in J_{max}, with the largest decrease observed at the 2% treatment (Figure 4.8 A). Li *et al.*, 2012 attributed the decrease in growth of *Gymnodinium breve* to increased reactive hydroxyl formation.[27] The effect of ROS induced damage is a known factor attributing to decreased carboxylation efficiency. Increased ROS formation have been found previously by Wang *et al.,* 2010 and Larue *et al.,* 2012a under nano-TiO_2 treatments, which may account for the decrease in carboxylation rate (PEPc activity), V_{pmax}, which was supported by an increase in ROS and relevant markers (Table 4.4). A decrease in *l* (calculated from the data in Figure 4.6 A), increases in maximal g_s and significant ($p \leq 0.05$) increases in C_i for both the 0.5% and 2% nano-TiO_2 treatments (Figure 4.9 A), further supports that the limitation was mainly carboxylation activity based, seeing that this indicated that no stomatal limitation existed. The phenomenon of increased stomatal conductance under nano-TiO_2 was also observed by Gao *et al.*, 2013, who reported an almost 300% increase in stomatal conductance in *Ulmus elongata* seedlings as a result of TiO_2 foliar spray treatments.[28] In addition to increased g_s, significant ($p \leq 0.05$) increases in water loss through increased transpiration were also observed (data tot shown). Increased water loss can lead to reductions in the WUE, which was indeed observed at the 0.5% and 2% nano-TiO_2 treatments (Figure 4.10 A). Significant decreases in the WUE were also reported by Gao *et al.*, 2013 under nano-TiO_2 foliar treatments.[28]

In the present study, the highest nano-SiO_2 treatment (2%) displayed significant ($p \leq 0.05$) decreases in V_{pmax} and J_{max} (Figure 4.7 B and 4.8 B). Significant ($p \leq 0.05$) increases in stomatal limitation (*l*) for the 0.5% and 2% nano-SiO_2 treatments were also observed, explaining the decrease in C_i at A_{360}, i.e. corresponding to the intercept of the supply and demand functions. Although decreases in the relative maximal g_s was seen for the 0.5% and 2% nano-SiO_2 treatments (Figure 4.9 B), only the 0.5% treatment exhibited a significant ($p \leq 0.05$) improvement in WUE (Figure 4.10 B). Parveen *et al.*, 2010 also found that exogenously applied Si significantly enhanced the plant-water use efficiency (WUE)

of maize.[57] Haghighi *et al.*, 2013 and Romero-Aranda *et al.*, 2012, both ascribed decreased stomatal conductance as the reason for increased drought and salinity tolerance with nano-SiO_2 treatments.[31,32] The absence of WUE improvement at the 2% treatment (Figure 4.10 B) is due to the relatively large decrease in the CO_2-assimilation efficiency at the 2% treatment (WUE = A/E). The relatively large decrease of g_s at the 2% nano-SiO_2 treatment also accounts for the decrease in V_{pmax} and J_{max}, through the respective decoupling of g_s (CO_2 absorption) and carboxylation activity as well as photosynthetic electron transport and carboxylation activity. Lower CO_2 availability will cause a decrease in the carboxylation activity of PEPc (V_{pmax}), which in turn decreases the electron demand function for carbon assimilation and PEPc regeneration (J_{max}).

From the PF and $MR_{820\ nm}$ curves various structural and functional PSII and PSI electron transport parameters were obtained. Differential normalization of sections of the PF transients were used to obtain information on the structural and functional changes that resulted from the various treatments. The appearance of ΔV_L-bands (Figure 4.13 A & 4.15 A) could be seen at the highest concentration (2%) of both types of nanoparticle treatments. Interestingly the nano-TiO_2 treatment caused the appearance of a negative ΔV_L-band, whilst a positive ΔV_L-band was observed for the nano-SiO_2 treatment. The ΔV_L-band has been suggested to be closely related to the cooperativity between chlorophyll antennae.[38] A negative ΔV_L-band for the nano-TiO_2 treatment may have been by a pseudo increase in cooperativity caused by the photon capture capability of the photo-catalytic nano-TiO_2 particles that can possibly transfer charges between each other and active chlorophyll antennae (see Figure 4.18).

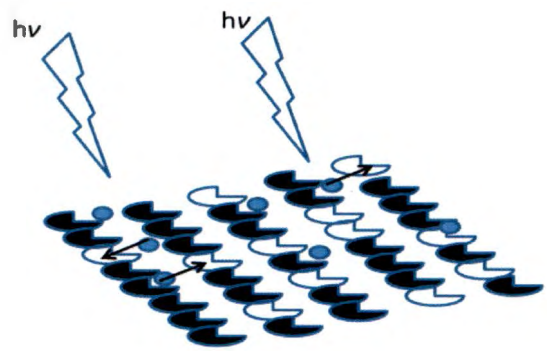

Figure 4.18: Original suggested possible charge transfer between active and non-active chlorophyll antennae. Open shapes indicate active antennae, closed shapes indicate inactive antennae and arrows indicate charge transfer. Small circles indicate infiltration sites of nano-TiO_2 amongst the chlorophyll antennae.

A positive ΔV_L-band obtained with the nano-SiO_2 treatment is indicative of decreased cooperativity between antennae. Increased ROS formation can cause damage to chlorophyll antennae, resulting in

decreased cooperativity. Although nano-TiO_2 has also been shown to cause ROS, the effect on cooperativity might be mitigated (in part at least) by the charge transfer capability of the nano-TiO_2. Significant ($p \leq 0.05$) increases of 65%, 105% and 34% in the ABS/RC and 37%, 58% and 21% in the DI_o/RC (Table 4.2) were also observed at the 0.5% and 2% nano-TiO_2 and 2% nano-SiO_2 treatments, respectively. Increases in these two parameters are indicative of reaction centre deactivation, resulting in the formation of silent centres, which dissipate excess absorbed energy in the form of heat. Furthermore, RC deactivation could also be seen from decreases in the $\varphi_{Po}/(1- \varphi_{Po})$ parameter, which is indicative of the quantum yield of primary photochemistry, i.e. the efficiency with which photons absorbed by active RCs are trapped and converted to photochemical energy for the reduction of Q_A. Significant ($p \leq 0.05$) decreases in the $\varphi_{Po}/(1- \varphi_{Po})$ parameter of 21%, 29% and 23% were also observed at the 0.5%, 2% nano-TiO_2 and 2% nano-SiO_2 treatments (Table 4.2). The difference in the type and extent of response elicited by the two types of nanoparticles suggests differential mechanisms of sensitivity/toxicity.

Positive ΔV_{Kn}-bands for both the nano-TiO_2 (Figure 4.13 D) and nano-SiO_2 (Figure 4.15 D) treatments were observed, becoming significant ($p \leq 0.05$) at 0.5% and 2% of both types of nano-particles. Positive ΔV_K-bands is indicative of damage to the oxygen evolving complex (OEC), which allows non-water electron donation from strong reducing entities such as ascorbate. In this case, electron donation from catalytically active nanoparticles could also be a source of electron donation.

The single turnover events involving Q_A reduction and Q_A^- re-oxidation are reflected by the ΔV_J-band. A positive ΔV_{Jn}-band can be interpreted as an accumulation of reduced Q_A, which is indicative of reduced electron transport past Q_A. In the present study, the appearance of positive ΔV_{Jn}-bands in Figure 4.13 D & Figure 4.15 D can be seen. The amplitudes of the ΔV_{Jn}-bands were markedly higher for the nano-TiO_2 treatments compared to the nano-SiO_2 treatments, which suggests a greater electron transport inhibition effect by the nano-TiO_2 treatments. Only the 2% nano-SiO_2 treatment (Figure 4.15 D) caused a significant ($p \leq 0.05$) change in the ΔV_{Jn}-band amplitude, whilst both the 0.5% and 2% nano-TiO_2 treatments caused significant ($p \leq 0.05$) ΔV_{Jn}-bands. Differences in decreases in $\psi_{Eo}/(1- \psi_{Eo})$, which is a measure of the probability that a trapped excitation moves an electron into the electron transport chain beyond Q_A, also suggests differential down-regulation caused by the two types of nanoparticles. Significant ($p \leq 0.05$) decreases of 26% and 42% in $\psi_{Eo}/(1- \psi_{Eo})$ were observed for the 0.5% and 2% nano-TiO_2 treatments respectively, whereas the highest nano-SiO_2 treatment only caused a significant ($p \leq 0.05$) 21% decrease in $\psi_{Eo}/(1- \psi_{Eo})$ (Table 4.2). A decrease in the amplitude of the ΔV_{IP} phase points to a reduction in electron transport to PSI end acceptors. In the present study, a prominent decrease in the amplitude of the ΔV_{IP} phase could be seen for both the 0.5% and 2% nano-TiO_2 treatments (Figure 4.12 C), whilst only the 2% nano-SiO_2 treatment (Figure 4.14 C) showed a decrease in the ΔV_{IP} amplitude, again suggesting differential sensitivities. The I and P-phases are two distinct phases in the PF transient, where the I-phase describes the multi-turnover

events around the intersystem electron carriers and the P-phase represents electron transport through PSI to the end acceptors of PSI. The events corresponding to these two phases can be separated using narrower normalizations between F_{10} to F_{100} for the I-phase and F_{100} to F_{300} for the P-phase. These normalizations give rise to narrower bands and sharper resolution. The ΔV_{In}-band can be interpreted as the electron transport around the intersystem electron carriers or the size of the reduced plastoquinone pool, while the ΔV_{Hn}-band is related to changes in the PSI end acceptor reduction. Interestingly, significant ($p \leq 0.05$) positive ΔV_{In}-bands could be seen for the 0.5% and 2% nano-TiO_2 treatments (Figure 4.13 D), whereas the 2% nano-SiO_2 treatment caused a significant ($p \leq 0.05$) negative ΔV_{In}-band (Figure 4.15 D). The negative ΔV_{In}-band is caused by reduced electron flow to intersystem electron carriers as a result of a build-up of reduced Q_A. Positive ΔV_{Hn}-bands were seen at the 0.5% and 2% nano-TiO_2 treatments as well as at the 2% nano-SiO_2 treatment. Positive ΔV_{Hn}-bands are indicative of an accumulation of reduced PSI iron-containing electron carriers before NADP. Significant ($p \leq 0.05$) decreases of 21% and 59% in $\delta_{Ro}/(1-\delta_{Ro})$ were also seen at the 0.5% and 2% nano-TiO_2 treatments, whereas only the 2% nano-SiO_2 treatment showed a significant ($p \leq 0.05$) decrease of 39% (Table 4.2), indicating decreased electron transport to the end acceptors of PSI. As CO_2-assimilation is the major sink for the reducing equivalents and energy produced by the primary photochemical reactions, diminished CO_2-fixation will induce a decrease in the ATP and NADPH demand, inevitably leading to electron accumulation in PSI and PSII. Down-regulated electron demand may either be caused by mesophyll limitation, i.e. damage to the primary carboxylation enzyme (PEPc) or by stomatal limitation imposed by decreased stomatal CO_2 uptake.[57] Both these limitations will eventually lead to increased ROS formation, which is supported by increased ROS markers ant antioxidant activity (Table 4.4). This will set of a cascade of electron accumulations, causing more ROS production and further damage to membrane, cellular and enzyme structures.

The use of $MR_{820\ nm}$ allowed us to observe the redox reactions around PSI. By analysing the modulated reflection curves, the maximum rate of PC and P700 oxidation (v_{ox}) and $P700^+$ re-reduction (v_{red}) could be obtained from the respective maximum slopes of the curves (See Figures 4.9 A & B). Furthermore, the MR_{min} for each treatment, which is defined as the steady state (equilibrium state) between oxidised and reduced PC and PSI or the maximum pool size of oxidised PC and PSI, was also extracted. Table 4.3 gives the calculated values of v_{ox}, V_{red} and MR_{min} relative to control values. Significant ($p \leq 0.05$) limitations on electron transport through PSI (v_{ox}) of 19% and 29% could be seen for the 0.5% and 2% nano-TiO_2 treatments, whilst the 2% nano-SiO_2 treatment showed a significant ($p \leq 0.05$) decrease in v_{ox} of 23%. The v_{red} of the 0.5% and 2% nano-TiO_2 treatments decreased significantly ($p \leq 0.05$) by 27% and 38% respectively, whereas a significant ($p \leq 0.05$) decrease of 27% was seen at the 2% nano-SiO_2 treatment. Decreases in v_{ox} could have been caused by structural damage to PSI electron carriers or it could be as a result of decreased electron demand by the carboxylation reactions. A similar co-regulatory modulation of electron transport and

carboxylation reactions has previously been reported.[60-64] A decrease in v_{red} is indicative of decreased electron transport between PSII and PSI (PSI re-reduction by PSII), which was also seen from the PF data (electron accumulation). Decreases of 22% and 30% in the relative MR_{min} can be seen for the 0.5% and 2% nano-TiO_2 treatments. The relative MR_{min} of the 2% nano-SiO_2 treatment also decreased by 21%. Decreases in the relative MR_{min} can be interpreted as a shift in the redox equilibrium between PSII and PSI towards the PSII side, which means that PSI oxidation (v_{ox}) became even more limiting, remembering that the PSII electron arrival rate (fast phase) is fundamentally much faster than the rate of PSI electron donation (slow phase) to $NADP^+$. This is in agreement with a decrease in the ΔV_{IP} phase (Figures 4.12 C and 4.14 C) and the accumulation of electrons before NADP as indicated by the positive ΔH_n-bands (Figures 4.13 D and 4.15 D).

Aldea *et al.*, 2005 suggested that it is possible that the transient activity of an alternative electron sink such as O_2 may have uncoupled the electron transport from primary CO_2-assimilation under stress effects caused by insect herbivory and plant interactions in soybean.[65] Fryer *et al.*, 1998 found that the $\varphi_{PSII}/\varphi_{CO2}$ ratio of maize seedlings increased under cold stress conditions, which suggests a change in the electron flux and CO_2-assimilation equilibrium, caused by a decrease in the NADPH and ATP demand of the Calvin cycle.[66] The change in this equilibrium causes the accumulation of electrons in the electron transport chain, resulting in electron donation to alternative electron acceptors such as O_2. When O_2 is reduced by these excess electrons, it results in the formation of ROS species such as O_2^- and OH^-, which was indeed observed by Fryer *et al.*, and indicated by significant increases in the activities of detoxification enzymes such as SOD, APX and GTR.[66] In this present study increases in ROS markers and antioxidant activities were also observed (Table 4.4). The occurrence of such alternative electron accepting activity can be approximated by correlating the relative v_{ox} to the relative J_{max}, seeing that the electrons that move through PSI are used to regenerate PEPc.

No marked deviation in ε was seen at the 0.05% treatments of both nanoparticle treatments suggesting that the coupling phenomena between electron transport and CO_2-assimilation stayed intact at these low concentration treatments (Figure 4.17 A & B). Marked decreases in ε (as seen in Figure 4.17 A & B for the 0.5% and 2% nano-TiO_2 treatments as well as 2% nano-SiO_2 treatment) suggests electron losses to alternative electron acceptors (O_2 etc.), leading to subsequent ROS formation. Increased concentration of well-known ROS markers (Table 4.4) further supports this hypothesis. Reduced O_2 (O_2^-) is detoxified by membrane bound SOD in the Mehler ascorbate peroxidase pathway (see Figure 4.5), resulting in the formation of H_2O_2, that in turn causes damage to membrane structures, causing increases in MDA. Furthermore, H_2O_2 can withdraw electrons from the photosynthetic electron transport chain in a reaction mediated by mono-dehydroascorbate reductase (MDHAR), which uses NADPH.[66] Significant ($p \leq 0.05$) increases in the activities of key detoxifying enzymes at the 0.5% nano-TiO_2, 2% nano-TiO_2 and 2% nano-SiO_2 nanoparticle concentrations, also suggests increased

ROS detoxifying activity. The activity of the ROS markers (H_2O_2 and MDA) and enzyme activities were clearly nanoparticle concentration dependent, with the highest concentration causing the greatest increase in ROS markers and enzyme activities.

In Figure 4.16 it became clear that increases in the nanoparticle concentration caused significant ($p \leq 0.05$) negative effects on the partial processes (light capture, primary photo-chemistry efficiency, Q_A-reduction and reduction of both PSII and PSI end electron acceptors), which ultimately resulted in a significant ($p \leq 0.05$) lowering of the overall efficiency (driving force) of photosynthetic electron transport.

4.5 Conclusions

According to the data obtained, it became clear that both the nano-TiO_2 and nano-SiO_2 caused limitations on the light dependent electron transport processes and CO_2-assimilation. These limitations were found to be concentration dependent, with the highest concentration resulting in the most down-regulation. The data suggested that the maize plants were more sensitive to nano-TiO_2 than to nano-SiO_2. Moreover, the data also suggested some differences in the mode of limitation between the two types of nanoparticles. These limitations were found to be as follows:

A differential response between the two types of nanoparticles was observed with regard to stomatal behaviour. The data (g_s, *l* and WUE) suggests that the nano-TiO_2 caused increased stomatal opening, whilst the nano-SiO_2 caused increased stomatal closure. To our knowledge, such a direct comparison to illustrate the difference in stomatal behaviour as a result of nanoparticle types has never been published.

Both types of nanoparticles also caused downregulation of both PSI and PSII photosynthetic electron transport. Numerous differential fluorescence bands (Figure 4.12-4.15) originating from the prompt fluorescence data suggested functional changes in the electron transport systems. These fluorescence bands are indicative of electron transport inhibition and subsequent electron accumulation at the single (Q_A-reduction) and multiple turnover (intersystem electron acceptors, PSII and PSI end electron acceptors) phases. Changes in the respective biophysical parameters and probabilities derived by the JIP-equations (Table 1.5 Chapter 1) suggested functional and structural changes in the photon capturing apparatus and reaction centre deactivation, as well as down-regulated PSI and PSII electron transport. The MR_{820nm} data also showed decreases in the v_{ox} and v_{red} PSI parameters (Table 4.3), which is indicative of decreased PSI oxidation (electron movement through PSI) and PSI re-reduction by arriving electrons from PSII. General down-regulation in electron transport efficiency was also evident from the dcrease in the DF_{total} parameter in Figure 4.16. This parameter gave a good visual

representation of how the impact of decreases in al of the partial transport processes eventually leads to a marked decrease in the efficiency of the total process.

The concentration of the ROS marker, H_2O_2, and the activity of detoxifying enzymes (Table 4.4) confirmed increased ROS formation. These ROS caused damage to membrane structures and a subsequent increase in the MDA concentration (Table 4.4). Reactive oxygen species have also been shown to cause damage to the PEPc enzyme structure, which likely brougth about the significant ($p \leq 0.05$) decline in the carboxylation efficiency at the 0.5% and 2% nano-TiO_2 as well as the 2% nano-SiO_2 treatments (V_{pmax} in Figure 4.5 B).

The photo-catalytic activity of the nano-TiO_2 was most likely the reason for the observed photosynthetic down-regulation. A product of nano-TiO_2 induced photo-catalysis is electrons produced during the photo-catalytic reaction. A significant ($p \leq 0.05$) increase in stomatal limitation at the 2% nano-SiO_2 may also be to blame for the decreased electron demand and subsequent electron accumulation in PSI and PSII. Over-reduction of PSI and PSII electron transporters will also lead to ROS formation, which was confirmed by an increase in ROS markers (Table 4.4).

Increased decoupling (ε) under amplified stress conditions was once again hypothesized and confirmed by measuring both photosynthetic gas exchange and MR_{820nm} at the various nanoparticle concentrations, whilst subsequently applying the model proposed in Chapter 3. Increased ε became evident with increasing nanoparticle concentration (Figure 4.17). Furthermore, the theory put forward in Chapter 3, which suggested that decreased coupling between PSI electron transport and electron usage in CO_2-assimilation (increased ε) will lead to increased ROS formation, was confirmed in this present study by measuring ROS markers and antioxidant activities.

In conclusion, the data showed that the particle matter caused marked downregulation of photosynthesis in the maize plants. This stresses the need to closely monitor the amount of particle matter being deposited into the environment, espescially in areas such as the Highveld priority are in South Africa with its high population density and large amount of industrial activity.

4.6 References

1. C. Ostiguy, G. Lapointe, L. M´enard et al., "Les effets `a la sant´e reli´es aux nanoparticules," Rapport R-451, Montreal, Canada, 2006.
2. E.J. Joner, T. Hartnik, and C.E. Amundsen, Environmental fate and ecotoxicity of engineered nanoparticles, in Norwegian Pollution Control Authority Report no. TA 2304/2007, pp. 1–64, Bioforsk, As, Norway, 2008.
3. S. Rana, P.T. Kalaichelvan, Ecotoxicity of Nanoparticles, Hindawi Publishing Corporation, ISRN Toxicology, 1-11, Volume 2013.
4. G.R. Cramer, K. Urano, S. Delrot, M. Pezzotti and K. Shinozaki, Effects of abiotic stress on plants: a systems biology perspective, BMC Plant Biology, 11, 163, 2011.
5. J.S. Boyer, Plant productivity and environment, Science, 218, 4571, 443-448, 1982.
6. J.T.K. Quik, Fate of nanoparticles in the aquatic environment. Removal of engineered nanomaterials from the water phase under environmental conditions. PhD thesis, Radboud University Nijmegen, The Netherlands, 2013.
7. G. Held, B.J. Gore, A.D. Surridge, G.R. Tosen, C.R. TurnerR.D. Walmsley, (Eds.), Air pollution and its impacts on the South African Highveld, Environmental Scientific Association, Cleveland, 144pp, 1996.
8. A. Kahru, H. Dubourguier, From ecotoxicology to nano-ecotoxicology, Toxicology, 269, 105–119, 2010.
9. F. Gottschalk, T. Sonderer, R.W. Scholz, Modeled Environmental concentrations of engineered nanomaterials (TiO_2, ZnO, Ag, CNT, Fullerenes) for different regions, Environmental Science and Technology, 43, 9216–9222, 2009.
10. N.C. Mueller, B. Nowack, Exposure modeling of engineered nanoparticles in the environment, Environmental Science and Technology, 42, 4447–4453, 2008.
11. F. Aslani, S. Bagheri, N.M. Julkapli, A.S. Juraimi, F. Sadat, G. Hashemi, A. Baghdadi, Effects of Engineered Nanomaterials on plants Growth: An Overview, Hindawi Publishing Corporation, Scientific World Journal Volume 2014, Article ID 641759, http://dx.doi.org/10.1155/2014/641759.
12. J. Gao, G. Xu, H. Qian, P. Liu, P. Zhao, Y. Hu, Effects of nano-TiO_2 on photosynthetic characteristics of *Ulmus elongata* seedlings, Environmental Pollution, 176, 63-70, 2013.
13. W.F. Falco, E.R. Botero, E.A. Falcão, E.F. Santiago, V.S. Bagnato, A.R.L. Caires, *In vivo* observation of chlorophyll fluorescence quenching induced by gold nanoparticles, Journal of Photochemistry and Photobiology A: Chemistry, 225, 65– 71, 2011.
14. P. P. Fu, Q. Xia, H. Hwang, P.C. Ray, H. Yu, Mechanisms of nanotoxicity: Generation of reactive oxygen species, Journal of Food and Drug Analysis, 22, 64-75, 2014.

15. C. He, Y. Hu, L. Yin, Effects of particle size and surface charge on cellular uptake and bio-distribution of polymeric nanoparticles, Biomaterials, 31:3657-3666, 2010.
16. N. Sakai, Y. Matsui, A. Nakayama, Functional dependent and size-dependent uptake of nanoparticles in pc12, Journal of Physics Conference Series, 304, 012049, 2011.
17. S.H. Wang, C.W. Lee, A. Chiou, Size-dependent endocytosis of gold nanoparticles studied by three-dimensional mapping of plasmonic scattering images, Journal of Nano-biotechnology, 8:33-45, 2010.
18. C. Boyoglu, Q. He, G. Willing, Microscopic studies of various sizes of gold nanoparticles and their cellular localizations. ISRN Nano-technol, http://dx.doi.org/ 10.1155/2013/123838, 2013.
19. L. Zheng, F. Hong, S. Lu, C. Liu, Effect of nano-TiO_2 on strength of naturally aged seeds and growth of spinach, Biological Trace Element Research, 104, 83-92, 2005.
20. F. Hong, J. Zhou, C. Liu, F. Yang, C. Wu, L. Zheng, P. Yang, Effect of nano-TiO_2 on photochemical reaction of chloroplasts of spinach, Biological Trace Element Research, 105, 269-279, 2005a.
21. F. Hong, F. Yang, C. Liu, Q. Gao, Z. Wan, F. Gu, C. Wu, Z. Ma, J. Zhou, P. Yang, Influences of nano-TiO2 on the chloroplast aging of spinach under light, Biological Trace Element Research, 104, 249-260, 2005b.
22. F. Gao, F. Hong, C. Liu, L. Zheng, M. Su, X. Wu, F. Yang, C. Wu, P. Yang, Mechanism of nano-anatase TiO_2 on promoting photosynthetic carbon reaction of spinach: inducing complex of rubisco-rubisco activase, Biological Trace Element Research, 111, 239-253, 2006.
23. Z.Y. Wang, X.L. Yu, D.M. Gao, W.Q. Feng, B.S. Xing, F.M. Li, Effect of nanorutile TiO_2 and multiwalled carbon nanotubes on the growth of Maize (*Zea mays L.*) seedlings and the relevant antioxidant response, Environmental Science, 31, 480-487, 2010.
24. A.S. Foltête, J.F. Masfaraud, E. Bigorgne, J. Nahmani, P. Chaurand, C. Botta, J. Labille, J. Rose, J.F. Férard, S. Cotelle, Environmental impact of sunscreen nanomaterials: ecotoxicity and genotoxicity of altered TiO_2 nanocomposites on *Vicia faba*, Environmental Pollution, 159, 2515-2522, 2011.
25. C. Larue, J. Laurette, N. Herlin-Boime, H. Khodja, B. Fayard, A.M., Flank, F. Brisset, M. Carriere, Accumulation, translocation and impact of TiO_2 nanoparticles in wheat (*Triticum aestivum* spp.): influence of diameter and crystal phase, The Science of the Total Environment, 431, 197-208, 2012a.
26. C. Larue, G. Veronesi, A.M. Flank, S. Surble, N. Herlin-Boime, M. Carrière, Comparative uptake and impact of TiO_2 nanoparticles in wheat and rapeseed, Journal of Toxicology and Environmental Health, 75, 722-734, 2012b.
27. F.M. Li, W. Zhao, Y.Y. Li, Z.J. Tian, Z.Y. Wang, Toxic effects of nano-TiO_2 on *Gymnodinium breve*, Environmental Science, 33, 233-238, 2012.

28. J. Gao, G. Xu, H. Qian, P. Liu, P. Zhao, Y. Hu, Effects of nano-TiO_2 on photosynthetic characteristics of *Ulmus elongata* seedlings, Environmental Pollution, 176, 63-70, 2013.
29. M.J. Akhtar, M. Ahamed, S. Kumar, Nanotoxicity of pure silica mediated through oxidant generation rather than glutathione depletion in human lung epithelial cells, Toxicology, 276:95-10, 2010.
30. A. Pluskota, E. Horzowski, O. Bossinger, A. von Mikecz, In *Caenorhabditis elegans* nanoparticle-bio-interactions become transparent: silica-nanoparticles induce reproductive senescence, PLoS One, 4, 2009.
31. M. Haghighi, M. Pessarakli, Influence of silicon and nano-silicon on salinity tolerance of cherry tomatoes (*Solanum lycopersicum L.*) at early growth stage, Scientia Horticulturae, 161, 111–117, 2013.
32. M.R. Romero-Aranda, O. Jurado, J. Cuartero, Silicon alleviates the deleterious salt effect on tomato plant growth by improving plant water status, Journal of Plant Physiology, 163, 847-855, 2006.
33. M. Haghighi, Z. Afifipour, M. Mozafarian, The effect of N-Si on tomato seed germination under salinity levels, Journal of Biological and Environmental Science, 6, 87-90, 2012.
34. K. Dietz, S. Herth, Plant Nanotoxicology, Trends in Plant Science, Vol. 16, No. 11, November 2011.
35. S. von Caemmerer, & R.T. Furbank, Modeling C_4-photosynthesis, C_4 Plant Biology (eds. R. F. Sage & R. K. Monson), Academic Press, San Diego, 1999.
36. G.D. Farquhar, T.D. Sharkey, Stomatal Conductance and Photosynthesis, Annual Review of Plant Physiology, 33: 317-345, 1982.
37. A.K. Knapp, W.K. Smith, Effects of water stress on stomatal and photosynthetic responses in Subalpine plants to cloud patterns, American Journal of Botany, 75(6): 851-858, 1988.
38. R.J. Strasser, M. Tsimilli-Michael, S. Qiang, V. Goltsev, Simultaneous in vivo recording of prompt and delayed fluorescence and 820 nm reflection changes during drying and after rehydration of the resurrection plant *Haberlea rhodopensis*, Biochimica Biophysica Acta, 1797: 122–122, 2010.
39. R.J. Strasser., A. Srivastava, M. Tsimilli-Michael, The fluorescence transient as a tool to characterize the situation photosynthetic samples. In M Yunus, U Pathre, P Mohanty, eds, Probing photosynthesis: mechanisms, regulation and adaptation. Taylor & Francis, London, UK, pp. 445–483, 2000.
40. T. Brennan, C. Frenkel, Involvement of hydrogen peroxide in regulation of senescence in pear, Plant Physiology, 59, 411–416, 1977.
41. D. Hodges, J. DeLong, C. Forney, R. Prange, Improving the thiobarbituric acid-reactive-substances assay for estimating lipid peroxidation in plant tissues containing anthocyanin and other interfering compounds, Planta, 207, 604–611, 1999.

42. M.M. Bradford, A rapid and sensitive method for quantitation of micro- gram quantities of protein utilizing the principle of protein–dye binding, Anals of Biochemistry, 72, 248–254, 1976.
43. Y. Nakano Y, K. Asada, Hydrogen peroxide is scavenged by ascorbate-specific peroxidase in spinach chloroplasts, Plant Cell Physiology, 22, 867–880, 1981.
44. W.F. Beyer, I. Fridovich, Assaying for superoxide dismutase activity: some large consequences of minor changes in conditions, Anals of Biochemistry, 161, 559–566, 1987.
45. I. Carlberg, B. Mannervik, Glutathione reductase. In: Meister, A. (Ed.), Methods in Enzymology. Academic Press, San Diego, CA, pp. 484–490, 1985.
46. R.C. Leegood, Strategies for engineering C_4-photosynthesis, Journal of Plant Physiology, 170, 378– 388, 2013.
47. N.W. Pammenter, Research letter, Clarification of an apparent anomaly in the supply function associated with the response of carbon assimilation to carbon dioxide determined using conventional field equipment, South African Journal of Science, 85:271-272, 1989.
48. D. Lombardozzi, J.P. Sparks, G. Bonan, S. Levis, Ozone exposure causes a decoupling of conductance and photosynthesis: implications for the Ball-Berry stomatal conductance model, Oecologia, 169:651–659, 2012.
49. I.R. Cowan, Stomatal behaviour and environment, Advanced Botany Research, 4:117-228, 1977.
50. R.J. Strasser, M. Tsimilli-Michael, A. Srivastava, Analysis of the chlorophyll *a* fluorescence transient. In: G. Papageorgiou, Govindjee (Eds.), Advances in Photosynthesis and Respiration. Chlorophyll *a* fluorescence: a Signature of Photosynthesis. Springer, Dordrecht, The Netherlands, pp 321-362, 2004.
51. M.A. Yusuf, D. Kumar, R. Rajwanshi, R.J. Strasser, M, Tsimilli-Michael, Govindjee and N.B. Sarin, Overexpression of γ-tocopherol methyl transferase gene in transgenic Brassica juncea plants alleviates abiotic stress: physiological and chlorophyll *a* fluorescence measurements, Biochimica et Biophysica Acta, 1797:1428-1438, 2010.
52. P. Haldimann, R.J. Strasser, Effects of anaerobiosis as probed by the polyphasic chlorophyll *a* fluorescence rise kinetics in pea (*Pisum sativum L.*), Photosynthesis Research, 62, 67–83, 1999.
53. A. Oikarroum, V. Goltsev, R.J. Strasser, Temperature effects on pea plants probed by simultaneous measurements of the kinetics of prompt fluorescence, delayed fluorescence and modulated 820 nm reflection, PLoS ONE, 8 (3), e59433, 2013.
54. E. Salvatori, L. Fusaro, E. Gottaradini, M. Pollastrini, V. Goltsev, R.J. Strasser, F. Bussotti, Plant stress analysis: applications of Prompt, Delayed Chlorophyll Fluorescence and 820 nm Modulated Reflectance. Insights from independent experiments, Plant Physiology and Biochemistry, In Press, 2014.
55. A. Kudo, Photocatalyst materials for water splitting, Catalysis Surveys from Asia, Vol. 7, No. 1, April 2003.

56. A.K. Shaw, S. Ghosh, H.M. Kalaji, K. Bosac, M. Brestic, M. Zivcak, Z. Hossain, Nano-CuO stress induced modulation of antioxidative defense and photosynthetic performace of Syrian barley (*Hordeum vulgare L.*), Environmental and Experimental Botany, 102, 37-47, 2014.
57. N. Parveen, M. Ashraf, Role of silicon in mitigating the adverse effects of salt stress on growth and photosynthetic attributes of two maize (Zea Mays L.) cultivars grown hydroponically, Pakistan Journal of Botany, 42, (3), 1675–1684, 2010.
58. A.J. Clark, W. Landolt, J. Bucher, R.J. Strasser, The response of *Fagus sylvatica* to elevated CO_2 and ozone probed by the JIP-test, based on the chlorophyll fluorescence rise: OJIP. In: De Kok LJ, Stulen I (eds) Responses of Plant Metabolism to Air Pollution and Global Change. Backhuys Publishers, Leiden, The Netherlands, pp 283–286, 1998.
59. P.D.R. Van Heerden, J.W. Swanepoel, G.H.J. Krüger, Modulation of photosynthesis by drought in two desert scrub species exhibiting C_3-mode CO_2-assimilation, Environmental and Experimental Botany, 61, 124–136, 2007.
60. S. Burkart, J. Bender, B. Tarkotta, S. Faust, A. Castagna, A. Ranieri, H.J. Weigel, Effects of Ozone on Leaf Senescence, Photochemical Efficiency and Grain Yield in Two Winter Wheat Cultivars, Journal of Agronomical Crop Science, ISSN 0931-2250, 2013.
61. F. Bussotti, R. Desotgiu, C. Cascio, M. Pollastrini, E. Gravano, G. Gerosa, R. Marzuoli, C. Nali, G. Lorenzini, E. Salvatori, F. Manes, M. Schaub, R.J. Strasser, Ozone stress in woody plants assessed with chlorophyll *a* fluorescence, A critical reassessment of existing data, Environmental and Experimental Botany, 73, 19–30, 2011.
62. B. Genty, J.M. Briantais, N.R. Baker, The relationship between the quantum yield of photosynthetic electron transport and quenching of chlorophyll fluorescence, Biochimica et Biophysica Acta, 990: 87–92, 1989.
63. F. Loreto, D. Tricoli, G. Di Marco, On the relationship between electron transport rate and photosynthesis in leaves of the C_4 plant *Sorghum bicolor* exposed to water stress, temperature changes and carbon metabolism inhibition, Australian Journal of Plant Physiology, 22: 885–892, 1995.
64. A. Lal, G.E. Edwards, Analysis of inhibition of photosynthesis under water stress in the C_4 species *Amaranthus cruentus* and *Zea mays*: electron transport, CO_2-fixation and carboxylation capacity, Australian Journal of Plant Physiology, 23: 403–412, 1996.
65. M. Aldea, J.G. Hamilton, J.P. Resti, A.R. Zangerl, M.R. Berenbaum, E.H. DeLucia, Indirect effects of insect herbivory on leaf gas exchange in soybean, Plant, Cell & Environment, 28: 402–411, 2005.
66. M.J. Fryer, J.R. Andrews, K. Oxborough, D.A. Blowers, N.R. Baker, Relationship between CO_2-Assimilation, Photosynthetic Electron Transport and Active O_2 Metabolism in Leaves of Maize in the Field during Periods of Low Temperature, Plant Physiology,116: 571–580, 1998.

67. D.R. Ort & N.R. Baker, A photo-protective role for O_2 as an alternative electron sink in photosynthesis, Current Opinion in Plant Biology, 5, 193–198, 2002.

Chapter 5

Chapter 5: Summary, conclusions, method assesment and future work

Chapter 5: Summary, conclusions, method assesment and future work

5.1 Summary

5.1.1 Environmental plant stress

Enviromental stress has been shown to cause significant adverse effects on the growth and productivity of plants. A rise in the world population, coupled with diminishing suitable agricultural environments, have placed great emphasis on the development of sustainable high yield agricultural practices.[1] A 2007 FAO report stated that only 3.5% of the global land area is not affected by some environmental constraint.[2] Environmental stress can be catagorized into 2 main types: i) naturally occurring abiotic stress and ii) abiotic stress of anthropogenic (industrial) origin. If we are to succeed in effectively feeding the growing population a multi-pronged approach will have to be employed. This approach includes the use of effective fertilizer and pest management regimes, choosing the correct crop species and cultivar for a given set of environmental conditions and if possible modifying (by genetic modification) the stress tolerance of crop species to produce higher yields under stressful conditions. Finally, minimizing our contribution towards creating unfavourable agricultural conditions through anthropogenic activities stands central in this multi-pronged approach.

Plant responses to stress have been shown to be very complex in nature.[3] Stress responses range from stress avoidance mechanisms, activation of stress related genes involved in stress signalling and finally the synthesis of substances involved in stress alleviating (quenching) mechanisms.[3] Plant responses to stress is determined by a number of factors, which include the following:[4]

i) Type of stress
ii) Severity of the stress (concentration dependence)
iii) Type of species and cultivar subjected to a specific stress
iv) Duration of the stress (how long does the stress last)
v) Growth stage of the plant

5.1.2 Industrial related plant stress in South Africa

As stated in Chapter 1, maize production is of particular importance in South Africa, not only from an economical but also from a food security point of view. Maize is primarily grown on the Highveld region in South Africa, which unfortunately also coincides with the largest concentration of industrial activities in South Africa (see Figures 1.3 and 1.4).[1,2] Industrial activities are a well known contributor to a range of environmental pollutions. Three main types of industrial related sources of pollution have been identified: i) Liquid (ionic pollution such as heavy metal ions), ii) gaseous (air pollution

such as ozone) and solid state particulate matter (such as very fine metal oxide nano-particulates). These pollution sources have been shown to have a significant impact on the environment.[3]

In South Africa, the mining industry has been signalled out as the major contributor to pollution, especially in the Highveld area, which subsequently caused it to be identified as a priority area in an attempt to monitor and reduce pollution emissions.[1,2] Not only mining itself, but other processes surrounding the processing and downstream beneficiation of the mined material has also been shown to be significant pollution sources. In Chapter 1, a detailed review of the processes involved in attributing to the liquid, gaseous and particulate matter sources of pollution was given. The review provided in Chapter 1 identified heavy metal pollution, O_3 pollution and metal oxide particle matter (nano-materials) as industrial related pollution sources that have the potential to have a major impact on maize production in the Highveld priority area.

This main focus of this thesis was mainly to investigate the impact of these identified industrial related abiotic stresses on South African *Zea mays L.* cultivars, by assessing the photosynthetic performance in terms of either their electron transport efficiency, CO_2-assimilation, or both. This was done in order to obtain a better understanding of the photosynthetic limitations imposed by the aforemention stress types on South African maize.

5.2 Conclusions

5.2.1 Chapter 2: Evaluation of the photosynthetic electron transport performance of a South African maize cultivar (IMP 52-11) under varying copper, manganese, iron and zinc concentrations

The aim of Chapter 2 was to establish whether rapid non-invasive tecqniques such as chlorophyll *a* fluorescence and modulated 820 nm reflection could be used as a rapid technique to detect and quantify simultaneously (using an M-Pea instrument) the effect of excess concentrations of various transition (heavy) metals (Cu, Mn, Fe and Zn) on PSI and PSII electron transport performance. The excess concentration was chosen in a way as to simulate previously reported metal concentrations in and around mining and other industrial sites in the Highveld area (see Chapter 1 and 2). The water has high concentrations of iron and other base metals, often reaching metal concentrations of up to 70-130 $mg.L^{-1}$ in water sources adjacent to the mine areas as well as water sources that are fed by AMD runoff streams.[4] As a result of the persistency of heavy metals in the environment, a significant build-up of metals in water sources and the soil have been reported to be in the order of 0.5-1.0 mM.[4] As mentioned in Chapter 1, these concentrations vary greatly, depending primarily on the amount of rainfall and the distance from the pollution site.

This study was done in order to gather more information on the mechanistic limitations imposed on both PSI and PSII electron transport in the South African IMP 52-11 maize cultivar. Not only excess,

but also deficient metal concentrations were evaluated. This was done to simulate metal deficiencies caused by excess metals of a different type, seeing that the absorption of these metals take place in a competitive manner.

Deficiency conditions of the various metals were found to have a deleterious effect on both PSII and PSI efficiency. The down-regulation of primary photosynthesis appeared to be site specific in some cases, which was due to the absence of the individual metal at its active site. The biophysical and biochemical parameters obtained by quantifying the chlorophyll *a* fluorescence transients of the treated plants suggested that the deficiency of all of the respective metals lead to a characteristic down-regulation of intersystem electron transport, reduction of end electron acceptors and apparent structural damage. MR_{820nm} data showed a significant ($p \leq 0.05$) decline in both the v_{ox} and v_{red} parameters for all metal deficiencies, which points to marked PSI electron transport inhibition. To our knowledge, the data presented in Chapter 2 was the first study to report on both PSII and PSI electron transport effciciency for the deficiency of such a range of plant essential metal types.

Excess concentrations (≥ 0.5 mM) of these metals showed a strong concentration dependent inhibitory effect, in which the highest concentration exhibited the greatest down-regulation of photosynthesis. This is in agreement with the theory of plant stress proposed by Levitt 1980, which is based on the model of physical deformation of a body placed under strain (stress).[9] Analysis of the chlorophyll *a* fluorescence transient and related JIP-parameters showed increasing electron inhibition with increasing metal concentrations. At the highest metal concentration (1 mM), all of the metal types exhibited similar changes in the fluorescence transient, with the data suggesting several sites of electron transport inhibition in the single and multiple turnover regions (see Figure 2.8 A-D in Chapter 2).

Previous studies have attributed this phenomenon to several possible mechanisms. One of which is the result of the inherent redox active nature of metals such as copper and iron, causing the formation of large amounts of ROS species (Fenton reaction) and subsequent damage to electron transporters.[11,12] The ROS concentration was not measured during the study in Chapter 2, so one can only speculate whether this indeed had an impact on electron transport. Other authors have presented evidence of electron transport inhibition by the exchange of divalent cations between excess amounts of certain metals that form vital constituents of transporters within the electron transport chain (see Figure 2.1 in Chapter 2). [11-15] The data obtained in the current study supported the hypothesis of cation exchange at specific sites within the electron transport chain. In this study we were able to distinguish clearly where the inhibitions sites were, by constructing and identifying specific differential fluorescence bands and calculating various JIP-parameters. By making use of MR_{820nm} measurements, significant ($p \leq 0.05$) down-regulation of PSI electron function at the highest metal concentrations (for all metal

types) was seen. To our knowledge both PSI and PSII electron transport has never been reported using South African maize cultivars, especially not for such a range of metal types.

Futhermore, deficient and excess metal concentrations resulted in a reduction of biomass as a consequence of the observed downregulation in electron transport efficiencies. Decreases in root and shoot biomass were also observed, but no obvious change in the root/shoot ratio was apparent.

In Chapter 2, chlorophyll *a* fluorescence and modulated 820 nm reflection was successfully used as a rapid technique to elucidate simultaneously (using an M-Pea instrument) the effect of excess and deficient concentrations of various transition metals (Cu, Mn, Fe and Zn) on PSI and PSII electron transport performance at previously reported metal concentrations.[4] Furthermore, valuable information on the mechanistic limitations imposed by these metal concentrations on both PSI and PSII electron transport in the South African IMP 52-11 maize cultivar, were obtained.

5.2.2 Chapter 3: Evaluation of the photosynthetic response of two South African maize cultivars IMP 52-11 and PAN 6114 under varying O_3 concentrations in Open-top chamber conditions

One type of gaseous environmental pollution that has been identified in the Highveld priority area is ozone (O_3). The prevalence of O_3 in the Highveld area has mostly been attributed to the coal-fired power stations and other volatile chemical manufacturing industries in the Highveld areas. Ozone is thus considered as a secondary atmospheric pollution, seeing that O_3 is not a direct result of the coal-fired powerstations, but rather a result of O_2 reacting with radicals produced during increases in NO_x gasses (See reaction equations 2 and 3 in Chapter 1). According to Figure 1.5, the highest O_3 concentration areas once again coincided with the Highveld maize production areas. Recently studies have reported (Figure 3.1) that the monthly maximum mean levels measured in the Highveld area were about 100 ppb O_3 and the annual average was 62 ppb O_3, with the hourly O_3 means reaching levels of up to 130 ppb.[5]

The aim of Chapter 3 was to evaluate the O_3 sensitivity of two popular South African maize cultivars (IMP 52-11 and PAN 6411) with regard to to the photosynthetic electron transport (JIP-test) and photosynthetic gas exchange. The reponse of the two cultivars at varying O_3 concentrations was monitored using chlorophyll *a* fluorescence coupled with MR_{820nm}, as well as photosynthetic gas exchange. The O_3 concentrations (40 ppb, 80 ppb and 120 ppb) were chosen in an attempt to closely simulate the reported O_3 levels in some of the most O_3 polluted sites in the Highveld. Furtermore, it was decided to use two maize cultivars in order to ascertain whether any difference in O_3 sensitivity between the two South African maize cultivars could be seen. The obtained data suggested a differential O_3 sensitivity between the two respective cultivars, which has only previously been

reported in two South African varieties of *Phaseolus Vulgaris L.*[6] To our knowledge this was the first study to report discernible differences in two maize cultivars (in South Africa at least).

Differences in percentage stomatal limitation (*l*), carboxylation efficiency (V_{pmax}) and PEPc regeneration rate (J_{max}) became apparent from the data (Figure 3.3 A and Figure 3.4 A & B in Chapter 3). The IMP 52-11 cultivar appeared to be more sensitive to increasing O_3 concentrations, exhibiting significant ($p \leq 0.05$) negative effects on the stomatal function and the efficiency of the primary carboxylation enzyme (PEPc), at O_3 concentrations as low as 80 ppb. PAN 6411 seemed to be more tolerant to O_3 with regard to these photosynthetic functions. Both cultivars showed significant ($p \leq 0.05$) decreases at the 120 ppb O_3 treatment. The data thus clearly suggested differences in stomatal behaviour and PEPc activity at the various O_3 concentrations.

The trends from the chlorophyll *a* fluorescence and MR_{820nm} data correlated well with the photosynthetic gas exchange data, with IMP 52-11 showing a larger decrease in electron transport efficiency, compared to PAN 6411. The data showed that the biophysical and biochemical (JIP) parameters (obtained by analysis the chlorophyll *a* fluorescence transients; see Figure 3.15 A & B) of the O_3 treated plants were significantly ($p \leq 0.05$) lower for the IMP 52-11 cultivar at both the 80 ppb and 120 ppb O_3 treatments, whilst significant ($p \leq 0.05$) down-regulation could only be seen at the 120 ppb O_3 treatment in the PAN 6411 cultivar. The $MR_{820\ nm}$ data also showed significant ($p \leq 0.05$) decreases in the v_{OX} and v_{red} values (Figure 3.14 A & B) at the 80 ppb and 120 ppb O_3 treatments in IMP 52-11, whereas PAN 6411 once again only showed a significant ($p \leq 0.05$) decrease at the 120 ppb O_3 treatment. The data from the chlorophyll *a* fluorescence and MR_{820nm} measurements suggested a difference in PSI and PSII electron transport O_3 sensitivity. This is also the first study to report differences in both PSI and PSII electron transport O_3 sensitivity in maize cultivars.

Furthermore, by relating the v_{ox} parameter from the MR_{820nm} measurements to the J_{max} parameter from the photosynthetic gas exchange measurements, a coupled (electron flux) model was constructed. The model could show for the first time (using a simple model), increased decoupling between the relative electron transport rate through PSI (v_{ox}) and electron transport rate used towards PEPc regeneration with increasing stress severity. This finding supports previous studies from Asada 2006 and Pospíšil 2009 who reported terminal electron losses at PSI.[7,8] A parameter describing the % decoupling between PSI and PEPc regeneration, ε, was also proposed for the first time. It was shown that at O_3 concentrations $\leq$ 40 ppb, no marked decoupling was seen for both maize cultivars. However, IMP 52-11 showed a significant ($p \leq 0.05$) increase in ε at the 80 ppb and 120 ppb O_3 treatments, whereas the PAN 6411 only showed a significant ($p \leq 0.05$) increase in ε at the 120 ppb O_3 treatment. These observations are in agreement with the observed changes in photosynthetic gas exchange, as well as the PSI and PSII electron transport for the two maize cultivars. The increase in ε (with increasing O_3 concentration) means that an increasing number of electrons are not being used in the carboxylation

reactions. In Chapter 3 we hypothesized that these electrons are lost to alternative electron acceptors such as O_2, which will result in an increase in ROS. However, the concentration of the ROS was not measured in Chapter 3, which prompted us test this hypothesis by constructing the same model (to illustrate the effects of particle matter (PM) on maize photosynthesis) in the following chapter, whilst also measuring the ROS and ROS marker concentrations, as well as some antioxidant activities. This was done to see if a correlation existed between ROS formation and increases in ε.

5.2.3 Chapter 4: Evaluation of the photosynthetic response of *Zea mays L.* to TiO_2 and SiO_2 nano-particulate foliar exposure using photosynthetic gas exchange and chlorophyll *a* fluorescence

Anbother type of environmental pollution that has been identified in the Highveld priority area is particulate matter (PM). As mentioned in Chapter4, emissions of PM caused by anthropogenic activities arise primarily from four source categories: fuel combustion, industrial processes (mining, construction), non-industrial fugitive sources (roadway dust from paved and unpaved roads, biomass burning, wind erosion of cropland, agricultural activities) and transportation sources. The total amount of PM of most major cities often register values above 50 $mg.m^{-3}$.[9,10] The industrial Highveld region accounts for approximately 90% of South Africa's scheduled emissions of particulate matter, SO_2 and NO_x.[11] The most distinguishing characteristics of PM are the particle size and the chemical composition. Particle size has the greatest influence on the behaviour of PM in the atmosphere with smaller particles tending to have longer residence times than larger ones.[11]

Recent advances in the field of nanotechnology have caused a dramatic increase in the manufacturing of such nano-material, which are exploited for their unique chemical and physical properties. Anthropogenic emissions are a big contributor to the release of nano-sized PM into the biosphere. No studies have been conducted in South Africa to determine the volume of such particles that are being released into the environment. Studies in Europe and especially countries like Switzerland have estimated significant amounts of such materials may be released into the environment annually, which have been shown to have a deleterious effect on a range of organisms and several plant species (See Chapter 4 for reported instances).[12,13] The point of origin of such particle releases into the invironment have been shown to coincide with heavily industrialized areas, which makes the industrialized Highveld region in South Africa a prime candidate as a possible contributor to such a type of environmental pollution.

The aim of Chapter 4 was to evaluate the influence of varying concentrations of two types of such nanoparticles (TiO_2 and SiO_2, which are known to be produced in very high worldwide quantities annually) on maize. Because no data on the amount of these particles in the environment exist for South Africa, the study was done with the aim to serve as a pilot study, in order to test the sensitivity

of the most important crop specie (maize) in South Africa to exposure of such particle types. Because of the sensitivity of photosynthesis to environmental stress, it should therefore provide a good indication of the sensitivity of the maize plants in response to such particle exposures. Photosynthetic activity of the maize plants was monitored by measuring their photosynthetic electron transport and gas exchange properties.

Firstly, the TiO_2- and SiO_2 nanoparticles were found to have contrasting effects on the stomatal behaviour of the maize plants. TiO_2 nanoparticles caused a progressive increase in stomatal conductance and C_i (decrease in stomatal limitation, *l*), whilst SiO_2 nanoparticles caused a progressive decrease in stomatal conductance and C_i (increase in stomatal limitation, *l*), with increasing concentration (see section 4.3.1.2 in Chapter 4). Subsequently, the increase in stomatal conductance with increasing TiO_2 nanoparticle concentration also caused a marked decrease in water use efficiency (WUE) of the treatment plants, becoming significant ($p \leq 0.05$) at the 0.5% and 2% TiO_2 treatments. Interestingly, at the SiO_2 treatments, only the 0.5% SiO_2 treatment resulted in an improvement in the WUE, which can be attributed to negative effects of the 2% SiO_2 treatment on the carboxylation reactions and hence A (assimilation), given that WUE = A/E.

Titanium dioxide exhibited significant ($p \leq 0.05$) limiting effects on both the carboxylation efficiency (V_{pmax}) and the regeneration rate of PEPc (J_{max}) at the 0.5% and 2% TiO_2 treatments, whereas only the 2% SiO_2 caused significant ($p \leq 0.05$) reductions in V_{pmax} and J_{max}, suggesting differential concentration dependent limiting effects between the two types of nanoparticles.

The 0.5% and 2% TiO_2 treatments also caused significant ($p \leq 0.05$) decreases in PSII and PSI electron transport efficiency (as seen from the chlorophyll *a* fluorescence and MR_{820nm} data in Figure 4.11-13, Table 4.2 and Table 4.3 in Chapter 4). These decreases were attributed to the photocatalytic activity of the TiO_2 nanoparticles, which have the capacity to generate large amounts of ROS, causing over-reduction of electron transporters and further ROS formation. Only the 2% SiO_2 treatment caused a significant ($p \leq 0.05$) decrease in PSII (JIP-parameters) and PSI (v_{OX} and v_{red}) electron transport efficiency. This decrease was attributed to a marked decline in stomatal conductance (CO_2 uptake), which lead to a decrease in the electron demand from carboxylation reactions, causing an accumulation of reduced PSII and PSI electron carriers.

The decoupling model proposed in Chapter 3 (which showed the increased electron losses between PSI and CO_2-assimilation reaction) was once again constructed to illustrate the increase in the % decoupling (ε) with increasing nanoparticle concentrations, suggesting that an increasing amount of electrons are lost between PSI and CO_2-assimilation. In Chapter 3 an increase in ε was also observed with increasing O_3 concentrations, where it was hypothesized that the electrons were being lost to alternative electron acceptors such as O_2, subsequently leading to increased ROS formation. In

Chapter 4 this hypothesis was supported by the measured increase in ROS, ROS markers and antioxidant activity (Table 4.4).

5.3 Method assessment

The process of photosynthesis consists of two different reaction phases, i.e. light-dependent - and light independent phases (more accurately called the biochemical phase). The light-dependent phase occurring in the thylakoid membranes comprises of a range of biophysical and biochemical processes, which includes photon absorption through light harvesting pigments, trapping of incoming excitation energy by special reaction centers (RCs) on the light harvesting pigments, in order to produce a chemical potential. At the same time water is split by an oxygen evolving complex (OEC) into protons, oxygen and electrons, followed by the reduction of a range of electron acceptors to finally produce the 'fuel' (NADPH and ATP) that drives the subsequent biochemical reactions. The biochemical phase, taking place in the stroma of the chloroplasts, involves a cyclic series of enzyme catalyzed reactions (Calvin cycle) in which CO_2 and electrons (from ATP and NADPH) are consumed to eventually produce carbohydrates (biomass).[14,15]

Although these two phases have mechanistically very different pathways and the end products are quite contrasting, they are closely interlinked. Several authors have shown that under 'normal' conditions, the light-dependent and biochemical phases of photosynthesis are closely co-regulated.[16,17] This co-regulatory phenomenon effectively implies that when one of the two phases is limited by some kind of stress (external or internal), the other responds accordingly, in an attempt to restore the equilibrium between the two phases (supply and demand). In order to gain a full understanding of the effect of a given stress on photosynthesis, the response of both these phases have to be monitored. One must first understand the underlying mechanisms involved, before observed changes caused by a particular stress can be explained.

Different techniques were developed over the years to elucidate the mechanisms involved in these distinct phases. In the current study, fast kinetics chlorophyll *a* fluorescence and MR_{820nm} was employed to follow the light-dependent reactions (energetic behaviour of a photosynthetic system) of PSII and PSI respectively, whilst *in vivo* photosynthetic gas exchange measurements was used to quantify the CO_2-assimilation and biochemical reactions of photosynthesis.

Fast kinetics chlorophyll *a* fluorescence and MR_{820nm} can be seen as indirect measurement techniques that link the fluorescence and reflection signals of the polyphasic fluorescence rise (O-J-I-P transient) and ratio MR/MR_0 to the biophysics of the photosynthetic system, if appropriate theory/methodology is applied.[18] Both signals have become widely accepted as effective *in vivo* techniques to follow the transfer and fate of excitation energy originating from incoming photons.[18] A model by which O-J-I-P transients can be analysed was developed by Strasser and co-workers 2000, by which rate constants of

energy fluxes (JIP-test) are used to correlate the changes in these inflection points (O-J-I-P) to biophysical parameters, with regard to structural changes in antennae pigments (size and absorption capacity), grouping or connectivity between pigment assemblies, as well as quantum yields and probabilities of electron (energy) transfer between the various electron transport entities (please see Figure 1.14 and Table 1.5 in Chapter 1 for a summary of popular parameters that can be calculated).[18] Furthermore, recently defined parameters described in papers by Strasser *et al.*, 2010, Oukarroum *et al.*, 2010 and Salvatori *et al.*, 2014, describe in detail the handling and nomenclature around some of the parameters that can be obtained by the MR_{820nm} signals.[19-21] The model by Strasser *et al.*, 2000 applied to fast kinetics chlorophyll *a* fluorescence transients together with the processed $MR_{820\ nm}$ data, was successfully employed in Chapter 2-4, where significant changes and logical trends in the related parameters were observed for the respective treatments.[18]

Whereas fast kinetics chlorophyll *a* fluorescence and MR_{820nm} signals are indirect measurements of the light-dependent reactions, photosynthetic gas exchange directly measures actual changes in CO_2-assimilation rates (CO_2-exchange and biochemical reactions) *in vivo*, using an infra-red photosynthetic gas exchange analysis system (IRGA). The model of Farquhar and Sharkey 1982 and von Caemmerer was used to calculate and interpret the gas exchange data. Limitations (at a given set of conditions) with regard to CO_2-acquisition (stomatal limitation), CO_2-assimilation rate (mesophyll limitation) could be distinguised.[22,24] As discussed in Chapter 1, applying the analysis method of Pammenter 1989, A:C_i response curves can be used to calculate C_i, V_{cmax} (carboxylation efficiency, CE), stomatal conductance to CO_2 (g_{CO_2}) as well the CO_2 compensation point (Γ).[23]

Although the independent techniques are efficient (in their own right) to analyse the distinct phases of the photosynthetic process, most authors agree that when using the respective techniques in combination, much greater detail is provided about possible changes in these phases that may be provoked by a certain set of conditions, given the fact that the light-dependent and biochemical phases of photosynthesis are co-regulated.[7,8] In Chapter 3 and 4, this fact was practically demonstrated by correlating the data obtained by the indirect measurement signal of MR_{820nm} to the direct gas exchange measurements, making use of a proposed coupled model (Figure 3.16 A & B; Figure 4.17 A & B). This allowed us to illustrate an increased 'decoupling' (energy or electron losses) between the two photosynthetic phases with increasing stress severity.

5.4 New knowledge gained

The current study allowed us to identify the sensitive parts of electron transport to different metal concentrations (Chapter 2). Downregulation of PSI and PSII electron transport could be visualized for a range of metal types and concentrations. As far as is known, this was the first study to measure (*in*

vivo), the effect on PSI and PSII electron transport, of such a range of essential metal types in *Zea mays L.*.

Moreover, this study was the first study to report differences in O_3 sensitivity between two respective *Zea mays L.* cultivars (PAN 6411 and IMP 52-11). The study can serve as a guideline for crop producers in O_3 affected areas on which type of cultivars to use. The current study was also the first to report, in so much detail, the influence of O_3 on both PSI and PSII electron transport as well as photosynthetic gas exchange in *Zea mays L.* (Chapter 3). Furthermore, the combination of $MR_{820\ nm}$ and photosynthetic gas exchange allowed the proposal of a coupled model, which made it possible to see increasingly greater 'decoupling' (ε) between PSI electron transport and CO_2-assimilation with increased stress severity. Such a model has never been put forward in the literature to describe this phenomenon.

In Chapter 4, the effect of nano-TiO_2 and nano-SiO_2 on a C_4-plant (*Zea mays L.*) was compared for the first time. No literature measuring the effect of any type of nanoparticle on PSI and PSII electron transport combined with photosynthetic gas exchange was available prior to this current study. This permitted much more insight into the mechanistic effects of the two types of nanoparticles on plants. In addition to these new insights, the coupled model from Chapter 3 was also constructed by using the CO_2-assimilation data (J_{max}) and PSI activity data (v_{OX}), which revealed an increase in ε (with increasing nanoparticle concentration). Together with the increase in ε, an increase in the concentration of ROS, ROS markers and the activity of key antioxidant enzymes was also seen, supporting the hypothesis (set forth for the first time in Chapter 3) that increasing amount of electrons were lost to alternative the electron acceptors (with increasing nanoparticles concentration), such as O_2.

5.5 Future work

For future research it is suggested that other *Zea mays L.* cultivars are screened for O_3 resistance characteristics, using the same techniques described in Chapter 3, in an attempt to find the most suitable cultivar for the most O_3 affected areas in South Africa. Furthermore, ROS markers and the activity of key antioxidant enzymes should also be monitored to confirm the hypothesis that variances in cultivar sensitivity does indeed originate from differences in antioxidant capcity between the various cultivars. Different cultivars of other economically important crop species such as *Sorghum bicolor* and *Glycine max,* that are planted in the O_3 affected areas, should also be evaluated in order to find the most resistant cultivar. These research studies are important to minimize yield losses resulting from increased O_3 levels.

Additionally, it is also suggested that the waste streams and irrigation water sources are monitored to determine the amount of nanoparticles that are being released from heavily industrialized areas, such as smelters, mining and manufacturing sectors. The most prevalent nanoparticles should be identified and the response of a range of species to these these nanoparticles should be studied, by using the techniques described in Chapter 4 as a direct and effective screening method.

It would be of considerable interest to apply the coupled model suggested in Chapter 3 and 4, to see whether the same phenomemon of 'decoupling' between electron transport and CO_2-assimilation, with increasing stress severity, can be observed for other species. It would be of particular interest to check if C_3-plant species exhibit the same increase in 'decoupling' with increasing stress severity.

Lastly, the authours of this thesis feel that the knowledge gained through in this thesis can be used to as a stepping stone, allowing for the rapid and non-invasive 'stress-screening' of vegetation in industrialized areas in South Africa (or anywhere else). Furthermore, because of the rapid and non-invasive nature of chlorophyll *a* fluorescence and photosynthetic gas exchange measurements, it becomes possible to map out entire polluted areas in terms of the stress severity experienced by vegetation in such affected areas. In addition, by using the non-invasive techniques, we were able to identify differential ozone sensitivity between two South African maize cultivar types. This information and tecqniques can be used to screen for other abiotic stress type resistant species and cultivars, in order to establish which are best suited for a specific set of conditions.

5.6 References

1. Report: Trends in the Agricultural Sector, South African Department of Agriculture, Forestry and Fisheries, 2013.
2. T.S. McCarthy, The impact of acid mine drainage in South Africa, South African Journal of Science 107, 712-719, 2011.
3. D.W. Blowes, C.J. Ptacek, J.L. Jambor, C.G. Weisener, The geochemistry of acid mine drainage, In: Holland HD, Turekian KK, editors. Treatise on geochemistry. Oxford: Elsevier, p. 150–204, 2003.
4. L. Coetzee, H.H. du Preez, J.H.J. van Vuren, Metal concentrations in *Clarias gariepinus* and *Labeo umbratus* from the Olifants and Klein Olifants River, Mpumalanga, South Africa: Zinc, copper, manganese, lead, chromium, nickel, aluminium and iron, ISSN 0378-4738 = Water SA Vol. 28 No. 4 October 2002.
5. L. Laakso, J.P. Beukes, P.G. Van Zyl, J.J. Pienaar, M. Josipovic, A. Venter, K. Jaars, V. Vakkari, C. Labuschagne, K. Chiloane and J. Tuovinen, Ozone Concentrations and Their Potential Impacts on Vegetation in Southern Africa, Developments in Environmental Science, Global Dimension of Air Pollution as Part of Climate Change, Vol. 13, Chapter 20, Elsevier, 2013.
6. C.W. Scheepers, R.J. Strasser, G.H.J. Kruger, Effect of Ozone on Photosynthesis and Seed Yield of Sensitive (S156) and Resistant (R123) *Phaseolus Vulgaris* L. Genotypes in Open-Top Chambers, T. Kuang *et al.*, Photosynthesis Research for Food, Fuel and the Future, Zhejiang University Press, Hangzhou and Springer-Verlag Berlin Heidelberg, 2013.
7. K. Asada, Production and scavenging of reactive oxygen species in chloroplasts and their functions, Plant Physiology, 141, 391–396, 2006.
8. P. Pospíšil, Production of reactive oxygen species by photosystem II, Biochimica Biophysica Acta, 1787, 1151–1160, 2009.
9. E.J. Joner, T. Hartnik, and C.E. Amundsen, Environmental fate and ecotoxicity of engineered nanoparticles, in Norwegian Pollution Control Authority Report no. TA 2304/2007, pp. 1–64, Bioforsk, As, Norway, 2008.
10. A. Pluskota, E. Horzowski, O. Bossinger, A. von Mikecz, In *Caenorhabditis elegans* nanoparticle-bio-interactions become transparent: silica-nanoparticles induce reproductive senescence, PLoS One, 4, 2009.
11. G. Held, B.J. Gore, A.D. Surridge, G.R. Tosen, C.R. TurnerR.D. Walmsley, (eds.), Air pollution and its impacts on the South African Highveld, Environmental Scientific Association, Cleveland, 144pp, 1996.

12. F. Gottschalk, T. Sonderer, R.W. Scholz, Modeled Environmental concentrations of engineered nanomaterials (TiO_2, ZnO, Ag, CNT, Fullerenes) for different regions, Environmental Science and Technology, 43, 9216–9222, 2009.
13. N.C. Mueller, B. Nowack, Exposure modeling of engineered nanoparticles in the environment, Environmental Science and Technology, 42, 4447–4453, 2008.
14. J.L. Hall, Cellular mechanisms for heavy metal detoxification and tolerance, Journal of Experimental Botany 53: 1-11, 2002.
15. J.B. Arellano, J.J. Lazaro, J. Lopez Gorge, M. Baron, The donor side of photosystem II as the copper-inhibitory binding site, Photosynthetic Research, 45:127–134, 1995.
16. K. Asada, Production and scavenging of reactive oxygen species in chloroplasts and their functions, Plant Physiology, 141, 391–396, 2006.
17. P. Pospíšil, Production of reactive oxygen species by photosystem II, Biochimica Biophysica Acta, 1787, 1151–1160, 2009.
18. R.J. Strasser, A. Srivastava, M. Tsimilli-Michael, The fluorescence transient as a tool to characterize the situation photosynthetic samples. In M Yunus, U Pathre, P Mohanty, eds, Probing photosynthesis: mechanisms, regulation and adaptation. Taylor & Francis, London, UK, pp. 445–483, 2000.
19. R.J. Strasser, M. Tsimilli-Michael, S. Qiang, V. Goltsev, Simultaneous *in vivo* recording of prompt and delayed fluorescence and 820 nm reflection changes during drying and after rehydration of the resurrection plant *Haberlea rhodopensis*, Biochimica Biophysica Acta, 1797: 122–122, 2010.
20. A. Oikarroum, V. Goltsev, R.J. Strasser, Temperature effects on pea plants probed by simultaneous measurements of the kinetics of prompt fluorescence, delayed fluorescence and modulated 820 nm reflection, PLoS ONE, 8 (3), e59433, 2013.
21. E. Salvatori, L. Fusaro, E. Gottaradini, M. Pollastrini, V. Goltsev, R.J. Strasser, F. Bussotti, Plant stress analysis: applications of Prompt, Delayed chlorophyll fluorescence and 820 nm modulated reflectance, Insights from independent experiments, Plant Physiology and Biochemistry, In Press, 2014.
22. G.D. Farquhar, T.D. Sharkey, Stomatal conductance and photosynthesis, Annual Reviews of Plant Physiology, 33: 317–345, 1982.
23. N.W. Pammenter, Research letter, Clarification of an apparent anomaly in the supply function associated with the response of carbon assimilation to carbon dioxide determined using conventional field equipment, South African Journal of Science, 85:271-272, 1989.
24. S. von Caemmerer, W.P. Quick, R.T. Furbank, The Development of C_4 Rice: Current Progress and Future Challenges, Science, 336, 1671–1672, 2012.